

Laser Transmission Micro-Machining of Transparent Material

Thesis submitted by

SUBHAM BISWAS

DOCTOR OF PHILOSOPHY (Engineering)

DEPARTMENT OF PRODUCTION ENGINEERING

**FACULTY COUNCIL OF ENGINEERING &
TECHNOLOGY**

JADAVPUR UNIVERSITY

KOLKATA-700032, INDIA

2022

**JADAVPUR UNIVERSITY
KOLKATA-700032**

**Index No. 192/15/E
Registration No. 1011516001**

TITLE OF THE Ph.D. (Engg.) THESIS:

Laser Transmission Micro-Machining of Transparent Material

**NAME, DESIGNATION & INSTITUTION OF THE
SUPERVISORS:**

(i) Dr. Arunanshu Shekhar Kuar

Professor, Department of Production Engineering,
Jadavpur University,
Kolkata – 700032, West Bengal, INDIA.

(ii) Dr. Ranjib Biswas

Associate Professor, Department of Mechanical Engineering,
Jadavpur University,
Kolkata – 700032, West Bengal, INDIA.

LIST OF PUBLICATIONS:

(a) International Journal

1. “Experimental Study of Partially Submerged Laser Transmission Channelling on Thick Poly(methyl methacrylate) (PMMA) Plate”, *Lasers in Engineering*, (2019), Vol. 44, pp. 289-311. ISSN: 0898-1507.
2. “Experimental Investigation of Varying Laser Pass on Micro-channel Characteristics of Thick PMMA by Laser Transmission Micro-machining”, *Materials Today: Proceedings*, Vol. 18 (2019) 3514–3520. DOI: <https://doi.org/10.1016/j.matpr.2019.07.280>.
3. “Study on kerf width deviation of microchannel with various medium in laser transmission cutting by diode pump fiber laser”, *Materials Today: Proceedings*, Vol. 26 (2020) 804–807. DOI: <https://doi.org/10.1016/j.matpr.2019.12.419>.

(b) National Journal : **NIL**

(c) Book chapter

1. “Experimental Investigations into Underwater Laser Transmission Micro-channeling on PMMA”, *Application of Lasers in Manufacturing; Lecture Notes on Multidisciplinary Industrial Engineering*, Eds: Dixit U., Joshi S., Davim J., Springer, Singapore, 2019, pp. 209-229. DOI: https://doi.org/10.1007/978-981-13-0556-6_9.

(d) International Conference

1. “Experimental Investigation on Underwater Laser Transmission Micro-channeling on PMMA”, *Proceedings of 6th International & 27th All India Manufacturing Technology, Design and Research Conference (AIMTDR-2016)*, December 16-18, 2016 at College of Engineering, Pune, Maharashtra, INDIA.
2. “Investigation on Depth of the Micro-Channels generated by Underwater Laser Transmission Micro-Machining”, *Proceedings of 10th International Conference on Precision, Meso, Micro and Nano Engineering (COPEN 10)*, December 07-09, 2017 at Indian Institute of Technology Madras, Chennai-600036, INDIA.

LIST OF PATENTS: NIL

LIST OF PRESENTATIONS IN NATIONAL/ INTERNATIONAL CONFERENCES/ WORKSHOPS:

Sl. No.	Name of Conference/Workshops	Type of Conference/Workshop (International/National)	Year	Organized by
1	6 th International & 27 th All India Manufacturing Technology, Design and Research Conference (AIMTDR 2016)	International Conference	2016	College of Engineering Pune, Maharashtra, India
2	International Conference on Precision, Meso, Micro and Nano Engineering (COPEN 10)	International Conference	2017	IIT Madras, India
3	9 th International Conference on Materials Processing and Characterization (ICMPC-2019)	International Conference	2019	GRIET, Hyderabad, India
4	10 th International Conference on Materials Processing and Characterization (ICMPC-2020)	International Conference	2020	GLA University, Mathura, India
5	Three Day National Workshop on Micromanufacturing	National Workshop	2016	Jadavpur University, West Bengal, India
6	One Day National Workshop on Laser	National Workshop	2016	Jadavpur University,

Sl. No.	Name of Conference/Workshops	Type of Conference/Workshop (International/National)	Year	Organized by
	Material Processing Technology			West Bengal, India
7	One Day National Workshop on Hybrid Manufacturing Technology	National Workshop	2017	Jadavpur University, West Bengal, India
8	One Day Workshop on Advanced Machining Processes	National Workshop	2017	Jadavpur University, West Bengal, India
9	Workshop on Laser Technology for Tactical Communication	National Workshop	2018	Jadavpur University, West Bengal, India
10	National Workshop on Intelligent & Micro-Manufacturing	National Workshop	2019	Jadavpur University, West Bengal, India
11	National Workshop on Intelligent Micro Manufacturing & Business Analytics	National Workshop	2020	Jadavpur University, West Bengal, India
12	National Workshop on Demystifying Pansophy	National Workshop	2022	Jadavpur University, West Bengal, India

“Statement of Originality”

I Subham Biswas registered on 28th December, 2015 do hereby declare that this thesis entitled “Laser Transmission Micro-Machining of Transparent Material” contains literature survey and original research work done by the undersigned candidate as part of doctoral studies.

All information in this thesis have been obtained and presented in accordance with existing academic rules and ethical conduct. I declare that, as required by these rules and conduct, I have fully cited and referred all materials and results that are not original to this work.

I also declare that I have checked this thesis as per the “Policy on Anti Plagiarism, Jadavpur University, 2019”, and the level of similarity as checked by iThenticate software is 8%.

Subham Biswas

.....
Subham Biswas

Date: 20/10/2022

Certified by Supervisor(s):

(Signature with date, seal)

Arunanshu Shekhar Kuar 20/10/22

1. Dr. Arunanshu Shekhar Kuar, Professor, Department of Production Engineering, Jadavpur University, Kolkata-700032.

Dr. Arunanshu Shekhar Kuar
PROFESSOR
Production Engineering Department
Jadavpur University
Kolkata - 700 032, India

Ranjib Biswas . 20/10/2022.

2. Dr. Ranjib Biswas, Associate Professor, Department of Mechanical Engineering, Jadavpur University, Kolkata-700032.

Associate Professor
Dept. of Mechanical Engineering
Jadavpur University, Kolkata-32

CERTIFICATE FROM THE SUPERVISORS

This is to certify that the thesis entitled "Laser Transmission Micro-Machining of Transparent Material" submitted by Shri. Subham Biswas, who got his name registered on 28th December, 2015 for the award of Ph.D. (Engg.) degree of Jadavpur University is absolutely based upon his own work under the supervision of Prof. (Dr.) Arunanshu Shekhar Kuar and Dr. Ranjib Biswas and that neither his thesis nor any part of the thesis has been submitted for any degree/diploma or any other academic award anywhere before.

Arunanshu Shekhar Kuar
20/10/22

Signature of the Supervisor
and date with official seal

Dr. Arunanshu Shekhar Kuar
PROFESSOR
Production Engineering Department
Jadavpur University
Kolkata - 700 032, India

Ranjib Biswas
20/10/2022

Signature of the Supervisor
and date with official seal

Associate Professor
Dept. of Mechanical Engineering
Jadavpur University, Kolkata-32

PREFACE

With the advancement of science and technology, there has been an increasing demand for new materials and processes to meet global competition and new duty conditions. The invention of various laser machining techniques has contributed immensely in this area. Laser produces highly collimated, coherent beam of light when it is focused to a small diameter; for which high energy density is produced and further utilized for machining applications. Laser beam machining is one of the most widely used thermal energy process that is used in different industries like automobile, aerospace, electronics, appliance and material processes. Due to the uniqueness of the process, it can be applicable for machining of most of the engineering materials. Furthermore, it is used due to advantages like non-contact type processing, adaptability of automation, accurate product with better surface finish with minimal heat affected zone (HAZ) and high productivity. It is difficult to fabricate micro-features on hard to machine materials in a series by using conventional machining processes. Laser beam machining (LBM) is a potential and successful technique which may be used to overcome such difficulties in machining advanced engineering materials to produce complex and intricate shapes with desired accuracy.

Laser cutting on transparent material is a challenging task as the laser possesses properties of light and can easily pass through the transparent material without affecting it. In case of thick transparent polymer, the direct laser machining causes burning, cracks, high heat affected zone. Laser transmission machining process may overcome these difficulties of machining transparent material. For this kind of workpiece (transparent material), the challenges can be addressed by using different machining aids, in different mediums and statistical tools.

Depending on the workpiece thickness and absorption coefficient of the absorbing material (coating material), the transmitted laser radiation is absorbed over a depth of that material, causing localized heating. This heat is transferred to the transparent material via thermal conduction, and the joining interface of both materials (transparent material and coating material) starts melting as the melting temperature or melting range is reached and the laser transmission micro-machining has appeared.

Laser transmission machining of transparent material is an emerging area of research. It is found that, research and development in this area is scarce and so far less progress has been achieved in this field. The transmission machining parameters, type of material and environmental factors significantly influence the quality of micro-machining. From the past research works carried out in this field, not much information is available so far as laser transmission machining of transparent material is concerned. Because of the capability to produce complex and intricate shapes in transparent material, effective utilization of the of laser transmission machining process is very much needed. Thus, it is obvious that for better control of the process, extensive research work is necessary to explore various aspects of this relatively newer process for machining transparent materials. The goals of the current research work have been combined as follows within the constraints of the available resources:

1. To study the chemical composition of the transparent PMMA, selected as the workpiece material and black sellotape as absorbent material using x-ray deffraction (XRD) test.
2. To understand the various subsystems of Nd: YAG & fiber laser micro-machining system so as to carry out laser beam micro-machining operation on PMMA.
3. To check the feasibility and study of the new processing technique of thick transparent polymethyl methacrylate (PMMA) which in turn helps to explore the possibility of machining on this kind of polymer using low power laser.
4. To set the design space from the observations of trial experiments, to carry out the final experiments based on central composite design (CCD) technique of response surface methodology (RSM).
5. To analyze the influence of process parameters on the quality characteristics of machined micro-channels on PMMA and also to carry out optimization analysis to determine the optimal parametric combination for achieving the desired value of responses at different assisted media.
6. To investigate and compare the quality characteristics of micro-channels when machined in dry medium (air) and wet medium (underwater).

The thesis is divided into nine chapters. An overview of each section is given below:

Chapter 1 provides a brief review of micro-machining, including the need for micro-machining and its characterization. This chapter discusses various types of laser systems used for micro-machining operations. Chapter 1 suggests that thermal machining is better suitable for laser beam machining than other unconventional micro-machining techniques in the micro-machining domain. In Chapter 1, discussion on assisted medium during laser beam micro-machining is followed by a thorough overview of laser matter interaction in both dry and wet medium. The impact of assisted medium to minimize the negative effects of laser beam micro-machining has been briefly described here. This chapter also covers particular applications for laser beam micromachining. In Chapter 2, the research objectives are outlined on the basis any information gaps that were discovered through the literature review. Chapter 3 provides information on the setup employed for laser beam machining and the development of a workpiece holding device for use in both air and water mediums. In Chapter 4, material specification has been discussed. This chapter also discusses various approaches that can be used to design experiments as well as analyse and improve experimental observations. Chapter 5 justifies the suitability of submerged conditions and the novelty of laser transmission technique (i.e., material removal technique) as well. A brief overview of the selection procedure of effective parameters for both types of lasers, the procedural steps for measurement of responses and primary investigations has been discussed in this chapter. In Chapter 6, experimental investigations of Nd:YAG laser transmission micro-channeling of transparent PMMA material in different mediums (i.e., air and underwater) has been conducted to study the influence of process variables on machining responses during machining a micro-channel on thick sheet. A second order polynomial model is developed during laser beam micro-channeling by response surface methodology (RSM) to establish the correlation between input and output of the process. Different Optimization techniques have been used to find out optimal parametric combination for PMMA work substrates and get the desired output within the chosen design space. In this chapter, laser passes were varied for each set of experiment to observe and analyze the process outcome. The effect of process variables on machining responses when generating a micro-channel on a thick sheet has been discussed in Chapter 7. Experiments of fiber laser transmission micro-channeling of transparent PMMA

material have been carried out in different mediums (i.e., air and underwater). Response surface methodology (RSM) is used to develop a second order polynomial model for laser beam micro-channeling in order to determine the relationship between input parameters and responses. Various optimization techniques are used to find out the best parameter settings for PMMA work substrates and to obtain the desired results within the design space that has been chosen. Chapters 5, 6 & 7 have also contained outcome of the research work after each experimental study. The comparative study of different environmental mediums (i.e., air and underwater) on machining responses during different laser (i.e., Nd: YAG and fiber laser) transmission micro-channeling of thick transparent PMMA material is the focus of Chapter 8. The overall findings of the current research work have been given in Chapter 9. The future scope of the present research work has also been included in this chapter.

Laser beam transmission micro-channeling on thick transparent material is a newly developed laser beam machining process. Till now, there is no such research work carried out by previous researchers in this field in which it has been reported that a 75-watt or 50-watt average power laser is capable of machining micro-channel on transparent PMMA material of 11.328 mm thickness. The experimental results obtained from the present research work can be useful in implementing laser transmission micro-channeling on PMMA with its end-use for application in the fields, like aerospace, biomedical, micro-electro-mechanical systems (MEMS), micro-fluidics, heat exchangers, etc. The outcome of the research will help industries and research institutes to utilize the laser machining process with improved effectiveness by reducing the time and effort required to generate the micro-fabricated or micro-machined features. Furthermore, this will help in finding the feasibility of using laser transmission micro-machining of transparent materials as well as the effect of parametric variation on selective materials. This will also provide an effective direction for further research that may be carried out in the field of advanced machining technology.

ACKNOWLEDGEMENT

Research work throughout last few years help me a lot to gain some new understanding and precious experience. The valuable work leading to the doctorate of philosophy (PhD) is impossible without help and support from many people and organization. At the very beginning, I would like to convey my warm gratitude and enthusiastic admiration to my PhD supervisors Professor (Dr.) Arunanshu Shekhar Kuar, Professor, Department of Production Engineering, Jadavpur University, and Dr. Ranjib Biswas, Associate Professor, Department of Mechanical Engineering, Jadavpur University, Kolkata, for their passionate guidance, valuable suggestions and constant support which are very much essential for the completion of my research work. I am so much grateful to both of them for their constant inspiration and consistent support through the inevitable ups and downs during the research and of course, continuous caring to focus and giving some fruitful advice in all aspects of my entire research. I always appreciate their contributions of valuable time, new ideas and keen interest to make my research experience fertile and motivating. And of course, it is an honor for me to be their Ph.D. student.

My sincere appreciation and thanks to Professor (Dr.) Bijan Sarkar, Head of the Department of Production Engineering, Jadavpur University, for his generous assistance and support in every stage of my research work. Thanks to other faculty members of the department especially Professor Bijoy Bhattacharyya, Professor Souren Mitra, Professor B. N. Doloi, Professor Soumya Sarkar, Professor S. Chakraborty, Professor D. Banerjee, Professor A. K. Dutta, Professor S. K. Debnath, Professor B. R. Sarkar, Professor A. G. Barman and Professor S. K. Saren of Department of Production Engineering, for extending all kind of help.

Author gratefully acknowledges the Centre of Advanced Study (CAS) Phase-V Programme of the University Grants Commission (UGC), New Delhi for their support, and Department of Production Engineering, Jadavpur University for providing the laboratory facilities. I also acknowledge the financial assistance provided by DST PURSE Phase II under Department of Science & Technology and center of excellence scholarship funded by TEQIP Phase III of Jadavpur University during the course of research study. Thanks are also extended to FET office and research section for their cordial assistance and administrative supports.

I would like to convey my deepest and heartfelt thanks to my seniors, juniors and my fellow colleagues Dr. Nilanjan Roy, Dr. Abhishek Sen, Dr. Subhrajit Debnath, Dr. Debal Pramanik, Dr. Somen Dey, Dr. Kingshuk Mandal, Md. Sahjahan Biswas, Mr. Rajat Dutta, Mr. Debojit Banerjee, Dr. Koushik Mishra, Mr. Sudip Santra, Mr. Himadri Sekar Panda, Mr. Naresh Besekar, Mr. Dhiraj Kumar, Mr. Santosh Kumar whose whole hearted support and cooperation in all spheres of activities during my entire tenure will remain in my memory.

Although it could not simply be expressed by words, I would like to thank my father Mr. Suresh Chandra Biswas and mother Mrs. Bibha Rani Biswas for their belief in education and endless support for education, sister Mrs. Suparna Biswas for their warm wishes, and all the family members and relatives for their constant encouragement and support in the pursuit of this research work, without their understanding none of this would have been possible.

Last, but not the least, there are limitless worth names, which deserve mention here, but it could not be possible to include in this section due to space constraints. I acknowledge their valuable contribution with gratitude.

Subham Biswas

TABLE OF CONTENT

	Page No.
TITLE SHEET	I
LIST OF PUBLICATIONS	II
LIST OF PRESENTATIONS IN NATIONAL/ INTERNATIONAL CONFERENCES/ WORKSHOPS	III
STATEMENT OF ORIGINALITY	V
CERTIFICATE FROM THE SUPERVISORS	VI
DEDICATION	VII
PREFACE	VIII
ACKNOWLEDGEMENT	XII
VITA	XIV
TABLE OF CONTENT	XV
LIST OF TABLES	XXIII
LIST OF FIGURES	XXV
Chapter 1: INTRODUCTION	1
1.1 Introduction	1
1.2 Laser Beam Micro-machining	2
1.2.1 Need and Advantages of Laser Micro-machining	2
1.2.2 Basic Principles of Laser Generation	7
1.2.3 Different Laser Sources	8
1.2.4 Different Types of Laser Pulses Regimes	12
1.3 Material Removal Process in Laser Beam Micro-machining	14

	Page No.
1.3.1 Absorptivity of Laser Irradiate Zone	14
1.3.2 Phase Change and Plasma Formation	15
1.3.3 Evaporation and Ablation	16
1.4 Applications of Laser in the Domain of Micro-manufacturing	17
1.5 Laser Beam Micro-machining with the Aid of a Different Assisted Medium	17
1.5.1 Laser Beam Micro-machining in the Compressed Air Medium	18
1.5.2 Laser Beam Micro-machining in the Underwater Medium	18
1.6 Importance of Micro-channeling of PMMA and its Application	19
Chapter 2: LITERATURE REVIEW AND OBJECTIVE OF PRESENT RESEARCH	23
2.1 Literature Review	23
2.2 Objective and Scope of Present Research Work	59
Chapter-3: DETAILS OF MACHINING SETUP AND FIXTURE OF WORKPIECE MOUNTING UNIT	61
3.1 Nd: YAG Laser Micro-machining System	61
3.1.1 Details of CNC Nd: YAG Laser Beam Micro-machining System	62
3.1.1.1 Laser Generation Unit	63
3.1.1.2 Beam Delivery and Focusing Unit	67
3.1.1.3 CCTV and CCD Camera	69
3.1.1.4 Cooling Unit	69
3.1.1.5 Work Holding Table and CNC Controller for X-Y-Z Axes Movement	71

	Page No.
3.1.2 Compressed Air Supply and Control Unit	72
3.2 Fiber Laser Micromachining System	72
3.2.1 Fiber Laser Generation Unit	75
3.2.1.1 Optical Fiber	76
3.2.1.2 Silicate Glass	77
3.2.1.3 Rare Earth Doped Elements	77
3.2.1.4 Fiber Bragg Gratings (FBGs)	78
3.2.1.5 Laser Diodes	78
3.2.1.6 Fiber Couplers	79
3.2.1.7 Fiber Laser Isolators	79
3.2.1.8 Fiber-Coupled Acousto-Optic Modulator	79
3.2.2 Fiber Laser Delivery System	80
3.2.2.1 Collimator	81
3.2.2.2 Beam Bender	82
3.2.2.3 Beam Delivery Unit and Focusing Lens	82
3.2.3 Assist Air Supply Unit	84
3.2.4 CNC Controller for X–Y–Z Movement	85
3.3 Fixture of Workpiece Mounting Unit	85
Chapter 4: MATERIAL SPECIFICATIONS AND EXPERIMENTAL	
METHODOLOGY	87
4.1 Material Specification	87
4.1.1 XRD Test of PMMA (Before Machining and After Machining) and Sellotape	89

	Page No.
4.2 Experimental Methodology	92
4.2.1 Response Surface Methodology	92
4.2.1.1 Central Composite Design (CCD)	95
4.2.1.2 Analysis of Variance (ANOVA)	95
4.2.1.3 Use of RSM Technique in the Present Study	96
Chapter 5: PRELIMINARY DETAILS AND INVESTIGATION OF THE STUDY	98
5.1 Introduction	98
5.2 Reason for Using Submerged Condition in Water	98
5.3 Material Removal Technique	99
5.3.1 Laser Transmission Technique	99
5.3.1.1 Advantages of this Novel Technique	101
5.4 Identification of the Effective Process Parameters	101
5.4.1 Selection of the Process Parameters for Nd:YAG Laser	101
5.4.2 Selection of the Process Parameters for Fiber Laser	102
5.5 Procedural Steps for Measurement of Responses	103
5.6 Primary Investigations	104
5.6.1 Preliminary Investigation for Micro-Channeling on PMMA Using Laser Transmission Technique in Nd:YAG Laser	104
5.7 Outcomes	111
Chapter 6: EXPERIMENTAL INVESTIGATION INTO PULSED Nd:YAG LASER MICRO-CHANNELING OF PMMA	112
6.1 Introduction	112
6.2 Background and Fundamentals	112

	Page No.
6.3 Parametric Study Based on Response Surface Methodology for Laser Beam Transmission Micro-channeling of PMMA with Air as an Assist Medium	113
6.3.1 Experimental Details	113
6.3.2 Results and Discussion	113
6.3.2.1 Development of Second-Order Polynomial Model	115
6.3.2.2 ANOVA of Machining Responses	116
6.3.2.3 Parametric Analysis of the Characteristics of Open-Air Laser Transmission Micro-Channeling of PMMA	120
6.3.2.4 Determination of Optimal Process Parameter Using Response Surface Methodology	130
6.3.2.5 Confirmation Test	133
6.3.3 Outcomes	134
6.4 Parametric Study Based on Response Surface Methodology for Laser Beam Transmission Micro-channeling of PMMA at Submerged Condition of Water Medium	135
6.4.1 Experimental Details	135
6.4.2 Experimental Results and Discussion	135
6.4.2.1 Development of Second-Order Polynomial Model	137
6.4.2.2 ANOVA of Machining Responses	138
6.4.2.3 Parametric Analysis of The Characteristics of Underwater Laser Transmission Micro-channeling of PMMA	142
6.4.2.4 Determination of Optimal Process Parameter Using Response Surface Methodology	152
6.4.2.5 Confirmation Test	155

	Page No.
6.4.3 Outcomes	156
6.5 Experimental Investigation of Varying Laser Pass on Micro-channel Characteristics of Thick PMMA by Laser Transmission Micromachining	157
6.5.1 Experimental Result and Discussion	158
6.5.1.1 For Depth of Cut	159
6.5.1.2 For Kerf Width	161
6.5.1.3 For HAZ width	163
6.5.2 Outcomes	165
Chapter 7: EXPERIMENTAL INVESTIGATION INTO DIODE PUMPED FIBER LASER MICRO-CHANNELING OF PMMA	167
7.1 Introduction	167
7.2 Background and Fundamentals	167
7.3 Parametric Study Based on Response Surface Methodology for Laser Beam Transmission Micro-channeling of PMMA with Air as an Assist Medium	168
7.3.1 Experimental Details	168
7.3.2 Results and Discussion	168
7.3.2.1 Development of Second-Order Polynomial Model	170
7.3.2.2 ANOVA of Machining Responses	170
7.3.2.3 Parametric Analysis	175
7.3.2.4 Determination of Optimal Process Parameter Using Response Surface Methodology	184
7.3.2.5 Confirmation Test	187
7.3.3 Outcomes	188

	Page No.
7.4 Parametric Study Based on Response Surface Methodology for Laser Beam Transmission Micro-channeling of PMMA at Submerged Condition of Water Medium	189
7.4.1 Experimental Details	189
7.4.2 Experimental Results and Discussion	189
7.4.2.1 Development of Second-Order Polynomial Model	191
7.4.2.2 ANOVA of Machining Responses	192
7.4.2.3 Parametric Analysis	196
7.4.2.4 Determination of Optimal Process Parameter Using Response Surface Methodology	206
7.4.2.5 Confirmation Test	208
7.4.3 Outcomes	209
Chapter 8: COMPARATIVE STUDY	211
8.1 Comparative Study of the Effect of Different Environmental Mediums on Machining Responses During Laser Transmission Micro-channeling of Thick Transparent PMMA Material	211
8.2 Trend of Parametric Effects on Responses at Different Mediums in Nd:YAG and Fiber Laser System with the Help of Polynomial Regression Equation	211
8.3 Comparative Study Based on Percentage Contribution of Parameters in Different Environmental Conditions	217
8.4 Comparative Study Based on Multi-Objective Optimization Results in Different Environmental Conditions	221
8.5 Comparative Study Based on the Average Value of Responses from the Experimental Data Table	223
8.6 Comparative Study Based on Percentage of Improvement of Responses	227

	Page No.
from Experimental Data Table in Different Laser Systems	
8.7 CCI and AFM Analysis of Micro-Channel in Different Medium	228
8.7.1 Open Air	228
8.7.2 Submerged in Water	230
Chapter 9: GENERAL CONCLUSIONS AND FUTURE SCOPE	
OF THE WORK	233
9.1 General Conclusions	233
9.2 Future Scope of Work	239
BIBLIOGRAPHY	240

LIST OF TABLES

Sl. No.	Table No.	Name of Tables	Page No.
1	Table 1.1	Various advanced micro-machining processes and their relative advantages, disadvantages, and applications	4
2	Table 3.1	Details of Nd:YAG laser machining set-up	61
3	Table 3.2	Details of chiller unit	70
4	Table 3.3	Specification of CNC table unit	71
5	Table 3.4	Specification of fiber laser beam machining system	74
6	Table 4.1	Property table of PMMA	88
7	Table 5.1	Physical characteristics used in the removal mechanism	99
8	Table 5.2	Influence of lamp current on the response criteria	105
9	Table 5.3	Influence of pulse frequency on the response criteria	106
10	Table 5.4	Influence of pulse width on the response criteria	108
11	Table 5.5	Influence of cutting speed on the response criteria	109
12	Table 6.1	Process variables and their levels	113
13	Table 6.2	Experimental results (micro-machining in Nd:YAG laser in air medium)	114
14	Table 6.3	ANOVA results of depth of cut at air medium	116
15	Table 6.4	ANOVA results of kerf width at air medium	118
16	Table 6.5	ANOVA results of HAZ width at air medium	119
17	Table 6.6	Confirmation test of laser micromachining at air medium	133
18	Table 6.7	Process variables and their levels	135
19	Table 6.8	Experimental result	136
20	Table 6.9	ANOVA results of depth of cut at submerged condition	138
21	Table 6.10	ANOVA results of kerf width at submerged condition	140
22	Table 6.11	ANOVA results of HAZ width at submerged condition	141
23	Table 6.12	Confirmation test of laser micromachining at air medium	155
24	Table 6.13	Range for input parameters of laser beam transmission micro-channeling	157

Sl. No.	Table No.	Name of Tables	Page No.
25	Table 6.14	Experimental results of single pass, double pass and triple pass for depth and HAZ width of the micro-channels	158
26	Table 7.1	Process parameters levels	168
27	Table 7.2	Experimental results (micro-machining in fiber laser in air medium)	169
28	Table 7.3	ANOVA result of depth cut at air medium	171
29	Table 7.4	ANOVA result of kerf width at air medium	172
30	Table 7.5	ANOVA result of HAZ width at air medium	174
31	Table 7.6	Confirmation test of laser micromachining at air medium	187
32	Table 7.7	Process parameter levels	189
33	Table 7.8	Experimental results (micro-machining in fiber laser in submerged medium)	190
34	Table 7.9	ANOVA result of depth of cut at submerged condition	192
35	Table 7.10	ANOVA result of kerf width at submerged condition	194
36	Table 7.11	ANOVA result of HAZ width at submerged condition	195
37	Table 7.12	Confirmation test of laser micromachining at underwater medium	209

LIST OF FIGURES

Sl. No.	Figure No.	Name of Figures	Page No.
1	Figure 1.1	Change of state and generation of photon	8
2	Figure 1.2	Different types of lasers	9
3	Figure 1.3	Different characteristics of laser	13
4	Figure 1.4	Underwater laser ablation processes	19
5	Figure 3.1	Schematic diagram of CNC Nd:YAG laser beam machining system	62
6	Figure 3.2	Photographic view of the CNC Nd:YAG laser machining system	63
7	Figure 3.3	Photographic view of RF-Q switch driver unit	66
8	Figure 3.4	Photographic view of intra cavity safety shutter	67
9	Figure 3.5	Photographic views of beam delivery and focusing unit	68
10	Figure 3.6	Schematic diagram of laser beam transformation	68
11	Figure 3.7	Photograph of CCD camera of Nd: YAG system	69
12	Figure 3.8	Schematic diagram of cooling unit	70
13	Figure 3.9	CNC controlled working table	71
14	Figure 3.10	Schematic view of compressed air regulating system	72
15	Figure 3.11	Photographic view of CNC pulsed fiber laser machining system	73
16	Figure 3.12	Schematic diagram of CNC fiber laser beam machining system	75
17	Figure 3.13	Photographic view of fiber laser generation unit	76
18	Figure 3.14	Optical fiber with refractive index distribution	77
19	Figure 3.15	Principle of AOM	80
20	Figure 3.16	Schematic representations of ytterbium-doped fiber laser head	80
21	Figure 3.17	Photographic view of the collimator	81
22	Figure 3.18	Photographic view of beam bender	82
23	Figure 3.19	photographic views of beam delivery unit and working table	83

Sl. No.	Figure No.	Name of Figures	Page No.
24	Figure 3.20	Photographic view of an air compressor with moisture separator	84
25	Figure 3.21	Schematic diagram of workpiece holding unit for laser transmission micromachining	86
26	Figure 3.22	Photographic view of workpiece holding unit for laser transmission micromachining	86
27	Figure 4.1	SEM view of PMMA (before machining)	89
28	Figure 4.2	X-RAY Diffractometer [RIGAKU, ULTIMA III, 40KV, 30mA (1.2kw)] Metallurgical and Material Engineering Department, JU)	89
29	Figure 4.3	Intensity vs. Two-Theta (PMMA test before machining)	90
30	Figure 4.4	Intensity vs. Two-Theta (sellotape material test)	90
31	Figure 4.5	Intensity vs. Two-Theta (micro-channel material test after machining)	91
32	Figure 5.1	Schematic diagram of laser transmission micro-channeling process (absorbent material used as black sellotape)	100
33	Figure 5.2	(a) PMMA workpiece without coating; and (b) Machining slots coated with gold after machining	100
34	Figure 5.3	OLYMPUS STM6 measuring microscope	104
35	Figure 5.4	Effect of lamp current on kerf width, HAZ width and depth of cut	105
36	Figure 5.5	Effect of pulse frequency on kerf width, HAZ width and depth of cut	107
37	Figure 5.6	Effect of pulse width on kerf width, HAZ width and depth of cut	108
38	Figure 5.7	Effect of cutting speed on kerf width, HAZ width and depth of cut	110
39	Figure 5.8	Machining samples and microscopic view of micro-channel characteristics	110
40	Figure 6.1	PMMA workpiece after Nd:YAG laser transmission cutting in air, (a) Parent sample, (b) Sliced micro-machined sample, (c) Gold coated micro-machined sample.	115

Sl. No.	Figure No.	Name of Figures	Page No.
41	Figure 6.2	Microscopic view of the PMMA micro-channel.	115
42	Figure 6.3	Contribution of parameters on depth of cut	117
43	Figure 6.4	Contribution of parameters on kerf width	118
44	Figure 6.5	Contribution of parameters on HAZ width	120
45	Figure 6.6	Surface plot of depth of cut versus pulse frequency and lamp current	121
46	Figure 6.7	Surface plot of depth of cut versus pulse frequency and cutting Speed	122
47	Figure 6.8	Surface plot of depth of cut versus lamp current and cutting speed	123
48	Figure 6.9	Surface plot of kerf width versus pulse frequency and lamp current	124
49	Figure 6.10	Surface plot of kerf width versus pulse frequency and cutting Speed.	125
50	Figure 6.11	Surface plot of kerf width versus lamp current and cutting speed.	126
51	Figure 6.12	Surface plot of HAZ width versus pulse frequency and lamp current	127
52	Figure 6.13	Surface plot of HAZ width versus pulse frequency and cutting speed	128
53	Figure 6.14	Surface plot of HAZ width versus lamp current and cutting speed	129
54	Figure 6.15	Single-objective optimization plot for the depth of cut of the micro-channel.	130
55	Figure 6.16	Single-objective optimization plot for the kerf width of the micro-channel.	131
56	Figure 6.17	Single-objective optimization plot for the HAZ width of the micro-channel.	131
57	Figure 6.18	Multi-objective optimization plot for the micro-channels	132
58	Figure 6.19	(a) Microscopic image of the micro-channel, (b) SEM micrograph	133

Sl. No.	Figure No.	Name of Figures	Page No.
59	Figure 6.20	PMMA workpiece after Nd:YAG laser transmission cutting in water medium, (a) Parent sample, (b) Sliced micro-machined sample, (c) Gold coated micro-machined sample.	136
60	Figure 6.21	Microscopic view of the PMMA micro-channel	137
61	Figure 6.22	Contribution of parameters on depth of cut	139
62	Figure 6.23	Contribution of parameters on kerf width	140
63	Figure 6.24	Contribution of parameters on HAZ width	142
64	Figure 6.25	Surface plot of depth of cut versus pulse frequency and lamp current.	143
65	Figure 6.26	Surface plot of depth of cut versus pulse frequency and cutting Speed	144
66	Figure 6.27	Surface plot of depth of cut versus lamp current and cutting speed	145
67	Figure 6.28	Surface plot of kerf width versus pulse frequency and lamp current	146
68	Figure 6.29	Surface plot of kerf width versus pulse frequency and cutting speed	147
69	Figure 6.30	Surface plot of kerf width versus lamp current and cutting speed	149
70	Figure 6.31	Surface plot of HAZ width versus pulse frequency and lamp current	150
71	Figure 6.32	Surface plot of HAZ width versus pulse frequency and cutting speed	150
72	Figure 6.33	Surface plot of HAZ width versus lamp current and cutting speed	151
73	Figure 6.34	Single-objective optimization plot for the depth of cut of the micro-channel	152
74	Figure 6.35	Single-objective optimization plot for the kerf width of the micro-channel	153
75	Figure 6.36	Single-objective optimization plot for the HAZ width of the micro-channel	153

Sl. No.	Figure No.	Name of Figures	Page No.
76	Figure 6.37	Multi-objective optimization plot for the micro-channels	154
77	Figure 6.38	(a) Microscopic image of the micro-channel, (b) SEM micrograph	155
78	Figure 6.39	Lamp current vs depth (1), depth (2) and depth (3)	159
79	Figure 6.40	Pulse frequency vs depth (1), depth (2) and depth (3)	159
80	Figure 6.41	Pulse width vs depth (1), depth (2) and depth (3)	160
81	Figure 6.42	Cutting speed vs depth (1), depth (2) and depth (3)	160
82	Figure 6.43	Lamp current vs kerf width (1), kerf width (2) and kerf width (3)	161
83	Figure 6.44	Pulse frequency vs kerf width (1), kerf width (2) and kerf width (3)	162
84	Figure 6.45	Pulse width vs kerf width (1), kerf width (2) and kerf width (3)	162
85	Figure 6.46	Cutting speed vs kerf width (1), kerf width (2) and kerf width (3)	163
86	Figure 6.47	Lamp current vs HAZ width (1), HAZ width (2) and HAZ width (3)	163
87	Figure 6.48	Pulse frequency vs HAZ width (1), HAZ width (2) and HAZ width (3)	164
88	Figure 6.49	Pulse width vs HAZ width (1), HAZ width (2) and HAZ width (3)	164
89	Figure 6.50	Cutting speed vs HAZ width (1), HAZ width (2) and HAZ width (3)	165
90	Figure 7.1	PMMA workpiece after fiber laser transmission cutting in air medium, (a) Parent sample, (b) Sliced micro-machined sample, (c) Gold coated micro-machined sample	169
91	Figure 7.2	Microscopic view of the PMMA micro-channel	170
92	Figure 7.3	Contribution of parameters on depth of cut	171
93	Figure 7.4	Contribution of parameters on kerf width	173
94	Figure 7.5	Contribution of parameters on HAZ width	174

Sl. No.	Figure No.	Name of Figures	Page No.
95	Figure 7.6	Surface plot of depth of cut versus pulse frequency and working power	176
96	Figure 7.7	Surface plot of depth of cut versus pulse frequency and cutting speed	176
97	Figure 7.8	Surface plot of depth of cut versus working power and cutting speed	177
98	Figure 7.9	Surface plot of kerf width versus pulse frequency and working power	179
99	Figure 7.10	Surface plot of kerf width versus pulse frequency and cutting speed	179
100	Figure 7.11	Surface plot of kerf width versus working power and cutting speed	180
101	Figure 7.12	Surface plot of HAZ width versus pulse frequency and working power	182
102	Figure 7.13	Surface plot of HAZ width versus pulse frequency and cutting speed	182
103	Figure 7.14	Surface plot of HAZ width versus working power and cutting speed	183
104	Figure 7.15	Single-objective optimization plot for the depth of cut of the micro-channel	184
105	Figure 7.16	Single-objective optimization plot for the kerf width of the micro-channel	185
106	Figure 7.17	Single-objective optimization plot for the HAZ width of the micro-channel	185
107	Figure 7.18	Multi-objective optimization plot for the micro-channels	186
108	Figure 7.19	(a) Microscopic image of the micro-channel, (b) SEM micrograph	187
109	Figure 7.20	PMMA workpiece after fiber laser transmission cutting in water medium, (a) Parent sample, (b) Sliced micro-machined sample, (c) Gold coated micro-machined sample	190
110	Figure 7.21	Microscopic view of the PMMA micro-channel	191

Sl. No.	Figure No.	Name of Figures	Page No.
111	Figure 7.22	Contribution of parameters depth of cut	193
112	Figure 7.23	Contribution of parameters on kerf width	194
113	Figure 7.24	Contribution of parameters on HAZ width	196
114	Figure 7.25	Surface plot of depth of cut versus pulse frequency and working power	197
115	Figure 7.26	Surface plot of depth of cut versus pulse frequency and cutting speed	198
116	Figure 7.27	Surface plot of depth of cut versus working power and cutting speed	199
117	Figure 7.28	Surface plot of kerf width versus pulse frequency and working power	201
118	Figure 7.29	Surface plot of kerf width versus pulse frequency and cutting speed	201
119	Figure 7.30	Surface plot of kerf width versus working power and cutting speed	202
120	Figure 7.31	Surface plot of HAZ width versus pulse frequency and working power	204
121	Figure 7.32	Surface plot of HAZ width versus pulse frequency and cutting speed	204
122	Figure 7.33	Surface plot of HAZ width versus working power and cutting speed	205
123	Figure 7.34	Single-objective optimization plot for the depth of cut of the micro-channel	206
124	Figure 7.35	Single-objective optimization plot for the kerf width of the micro-channel	207
125	Figure 7.36	Single-objective optimization plot for the HAZ width of the micro-channel	207
126	Figure 7.37	Multi-objective optimization plot for the micro-channels	208
127	Figure 7.38	(a) Microscopic image of the micro-channel, (b) SEM micrograph	209
128	Figure 8.1	Effect of parameters on depth of cut at air medium in different laser systems	213

Sl. No.	Figure No.	Name of Figures	Page No.
129	Figure 8.2	Effect of parameters on kerf width at air medium in different laser systems	213
130	Figure 8.3	Effect of parameters on HAZ width at air medium in different laser systems	214
131	Figure 8.4	Effect of parameters on depth of cut at submerged in water medium in different laser systems	215
132	Figure 8.5	Effect of parameters on kerf width at submerged in water medium in different laser systems	216
133	Figure 8.6	Effect of parameters on HAZ width at submerged in water medium in different laser systems	216
134	Figure 8.7	Percentage contributions of parameters on depth of cut in different mediums (i.e., Air and water)	218
135	Figure 8.8	Percentage contributions of parameters on kerf width in different mediums (i.e., Air and water)	218
136	Figure 8.9	Percentage contributions of parameters on HAZ width in different mediums (i.e., Air and water)	219
137	Figure 8.10	Percentage contributions of parameters on depth of cut in different mediums (i.e., Air and water)	220
138	Figure 8.11	Percentage contributions of parameters on kerf width in different mediums (i.e., Air and water)	220
139	Figure 8.12	Percentage contributions of parameters on HAZ width in different mediums (i.e., Air and water)	221
140	Figure 8.13	Optimal results from multi-objective optimization at different environmental conditions in Nd:YAG laser	222
141	Figure 8.14	Optimal results from multi-objective optimization at different environmental conditions in Nd:YAG laser	222
142	Figure 8.15	Average value of depth of cut at air & submerged in water medium for Nd:YAG laser system	224
143	Figure 8.16	Average value of kerf width at air & submerged in water medium for Nd:YAG laser system	224

Sl. No.	Figure No.	Name of Figures	Page No.
144	Figure 8.17	Average value of HAZ width at air & submerged in water medium for Nd:YAG laser system	225
145	Figure 8.18	Average value of depth of cut at air & submerged in water medium for Nd:YAG laser system	226
146	Figure 8.19	Average value of kerf width at air & submerged in water medium for Nd:YAG laser system	226
147	Figure 8.20	Average value of HAZ width at air & submerged in water medium for Nd:YAG laser system	227
148	Figure 8.21	Percentage improvement of depth of cut, kerf width and HAZ width in Nd:YAG and fiber laser system	228
149	Figure 8.22	CCI image of the micro-channel (Nd:YAG laser transmission micro-machining in air medium)	229
150	Figure 8.23	Surface roughness profile of the micro-channel (Machining in air medium)	229
151	Figure 8.24	Depth profile of the micro-channel (Machining in air medium)	230
152	Figure 8.25	AFM image of the micro-channel (Nd:YAG laser transmission micro-machining in air medium)	230
153	Figure 8.26	CCI image of the micro-channel (Fiber laser transmission micro-machining in underwater medium)	231
154	Figure 8.27	Surface profile of micro-channel (Machining in submerged medium)	232
155	Figure 8.28	Depth profile of micro-channel (Machining in submerged medium)	232
156	Figure 8.29	AFM image of the micro-channel (Fiber laser transmission micro-machining in underwater medium)	232

Chapter 1

INTRODUCTION

1.1 Introduction

Nowadays, engineered plastic materials become more demanding in research and development industries as a result of the rapid growth of science and technology due to their biocompatibility, favourable thermal and chemical resistance, molding temperature, surface deviation qualities, transparency, low cost, ease of availability. PMMA (Polymethyl methacrylate) is one of the most often used polymers in engineering industries which has emerged as a supernumerary solution where it is difficult to use silica glass. In the present scenario, the application of engineered polymer, like PMMA has the utmost importance in industries such as medical, optoelectronics, automobile, micro-fluidic sector. Processing the aforesaid material in a clean way poses a significant challenge to the micro-machining community. Laser micro-machining is one of the most convenient technologies due to its various advantages like high productivity, force-free, and clean machining process, as well as its ability to process varied intricate shapes. Regardless of mechanical characteristics, lasers are widely used for a variety of engineering applications to machine a wide range of engineering materials, such as polymers, metals, semiconductors, ceramics, etc.

Precise micro-channeling geometry, i.e., the aspect ratio of the micro-channel profile, is the most important aspect of microfluidic systems. Owing to the transparency of PMMA, no linear absorption of the incident laser beam with a near-infrared wavelength on PMMA takes place. Therefore, the process becomes rather difficult to control and predict. However, optimization of the different input process parameters not only controls the micro-channel geometry but also reduces the possibility of deviation in the width and depth of the desired value.

Laser micro-machining operation can be utilized to generate micro-channels for different microfluidic systems, which include telecommunication systems, micro-sensors, inkjet printers, nozzles, medical devices, biomedical catheter drilling, thin-film scribing, etc. The applications of microfluidic devices are further extended to

blood and protein analysis systems, optical vibration sensors and three-dimensional (3D) binary data storage systems.

1.2 Laser Beam Micro-machining

There are enormous applications of laser technology, in the fields of semiconductor processing and packaging, optical communication, and medicine. For materials like ceramics, composites, glass, and stainless steel that are difficult to process mechanically, lasers can easily fabricate microstructures down to the micrometer scale ($1\mu\text{m} = 10^{-6}\text{m}$). Laser beam has the ability to be focused into a very tiny spot which allows it to perform micro-machining operations. A laser spot diameter, as small as 10-15 μm can be achieved with a high-magnification concave objective lens. In semiconductor manufacturing, the laser plays an important role as an illumination source of photolithography. In the early 1990s, the critical dimension of circuit designs etched onto silicon wafers by imaging a mask was decreased by using lasers instead of halogen lamps in photolithography. On the manufacturing line, photolithography now has a critical dimension of 0.18 μm ; nevertheless, a minimum pattern size of 70 nm has previously been achieved [1]. Almost all laser micromachining applications are based on the absorption of laser light by the workpiece, which results in high amount of heat and chemical changes in the machining zone of the workpiece. For the development of a laser micro-processing technique and its application, a thorough understanding of the thermal, physical, and chemical phenomena that occur during laser beam interaction with materials, as well as their variation with respect to key laser parameters such as wavelength, pulse width, and energy, is required.

1.2.1 Need and Advantages of Laser Micro-machining

Miniaturization is a critical imperative trend in many modern technology sectors, and it is becoming progressively popular. Material processing at micron or sub-micron range at high speed and low unit cost of high-tech micro-products in biotechnological, microelectronic, telecommunication, MEMS, and medical applications is becoming increasingly important as the world's population continues to grow. In the early 1990s, Masuzawa [2] was the first to draw attention to the need for micro-machining characterization, as well as the need for direct determination of the shape of the products produced by micro-machining. Micro-machining can be defined as the

removal of small amounts of material in the micron range. CIRP's Scientific Technical Committee on Physical and Chemical Machining Processes has established a dimension range of 1 to 500 μm for micro-machining work [3]. The specific requirements of the part to be produced for micro-fabrication dictate which technologies are used. Mechanical micro-machining, such as micro-drilling and micro-milling, micro-ultrasonic machining, laser micro-machining, electron beam machining, ion beam machining, and micro-ion beam machining are examples of technologies that are used. The various advanced micro-machining processes and their relative advantages, disadvantages, and applications are depicted in Table 1.1. Laser beam micro-machining is gaining popularity for producing micro-components on a variety of metals, ceramics, and polymers for usage in a variety of industries, including the medical and automotive industries. With its superior characteristics such as contact and wear-less machining, greater flexibility, and the possibility of high levels of automation, laser micromachining has emerged as one of the most adaptable fabrication processes available today. A wide range of pulse duration from femtosecond to microsecond, as well as a variety of wavelengths and pulse repetition rates ranging from single to megahertz, makes laser micro-machining an excellent choice for fabricating complex micro parts with a high aspect ratio.

The advantages of laser micro-machining over other non-traditional micro-machining processes are as follows:

- (i) Suitability to a wide range of engineering materials-from metals, alloys, plastics, ceramics to superalloys;
- (ii) Potentiality for different micro-machining applications;
- (iii) Low processing time;
- (iv) Less wastage of material;
- (v) High automation as well as easy integration;
- (vi) A wide range of power variations ranging from very low output power (mW) to extremely high output (kW).

The pulsed mode of the fiber laser system, which has an output power of less than 200 W and superior characteristics such as quality, ruggedness, cost-effectiveness, low maintenance requirements, higher efficiency, greater reliability, and smaller spot size, is best suited for micro-machining of a wide range of engineering materials [4]. Fiber

Table 1.1 Various advanced micro-machining processes and their relative advantages, disadvantages, and applications

Name of the micro-machining processes	Basic principle of material removal	Critical parameters	Advantages	Disadvantages	Applications
Abrasive jet micro-machining (AJMM)	Brittle fracture by impinging abrasive grains at high speed	Abrasive flow rate and velocity, nozzle tip distance from the work surface, abrasive grain size, and jet inclination	Wide range of material compatibility, no heat-affected zone, ability to machine complex shapes, environmentally friendly, etc.	Slow material removal rate, equipment complexity, and cost, surface contamination, debris accumulation, recirculation, etc.	Microelectronics and semiconductor industry, medical device manufacturing, precision optics, etc.
Ultrasonic micro-machining (USMM)	Brittle fracture caused by impact of abrasive grains due to tool vibrating at high frequency	Frequency, amplitude, tool material, grit size, abrasive material, feed force, slurry concentration, slurry viscosity	High precision, reduced cutting forces, improved surface finish, wide material compatibility, etc.	Limited material removal rate, size limitations, complex setup and tooling, tool fragility, maintenance, etc.	Medical device manufacturing, optics and photonics, aerospace and aviation industry, microfluidics and lab-on-a-chip devices, etc.
Electrochemical micro-machining (ECMM)	Electrolysis	Voltage, current, feed rate, electrolyte, electrolyte conductivity	High precision, burr-free machining, material versatility, capability for complex shapes and small features, minimal heat-affected zone, etc.	Limited material compatibility, complex setup and process control, slow material removal rate, high-Cost considerations, etc.	Microelectronics and semiconductor industry, medical device manufacturing, aerospace, and aviation industry, etc.
	Plastic shear and	Voltage and current,	Burr-free machining, high	Limited material	Microelectronics

Name of the micro-machining processes	Basic principle of material removal	Critical parameters	Advantages	Disadvantages	Applications
Electrochemical micro-grinding (ECMG)	ion displacement	electrolyte composition, grinding wheel characteristics, feed rate, wheel speed, gap between grinding wheel and workpiece	precision, improved surface finish, enhanced material removal rates, etc.	compatibility, equipment complexity, complexity in tool design, etc.	industry, tool and die manufacturing, medical device manufacturing, etc.
Chemical machining (CHM)	Corrosive reaction	Etching time, temperature control, agitation, and flow rate	High precision, versatility in material compatibility, cost-effectiveness for large production runs, and the ability to produce complex shapes with minimal material waste.	Limited depth control, chemical disposal, and safety, limited material thickness, surface finish limitations etc.	Medical devices, automotive, defence, and military, etc.
Electric discharge machining (EDM)	Melting and evaporation aided by cavitation	Voltage, capacitance, spark gap, dielectric circulation, melting temperature	Precision, versatility, capability for complex shapes, and the ability to work with hard or difficult-to-machine materials	Slow material removal rate, Limited material thickness, surface finish limitations, etc.	Mold and die making, aerospace industry, medical device manufacturing, etc.

Name of the micro-machining processes	Basic principle of material removal	Critical parameters	Advantages	Disadvantages	Applications
Electron beam machining (EBM)	Melting, vaporization	Accelerating voltage, beam current, beam diameter, work speed, melting temperature	High precision, high aspect ratio machining, etc.	Slower material removal rates, high equipment costs, etc.	Nuclear industry, mold and die making, electronics and semiconductor industry, etc.
Ion beam machining (IBM)	Elastic and nonelastic collisions, atomic displacement, sputtering	Ion beam current, incident angle, beam dwell time, beam scanning pattern, vacuum environment	Minimal heat affected zone (HAZ), burr-free and stress-free machining, etc.	Slow material removal rates, beam scattering and penetration depth etc.	Thin film deposition, surface modification and etching, etc.
Plasma arc machining (PAM)	Melting	Voltage, current electrode gap, gas flow rate, nozzle dimensions, melting temperature	Easy operation and automation, enhanced weld appearance, high energy concentration, etc.	Low accuracy	All materials conducting

laser micro-machining approaches to various difficult-to-machine materials for the creation of precise micro-features such as channels, grooves, and holes. The development of fiber laser systems is considered to be the most versatile and rapidly-growing laser systems in the last decade, primarily for applicability in the biomedical, automotive, and aerospace engineering domains.

1.2.2 Basic Principles of Laser Generation

Laser light is essentially a beam of photons that is coherent (has the same frequency as the source) and monochromatic (has the same wavelength as the source). Additionally, it exhibits high brightness with extremely high-power intensity and is highly directional (with less angle of divergence). A laser is a modified light source that through stimulation and amplification, converts photon energy into a high energy density coherent beam of light. An external source, such as an electrical discharge or a flash lamp, can cause electrons in the lasing medium to be excited and forced to emit photons, which are referred to as stimulation. An excitation process, also known as pumping, is responsible for supplying the energy required to raise a free electron from one energy state to another. There are numerous losses associated with the lasing process; the rate at which the power is supplied by the excitation process must be greater than the rate at which power is lost by the laser. In most cases, the lasing medium contains ions, atoms, or molecules that have a discrete electron energy level, and this is known as the lasing medium. The wavelength is produced as a result of the lasing medium's physical characteristics. To begin with, photon emissions are sporadic in nature, and each photon stimulates the emission of additional photons by other excited electrons during the lasing process. The new photons should have exactly the same wavelength, direction, and phase characteristics as the original photon. A stream of photons with the same wavelength, direction, and phase is required to be produced as a result of this process. Optical resonators are used in lasers to increase the amount of light that is amplified. An optical resonator is composed of a cavity with the lasing medium sandwiched between two highly precise, aligned mirrors. In order to allow the laser beam to transmit as reflective and the other one partially transmissive. Mirrors reflect light back into the lasing medium; as photons pass back and forth through the lasing medium, they stimulate an increasing number of emissions. Photons that are not aligned with the resonator are not redirected by the mirrors, and this results in a reduction in the amount of

stimulated emissions. The cavity only amplifies photons that are oriented in the proper direction. Figure 1.1 also depicts Planck's theory of black body radiation, which is shown in more detail in the text. An atom is made up of a positively charged nucleus surrounded by electrons on orbits around it. These electrons on their specific orbits, are called energy levels. Whenever energy is supplied to an electron in an orbit, the electron changes its orbit (energy level) and, upon returning to the ground state, emits the energy that was supplied. From Planck's law, it is given as:

$$E_2 - E_1 = \Delta E = h\nu \quad (\text{Eq}^n.1.1)$$

Where h is plank's constant and ν is the frequency of the emitted photon.

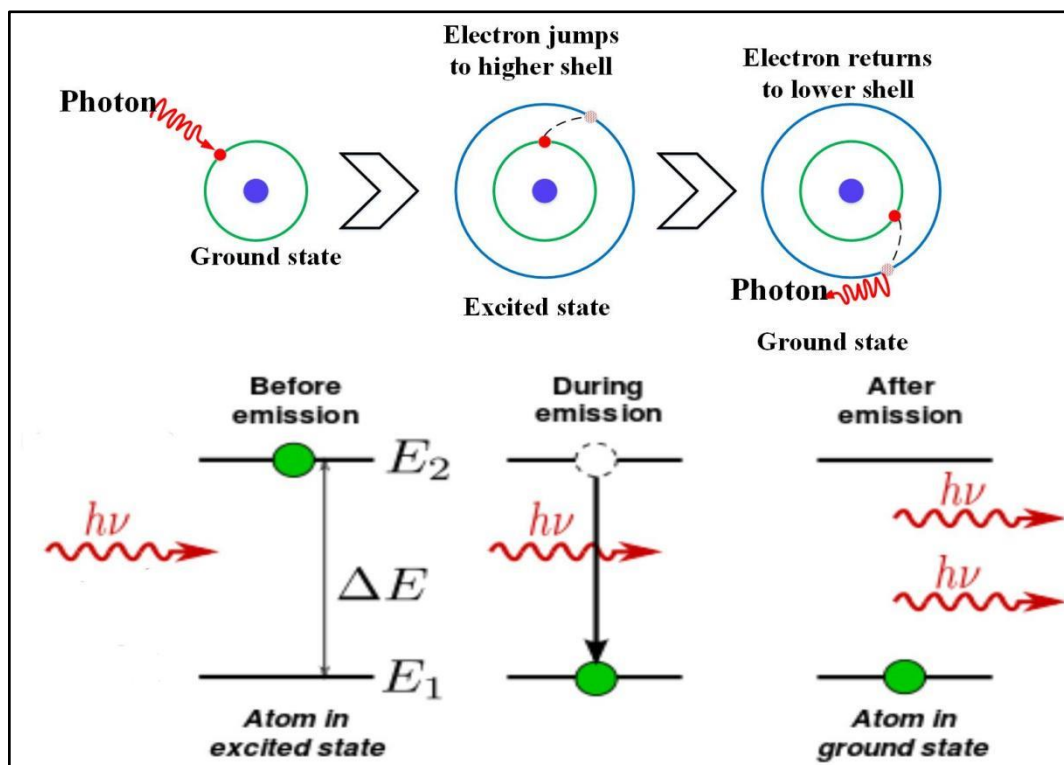


Figure 1.1: Change of state and generation of photon

1.2.3 Different Laser Sources

A laser is a device that amplifies light through the use of stimulated emission of radiation. Practical lasers are available in a variety of configurations for commercial and research applications. Different types of lasers are shown in Figure 1.2.

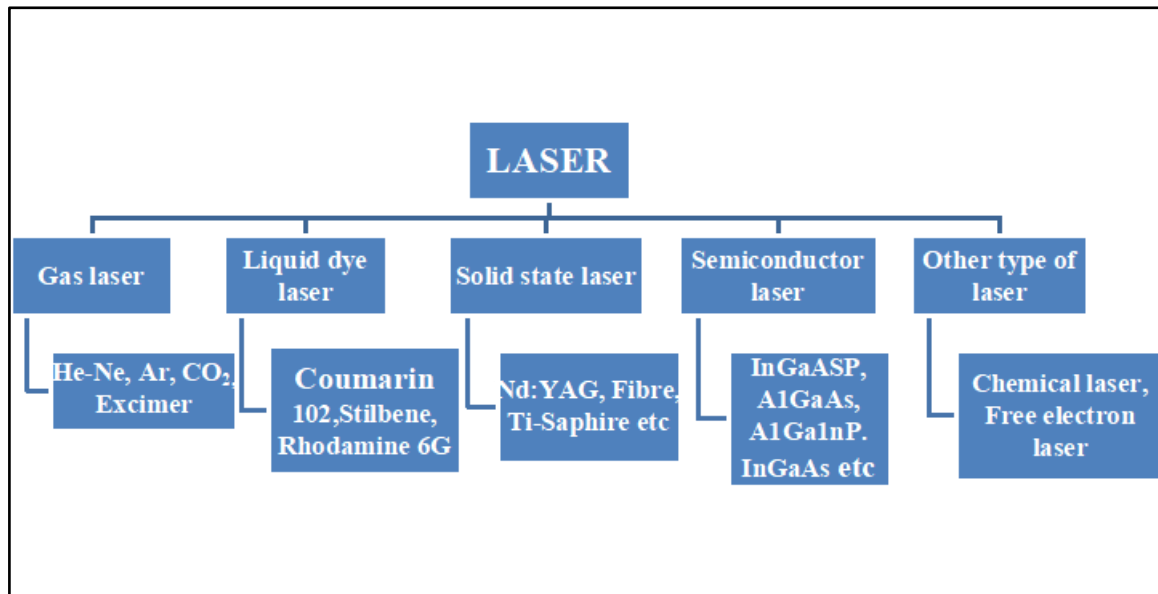


Figure 1.2 Different types of lasers

In the gaseous state, lasers are used, namely helium-neon (He-Ne), argon (Ar), carbon dioxide (CO₂), and excimer lasers, and their active medium are Ne, Ar⁺, CO₂ and noble gas + halogen gas accordingly. The applications of gaseous lasers are lithography, holography, cutting (plastic, metal), welding, marking, micro-fabrication, eye surgery, etc.

Lasers, specifically dye lasers, are used in the liquid state, and their active medium is an organic dye. This laser is mainly used in the fields of research and diagnostics.

Solid state lasers are classified into a couple of types due to the range of host materials available and the numerous dopant ions: Nd: YAG, fiber, semiconductor, and Ti-sapphire. Nd: YAG lasers are the most common type. This type of laser uses Nd³⁺ rare earth materials, semi-conducting compounds, and titanium sapphire as its active medium. Solid state lasers are used in a variety of applications such as welding, drilling, marking, telecommunication, data storage, micro-machining, and so on.

In general, the CO₂ laser, Nd: YAG laser, DPSS laser, free-electron laser, and excimer laser are used for micro-machining because of their specific characteristics. The feature of various laser systems used for micro-machining is given below,

a) Gas laser

Gas is the active medium in a laser, and the name reveals this fact. It has some significant advantages. Some of the perks include:

- I. Gases perform like homogeneous laser medium
- II. Easy transportation of gasses can be made for cooling and replenishment

III. Gasses are comparatively less costly.

Classification of gas lasers into atomic, ionic, and molecular lasers can be done based on laser transitions occurring between the energy levels of atoms, ions, and molecules. The CO₂ laser appears to be a molecular gas laser due to the use of a gas mixture as the gain medium. This gas mixture includes carbon dioxide, helium, nitrogen, water vapour, and possibly hydrogen and xenon. DC current or AC current and radio frequency can be used to power this type of laser, which is powered by an electrical gas discharge. An electric discharge into a metastable vibrational level is used to excite nitrogen molecules and transfer the excitation energy to CO₂ molecules at the time of collision. Carbon monoxide can be re-oxidized to carbon dioxide with the help of other elements like hydrogen or water vapour. At 10.6 μm, CO₂ lasers leave behind lines in the 9–11 μm range when they emit. There is a wide range of average output power in most cases.

b) Liquid dye laser

Liquid dye lasers are produced by the liquid solutions in which organic dyes are dissolved in a suitable liquid solvent and used as active laser medium in liquid dye lasers. The physical characteristics of the liquid medium (homogeneity, low density, and so on) make the production of liquid dye lasers relatively simple, and the liquid medium has the advantage of being easily cooled and replenished in the laser cavity. The dye laser's tunability is an important quality because it allows to operate over a wide range of wavelengths (0.2-1.0 μm). The spectral characteristics of the organic dye molecules are responsible for this. The dye molecules have a high absorption capacity for radiation throughout a broad range of wavelengths and a high reemission capacity for other board brands over longer wavelengths, making them ideal for use in solar panels. An organic dye persists in the gain medium used by a dye laser after the laser is turned off. The organic dye is a carbon-based soluble strain that retains its overall fluorescent properties, much like the dye in a high-lighter pen. The dye is mixed with an appropriate solvent in order to ensure that the molecules diffuse evenly throughout the liquid. The use of a dye jet allows for the circulation of dye solution through a dye cell or the streaming of dye solution through open air, respectively. A high-energy light source is required in order to push the liquid over its lasing threshold. It is necessary to employ either a fast discharge flash tube or an external laser in order to achieve the goal. Due to the oscillation of the light generated by the dye's fluorescence, which is magnified with each passage through the liquid, mirrors

are required to get the desired result. When the reflectivity of all other mirrors is larger than 99.9%, the usual output mirror has a reflectivity of 80%, which is the case when the reflectivity of all other mirrors is greater than 99.9%. The dye solution is often circulated at a high rate in order to avoid triplet absorption and to reduce the degradation of the dye. The installation of a prism or a diffraction grating in the beam path is commonly done to allow for the tuning of the beam to be accomplished.

c) Solid state laser

Solid state lasers use an active medium composed of a small percentage of impurity ions doped in a solid host material as their active medium. It was in 1960 that Maiman was successful in developing the world's first practical solid-state Ruby laser. This category includes a diverse range of lasers, including Nd: YAG, fiber lasers, Alexandrite, Nd: Glass, and Ti-sapphire lasers. The Nd: YAG laser and fiber laser are the two most popularly used for machining applications. As an exciter, a flash and an arc lamp are employed in this instance. Because of its wavelength in the near infrared region (1.06 μm), it delivers laser radiation through optical fibers, which is more advantageous than CO₂ lasers in the industry. The output power is in the range of a few watts to a few KW, this while operating in continuous wave mode. The output energy of pulsed lasers is ranging from a few milli-joules to a few tens of Joules, depending on their design. Experiments are being carried out to develop sensitizer atoms that contain new active materials in order to improve their overall efficiency. On a micro-scale, the pulsed Nd:YAG laser is primarily used for materials processing like cutting, welding, drilling, marking, and surface engineering.[5, 6]

d) Semiconductor or diode lasers semiconductor

Gradually popular as pump sources for solid-state lasers and as materials processing tools, lasers are becoming increasingly popular due to their unique characteristics such as small size, low weight, high efficacy, and dependability, among others. Diodes based on double hetero-junctions, such as AlGaAs (p) and GaAlAs/GaAlAs, are among the most commonly used semiconductors. It is the recombination of electrons in the conduction band with holes in the valence band responsible for the stimulated emission observed in this type of laser system. The mounting of more than one diode bar into the multi-channel heat sinks, which are stacked one on top of the other, results in an increase in the amount of emitted radiation [7].

e) Other types of lasers

1. Chemical laser

The source of a chemical laser is a chemical reaction. Chemical lasers are capable of producing waves with power that can reach up to megawatt levels on a continuous basis. Cutting and drilling are two of the most common industrial applications of chemical laser technology. Chemical lasers that are commonly used include chemical oxygen, iodine laser (COIL), all gas-phase iodine lasers (AgIL), and hydrogen fluoride (HF) and deuterium fluoride lasers that have operational capacity in the mid-infrared section. The DFCO₂ laser (deuterium fluoride carbon dioxide) retains its transfer laser characteristics, similar to the COIL laser. An unusual phenomenon appears when several molecular energy transitions occur in high-frequency and deep-frequency lasers with sufficient energy to cross the threshold requirement for lasing. As long as there is no collision of molecules, the operation of many of these laser modes has been conducted either simultaneously or in extremely rapid succession and is frequently made possible by the redistribution of energy. As a result, if the wavelength selection device has not been incorporated into the resonator, HF and DF lasers operate at the same time on multiple wavelengths at different frequencies. [5-6, 8]

2. Free electron laser

The optical amplification of a free electron laser is achieved in an undulator that is fed with high energy level electrons from an electron accelerator. In order to demonstrate the effectiveness, such devices may be used to emit wavelengths whose emission ranges from the terahertz domain through the far and near-infrared, the visible and ultraviolet ranges, and the X-ray domain when the entire wavelength range cannot be covered by a single device. By arranging magnets in a periodic pattern, an undulator generates a periodic varying Lorentz force that varies with time. This causes electrons to radiate at a frequency that is dependent on the electron energy, the undulator period, and, to a lesser extent, the strength of the magnetic field. The emission of spontaneous and stimulated light in a specific wavelength range allows for optical amplification within that wavelength range.

1.2.4 Different Types of Laser Pulses Regimes

The difference in wavelength or duration of the laser emission between a continuous wave laser and a Q-switched laser determines the characteristics of each type of laser. The different types of laser pulse regimes are shown in Figure 1.3.

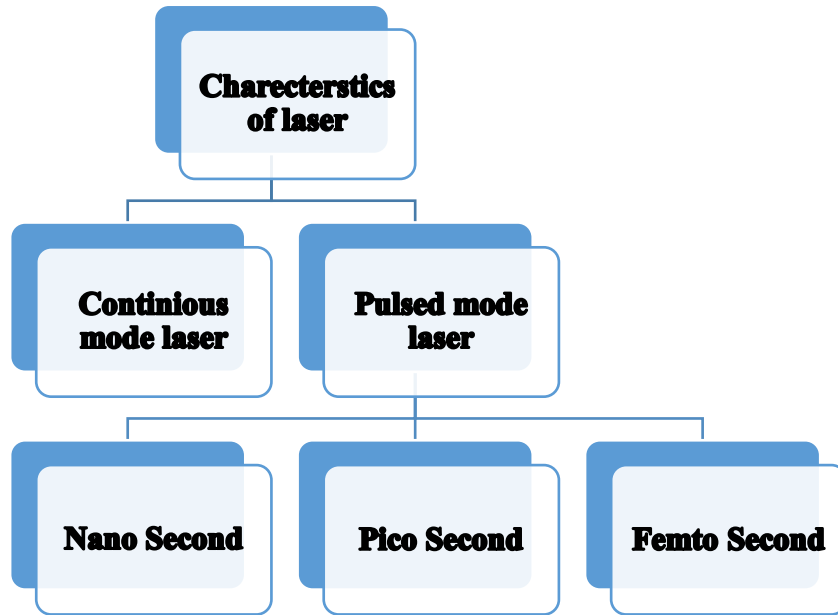


Figure 1.3 Different characteristics of laser

Continuous wave laser operation necessitates the use of output power that is stable or continuous. When measuring the output power of a continuous wave laser, the unit of measurement is in watts. In recognition of the fact that the output characterization is accomplished by energy pulses occurring at fixed pulse repetition energy, the laser is classified as a pulsed laser. The Q-switch is a nonlinear crystal that is located within the cavity of a Q-switch laser. It is responsible for preventing any release of laser light prior to the Q switch being opened. After the energy has been built up in a Q-switched laser, it is released at the opening of the Q-switched, resulting in the production of a very strong laser pulse.

The production of nanoparticles and manipulation of nanoparticles have been accomplished through the use of different laser pulse regions such as nanosecond, picosecond, and femtosecond. The various types of lasers may be used to enable both the synthesis of new materials and the ultra-precision micro and nano-machining that they have previously achieved. Laser processing with high precision can be accomplished by the use of lasers with short and ultra-short pulse durations. When compared with nanosecond or longer laser pulses, femtosecond to picosecond pulsed lasers demonstrate a significant improvement in quality for a wide range of materials. These lasers are better suited for material removal or ablation than other types of lasers. Short-pulse duration lasers (picosecond lasers) and ultra-short pulse duration lasers (femtosecond lasers) can be employed to provide superior outcomes in some

applications. These lasers are well suited for nano-machining applications, requiring ultra-precision. [9]

1.3 Material Removal Process in Laser Beam Micro-machining

Radiation in the form of electromagnetic waves starting with an electronic excitation, the laser-matter interaction often results in local heating as a result of photon-electron interactions.

1.3.1 Absorptivity of Laser Irradiate Zone

Electromagnetic wave (laser beam) interaction causes physical phenomena such as reflection, refraction and absorption, scattering and transmission. Laser matter interaction is dominated by the effects of linear and nonlinear absorption. There are a number of other elements that influence the absorption of irradiated material, including the laser wavelength, angle of incidence, and surface roughness. It is inversely related to the electrical resistivity of a material's absorption coefficient, which increases with wavelength. Nonlinear absorption is more likely phenomenon at higher laser intensity. It is for this reason that shorter laser-material interaction times allow for multi-photon excitation processes to occur at constant laser fluence. Electron-nucleus interactions in the target material's lattice are one way to explain laser energy absorption. The nuclei's lattice and electrons vibrate as a result of the electromagnetic radiation's optoelectronic field. In this way, the absorbed radiation results in the electrons' surplus energy, such as the kinetic and excitation energy of the free electrons and the bound electrons [10]. Collisions with the vibrating lattice of nuclei are thought to help minimize the extra energy created by electrons. Furthermore, some incident laser energy is transmitted to the lattice, causing heat to be generated. The absorption of laser energy in the target substrate is commonly represented by the Beer-Lambert law [11].

$$I(Z) = I_0 e^{-\mu Z} \quad (\text{Eq}^n.1.2)$$

Where, I_0 represents incoming intensity, $I(Z)$ represent intensity at depth Z , and m represents the absorption coefficient. The strength of the laser beam fades as the depth of the material increases. Attenuation length (L) is the length over which the intensity of laser radiation is significantly reduced and is represented as the reciprocal of the absorption coefficient (μ) of the target substrate [12].

$$L = \frac{1}{\mu} \quad (\text{Eq}^n.1.3)$$

In general, the absorptivity of opaque materials may be described as the fraction of incident radiation absorbed at normal incidence, which is represented [13] as,

$$A = 1 - R \quad (\text{Eq}^n.1.4)$$

Where A is the absorbance of the irradiated substrate, and R is the reflectivity. The substrate can be heated, melted, or vaporized depending on the temperature distributions in the material, which can result in various physical effects. Through thermal conduction, convection, and radiation, heat is transferred from the substrate's surface to the interior.

1.3.2 Phase Change and Plasma Formation

Surface melting and evaporation are examples of phase changes that occur when the laser intensity is sufficiently high, which is referred to as the melting (I_m) and vaporization (I_v) threshold intensity, respectively. When the laser intensity achieves the melting threshold energy during laser irradiation, the melting process begins at a certain temperature and results in the production of a solid liquid interface at the surface of the material being irradiated. With an increase in laser energy density, a solid liquid interface flows away from the surface along the depth of the laser beam, resulting in the formation of a melt pool. Because of the pulsed off time, the depth of melting is reduced, and vice versa [14]. The to-and-fro movement of the solid liquid interface at a very high velocity (≤ 30 meters per second) at the machining zone causes surface melting and subsequent resolidification at the machining zone in pulse duration [15]. When the laser irradiates, the surface temperature reaches its boiling point and the depth of melting achieves its maximum. Evaporation occurs as a result of an increase in laser power density or pulse on time, which leads to the removal of material from the irradiated area. Following the initiation of vaporization, the liquid-vapor interface travels within the material under the influence of continuous laser irradiation. Calculations can be made to determine the depth of vaporization [11], the quantity of material lost per unit of time, and the velocity of the liquid-vapour interface.

$$\dot{m} = V_s \rho \quad (\text{Eq}^n.1.5)$$

Where, \dot{m} is the mass of material removed per unit time, V_s the liquid-vapor interface velocity, and ρ is the density.

$$d = V_s t_p \quad (\text{Eq}^n.1.6)$$

Where, t_p is the pulse time and d is the depth of vaporization.

$$V_s = \frac{H}{\rho(cT_b + L_v)} \quad (\text{Eq}^n.1.7)$$

H stands for absorbed laser power, T_b for surface boiling temperature, and L_v for latent heat of vaporization in this equation. When laser beam processing is done, such as drilling, cutting, marking, welding, cladding, and other tasks, the evaporation-induced recoil pressure is higher than the maximum surface tension pressure. The evacuation of melt from the machining zone during materials processing is influenced by recoil pressure [11]. Plasma interactions occur when a vapour or surrounding gas is exposed to high laser irradiance ($I \geq 10^9 \text{ W/cm}^2$), and the resulting vapour or gas becomes ionized as a result of collisions between the subsequent vapour and the incident laser beam. Plasma is formed after around 10-12 picoseconds. A plasma plume produces a shield over the machining area, reducing the amount of energy available to the workpiece during the machining process. Plasma can be released in time frames ranging from the picosecond to well beyond the millisecond when guided by shock waves [16].

1.3.3 Evaporation and Ablation

Rapid vaporization begins when the incident laser energy on the target surface is sufficient to achieve the target material's boiling temperature. As the pressure and evaporation rate fall, the size of the vapour particle decreases [17]. When a high laser irradiance ($I \geq 10^9 \text{ W/cm}^2$) is applied, plasma is generated in which the vapour or the surrounding gas becomes ionized as a result of interactions between the incident laser beam and the produced vapour. Because of the shielding effect of the plasma plume, there is less laser energy available in the machining zone. Thermal stresses and surface vaporization are responsible for the removal of material during the photo-thermal ablation process. However, material elimination occurs through molecular fragmentation rather than considerable heat damage in photo-chemical ablation,

where the high-energy photon induces the direct bond breakage of the molecular chains in organic materials [18].

1.4 Applications of Laser in the Domain of Micro-manufacturing

The applications of lasers in various domains of micro-manufacturing are described below.

- i. Fabrication of integrated chips (I.C).
- ii. Printers and plotters.
- iii. Medical device fabrication and pharmaceuticals.
- iv. Machining of hard materials like satellites and diamonds etc.
- v. Processing nuclear fuel rods.
- vi. Heat treatment, surface hardening, alloying, cladding, welding, drilling and trepanning etc.
- vii. Register trimming and wafer labeling in microelectronics.
- viii. Communication and space applications.
- ix. Welding of super alloys used in multi-layer aerospace industry.
- x. Cutting of brittle materials using controlled fracture technique.
- xi. Drilling of minute holes in nozzles and artificial ceramic hip joints.
- xii. Laser beam micro-welding using a new technique called Steeples High Speed Accurate and Discrete One Pulse Welding (SHADOW).
- xiii. Laser assisted forming.

1.5 Laser Beam Micro-machining with the Aid of a Different Assisted Medium

In order to achieve the desired quality characteristics in the micro-domain, the laser beam machining process may be carried out under a variety of atmospheric circumstances, such as submerged conditions, preheated conditions, vacuum, or a combination of various conditions.

1.5.1 Laser Beam Micro-machining in the Compressed Air Medium

In order to perform good micro-machining operations, assist gas must be delivered at a specified pressure. The quality of the machined surface can be increased by varying the amount of pressure applied. When it comes to the laser machining system, compressed air is used as an aid gas. The gas is mostly necessary for the purpose of clearing debris from the machining zone. It is necessary to modify the pressure of the assist gas in order to investigate its effect on the laser machining quality. Assistance gas is also employed to shield the lens from the evaporating gas, which is a novel technique.

1.5.2 Laser Beam Micro-machining in the Underwater Medium

By irradiating the workpiece material while submerged in water, it is possible to eliminate or partially correct undesirable quality aspects such as dross formation, heat affected zone formation, recast layer formation, difficulties in debris removal, and desired surface morphology during laser micro-machining operations. In comparison to other laser beam micro-machining or laser-assisted micro-machining techniques, the underwater Laser beam machining process is more suitable due to the reduction in heat affected zone, the reduced risk of atmosphere contamination, the increased absorptivity of the work substrate, and the enhancement of debris removal due to hydrodynamic force generated by bubble dynamics. In addition to absorption, heating, melting/vaporization, and ablation, several other events occurred during nanosecond pulsed laser beam micro-machining in submerged circumstances. The existence of a high drag force and a low settling velocity in liquid helps to remove debris as rapidly as possible from the machining zone. In general, fluid in a flowing state is recommended to prevent laser light diffraction and absorption by garbage during the production process. Laser-induced plasma temperatures and plasma UV/IR radiation have the ability to excite, ionize, and dissociate liquid molecules, allowing them to become chemically active [84]. Because of the restriction of plasma expansion in confined spaces, laser irradiation has a greater effect on the target. In supercritical water, which is created by a high-intensity laser beam, the dissolution of the workpiece and debris takes place. Debris from the machining zone is easily removed as a result of the mechanical impact that the vapour bubbles' collapse causes in the micro jets [19]. Submerged laser ablation, underwater water-jet guided laser beam machining, underwater gas-assisted laser beam machining, and chemical-assisted

laser beam machining are among the liquid-assisted laser beam machining methods being investigated by researchers. Processing with a laser beam in chemical solutions produces a better surface quality than processing with a laser in pure water, according to some research [20]. The effects of electrochemical dissolution or localized breakdown are accelerated by the use of a laser beam in neutral sodium solution. As a result of water's greater refractive index, the optical absorptivity of the workpiece substrate increases when it is submerged in water [21]. Underwater laser ablation process is shown in Figure 1.4.

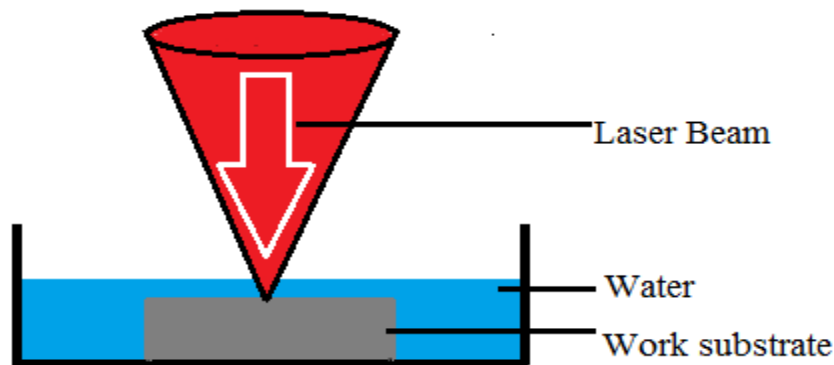


Figure 1.4 Underwater laser ablation processes [22]

1.6 Importance of Micro-channeling of PMMA and its Application

Due to the complexity of the overall size and shape of the products, micro-channeling is an exciting and quickly growing field in micro-machining. For example, over the past three decades, the feature size of integrated circuit chips has been reduced by roughly 20 times. In recent years, there has been a significant tendency toward the reduction of numerous components used in a variety of applications, including MEMS, electronics, photonics, and biomedical devices, among others. Recent years have seen a significant increase in the use of micro-machining operations on a wide range of modern engineering materials such as ceramics, composites, diamonds, glass, quartz, polymers, and other polymers. Micro-machining operations include micro-turning, micro-grooving, micro-drilling, and engraving, among others. It is most widely employed in micro-fluidics and in tiny heat exchangers, among other applications. In response to advancements in micro-fluidics and MEMS technologies, miniaturized devices have been developed in stages. When it comes to the creation of integrated micro-systems, micro-fluidics has been one of the foundational technologies. It has been known for several decades that MEMS combined with

micro-fluidics is an emerging topic of discussion among researchers in the fields of biological sciences, chemistry, physics, and engineering. This combination allows researchers to operate laboratories on a small scale by integrating microfluidic devices on lab-on-a-chip devices. The key advantages of miniaturized systems are their small volume, convenience of use, the ability to do point-of-care diagnostics, and the speed with which the sample reacts. The development of microfluidic devices on materials like, silicon, glass, quartz, and plastic has received extensive attention in the last ten years. As a result, silicon and glass-based materials frequently exhibit undesirable properties such as poor optical clarity, low impact strength, poor compatibility, a low limiting aspect ratio, a time-consuming fabrication process, and fragility due to their inherent brittleness, which prevents their widespread use in microfluidic devices from becoming widespread. Micro-structures on polymers, on the other hand, are becoming increasingly important, particularly when considering polymers as a low-cost alternative to silicon or glass-based MEMS technology for single-use disposable biological sensors. Silicon is a fantastic choice for producing modest quantities of long-lasting systems. Single-use systems, on the other hand, are preferred in clinical applications, in order to prevent contamination from occurring. Polymers are a viable alternative to silicon and glass—because they can be made quickly and inexpensively utilizing low-cost polymers. At present, micro-fluidic systems are becoming increasingly popular. As an added benefit to their use, polymer-based materials have a diverse spectrum of physical and chemical qualities, including low electrical conductivity and good chemical stability. Currently, polymer materials such as polycarbonates (PC), polypropylene (PP), and polymethyl methacrylate (PMMA) are extensively employed in micro-machining applications. PC is a transparent material with outstanding physical qualities, excellent toughness, extremely good heat resistance, high impact resistance, high stiffness, good dimension ability, and good electrical capabilities. PC is also a transparent material with excellent electrical properties. PP is one of the thermoplastics that have a high rigidity, strong strength even at relatively high temperatures, abrasion resistance, good elastic qualities, and a hard, glossy surface. It is also resistant to corrosion. PMMA, in, is a strong and stiff substance with a significantly higher weather resistance feature. Both its tensile and flexural strengths are very high. Surface hardness of PMMA is higher than that of all other popular thermoplastics, and it is also scratch resistant. PMMA is transparent to

the same degree as glass and is widely employed in optical applications. The impact resistance of this material is ten times greater than that of glass. It has a high level of biocompatibility and stability in the environment. Due to the fact that PMMA sheet is a non-porous solid, contamination induced by bimolecular adsorption is less prevalent. When applied to neutral aqueous solutions, it is inert, and no hydrolysis occurs as a result of the application. PMMA is a translucent plastic polymer that is frequently used as a substitute for glass in the construction industry. In addition to its moderate properties such as transparency, susceptibility to stress cracking, sensitivity to ultraviolet radiation, resistance to weak acids, weak alkaline solutions, salts, non-polar solvents, oils, and water, low cost, ease of availability, thermal and chemical resistance, moldability temperature, and surface derivation properties, PMMA is an important material in micro-machining, particularly in microfluidic devices.

For example, the use of micro-channeling in fluid control, also known as microfluidics, is the science and technology of manipulating and analyzing fluid flow in structures with sub-millimeter dimensions, as well as heat transfer in micro heat exchangers, in the context of micro-manufacturing. Micro-channeling has a wide range of applications in the fields of micro-fluidics and heat exchangers, to name a few. The applications are highlighted as follows:

- I. Micro-electromechanical systems (MEMS): As a result of recent improvements in MEMS technology, numerous MEMS devices are being used in an increasing number of consumer products. Understanding micro-flows is critical for the design and characterization of devices such as electrostatic comb drives, micro-motors, and other similar devices, among other things. Micro-flows can also occur in hard disc read/write heads, CD drives, inkjet printers, and other electronic devices as well.
- II. Electronic cooling: Micro-flows have the potential to be utilized in the electronic packaging sector to disperse the large heat fluxes created by modern electronic chips. The reason for the high level of study in this field is that it is possible to incorporate a micro-channel within the chip itself, so reducing contact resistance between the heat source and the fluid.
- III. Biochemistry: The fields of chemistry and biochemistry have developed a variety of instruments, such as micro-reactors, for researching the reactions of potentially hazardous or expensive molecules. In this laboratory, investigations are carried

out with a minuscule amount of material. To design successful experiments in this discipline, it is necessary to have a thorough understanding of the flow in micro domains.

IV. Biomedical Engineering: There are different types of applications of micro-channeling in biomedical engineering which are as follows:

- a. PMMA is being used in emerging biotechnology and biomedical research to produce microfluidic lab-on-a-chip devices, which require 100 micrometer-wide geometries for routing liquids in order to function properly. These tiny geometries lend themselves to the use of PMMA in the production of biochips, and the material has a modest level of biocompatibility.
- b. A controlled drug delivery system is a method of delivering medicine into the body in a regulated manner. The precise dosing of liquids through micro-channels is critical in this application.
- c. It also includes micro-channels for transporting the fluid, reaction chambers and other structures for various required operations (cleaning, molecule separation, mixing, and chemical reactions), and a sensor for detection, among other things. The purpose of a biosensor device in biological fluids is to detect specific biomolecules that are present fast and sensitively, such as certain proteins or DNA (e.g., blood).
- d. Electrophoretic application: Electrophoresis can benefit from the use of micro-channels made of acrylic. In order to retain an electrophoretic liquid, the subject micro-channels might take a number of forms. When electrophoresis is applied, the subject micro-channels have significantly less EOF and/or adsorption than fused silica. A wide variety of electrophoretic applications can benefit from their utilization, including the transport of charges in media under the influence of an electric field.
- e. Heat sink and fuel cell plates: Liquid-cooled micro-channel heat sinks and coolers are very effective for high performance of electronic devices (CPU, graphics cards, power amplifier and other devices).
- f. Micro-channel fuel cell plates: A possible power sources for portable electronic devices (Note book, computers PDAS, cellular phones etc.).

Chapter 2

LITERATURE REVIEW AND OBJECTIVE

2.1 Literature Review

The laser was first proposed in 1960 by Theodore Harold Maiman. The laser beam machining process has been the subject of numerous investigations. When CO₂ and Nd: YAG lasers were first produced in the late 1970s, being the main candidates in micro-machining applications. To carry out various processes, such as heat treatment, machining, welding and cutting — while also performing the most complex micro-grooving and micro-channeling operations in air and water on wide variety of engineering materials a laser beam is the most versatile instrument accessible to material scientists and engineers.

A fiber laser micro-cutting technology was used by Kleine K. F. et al. [2002] to create stainless steel stent implants using a fiber laser. The authors took into account two essential response criteria, namely, the kerf width and the surface finish of micro channels, both of which are important elements in determining the overall quality of a manufactured product. In addition, the heat-affected zone (HAZ) is an essential consideration, which has been minimized in this work. Controlling process parameters results in considerable improvements in surface quality and the recast layer. [23]

G. A. Demir et al. [2012] investigated laser micro-machining of the AZ31 magnesium alloy. This material is commonly employed in the production of human cardiovascular stents. In addition, the scientists looked into tubular cutting on a common stent material, AISI 316L tubes with a diameter of 2 mm and a thickness of 0.2 mm. Apart from that, AZ31 tubes with a diameter of 2.5 mm and a thickness of 0.2 mm were made to investigate cutting efficiency. In both cases, the process parameter settings for reactive and inert gas cutting solutions have been compared, as well as the final stent quality. [24]

Andrew S. Holmes [2001] described the use of high-power lasers in the creation of micro-electromechanical systems (MEMS). Ablation in the direct fabrication of MEMS devices and to define polymer masters for subsequent replication by electroforming and moulding (the so-called Laser-LIGA process) have been discussed

in this study. Laser-assisted deposition and etching on planar and non-planar surfaces, laser-assisted manipulation of micro-parts, and laser-assisted assembly also have been discussed. Lasers have the potential to revolutionize MEMS assembly and packaging because they can move and combine parts. [25]

M. Presby et al. [1990] studied the use of CO₂ waveguide laser for the reproducible manufacture of efficient micro-lenses on single-mode optical fiber. Short, powerful laser pulses are utilized to melt micro-lens tips with a specified radius, resulting in the ablative removal of small regions of glass from the surface of the optical fiber. It is necessary to fabricate the micro-lenses with the help of a laser micro-lathe, in which spinning fiber is generated by cutting and heating in the pulsed CO₂ laser beam. It demonstrated outstanding laser-fiber coupling with losses in the 1.5–3 dB range, representing a more than 2 dB improvement above coupling with typical micro-lenses manufactured using the etch and melt process, which was previously reported.[26]

Giorleo L. et al. [2016] created structural scaffolds for the purpose of directing cell development, orientation, and location. Furthermore, lasers can be used to create complicated channel nets into which cells can be seeded or to pattern channels for microfluidic devices, both of which are possible applications. In particular, laser machining is used to produce a high-quality surface that lowers the turbulence of the liquid flow, so preventing the production of micro-cavities and the multiplication of germs. Moreover, the authors studied the process capability of laser ablation to fabricate micro-pockets on titanium sheet (0.5 mm thick). An experimental examination has been conducted in order to determine the nature of the laser ablation procedure. It has been shown that altering process factors such as scanning speed, laser power, q-switch frequency, loop number, and duty cycle can increase the accuracies of micro pockets. Parametric optimization has been carried out, which results in the creation of accurate pockets with a very smooth surface. [27]

Philip R. Miller et al. [2009] have been made contributions in the field of laser-based micro-machining, which include machining processes, laser types utilized in micro-machining and laser-material interaction. The use of laser micro-machining in biomedical applications is also discussed. Laser intensity, aperture, and repetition rate were investigated in relation to the ablation behaviour of silicon in this study. Experiments in vitro have demonstrated that micro-scale grooves on silicon substrates

can be utilized to direct the orientation of human aortic vascular smooth muscle cells. This study describes the application of laser micromachining for the modification of medical equipment, prosthesis, and dental devices. [28]

H. Berrie and F. N. Birkett [1980] conducted experiments to investigate the effects of lens, position, focal plane, speed of cut, and power on the cutting and drilling rates of perspex. It was determined whether the results agreed with the thermal conductivity and vapour removal hypotheses that had been created and given in the study. Interestingly, the latter was found to be in good accord with the experimental observations, and it serves as a firm foundation for the evaluation of laser machining of other materials with comparable behaviour. [29]

Bingkun Zhou et al. [1984] studied the use of GaAlAs diodes in the end pumping of a small Nd: YAG laser results in a long-lived, high-efficiency CW Nd: YAG. It was showed that an Nd: YAG laser oscillator for remote coherent doppler anemometry applications could be made with low power laser diode pumping. Nd: YAG oscillators pumped by laser diodes can be operated at a frequency stability superior to that of conventionally pumped Nd: YAG oscillators, according to this study. [30]

In 2018, G. Trotta et al. improved micro-injection moulding technology through the use of fs-laser micro-fabricated inserts in a standardized mould, called as "micro-fabrication." Making polymeric microfluidic devices on a large scale is made simple and inexpensive by using a combination of technological approaches. When the geometrical characteristics of the device change, the modular technique merely necessitates the replacement of a few minor inserts in the mould. In this case, fs-laser micro-machining can be efficiently used to shape the inserts, which can reproduce the appropriate micro-feature geometry with micro-metre precision without the disadvantage of the lengthy processing time required by the entire mold machining process. The development of this novel technology resulted in the fabrication of a mold prototype. In order to create a benchmark PMMA microfluidic optical stretcher with complicated 3D micro-features such as a micro-channel and two V-grooves, perpendicular to the channel and separated from it by thin walls, the material was first melted down. After that, the material was melted down again. [31]

In a study, Mustafa Tahsin Guler et al. [2021] devised a new approach for the production of polydimethyl siloxane (PDMS) micro-channels by replicating plexiglass moulds in a laboratory setting. Molding of a plexiglass slab using a CO₂ laser in the "raster mode" is used to create the PDMS casting from which it will be cast. Once this is accomplished, an additional layer of PDMS replica has been applied to the substrate with greater pressure in order to overcome the surface roughness left over from the laser machining process. Depending on the complexity of the channel design, a ready-to-cast mold of size of a glass slide has been created in 5–20 minutes, including the design, machining, and cleaning procedures. This fully automated and cost-effective mold-making approach proved to be the quickest of all the methods tested, and it allows for micro-channels with up to a 2.5 aspect ratio to be produced with a width of 60 μm and a height of 23 μm, the smallest of all. Raster mode of the laser creates features that are smaller in size than the radius of the laser beam's circumference. Droplets were formed in the micro-channels, nano-fibers were formed in the channels, and viscoelastic micro-particles were focused in them. [32]

Cyclic olefin polymer films can be used to create micro-channels for micro-fluidics and chemical sensing, according to Ronán McCann et al. [2016]. Scanning electron microscopy (SEM) and optical profilometry were used to examine the effects of a 1064nm Nd: YAG laser on the micro-channel morphology and size. Nd: YAG picosecond pulsed lasers can be used to create continuous micro-channels on thin COP substrates by direct writing. In addition, dimensional control and homogeneity were evaluated using numerous lasers. SEM was utilized to examine the changes in surface morphology in relation to the dimensions of the micro-channels. The surface chemistry was studied using Raman and infrared spectroscopies to determine the influence of laser processing. [33]

Wilhelm Pfleging et al. [2009] investigated the laser processing technologies, such as structuring, surface functionalization, and packaging to manufacture functional capillary electrophoresis (CE) chips on polymethyl methacrylate (PMMA) in a short amount of time. In this study, it was proved that the manufacturing capability of CO₂ laser-assisted micro-patterning has tremendous potential for the fabrication of micro-channel devices, and the production capability of CO₂ laser processes has been extended to micro-channels less than 30 μm in width. It was possible to achieve a high degree of reproducibility in the geometry of the micro-channels. More than 3%

of the variance between the cross-sectional areas of micro-channels that were created and those which were from the fabrication process. Using high-power diode laser radiation and a laser transmission welding process, the packaging of these micro-structured transparent polymers was successfully achieved. Based on the pattern quality and analytical results, it appears that laser-based technologies have a great deal of potential for use in the flexible and cost-effective manufacturing of polymeric microfluidic devices. [34]

Shashi Prakash and Subrata Kumar [2021] investigated three approaches, namely, focused cutting, defocused cutting, and the raster scanning method. Authors used three different fabricating strategies for these three approaches. The focused processing approach can be applied in two different ways, single-pass processing and multi-pass processing, each of which has its own advantages and disadvantages. Similarly, the raster scanning approach can be employed both with and without the application of a mask to achieve the desired result. Various experiments have been carried out to manufacture micro-channels of varying dimensions utilizing a variety of fabrication processes. Surface quality, cross-sectional profile, micro-channel width, and heat-impacted zone have been selected as measures for evaluating and comparing these two methods of fabrication. While the single-pass technique was found to be the most efficient in terms of time consumption, the raster scanning method with masks was shown to be the most effective in terms of constructing micro-channel walls with rectangular cross-sections. The construction of micro-channels on a PMMA substrate using a CO₂ laser has been described in this study. It has been found experimentally and conceptually that direct writing/vector cutting and raster scanning are superior ways of image generation. The single-pass processing method consumes the least amount of time. In contrast, though multipass processing and defocused processing require a greater investment of time and complexity, they result in a lower number of heat-affected zones and smoother microfluidic channels due to the lower amount of energy deposition, defocused beam, and predominance of melting during the processing process. Multi-pass processing has the potential to produce the smallest width micro-channels with significantly smoother micro-channel walls, as well as the highest aspect ratio of any of the three methods. [35]

With the help of heat-accumulated ablation powered by femtosecond fiber laser pulses with high repetition rates, Chong Zheng et al. [2015] have investigated that unique CMBLs can be successfully constructed inside PMMA slices. The CMBL's optimal working parameters were discovered through a thorough investigation of the device's fabrication circumstances, which were 1.5 W average powers at 120 kHz repetition rate for 30 seconds of irradiation. The heat diffusion model indicates that when 12.5 J laser pulse is irradiated at 120 kHz, the PMMA base temperature rises linearly with processing time, reaching the melting point in 567 s and the random scission temperature in 1.70 ms, respectively, when the processing duration has been increased to 567 s. (1.5 W average power). The microscopic imaging of the CMBL generation demonstrates that cracks were first produced at the commencement of irradiation and then gradually melt into the affected zone as processing time increased. The solidification of melted PMMA after the laser irradiation stops results in the development of a smooth and spherical cavity at the end of the procedure. The CMBL can be used to construct a reverse Galilean micro-telescope with a field of vision (FOV) of up to 350 degrees when combined with a microscope. The EFL increases linearly with an increase in CMBL cavity width and progressively declines with the rising refractive index of the slightly compressed affected zone surrounding the cavity. The thickness of the top layer as well as the width of the hole in the bottom layer determines the maximum viewing incidence angle of a CMBL. In comparison to other fabrication processes, the new method is superior as it is simpler to set up for fabrication, produces results more quickly, and has a larger variety of optical properties, such as effective focal length and viewing angles. [36]

Shashi Prakash and Subrata Kumar [2017] worked on a thin copper sheet of 40 mm that was utilized as a mask over the PMMA (Polymethyl-methacrylate) substrate while constructing the micro-channels using the raster scanning function of the CO₂ lasers. It has been demonstrated that a CO₂ laser can be used to create micro-channels of varying width dimensions in both mask and non-mask configurations. It has been discovered that the masking technique may be used to efficiently manufacture micro-channels with a U-shaped cross-section as well as micro-channels with a rectangular cross-section. Additional benefits include complete dimensional control and improved surface quality of the micro-channel walls, which can be achieved with this technology. When it comes to mask preparation, heat-related problems have been

eliminated by using an underwater laser fabrication technique. Overall, the technique was found to be simple to implement, and considerable improvements in micro-channel creation were reported. The influence of process factors on the shape and size of the manufactured micro-channels has been studied in detail. [37]

Jian C. Y. et al. [1993] investigated the laser beam intensity distribution and laser-matter interaction in order to develop a theoretical model for predicting machining depth during laser machining with a 50 ns pulse tripled Nd:YAG laser, which was used to machine titanium. A preliminary estimate of the kerf/slot, as well as the shape of the transverse section, has been performed. This model also aids in the calculation of the threshold radius of laser beam propagation along the thickness of the job sample using the thickness of the job sample. In addition, an experimental investigation was carried out to determine the effect of the focal spot on the depth of cut. During the course of the studies, it was discovered that the diameter of the material being removed is smaller than the diameter of the spot. It has been determined that the highest depth of cut is reached when the focal spot is adjusted to 1~2 mm below the top surface of the workpiece. [38]

An experimental study of laser beam micro-drilling was carried out by Tunna L. et al. [2001]. Laser micro-drilling on 0.25 mm thick 99% pure copper sheet was accomplished using a diode pumped solid state laser with normal (1064 nm), doubled (532 nm), and tripled (355 nm) frequencies. The physical features of the drilled hole and recast layer have been studied in depth as a function of wavelength and intensity. At the second harmonic wavelength, the maximum etch rate was seen. When NIR wavelengths at all specified intensities are used to treat copper, the directionality of the shielding gas helps the melt flow at the top surface to create a unique flow structure. [39]

It was noted that the underlying principles and phenomena for laser beam cutting of thick work samples were fundamentally different from that of laser beam cutting of thin job samples. According to Tsai C. H. and Chen H.W. [2003], controlled fracture technique has been used to cut through thick ceramic substrates with a laser beam using a controlled fracture approach. In this experiment, the Nd: YAG and CO₂ lasers were used in conjunction to create an engraved groove on the top surface of the substrate, which was followed by the formation of a fracture by thermal stress along

the edge of the groove, resulting in controllable separation of the substrate along the path of the laser movement. In order to cut 10 mm thick alumina ceramic substrate, a 60-watt Nd: YAG and CO₂ laser were used. In the micro-structural study, the analysis of the experimental results in conjunction with the SEM image reveals that fracture growth in the transverse direction due to tensile stress at the groove crack edge was stable, whereas it was unstable along the direction of thickness, and that the fracture region was not uniform throughout the thickness for higher cutting speed. [40]

Kuar A.S. et al. [2006] performed CNC pulsed Nd: YAG laser micro-drilling of zirconium oxide (ZrO₂) in order to experimentally explore the thickness of the HAZ and the phenomenon of hole taper in zirconium oxide (ZrO₂). A response Surface Methodology-based optimal parametric analysis has been carried out to determine the optimal setting of process parameters such as pulse frequency and pulse width, lamp current, and assist air pressure in order to achieve the minimum HAZ thickness and taper of the micro-hole while maintaining the highest possible quality. According to the experimental results, a 0.0675 mm HAZ thickness may be attained by selecting the following values for the lamp current, pulse frequency, assisted air pressure, and pulse width: 17 amps, 2.0 kHz, 2.0 kg/cm², and 2 percent of the duty cycle, respectively. Also, it has been noted that at lower lamp current values, taper creation rises with an increase in pulse width, but at higher lamp current values, taper formation becomes inconsequential. [41]

In 2008, Samanta A. N. and Dahotre N. B. studied the effect of multiple reflections on the amount of laser energy absorbed, the thermal effects for melting the material, the vapour pressure effect for expelling out the molten material, the loss of material through the process of evaporation, the inverse effect of surface tension on the expelled depth, and the transient effect of laser beam de-focusing due to the change in machined depth as a function of expelled material during machining. Using a pulsed Nd: YAG laser at a wavelength of 1064 nm, these data are fed into a hydrodynamic computational model, which predicts the desired cut depth and the related amount of heat energy. [42]

The laser micro-drilling of gamma-titanium aluminide has been conducted by Biswas, R. et al. [2010]. The effect of process parameters on hole circularity at exit and hole taper of the drilled hole has been investigated using a central composite design (CCD)

technique based on response surface methodology (RSM). Lamp current, pulse frequency, air pressure, and job thickness were considered as process variables. The desired value of hole circularity can be achieved at lower lamp currents, higher thicknesses, and moderate air pressure and pulse frequency, according to the results of the experimental study, whereas the optimum value of hole taper has been discovered at a lower lamp current, lower air pressure, higher pulse frequency, and higher thickness, respectively. [43]

In order to obtain desired micro hole characteristics, such as minimum hole taper and HAZ width, Kuar A.S. et al. [2011] conducted an experimental investigation into pulsed Nd: YAG laser micro-drilling of alumina. The results indicate that the technique can be used to produce high-quality micro-drills. Taguchi-based Grey analysis has been used to achieve simultaneous optimization of both the quality parameters and the cost aspects of the product. The validity of the suggested multi-objective optimization method has been demonstrated by experimental findings. In order to make the optimization approach more straightforward, the translation of several quality characteristics into a single performance characteristic known as "grey relational grade" has been performed. [44]

With the use of a frequency-tripled Nd:YAG laser operating at a wavelength of 355 nm, Das R.N. et al. [2007] fabricated the thin film capacitors with high capacitance density and low loss. The surface topography of a laser-ablated polymer nano-composite has been investigated using optical imaging, scanning electron microscopy, and atomic force microscopy. According to the analysis, the thickness of the capacitors decreases with an increase in laser pulses. Because the surface smoothness of the ablated areas that define the laser micro-machined capacitors was dependent on the uniformity of the spatial energy distribution of the laser beam. It was important to maintain uniformity in the spatial energy distribution of the laser beam. Images taken with a scanning electron microscope show a noticeable transformation of the laser processed as-deposited BaTiO₃ layer from a smooth surface to a wavy hollow structure. An atomic force microscope (AFM) image of a micro-machined BaTiO₃ edge at the glass surface revealed the presence of an acute micro-machined BaTiO₃ edge, which is highly useful for micro-fabricating membranes for MEMS applications. [45]

To accomplish direct-writing ablation on polymethyl-methacrylate (PMMA) substrates for microfluidic applications, Ting-Fu Hong et al. [2010] employed a commercial CO₂ laser scribe. The direct-write laser machining process has been carried out utilizing both focused and unfocused laser beam technologies, depending on the spot size region and ablation channel geometry. The focusing beam method has a higher energy density in the direct-writing ablation region, resulting in a smaller spot size that was less susceptible to overlapping in the ablation region than the conventional method. The focusing method has been used to create the wave shape in the channel, which has a rougher surface than the rest of the wave. In the direct-writing ablation region, the energy density of the defocusing beam approach was smaller than that of the focusing beam method. The spot size was larger, and because of this, it might easily overlap in the ablation region. Thus, the wave shape can be eliminated and the surface roughness may be enhanced. Scanning electron microscopy and atomic force microscopy surface measurement techniques were used to assess the aspect ratio and surface quality of the ablated micro-channels. As a result of the scribing process, which was carried out with the CO₂ laser beam in an unfocused condition, it was demonstrated that a smooth channel wall could be created without the need for any post-machining annealing operations. [46]

A KrF (krypton-fluoride) excimer laser was used in the experiments by T-C. Chang and P.A. Malian [1999] performed ultraviolet pulsed laser ablation of polymethyl methacrylate (PMMA), polypropylene (PP), and polyethylene (PE) in various media, including air, methanol, and ethyl alcohol. The organics were seen to have a modestly positive effect on the size of the hole and etch depth in PMMA, but to have a significant negative effect on the etch depth in PP and PE. According to existing polymer ablation models, organics have a number of beneficial and detrimental effects on the taper of the hole, contamination, thermal damage, and cracking, which can be explained on the basis of laser-liquid-polymer interactions. These interactions include self-focusing, chemical reactions, pressure-wave generation, and thermal quenching. In the extensive molecule network that allows absorption into singlet electronic states, the interaction of UV light with polymers differs from the interaction of UV light with inorganic materials in several ways. Furthermore, the absorbance coefficient of polymers is directly proportional to the number of delocalized molecular orbitals in the polymer and is sensitive to the presence of impurities in the

polymer. The incubation effect is particularly strong for materials that are poorly absorbent, such as PMMA. The number of incubation pulses required to convert the surface layers of PMMA into chemically different materials reduces with increasing fluence, but some seed pulses are still required to convert the surface layers into chemically different materials. [47]

Raffaella Suriano et al. [2011] used femtosecond laser processing technology to investigate the physical and chemical properties of micro-channels formed in thermoplastic polymeric materials such as poly (methyl methacrylate) (PMMA), polystyrene (PS), and cyclic olefin polymer (COP). The dimensions of micro-channels in the polymers were found to be easily adjustable using surface electron microscopy and optical profilometry, with surface roughness values equivalent to those achieved using typical prototyping techniques like micro-milling. According to colorimetric studies and optical microscopy, PMMA remained essentially transparent after ablation, although COP and PS darkened substantially. The darkening in PS and COP was due to significant oxidation and dehydrogenation during laser ablation, as opposed to PMMA, which was discovered to degrade via thermal depolymerization process. PMMA is the most viable thermoplastic polymer for femtosecond laser production of microfluidic channels due to its stable molecular structure. The results reveal that the rate of elimination was substantially influenced by the laser fluence. However, high-fluence femtosecond laser pulses severely degrade the surface of certain polymers at low scan rates. PMMA may be a suitable material for the creation of microfluidic channels. [48]

Using the femtosecond (fs) direct writing approach, Deepak L. N. Kallepalli et al. [2010] generated buried gratings, surface gratings, surface micro-craters, and micro-channels in bulk poly (methyl methacrylate) (PMMA) and poly (dimethylsiloxane) (PDMS). Because of the minimal damage caused by stress waves, heat conduction, or melting, femtosecond laser direct writing (LDW) has been established prospective approach for accurate structuring of well-defined, three-dimensional submicron structures, notably in polymers. A comprehensive examination of the diffraction efficiency (DE) of the produced gratings as a function of scanning speed, energy, and focused spot size was carried out in both PMMA and PDMS. In both cases, an optimal set of writing parameters for constructing efficient gratings has been

determined. With a single scan using a 0.65 NA (40 X) objective, the greatest DE found in a PDMS grating was ~10%, while it was ~34% in a PMMA grating. To understand the mechanism responsible for physical changes at the focal volume, the fs laser-modified regions were examined using spectroscopic techniques such as Raman, UV-visible, and electron spin resonance (ESR), as well as physical techniques such as laser confocal and scanning electron microscopy (SEM). The bond softening or stress-related mechanisms responsible for structural alterations were suggested by Raman spectra recorded from the changed regions of PMMA. The structural alterations at the focal volume are thought to be caused by multi-photon and tunneling ionization. [49]

Baudach et al. [2000] conducted tests on polymers PC (Poly Carbonate) and PMMA (PolyMethyl Methacrylate) in the air using ultra short laser pulses with pulse duration of 150 fs and a wavelength of 800 nm, which are significant to biomedical technology. Optical, atomic force, and scanning electron microscopy were used to assess the lateral and vertical machining precision. The ablation threshold ranges from 0.5 to 2.5 J/cm² and is highly dependent on the number of laser pulses administered to the same location. The laser fluence and the number of laser pulses have an impact on the hole sizes. An incubation model has been used to describe the relationship between the ablation threshold and the number of laser pulses administered to the same area. A strong incubation effect has been observed for lower pulse numbers $N < 100$, i.e., increasing threshold fluence as pulse numbers decrease. Morphological surface alterations such as swelling, melting, and bubble formation occur at higher fluence or increased numbers of laser pulses. PMMA material may not be removed by a single laser pulse with a maximum fluence just above the single-shot threshold; hence there may be no cavity and no redeposition of the removed material. [50]

The relation between process variables (laser power and scanning velocity) and the response parameters (profile and depth of laser-ablated channel) has been established by Dajun Yuan and Suman Das [2007]. The laser power utilized for channel manufacture ranged from 0.45 to 1.35 W, with scanning speeds ranging from 2 to 14 mm/s. The scanning speeds used for channel construction range from 2 to 14 mm/s. The width of the channels was created between 44 to 240 μm , while their depths ranged from 22 to 130 μm . The depth and profile of laser-ablated channels are predicted using physical models. The threshold fluence for CO₂ laser ablation of PMMA incorporated into the profile model to account for the partial ablation

throughout the beam diameter caused by the laser beam. For a particular scanning speed, the channel depth was proportional to the laser power in a linear fashion. When using a fixed laser power, the depth of the channel was inversely proportional to the scanning speed. Channel width was proportional to laser power for a given scanning speed and inversely proportional to scanning speed for a given scanning speed. [51]

Z. Q. Liu et al. [2000] used a 248-nm long-pulsed KrF excimer laser with a pulse repetition rate (PRR) of 2 and 10 Hz and a fluence ranging from 0.4 to 2 J/cm² to ablate polymethyl methacrylate (PMMA). The impacts of the number of shots, PRR, and fluence on the coupling effects of PMMA in relation to etching depth data and topography of the material were discussed. A rise in the pulse repetition rate (PRR), fluence, or number of pulses accelerates the etching efficiency in terms of ablation rate due to enhanced thermal effects reported. The craters' raptness, porosity, and pollution were all highly dependent on the precise laser operating settings. The increased PRR and the number of pulses both resulted in a crater with a smoother and less porous bottom. [52]

Carmela De Marco et al. [2012] studied the properties of micro-channels and waveguides created by femtosecond laser technology in thermoplastic methacrylate-based polymers, such as poly (methyl methacrylate) (PMMA), and a new material prepared by a high-efficiency UV-curing process of methacrylic monomers bearing hydrophilic polyethylene glycol chains, e.g., tetraethylene glycol dimethacrylate and poly (ethylene glycol) (PEG-MA). Micro-machining on methacrylate-based substrates using fs-laser ablation is a highly successful method for producing micro-channels with controlled geometry and improved surface roughness when compared to using bare substrates. PMMA substrates exhibit a large fluctuation in roughness characteristics as a function of the laser energy density, as demonstrated by profilometry experiments. PEG-MA polymer has several important advantages over PMMA, including enhanced hydrophilicity even after laser ablation and higher stability of buried waveguides due to its cross-linked structure. However, it has been found that ablated micro-channels that are devoid of discolouration and have a suitable level of roughness can be generated. [53]

Daniel Day and Min Gu [2005] used high repetition rate, nano-joule femtosecond laser pulses to machine micro-channels in a polymethyl methacrylate substrate. The

mechanism of micro-channel was based on the localized heating of the substrate caused by the high repetition rate of the laser, resulted in cylindrical channels with smooth walls and a smooth surface finish. Micro-channels with widths ranging from 8-20 μm may be machined at a speed of 800 $\mu\text{m/s}$ utilizing 80 fs pulses with a repetition rate of 80 MHz and an energy of 0.9 nJ/ pulse, with a repetition rate of 80 MHz. The absorption of multiple pulses causes a large increase in the temperature of localized region surrounding the focus spot, which becomes the dominant fabrication process due to the absorption of multiple pulses. It has been found that as the speed of fabrication is increased, both the width and depth of the channels decrease in length. Increasing the width and depth of the channel for a certain manufacturing speed had been correlated with the number of repeats for that particular speed. In order to fabricate channels at greater speeds, there was a minimum energy level below which they cannot be produced. This limit was reached at increasingly higher energy levels. When a fabrication has been performed more than once, it should be heated the following time so that the surrounding medium is heated more evenly in the irradiation zone. This created a channel of almost circular in shape. [54]

Prakash S. et al. [2013] developed an underwater Nd: YAG laser micro-channeling technique on polymethyl methacrylate to reduce the heat-affected zone, micro-cracking, and burr formation surrounding the micro-channeling site. Lamp current, pulse frequency, pulse width, and cutting speed were taken as process parameters, whereas micro-channel width, micro-channel depth, burr width, and burr height were considered as response factors. They also discovered that the properties of burr creation, high-angle heat affected zone (HAZ), and micro-channel dimension are exclusively governed by the parameter settings of the laser processing technique. Researchers have also looked at how water can be used as a cooling medium and to stop molten material from resolidifying in and around the machining zone. They found that the lamp current and pulse width are the most important factors that affect the depth of the micro-channels. [55]

Riahi M. [2011] revealed a novel method of manufacture for the passive 3D mixer. Matrices and mixers are among the most critical components of microfluidic and micrototal analysis systems. With the use of CO_2 laser ablation of Polymethyl Methacrylate (PMMA), the author stated that bending and straight cone formations could be created by varying the laser scanning settings. The influence of bending

cones on the flow direction of a fluid was investigated by the author using computer simulation, and a passive mixer based on such structures was also developed. The PDMS structure was formed into two half-channels with bending and straight cones extending out of the surface, which were then glued together. [56]

To create micro-channels in polymeric substrates, Klank et al. [2002] used a CO₂ laser system that was initially built for the marking of parts in an industrial context to scribe the channels. In the experiments, it was discovered that by employing a laser with a power of 10–60 W and a scanning speed of 80–400 mm/s, it was possible to create a micro-channel with a depth of 100–300 μm and width of approximately 250 μm. This was accomplished by performing the scribing process. [57]

According to Florian et al. [2014], the effects of laser ablation on the surface of polymethyl methacrylate were investigated (PMMA). Experiments were carried out using a femtosecond laser that delivered pulses with a duration of 450 fs and a wavelength of 1027 nm. The laser beam energy was adjusted via a polarizer-based attenuator, and the photodiode energy meter was calibrated to ensure that it was accurate. To position the sample on the beam waist, a focusing technique known as z-scan was employed. The absorption was determined by comparing the results of both energy meters. Using the z-scan approach, the laser ablation in three distinct places between the sample and the laser beam waist was studied to assess its effectiveness. Additionally, it was shown that the concentrating condition is dependent on threshold energy. The absorbance of the samples increased in proportion to the energy of the pulses. When different pulse energies were used to create craters, dimensional analysis of the craters was undertaken in order to establish the ideal focusing circumstances and ablation threshold for the ablation of PMMA samples. [58]

A polymethyl methacrylate substrate was micro-channeled by femtosecond laser pulses with a high repetition rate and nano-joule energy has been demonstrated by Day, D. and Gu, M. [2005]. The mechanism of channel creation was based on the localized heating of the substrate caused by the high repetition rate of the laser, which results in cylindrical channels with smooth walls and a smooth surface finish. Micro-channels with diameters ranging from 8 to 20 μm may be created at a speed of 800 μm/s utilizing 80 fs pulses with a repetition rate of 80 MHz and an energy of 0.9 nJ/pulse, with a repetition rate of 80 MHz. The absorption of multiple pulses causes a

large increase in the temperature of a localized region surrounding the focus spot, which becomes the dominant fabrication process as a result of the absorption of multiple pulses. It has been found that as the speed of fabrication is increased, both the width and depth of the channels decrease in length. Increasing the width and depth of the channel for a certain manufacturing speed was correlated with an increase in the number of repeats for that particular speed. In order to fabricate channels at greater speeds, there was a minimum energy level below which they cannot be produced. This limit was reached at increasingly higher energy levels. The subsequent reheating of the irradiation zone resulted in a more uniform heating of the surrounding medium, resulting in a channel cross-section that was nearly circular in shape as the number of times a fabrication was repeated increased. [59]

Romoli et al. [2007] described an innovative technique for using CO₂ laser machining to generate 3D cavities that may be utilized as molds for polymer resin casting by vaporizing PMMA layer by layer. The influence of cutting sequence, number of passes, laser beam scanning speed, and radiant flux on the groove profile (depth and width) was examined using theoretical models. The removal depth changed proportionally with the number of layers; however, the surface roughness, which was determined by groove spacing and scanning direction orientation between subsequent layers, could not be reduced below a certain level. [60]

Teixidor et al. [2012] studied the geometry of micro-channels manufactured from polymethyl methacrylate using nanosecond laser processing parameters (PMMA). The wavelength of the Nd: YAG solid state pulsed laser was 1064 nm, with a measured maximum output of 4.15 W. The scanning speed was varied from 400 to 800 pulses/mm, the pulse frequency was varied from 5 to 11 Hz, and the Q-switch delay period was varied from 170-180 μ s. The authors used a main effects plot and micro-channel images to determine the impacts of process parameters on material removal rate and surface quality for laser micro-machining of micro-channels in PMMA polymer at the same time. Channel width and depth were found to decrease linearly with increasing Q-switch delay time (therefore average power) and rise non-linearly with greater scanning rates, with pulse frequency having no effect. [61]

Choudhury et al. [2010] looked at the impact of CO₂ laser cutting parameters (laser power, cutting speed, and compressed air pressure) on the laser cutting quality of

three polymeric materials: polypropylene (PP), polycarbonate (PC), and polymethyl methacrylate (PMMA). The researchers studied the various polymers and devised model equations that connected the input process parameters to the output. Heat affected zone (HAZ), surface roughness, and dimensional correctness were the response quality criteria. Based on the primary composite design, twelve sets of tests were done for each of the polymers. The response surface approach (RSM) was used to create predictive models. The adequacy of first-order response models for HAZ and surface roughness was tested using analysis of variance (ANOVA). A linear dependence of the input parameters was shown to be a good model for the response. Surface roughness and HAZ response surface contours were created. For various input laser cutting settings, mathematical model equations are presented that estimate HAZ and surface roughness. The dimensional divergence of the actual value from the nominal value was used to assess the dimensional accuracy of laser cutting on polymers. PMMA has the lowest HAZ, followed by PC and PP, according to the research. PMMA has a better cut-edge surface quality than PP and PC in terms of surface roughness. The response models were developed with the intention of being used in the manufacturing industry. Even though the qualities of the three polymeric materials were different, they all had a similar tendency to be off in terms of diameter. [62]

Romoli et al. [2011] investigated the CO₂ laser machining of an amorphous polymer (PMMA) was a versatile technology for the quick manufacture of microfluidic devices. It was demonstrated how to estimate the key dimensions (e.g., depth and width) of the grooves created by the laser on PMMA. The effects of the key process parameters were taken into account in this model (e.g., power, speed, and spot diameter). This theoretical model was able to regulate the engraving process, demonstrating that the laser could be a viable alternative for micro-channel fabrication. In comparison to traditional glass or silicon items, PMMA single-use gadgets were thought to be easier to manufacture. A single layer of PMMA was removed in a second step using IR laser vaporization. Multiple overlapping sequences of straight grooves with varying scanning directions were used to achieve this. The suggested technique revealed that removal depth varied proportionally with the number of layers machined, whereas surface roughness was affected by groove spacing and scanning direction orientation between consecutive layers. A method for

thermally attaching the PMMA sheets that make up the chip's 3D structure was also demonstrated. It was able to create a bulk connection using a combination of high temperatures and low bonding pressures, resulting in good sealing qualities. [63]

Bhuyan et al. [2010] studied the creation of glass channels with minimum taper using a femtosecond laser. An ultrafast laser system with a simple Gaussian beam profile and lens configuration was used to fabricate tapered channels. In addition, the cross-sectional shape created during femtosecond laser ablation for both hard and soft materials was examined. For the construction of tapered channels, the Gaussian laser beam was a good choice because of its uniformity. The materials were treated utilizing a computer-controlled motion system, with the speed of the workpiece, the energy of the laser pulse, and the number of passes being varied. The channel cross-sections obtained as a result of the experiment were characterized using optical microscopy. It was observed that the relationship between channel height and the non-dimensional number of laser pulses per channel width was a single curve for all of the materials investigated in this work. [64]

Using a continuous wave unfocused CO₂ laser beam, Hong et al. [2010] exhibited a new technique for scribing micro-channels in PMMA substrates. The aspect ratio and surface quality of the ablated micro-channels were assessed using scanning electron microscopy and atomic force microscopy surface measuring techniques. With a laser power of 2.4 W, an unfocused height of $\lambda = 40$ mm, and a scanning speed of 80 mm/s, a micro-channel surface roughness of less than 40 may be created without the requirement for a post-machining annealing step, according to SEM and AFM examinations. The manufacture of a capillary electrophoresis microchip, a cytometer, and an integrated microfluidic chip revealed the feasibility of the suggested unfocused laser beam machining approach. Finally, the results showed that the suggested technique provides a low-cost, customizable option for rapid prototyping of PMMA-based micro fluidic devices. [65]

The surface of a commercially available 1.1 mm thick soda lime glass substrate, microscope slide Cat No. 7101, was irradiated by a CO₂ laser beam (Synrad J48-2W) by Wang et al. [2010]. The laser beam was focused by an F-Theta-Ronar lens with a focal length of 150 mm and scanned on the glass surface by a galvanometer scanner at a scan speed of up to 2000 mm/s in continuous wave (CW) mode. By altering the

power duty cycle (DC, 0.0 to 1.0), i.e., pulse width modulation, at a fixed laser frequency of 5 kHz, different ranges of power were used to analyse the channel-building process. The authors used mathematics to create a quantitative model that could predict a class label for an input object. Without physically conducting the experiment, the regions might be identified using this model for any input combination of scan speed and power duty cycle. [66]

Darvishi et al. [2012] enumerated the effects of critical processing factors during ultrafast laser micromachining of micro-channels made in borosilicate glass, soda-lime glass, and polydimethyl siloxane elastomer (PDMS). An ultrafast laser with a wavelength of 800 nm, nominal pulse duration of 120 fs, a maximum energy of 2.1 m-J/pulse, and a pulse frequency of 1000 Hz was used to create tapered channels. The ultimate channel width as a function of laser processing parameters was accurately predicted using a simple model based on the total amount of laser energy delivered and the threshold for ablating glass. [67]

Huang et al. [2010] used CO₂ laser cutting to increase the surface roughness of PMMA-based microfluidic chip chambers. A non-contact 3D surface profiler was used to investigate the surface roughness of the sections cut using varied laser parameters and ambient temperature in the chamber of the PMMA-based microfluidic chip. The findings revealed that the surface roughness is caused mostly by residues on the laser cut edge, which are caused by the bursting of bubbles. To reduce the surface roughness of the cut piece that was preheating the PMMA sheet to a sufficient ambient temperature during laser processing, a new strategy was developed. The testing results showed that a preheat temperature of 70-90 °C lowered the surface area created by the cut. Finally, when the PMMA sheet was heated to 85 °C, the arithmetical roughness was $R_a = 100.86$ nm, which was the best result. [68]

Sola et al. [2011] used laser ablation to process 8YSZ, alumina, and glass-ceramic samples, irradiating using pulse bursts, and carving grooves into the samples. In this study, a commercial diode-pumped Nd: YAG laser was used to achieve the desired results (Rofin-Sinar E-Line 20). Using a fundamental wavelength λ of 1064nm and a maximum mean power of 11 W, the laser system achieved its maximum performance. There were noticeable differences in the geometrical parameters obtained when the samples were processed using pulse bursts rather than grooves compared to when the

samples were machined. The machining depth was maximal in the first example, at the focus point, whereas it was negligible in the second case. The reduced volume was low at the focus point in both of these instances. While machining samples to create grooves, it was discovered that when the surface to be cut was placed out of focus, the maximum depth and volume were obtained. The location of the maximum values is determined by whether the focus was positioned within or outside of the surface's perimeter. Because of the relationship between geometrical parameters and ablation yields, the mechanical and thermal properties of the substrate are important. A lower hardness of the substrate results in higher values for the parameters. An association was discovered between the optical and thermal lengths of a piece of material and the amount of material that could be removed. [69]

Acherjee B. et al. [2012] investigated the influence of several laser beam machining parameters such as laser power, welding time, weld width, beam width, power density, irradiation time, and depths of penetration on the quality of laser-cut parts. The purpose of this study was to investigate the impact of process factors on the temperature field and the size of the weld bead. It was revealed that a three-dimensional finite element model (FEM) of a simultaneous laser transmission welding process could be created and validated. The second-order equations established by RSM were able to accurately anticipate the outcomes with a high degree of precision. In order to ensure the adequacy of the equations, authors tested using a 95% confidence interval. Increasing laser power and welding time resulted in greater increases in all responses (T_{\max} , T_{weld} , WW, DT, and DA). With the exception of WW (weld width), all of the responses dropped as the beam width was increased. Among the variables studied, laser power had the greatest influence on the maximum time, the welding time, and the width of the weld, followed by welding time and beam width. DT (depth of penetration in transparent material) and DA (depth of penetration in absorbing material) were most affected by welding time, which was followed by power and beam width as the most significant factors. In this case, the welding conditions obtained from the graphical optimization might be used to realize the process window necessary for obtaining a satisfactory weld. The use of an overlay contour plot facilitated the search for the most effective welding parameters. [70]

Choudhury et al. [2012] examined the effects of four input-controlled laser cutting factors on the hole taper and hole circularity in laser trepan drilling of polymeric

materials. Experiments were carried out on polymer sheets made of acrylonitrile butadiene styrene (ABS) and polymethyl methacrylate (PMMA), respectively. The process factors that were chosen as independent variables were laser power, assist gas pressure, cutting speed, and stand-off distance. To achieve a 5mm thickness in those work materials, three separate holes with diameters of 2mm, 4mm, and 6mm were drilled to 5mm thicknesses. In order to gather the essential information with a reduced number of tests, a Taguchi L9 orthogonal array with four factors and three levels of each factor was utilized to organize and run experiments. The process performance was measured in terms of hole taper and hole circularity to determine how well the process worked. The ANOVA analysis was used to determine the optimal amounts of the four process variables in relation to the materials and hole diameters used in the experiment. It was found that the optimum amounts of four process variables changed depending on the hole size and material used in the experiment. An additional study was carried out in order to account for the effect of the material and hole diameter on the hole tapering. Following an examination, it was observed that compressed air pressure of 2.0 bar, laser power of 500 watts, cutting speed of 0.6 m/s, stand-off distance of 5.0mm, hole diameter of 2.0mm, and PMMA as the material produced the best possible results. The hole with the least degree of taper was the result of these combinations. [71]

Kruger et al. [2005] used a femtosecond and nanosecond laser ablation approach to study the femtosecond and nanosecond laser ablation of Polymethyl methacrylate (PMMA) and PMMA doped with a linear absorber in the infrared spectral range. Ablation and incubation phenomena thresholds were established and incubation phenomena were identified. A phenomenological model of awareness was used to determine the degree of incubation. This research looked into the effect of pulse duration on polymer machining quality. For a controlled fs-laser structure, unlike with the ns-treatment, the presence of an absorbing chromophore was not a need, unlike with the ns-treatment. Surface swelling was usually present when ablation was performed. [72]

To compare the percussion drilled holes in fiber reinforced polymer and non-reinforced thermoplastic sheets, Yalukova O. and Sarady I. [2005] employed three different wavelengths: 1064nm, 532nm, and 266nm. The majority of bulk

thermoplastic and thermoset polymers were somewhat transparent at near-infrared and visible wavelengths, 1064 and 532nm, respectively, when measured at these wavelengths. Depending on the amount of crystallinity present, the degree of transparency varies. The hole drilling process was greatly enhanced and the risk of heat damage was significantly reduced for both materials when the fourth harmonic ultraviolet light (266nm) of a diode-pumped and AOQ-switched Nd: YAG laser with pulse duration of roughly 100 ns was used. The material was altered in the vicinity of the irradiation spot or the drilled holes. When ultraviolet light with high photon energy was used, there was unequivocal evidence of a shift in the interaction mechanism. It was discovered that by employing UV light, bond breaking happened rather than thermal material loss and that the major interaction mechanism changed from thermal to photochemical dissociation or photo-ablation. The results obtained indicate that contour cutting of epoxy and polyester polymer sheets reinforced with different fibers would be conceivable with even higher average UV power at 266nm and higher repetition frequency when utilizing even higher average UV power at 266nm and higher repetition frequency. It was possible to reach higher power outputs by employing a longer BBO crystal, which allowed for a 10 W increase in the average power of the current laser in the ultraviolet. This level of power was sufficient for cutting polymer sheets with a thickness of up to 2 mm. [73]

Jiang, X., et al. [2014] employed a diode laser to fuse two PMMA substrates together at the interface, with a thin film metal spot-based intermediary layer acting as a localized absorber. The laser micro-welding procedure was done with a broad laser beam with a top-hat profile. The effect of laser power and processing time on the heat affected zone (HAZ) and melted zone produced by laser processing was studied. A 22-spot array of thin-film metal spots was used for large-area welding to assess the impact of spot spacing on the interfacial bond produced between the two polymer substrates after the welding process was completed. A big area of titanium film with a size similar to the 22 arrays was also explored to provide a point of comparison. Due to the higher temperature rise associated with the discrete film pattern-based design, the results showed that it outperformed a single large-area film in terms of decreasing the effect of substrate distortion induced by the latter's higher temperature rise. This work demonstrates the successful use of laser micro-welding technology in the leak-free encapsulation of a microfluidic channel. The interaction between the weld zone

and the heat affected zone, as well as the laser power and processing time, were studied. It was determined that a laser power of 25 W, corresponding to a beam intensity of roughly 70 W/cm², was sufficient to establish an acceptable bond after 15 seconds of processing. It is feasible to create a continuous weld between neighbouring circular titanium film spots by altering the spacing between the adjacent circular titanium film spots. When it comes to minimizing the influence of substrate distortion on big-area substrate joining, the results of the examinations of numerous film patterns revealed that the spot array design was preferable to the large thin film patch design. [74]

Huang Y. et al. [2010] used CO₂ laser cutting to fabricate the chambers of the polymethyl methacrylate (PMMA)-based microfluidic chip. The surface roughness of the sections was measured using a non-contact 3D surface profiler after the chambers were cut using different laser parameters and the ambient temperature was measured. It was concluded that the surface roughness was mostly caused by residues on the laser-cut edge, which were created as a result of the bubbles bursting. A novel approach was developed to minimize the surface roughness of the cut portion that was used to pre-heat the PMMA sheet to an appropriate ambient temperature before laser processing. The results showed that by preheating the surface to a temperature between 70 and 90 degrees Celsius, the surface roughness caused by the cut may be decreased and that the temperature-controlled preheat method might be used to improve surface roughness. [75]

Waddell et al. [2002] investigated the physical shape of the channels as a function of the local atmosphere in which ablation takes place. PMMA ablation was carried out in the presence of nitrogen, methanol, and water to provide the best results possible. A rectangular channel profile was produced by ablation under nitrogen and methanol conditions, but a wedge-shaped profile was produced by ablation under water. According to the researchers, this variation in cross-section is likely to be the result of the laser beam self-focusing or re-focusing as it travels through water, according to the researchers. Beyond the self-focusing effect, the water also contributes to the liberation of debris that was typically left behind after the laser ablation process. Ablation of PMMA, while submerged in methanol, leads to cracking of the material, which was most likely caused by methanol migrating into cracks and exploding when

exposed to laser energy. It has been shown in the study that the physical morphology of the ablated region was influenced by the temporal profile, the spatial profile, and the wavelength of the laser pulse that was used. As the length of the laser pulse length increases, the fluence required to ablate the substrate increases proportionally. This was due to the fact that the ablation of the surface of the polymer is a function of the amount of energy deposited in a certain amount of time. Ablation pulse lengths can range from hundreds of femtoseconds to tens of nanoseconds, and they are determined by the physical parameters of the laser used to perform the ablation. Additionally, for the same substrate material, varied ablation wavelengths result in a range of distinct limiting aspect ratios. Because the geometric shape of the ablated area is dictated by the spatial profile of the laser beam, a bad spatial profile of the laser beam results in poor feature quality and repeatability. In addition, a slower scanning speed and a higher laser pulse frequency result in a greater number of pulses applied per site and a greater ablation depth for a specific area when compared to other methods. [76]

Hong T. et al. [2010] explained the direct writing ablation of polymethyl methacrylate (PMMA) substrates for microfluidic applications using a commercially available CO₂ laser scribe. In this study, commercial layout software was used to produce the microfluidic designs, which were then transformed into the command signals needed to drive the laser scribe and replicate the necessary micro-channel configuration on the surface of a PMMA substrate. The aspect ratio and surface quality of the ablated micro-channels were studied using scanning electron microscopy and atomic force microscopy surface measuring techniques. It was observed that by completing the scribing process with the CO₂ laser beam in an unfocused state, smooth channel walls could be achieved without the requirement for additional post-machining annealing processes. The researchers confirmed that their unfocused ablation technique was a feasible alternative for the speedy and cost-effective production of a wide range of PMMA-based microfluidic devices. [77]

The huge potential of a CO₂ laser system for rapidly creating polymer micro-fluidic devices was highlighted by Klank H. [2002]. The depth and width of laser-cut channels were evaluated in relation to the laser beam power and the number of passes the beam made along the same channel. The laser beam power was changed between 0 and 40 W, and the passes were varied from 1 to 7 times in the experiments. Channel

depths were normally between 100 and 300 μm , and channel widths were typically 250 μm . The narrowest channel constructed was 85 μm wide. Solvent-assisted gluing, melting, laminating, and surface activation with a plasma asher were all studied as bonding procedures for micro-structured PMMA [poly (methyl methacrylate)] parts. The most time-efficient approach was found to be solvent-assisted heat bonding. Different bonding approaches were studied, and an ethanol-based bonding method for bonding a four-layer micro-system was shown to be successful. [78]

In an experimental and theoretical investigation, Yuan and Das (2007) studied the micromachining of PMMA using a CO₂ laser ablation technique. According to the findings, micro-channels with widths ranging from 44 to 240 μm and depths ranging from 22 to 130 μm could be created using a laser power of 0.45-1.35W and a scanning speed of 2–14 mm/s. According to the findings, channel depth and width are directly related to laser power and inversely proportional to scanning speed for a certain scanning speed. Physical models were developed based on the findings of the experiments to estimate the depth and form of the ablated channel as a function of laser processing characteristics such as laser power and speed of movement over the surface. [79]

M. Jensen et al. [2003] demonstrated the use of a CO₂ laser to construct cavities and microstructures in poly (methyl methacrylate) (PMMA). The laser beam was moved in a raster pattern across the PMMA surface, creating cavities and microstructures. The topography of the cavities that were created as a result of this process was investigated using stylus and optical profilometry, as well as scanning electron microscopy (SEM). Several artifacts from the laser ablation process were visible in the micro-structures, and optimization of laser ablation settings has been done to reduce the appearance of these artifacts. It was feasible to construct structures with a depth of 50 μm and a minimum width of roughly 200 μm using this technology, with a depth dictated by the beam size and laser settings ranging from a few μm to several μm . The rather wide beam width of the laser was responsible for determining the smallest possible feature size (around 290 μm with significant energy in a beam envelope of 160 μm). That is, it was critical to use the best laser settings possible for a generation of functional structures. [80]

Heng, Q. et al. [2009] experimentally investigated a microfluidic channel on a 1.5 mm thick PMMA sheet using a 248 nm excimer laser direct-writing method. Increased laser fluence leads to an increase in the depth of the channel as well as the roughness of the surface. Surface roughness decreases as the length of time between irradiation pulses have been increased. In contrast, if the irradiation pulse period is too long, some tenuous stripes along the channel's edge may be created, which is undesirable. The excimer laser fluence is one of the most important factors in determining the surface roughness of the microfluidic channel's surface. Under the fixed translational speed of the working platform, the depth and surface roughness of the micro-fluidic channel both gradually rise as the fluence of the excimer laser is increased. The surface roughness of microfluidic channels can be improved when excimer laser polishing is used during the processing. As the irradiation period is increased, the surface roughness decreases; however, if the irradiation time is raised too much, certain tenuous stripes on the channel's edge appear, causing the surface roughness to worsen. [81]

Kim C. S. et al. [2012] conducted research on focused ion beam (FIB) technology. A variety of approaches to fabricating micro- or nanoscale structures and geometrically complicated structures were studied, and their efficacy as well as structural stability was examined. The capability of the FIB to build such intricate structures with micro or nano-scale features was directly tied to the ability of the FIB to perform both destructive and constructive activities. There are four fundamental types of operation that could be used for alteration and imaging. The manufacturing procedures, which included milling as well as deposition, were related to the precision manufacture of samples at the micro and nano-scales, according to the researchers. Surface morphologies with nanoscale effects could be better understood if the rates at which materials are processed were taken into consideration. Ion dose, dwell time, refresh time, current density, spot size, ion current, incidence angle, ion energy, overlapping, ion species, and precursor gas were investigated to enhance nanoscale fabrication. Aspect ratio, smooth surface roughness, and sidewall angle were calculated to determine efficiency and structural stability, and the complex physical and chemical phenomena were examined with a specific contribution. It was possible to create complex 3-D micro- or nanoscale structures using the FIB method. [82]

In the case of biochips, Chantal and Khan [2006] investigated laser-based approaches for the manufacturing of microfluidic devices, as well as resolving some of the challenges associated with their fabrication. Special focus was paid to the use of lasers for rapid prototyping and the production of biochips. Other topics discussed include femtosecond laser ablation applications and devices, laser-induced micro-joining, and the creation of micro-replication tools with laser assistance for future polymeric chip replication using a process such as laser LIGA. Direct patterning with a variety of laser sources (e.g., UV laser sources with masks, IR lasers) or an indirect technique in which polymer chips are copied via laser-aided micro-machining of mold inserts are two methods for rapidly fabricating polymeric microfluidic devices. It is now possible to generate three-dimensional channels and nano-channels inside transparent materials because of recent improvements in femtosecond laser technology. The CO₂ laser was a fast, dependable, and cost-effective tool for the rapid manufacturing of specialized polymer biochips. Rapid prototyping was made possible for functional prototypes by combining laser patterning with laser welding techniques such as laser transmission welding. [83]

Although Kruusing, A. [2004] focused on subtractive processes like laser etching and cutting in the presence of liquid water, the article also covered water-assisted or underwater laser processing techniques like welding, silicon wafer breaking, polymer surface modification, pulsed laser deposition, particle formation, and water-mask defined micro-structure fabrication. Cutting and etching under water resulted in tighter tolerances and narrower heat-affected zone widths, as well as less debris re-deposition. Laser ablation in water vapour results in the deposition of highly crystalline hydroxyapatite coatings on the surface of the object being treated, while irradiation beneath water results in increased wetting of fluoropolymers. [84]

Gomez, D. et al. [2005] exhibited the micro-structured passive microfluidic devices (channels, reservoirs, and through-holes) in polymers such as PMMA, polyimide (PI, Kapton), and glass (Pyrex) using a doubled Ti: sapphire femtosecond laser ($\lambda = 400$ nm; pulse width, 90 fs; pulse energy up to 350 μ J; pulse repetition rate, 1 kHz). These materials were chosen due to their widespread use in the production of microfluidic chips. Fluid transport channels of a few tenths of micro-meters are accomplished with a high-quality finish in all scenarios. The same principles apply to

the formation of reservoirs and holes. Due to the lack of heat effects, ultra-short pulses are well-known for having little edge effects, allowing for good sealing. For PMMA, polymer bonding processes are used. Pyrex has chosen the well-known anodic bonding method for silicon sealing. Fabricated prototypes perform well in both conditions, with no leakage and good flow behaviour. [85]

Cheng et al. [2004] demonstrated that by carefully modifying the CO₂ laser system settings, microfluidic devices with channel aspect ratios ranging from 0.5 to 7 may be built on a single PMMA substrate. Due to the harsh surface of machined trench walls (i.e., 5–10 µm surface roughness) and the limited potential for surface chemical alteration, the CO₂ laser's utility for direct writing of PMMA substrates is limited. The channel depth can be changed by adjusting the laser strength, motion speed, and number of passes of the laser beam utilized in scribing. The channel width is controlled by adjusting the beam size. When the substrate is positioned at the beam focusing plane, the smallest width is achieved. A broad channel width is achieved by moving the substrate away from the focal plane. The report also discusses the advantages of using PMMA as a substrate. Contamination from bio-molecule adsorption is reduced because the PMMA sheet is non-porous. Furthermore, PMMA is non-hydrolyzable and inert in neutral aqueous solution. [86]

Wu et al. [2006] experimentally investigated the micro-machining process on polymethyl methacrylate with oblique KrF excimer laser beams. The results show that the ablation rate decreases monotonically as the incident angle increases for a variety of reasons with low aspect ratio ablations. High-aspect-ratio drilling with an opening center on the focal plane ablation rate was almost fully independent of incidence angles and was lower than low-aspect-ratio drilling with an opening center on the focal plane ablation rate. The apertures of the holes placed at a distance from the focus plane are expanded after high-aspect-ratio ablations, and the margins of the openings appear to have been blurred. Furthermore, the depth of a hole in samples oblique to the laser beam at a distance from the focus plane decreases as the distance between the focal plane and the sample increases. As the angle of incidence of the laser beams increases, the number of deep holes produced by oblique laser beams travelling through a matrix of apertures decreases. These occurrences demonstrated a hitherto unknown effect of local light intensity on micro-drilling into an oblique surface. [87]

Pan et al. [1996] looked into the unique expansion of the heat-affected zone generated by laser energy, as well as the anisotropy of heat conductivity caused by the anisotropic organization of the fiber reinforcement in the composite material. Furthermore, it applies the principle of enhancing cut quality by lowering the workpiece's resulting temperature, resulting in laser machining at a low temperature. The cutting of a unidirectional laminated carbon/epoxy composite perpendicular to and parallel to the fiber axis was investigated using a cool nitrogen jet to reduce thermal damage. In order to estimate the level of thermal damage in connection to process parameters and material qualities, a theoretical study based on the moving-point heat-source theory was used. The "mirror image approach" was used to modify the analytical answer for a specimen with a finite thickness in this case. With the help of the isotherm of the matrix char temperature, it was possible to estimate the range of the heat-affected zone. It was discovered that heat conduction is greatest along the carbon fibers, with the form of the heat-affected zone being influenced by the direction of the beam scanning in relation to the orientation of the fibers. [88]

Yilbas et al. [1997] investigated the effect of laser parameters and material qualities on the hole quality of the holes created by a pulsed laser. To determine the significance level of the elements that influence hole quality, a statistical approach known as factorial design was used in this study. Stainless steel, nickel, and titanium were all examined as potential materials for the project. When it came to evaluating the hole geometry, marks were assigned to each geometric feature, with the marking scheme chosen in accordance with the significance of the hole feature. [89]

For the CO₂ laser cutting process, Yilbas et al. [1997] developed a mathematical model and solved the heat transfer equation using a numerical method. The melting front velocities at various laser output levels and workpiece thicknesses were anticipated. The melting front profile's temporal evolution was calculated. Experimental studies of the transitory behaviour of vapour expelled from the kerf during the cutting process have been added to the research. Findings from experiments show that the melting front velocity is high at this early stage of the cutting process. [90]

Mathew et al. [1999] conducted studies on carbon fiber reinforced plastic (CFRP) using a pulsed Nd: YAG laser at the optimum process parameter ranges. On the basis

of critical process characteristics, such as cutting speed, pulse energy, pulse duration, pulse repetition rate, and gas pressure, predictive models have been built for use in a variety of applications. The heat-affected zone (HAZ) and the taper of the cut surface were the reactions that were taken into consideration. The response surface methodology was used to optimize the process parameters during the optimization phase (RSM). They were thought to be the most important parameters that influence cutting performance, together with the thermal properties of the constituent materials and the volume fraction of the fibers. Additionally, the impact of process factors on the output reactions was examined. [91]

To forecast the quality of the cut under a variety of cutting situations, Kaebernick et al. (1999) developed a three-dimensional analytical model of pulsed laser cutting with the goal of improving accuracy. Modeling the effect of a laser beam on surfaces inside a cutting zone is done using tiny point heat sources, which represent the effect of a laser beam on surfaces inside a cutting zone, and it takes into account the contribution of the oxygen reaction to the heating of the metal. In order to verify the expected cutting outcomes for various speeds, powers, and pulse characteristics, experiments with an Nd: YAG laser were carried out on mild and stainless steel cutting blades. [92]

Low et al. [2001] used a fiber optic delivered Nd: YAG laser to characterize the spatter deposited on laser-drilled holes in a Nimonic alloy and analyze the various laser processing parameters. The main findings were that: (a) a large portion of spatter (approximately > 70%) was accumulated due to the initial laser pulses required to drill a through hole; (b) short pulse width, low peak power, and high pulse frequency produced small spatter areas; (c) the spatter distribution can be altered at high frequencies due to the interaction between the laser beam and ejected material; and (d) focal position between -0.5 and +1.5 mm produced similar spatter areas. [93]

Most et al. [2003] developed a laser projection etch approach to build linear arrays on single crystal (0 0 1) SrTiO₃ substrates. With a depth to breadth aspect ratio of 4:1, 17.5 μm feature sizes were produced. The influence of laser fluence on etching was investigated, and it was discovered that as laser fluence increased, straighter sidewalls and flatter trench floors were attained. Higher laser fluence, on the other hand, increased the heat impacted zone by post-pulse plasma and roughened the top surfaces

due to the deposition of evaporated materials. Deposition and subsequent pull-off of $\text{YBa}_2\text{Cu}_3\text{O}_7$ sacrificial layer resulted in clean top surfaces for the features. In addition, four-circle X-ray diffraction using a 2-D area detector was used to characterize the phases of recast layers on the sidewalls before and after they were removed with a wet chemical etch solution. The application of a wet etchant was shown to be effective in removing the thin polycrystalline recast layers. [94]

Booth [2003] demonstrated the laser micro-processing techniques, utilized to produce microstructures over large areas with excellent precision and accuracy. The techniques used are laser mask projection, synchronized image scanning (SIS), bow tie scanning (BTS), and direct beam micro-machining. These techniques can be utilized in industrial production for solar cell scribing, micro-optical device fabrication, inkjet printer nozzle drilling, and plasma display panel patterning, to name a few. [95]

Abedin et al. (2004) found that cutting copper with a high-repetition-rate (10 kHz) Q-switched Nd: YLF laser was more efficient. When the speed of lateral translation of the thin copper sheet over the beam focus was reduced, machining efficiency (material removed per unit time) increased significantly. Increased efficiency was attributed to the effects of pulse adjacency (i.e. partial overlapping) of many pulses at a given spot on the target surface. The effect could be caused by a number of mechanisms, which were discussed. Similar outcomes came from laser trepanning experiments. Increases in ablation rates have been recorded, which could lead to advances in several industrial operations such as laser drilling, cutting, and marking. [96]

Nikumb et al. [2005] investigated the use of short-pulse solid-state lasers with pulse lengths ranging from ns to fs to generate short pulses to process several types of glass materials. In order to expose the underlying thermal effects and nonlinear processes, a study was done to determine the effect of the pulse length and other process factors on the machined features. Edge quality, circularity, aspect ratio, redeposit material formation, and machining rate were all studied in connection to processing variables such as focusing optics, laser power, wavelength, and repetition rate, among others. A variety of drilled micro-hole patterns and manufactured micro-features, as well as the potential applications for these designs were exhibited. [97]

Micro-welding, soldering, selective silicon and glass bonding, micro-structuring, and laser-aided shaping are some of the laser applications studied by Gillner et al. [2005]. In the past, most micro-part manufacturing and machining were accomplished using electronic industry technologies, which were founded on silicon etching techniques for the production of, for instance, sensor elements. Suitable procedures for machining parts from non-silicon materials have become increasingly relevant due to the increasing need for micro-products in various industrial fields such as the medical, automotive, optical, and chemical industries. Because of its great lateral resolution, minimal focusability down to a few microns, low heat input, and high adaptability, laser technology has been qualified for micro-technology. [98]

Chen and Darling [2005] studied the use of a near-ultraviolet Nd: YAG laser for quick micro-machining of sapphire and silicon, and their findings were published in *Nature*. With the use of a high-speed x–y galvano-mechanical beam positioner, cutting, marking, and surface ablation of both materials have been accomplished through direct writing. The results of machining, such as the ablation rate and efficiency, are discussed. The findings demonstrate that a number of parameters, including focus length, beam feed rate (cutting speed), and pulse repetition rate, have an impact on the quality and efficiency of laser machining. When using near UV nanosecond pulses, the surface morphology and ablation rate of sapphire indicate that the laser ablation process could be a mixture of photo-thermal and photochemical processes, whereas the laser ablation process of silicon appears to be dominated by a photo-thermal process when using near UV nanosecond pulses. [99]

Kuar et al. (2006) used the Response Surface Methodology (RSM) to investigate the impact of a variety of laser machining parameters on the thickness and taper of micro-drilled holes on alumina–aluminum composite work samples. Mathematical modeling of Nd: YAG laser performance criteria that correlate with numerous process parameters had also been conducted. [100]

E. Beal et al. (2006) utilized response surface methodology (RSM) to explore the laser fusing of a mixture of H13 and Cu powders to eliminate or minimize cracks and porosity in order to understand the link between laser processing parameters and defects (cracks and porosity). The methodologies of Box and Behnken were used in this investigation. In the following step, a factorial analysis was conducted utilizing

the most significant factors identified through the Box-Behnken analysis. Cracks and porosity were successfully minimized, according to the results of the analyses. In order to forecast the fault model, regression studies were carried out on both modalities of data collection. Cracks and porosity are reduced from 15.32% to 2.54% as a result of the optimized process parameters. Micro-hardness tests performed on both specimens prepared using default and optimized settings reveal no significant variation in performance. [101]

Yung et al. [2007] systemically investigated the Nd: YAG laser drilling performance of blind vias in epoxy/aluminum nitride (AlN) composites and virgin epoxy. The average laser power, repetition times, and pulse repetition rate varied from 0.2 W to 1.2 W, 12 to 48 seconds, and 3 KHz to 20 KHz, respectively. The findings show that, in comparison to pure epoxy, the drilling conditions of blind vias in epoxy/AlN composite may be changed across a wide range, with no significant residue discovered at the entrances of the blind vias. While there is a strong relationship between the repetition rate and other parameters of the Nd: YAG laser, there is a stronger relationship between the average laser power, laser repetition rate, and repetition times, and this relationship should be closely monitored. [102]

Kazari et al. [2009] developed four models to forecast the width and depth of CO₂ laser-formed micro-channels in glass. The power (P), pulse repetition frequency (PRF), and traverse speed (U) of the laser machine were chosen as the parameters for examination in a 33 statistical design of experiments (DoE) model. Three artificial neural network (ANN) models with feed-forward and back-propagation were also created. Variations in the number and selection of training data were used to test the impact of these ANN models. Model A was developed using 24 randomly picked data points based on the trial results, leaving three data points for testing. Model B was constructed using the experimental data space's eight corner points and seven others randomly picked data points, leaving 12 data points for testing. Model C was developed using 15 data points that were picked at random. These models were developed individually for predicting microchannel width and depth. Lab VIEW code was used to create these ANN models. These ANN models and the DoE model were compared in terms of performance. Two of the ANN models had a higher average percentage error than the DoE model when compared to the actual results. The other

ANN model had a prediction power that was roughly twice as good as the DoE model. [103]

Niino et al. (2011) used a continuous wave fiber near-IR laser ($\lambda = 1090$ nm) to laser cut various micro-patterns on carbon fiber reinforced polymer (CFRP) to achieve precise cutting of CFRP with no debris or thermal damage surrounding the grooves. During fiber laser irradiation on CFRP, a fast beam galvanometer scanning using the multiple-scan-pass approach was done. At 15 multiple scans passes at a scanning speed of 0.8 m/s, the kerf width dimension of 600 μm was measured around the periphery of the micro-machining zone of the CFRP sample, devoid of debris and other thermal damage. [104]

Jäschke et al. (2018) investigated CFRP micro-cutting with a 6 kW fiber laser in a follow-up study. A thermoplastic carbon fiber-reinforced polyphenylene sulphide (CF/PPS) matrix and a thermosetting carbon fiber-reinforced epoxy (CF/epoxy) matrix were used in the testing by the authors. Results indicated that the amount of HAZ reduced as the cutting velocity and laser power was increased. Conclusions Aside from that, it was discovered that the maximum measured HAZ for a CF/PPS workpiece was larger than that for a CF/epoxy workpiece when the cutting velocity was 20 m/min. [105]

Herzog et al. (2016) performed laser cutting operations on a 6 mm thick CFRP workpiece with a high delay between each pass of 2 seconds in order to reduce the accumulation of heat from the cutting zone. According to the findings, the repeated pass technique paired with ultra-high-power pulses could greatly eliminate HAZ from the cutting zone. [106]

Mizunami et al. (2011) employed a 1.56 μm erbium-doped fiber laser oscillator-amplifier system, as well as direct amplification and pulse extraction, to perform femtosecond pulsed micro-machining on an amorphous carbon film and a polyvinyl chloride film. It was possible to achieve peak power of up to 25 kW during the pulse extraction and amplification processes. In addition, using the procedure of pulse extraction and amplification, a trail of ablation measuring 6 μm was discovered. For micro-machining with a fiber laser on polyvinyl chloride film, on the other hand, direct amplification was shown to be more effective than indirect amplification in this case. It was observed during the experiment that the cut width dimension was 4 μm .

In addition, the optical damage was reduced with a higher repetition rate of 100 kHz, owing to the lower peak power of the fiber laser used in the experiment. [107]

During the manufacturing of a cardiovascular stent made of NiTi alloy tube, Liu et al. [2016] investigated the effect of fiber laser process parameters on responses such as surface roughness, kerf width, heat affected zone (HAZ), and the production of dross (outer diameter of 1.8 mm and a wall thickness of 240 μm). Materials used to manufacture the cardiovascular stents include nickel-titanium (NiTi) alloys and stainless steel, among others. A steady stream of water was forced through the tube's interior walls while argon served as an inert gas, allowing the trials to be completed successfully (constant pressure of 0.45 bar). It was observed that under the wet cutting circumstances, no striation was generated on the surface topography of the surface. The mixed topography striation ratio for the micro-cuts proved to be the most effective method for achieving low surface roughness, narrow kerf width, and a thin recast layer. The power density had an effect on the geometry of the kerf width. An increase in power density resulted in an increase in the energy of the pulses. An increase in the dimensions of the kerf breadth was noted as a result of this. The narrowest entry width of 25.53 μm was attained using a medium power density in conjunction with a low cutting speed, according to the researchers. On the other hand, an entry kerf width of 38.59 μm was achieved by using a high-power density in conjunction with a fast cutting speed during the cutting process. It was observed that as the power density was raised, both the surface roughness and the kerf width increased as well. Cutting speed was shown to be the most important process parameter for achieving a high-quality surface finish when compared to the other process factors. Specifically, the uniformity and smoothness of the micro-machined profiles are determined by the spot overlapping factor; in other words, the higher the spot overlapping factor, the greater the uniformity and smoothness of the profiles. It was found that the spot overlapping factor was low when the cutting speed was high. With an increase in cutting speed, the phenomenon became the inverse of what it was. [108]

Kliene and Watkins (2003) examined the results of micro-cutting using pulsed fiber lasers and pulsed Nd-YAG lasers in order to determine their suitability. It was exhibited that the micro-cuts created by the fiber laser were identical in appearance to

those made by the Nd-YAG laser. The surface quality of the cut was impaired from the bottom to the top edge of the cut when the peak power was reduced. As a result, the roughness of the surface has been improved. [109]

William Streifer et al. [1988] studied the semiconductor diode lasers which are already being utilized as pumps for low-power commercial continuous-wave Nd-doped solid-state lasers of the type used in telecommunications. Increasing the power and efficiency of diode laser technology (which could eventually reach 65 or 70% efficiency), it was reported that their employment in larger solid-state laser systems will grow. Furthermore, it is revealed that the cost decreases as manufacturing volumes and yields increase, and the quality of the diode pumps continues to improve. [110]

A model for pulsed laser micro-machining for polymers with high absorption at the irradiation wavelength has been developed by D.E. smaeilpour Ghoochani et al. [2019]. The utilization of CO₂ laser micromachining of Poly-Ether-Sulfone (PES) polymer, which has been widely used as a biocompatible material. Various types of nanosecond pulsed lasers have been discussed in detail in this paper, which includes a thorough model. The suggested model makes use of the experimental parameters in order to predict the physical features of micro-channels, such as depth, width, and profile. The controlling input variables include the laser fluence, the scanning speed of the mini-CNC router table, the pulse repetition frequency, the laser beam radius at the focal length, the pulse duration (FWHM), and the thermo-physical characteristics of the PES polymer. To evaluate the suggested model validation, the theoretical and experimental results were compared. The results revealed acceptable average variances of 8.1%, which was within acceptable limits. [111]

Ivan-Lazar Bundalo et al. [2014] showed fiber Bragg grating (FBG) writing in PMMA micro-structured Polymer Optical Fibers (mPOFs) using the UV Phase Mask approach, with writing periods less than 10 minutes. There was a difference between the shortest writing time (6 minutes and 50 seconds) and the longest writing time (8 minutes and 50 seconds). The FBGs were written in a 125 m PMMA mPOF with three rings of holes and a thickness of 0.5 mm. A total of 26 dB of reflectivity was observed between the reflection peak at 632.6 nm and the center of the reflection peak

at 632.61. They also demonstrated how the dynamics of writing are affected by the amount of energy emitted by the writing beam. [112]

2.2 Objective and Scope of Present Research Work

From the review of the past research and literature, it is found that a lot of research work has already been done on various aspects of the laser beam machining process. In the laser micro-channeling process, transparent material machining is one of the challenging tasks, as well as proper kerf width, depth of cut, and minimization of heat affected zone (HAZ), are difficult to maintain. Few past researchers have used different assist media aiming to enhance the machining characteristics. Some of them also used a combination of two different kinds of assist media to get improved results whenever a single environmental change around the machining zone gives a better machining response. From the referred literature, it is understood that considerable attention needs to be given through further in-depth study to find out proper technological knowledge of laser beam machining of the transparent polymer at different assisted media utilizing different kinds of laser power sources.

The present research works an endeavor is made to investigate the Nd: YAG laser and fiber laser micro-machining quality characteristics during machining on engineering transparent thick plastic material i.e., polymethyl methacrylate (PMMA). Within the limitation of resources and keeping in view of the above-mentioned aims of study for successful utilization of laser beam machining process for micro-machining on PMMA, the objectives of the present research work have been formulated as follows:

1. To study the chemical composition of the transparent PMMA, selected as the workpiece material and black sellotape as absorbent material using x-ray diffraction (XRD) test.
2. To understand the various subsystems of Nd: YAG & fiber laser micro-machining system so as to carry out laser beam micro-machining operation on PMMA.
3. To check the feasibility and study of the new processing technique of thick transparent polymethyl methacrylate (PMMA) which in turn helps to explore the possibility of machining on this kind of polymer using low power laser.

4. To set the design space from the observations of trial experiments, to carry out the final experiments based on central composite design (CCD) technique of response surface methodology (RSM).
5. To analyze the influence of process parameters on the quality characteristics of machined micro-channels on PMMA and also to carry out optimization analysis to determine the optimal parametric combination for achieving the desired value of responses at different assisted media.
6. To investigate and compare the quality characteristics of micro-channels when machined in dry medium (air) and wet medium (underwater).

The present research work includes a detailed study on CNC-based pulsed Nd:YAG laser and fiber laser micro-machining of engineering material of transparent and thick PMMA to achieve quality micro-machining characteristics in different assisted mediums. Moreover, the present research work may open up new directions of research in the area of micro-machining of transparent material like PMMA and explore the possibilities of future scope of research on other transparent material and their surface characteristics features as well as improve the transmission technique.

Chapter 3

DETAILS OF MACHINING SETUP AND FIXTURE OF WORKPIECE MOUNTING UNIT

DETAILS OF MACHINING SETUP AND FIXTURE OF WORKPIECE MOUNTING UNIT

The Nd: YAG laser and the Fiber laser are the two types of solid-state lasers used in the present study. Both are employed for commercial purposes as well as research in various production units for micro-machining applications. The fiber laser is newer than the Nd:YAG laser. The cooling unit system is present in the Nd: YAG laser, however, it is not required in the case of the fiber laser. The Nd: YAG laser system in this study has a beam diameter of 100 μm , whereas the fiber laser has a beam diameter of 21 μm .

3.1 Nd: YAG Laser Micromachining System

The experimental investigations are carried out using a CNC pulsed Nd: YAG laser machining set-up manufactured by 'M/s Sahajanand Laser Technology', India (Model no.: SLT-SP-2000). Figure 3.1 depicts a perspective view of the CNC pulsed Nd: YAG Laser machining system. Table 3.1 presents the technical specifications of the laser machining setup in detail.

Table 3.1 Details of Nd:YAG laser machining set-up [113]

Details	Description
Type of Laser	Nd:YAG Laser
Wave Length	1064 nm
Average power	75 watts
Operation Mode	Q-Switched (Pulsed)
Q-switch Used	Acousto Optic Q-Switch
Laser Beam Mode	Fundamental Mode (TEM_{00})
Reflectivity of Mirror	Rear Mirror (100%), Front Mirror (80%)
Diameter of Beam $1/e^2$	1mm
Spot Diameter of Laser Beam	100 μm
Pulse Width	120 ns to 150 ns

One fixture for CNC Pulsed Nd:YAG laser machining set-up has been used for holding the workpiece samples. The details of the LBM experimental setup for experimentation have been described in subsequent discussions.

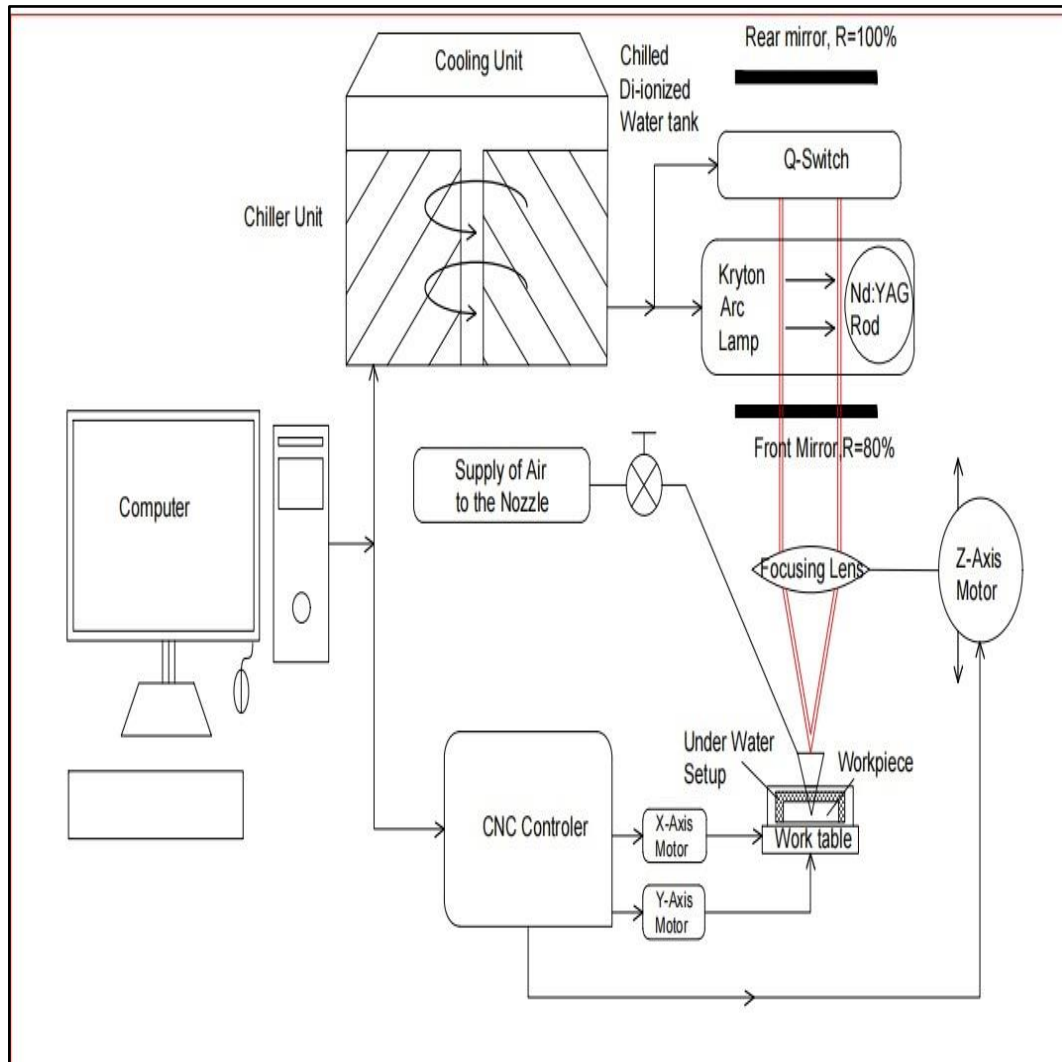


Figure 3.1 Schematic diagram of CNC Nd:YAG Laser Beam Machining System

3.1.1 Details of CNC Nd: YAG Laser Beam Micro-machining System

Figure 3.2 shows the photographic view of the CNC Nd:YAG laser machining system.

The Nd:YAG laser machining system consists of the following major sub-systems:

- (i) Laser Generation Unit;
- (ii) Beam Delivery and Focusing Unit
- (iii) CCTV and CCD Camera
- (iv) Cooling Unit and
- (v) Work Holding Table and CNC Controller for X-Y-Z Axes Movement.



Figure 3.2 Photographic view of the CNC Nd:YAG laser machining system

3.1.1.1 Laser Generation Unit

Yttrium Aluminum Garnet (YAG) crystals serve as hosts for Neodymium (Nd) atoms (lasing media) in Yttrium Aluminium Garnet (YAG) lasers. The YAG crystal is typically in the shape of a rod, with a diameter roughly equal to that of a pencil. This host contains atoms of the rare earth metal Neodymium. The amount of Nd present in YAG crystal is around 1 percent by weight of the crystal. This is due to the fact that it is employed as a lasing medium for high power laser operations, which results in it exhibiting favourable optical and mechanical qualities as well as favourable thermal properties. The pump source is a krypton arc lamp that is positioned parallel to the Nd: YAG crystal. To achieve optimal efficiency, both the Nd: YAG rod and the krypton arc lamp are contained in a gold-plated circular chamber. The elliptical-shaped cavity is utilized because the ellipse has the unique quality of having two foci, and the light released from one focus is completely concentrated on the second focus, which is why it is used. Therefore, in the cavity, one focus is used to keep the krypton arc lamp,

while another focus is for the Nd: YAG rod. The high reflectivity of the gold-plated cavity at the wavelength of the pump light makes it an excellent choice for this application. The optical feedback is provided via a rear mirror that is with 100 % reflectivity and a front mirror that is partially transmitting. The main laser generation unit in the laser machining system consists of the following units as described herein:

(i) Power Supply Unit for Krypton Arc Lamp:

This is the main power supply unit that is in charge of controlling the laser's output power. It primarily serves to ignite the Krypton arc lamp and regulate the intensity of the light provided by it. The Nd atoms in the Nd: YAG rod is pumped by the lamp's intensity of light, which is controlled by the lamp's intensity of light. To turn on the lamp, which has a very high impedance, a high-voltage pulse must first be applied to it before it can be turned on. It is possible to adjust the intensity of the light output by the lamp once the discharge in the lamp has been formed. This can be accomplished by varying the current flowing through the bulb. Due to the fact that many applications do not require the laser to be in operation all of the time, the power supply is equipped with a special feature called standby mode, which maintains the discharge in the lamp alive while not in use. This power supply unit is equipped with an interlocking arrangement to control the ignition of the lamp with respect to the operation of the cooling arrangement.

(ii) Resonators for Amplification:

Light can only be amplified with the help of a feedback system, which is provided by two mirrors in this case. The two mirrors are designed in such a way that one, referred to as the back mirror or rear mirror, has ~100 % reflectivity, and the other, referred to as the front mirror, has high reflectivity depending on the gain of the lasing medium through which useful laser output is intended to be delivered. When using an Nd: YAG laser, the back mirror has a reflectivity of 100 %, while the front mirror has a reflection of about 80 %.

(iii) Q-Switch and R.F. Driver Unit:

The Q-switched mode of operation is used by the present laser production unit in order to provide a pulsed laser output with high peak power. Q-switching is achieved

by modulating the laser beam energy in the resonators at the frequency of the pulse repetition cycle. This is accomplished by the use of an acousto-optic Q-switch. In order for this Q-switch to function, it must be powered by a particular power supply. An acousto-optic Q-switch makes use of a radio frequency source operating at 27.2 MHz that is modulated with a frequency spanning from 0.1 kHz to 19.9 kHz to achieve its function of switching. This radio frequency is generated by means of an RF generator. This type of Q-switch is made of a transparent material, commonly quartz, with a piezoelectric-electric acoustic transducer attached to one side of the switch. RF signals given to the transducer cause an acoustic wave to be projected through the quartz, which periodically modifies or modulates the reflective index of the quartz, which is determined by the crystal and the velocity of the wave propagating through it. Since quartz's index of refraction changes periodically, some light going through the Q-switch is diffracted to a small angle and misses the rear mirror, resulting in the absence of optical feedback and the termination of stimulated emission and amplification. For the time period in which RF is connected to the Q-switch, stimulated emission is suspended, but the population of the upper laser level continues to grow as more atoms absorb lamp energy. For this reason, atoms already present at the upper level will not immediately decay to lower levels, despite the fact that their lifetimes are longer. This results in a significant quantity of energy being stored at the top level even when the laser is not active. An intense burst of laser light with many kilowatts of peak power will be generated after the RF signal has been withdrawn and the optical feedback has been restored. Using a CW (continuous wave) low power laser, the Q-switch is a good approach for producing a very small pulse width and an extremely high peak power pulse of light from the laser. A radio-frequency power source is required for the operation of the transducer in the acousto-optic Q-switch. The cooling of the quartz cell is required because of the high frequency at which it is switched. As a result, the Q-switch is also kept cool with water. Figure 3.3 depicts the photographic view of RF-Q Switch driver unit front panel.



Figure 3.3 Photographic view of RF-Q Switch driver unit front panel

(iv) Intra Cavity Safety Shutter:

Figure 3.4 shows the photographic view of intra cavity safety shutter. One of the most significant components in the laser cavity is the safety shutter, which is operated by electricity. In addition, unlike the Q-switch, it prevents refraction from occurring between the optical feedback mirrors. For a prolonged period of time, the safety shutter is a mechanical mechanism that prevents the lasing operation from taking place. Because of the way the shutters are constructed, in the case of an electrical failure, gravity will cause the shutter to descend into the closed or non-lasing position, preventing further damage. There is also a shutter, which may be controlled remotely via the computer system. It is necessary to provide a beam attenuator (Safety Shutter) that will allow the user to discontinue lasing without having to turn off the main power switch. The safety shutter is housed within the laser head assembly and is controlled by a toggle switch on the front panel. Laser lasing is terminated by the shutter, which prevents the laser beam path from being blocked and the emission of laser radiation from the head assembly enclosure from occurring.



Figure 3.4 Photographic view of intra cavity safety shutter

(v) Intra Cavity Aperture:

When the laser is in fundamental mode (TEM_{00}), two pin holes called apertures are utilized in the resonator on the optical axis to limit the amplification to the off-axis of the resonator. The name "intra-cavity aperture" comes from the fact that these apertures are employed inside the cavity.

3.1.1.2 Beam Delivery and Focusing Unit

A beam bender and a focusing lens make up this unit. The beam from the laser source's beam expander will be directed to the work surface. A beam bender does this by bending the beam at 90 degrees, after which the focusing lens focuses it. The power density and depth of focus produced by a laser beam of a given diameter can be altered by adjusting the focal length of the focusing lens. For the same beam diameter falling through a focusing lens, a lens with a shorter focal length has a higher power density but a smaller depth of focus, whereas a lens with a longer focal length has a lower power density but a larger depth of focus. The alignment of the focusing lens is critical because if the beam centre does not correspond with the lens's centre, the beam following the lens will not be straight, reducing the cutting efficiency significantly. The Photographic and schematic diagram of the beam delivery unit is shown in Figure 3.5 and Figure 3.6 respectively.

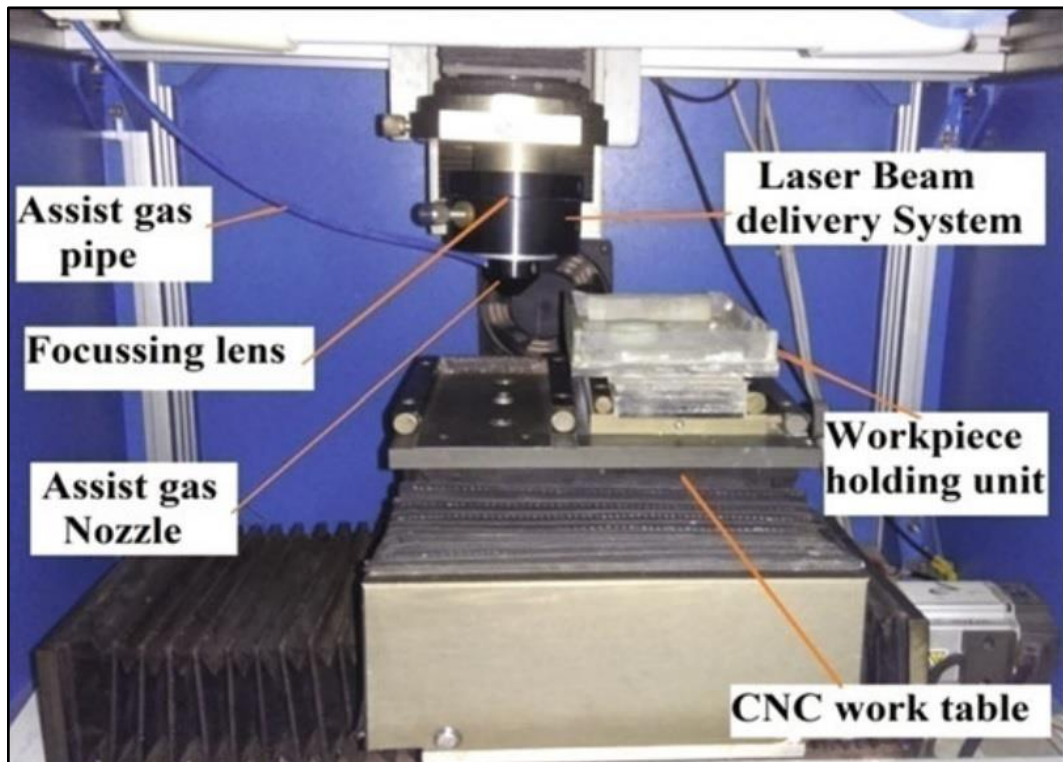


Figure 3.5 Photographic views of Beam Delivery and Focusing Unit

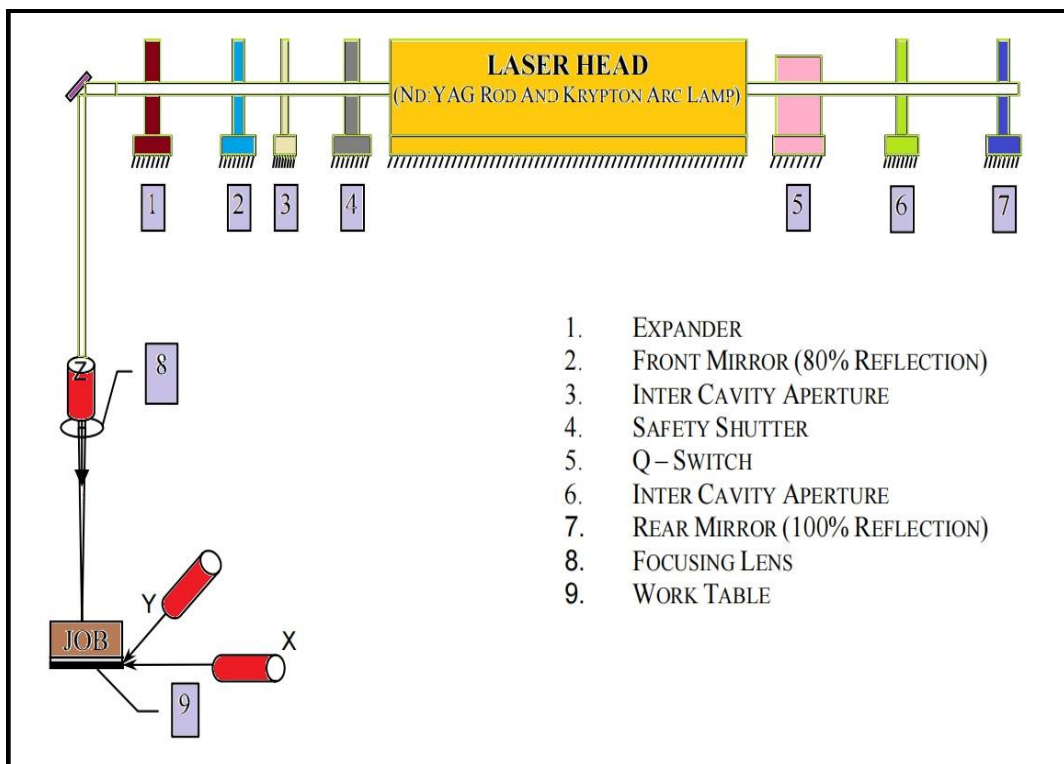


Figure 3.6 Schematic diagram of laser beam transformation

3.1.1.3 CCTV and CCD Camera

An image capture device and a monitor are used to see the workpiece and to provide the necessary observation required for aligning the workpiece before the laser beam is employed for micro-machining the workpiece. The alignment procedure consists in positioning the picture of the laser spot in the centre of the monitor, over which a cross wire is drawn, as shown in Figure 3.7. The laser point, both with and without a lens, should be aligned with the centre of the cross wire in both directions. A view of the work surface taken by a CCD camera can be displayed on a television screen by a CCTV camera. Having a clear picture or perspective of the job surface where laser machining is required helps to determine the position of the lens, which is important for accurate focusing as well as maximum utilization of laser beam energy. The three-phase power for the CCD camera is provided by a 12V power adaptor. A BNC cable connects it to the surveillance system. The power for CCTV is provided by a single phase.



Figure 3.7 Photograph of CCD camera of Nd: YAG system

3.1.1.4 Cooling Unit

When a laser is produced, a significant amount of heat is generated within the pumping cavity of the laser unit. Insufficient removal of generated heat from the

cavity may result in damage to the expensive components of the laser production unit. It is necessary to install a cooling system in order to avoid the following outcomes [114]:

- (a) Nd:YAG rod may be damaged,
- (b) Gold plating of cavity deteriorates,
- (c) Krypton arc lamp operating life reduces,
- (d) Resonator alignment may be changed etc.

The current Nd: YAG laser machining system cooling unit consists of two subsystems: a chiller for cooling water and a heat exchanger and pump for de-ionized water supply. Table 3.2 lists the specifications for the chiller unit and the schematic diagram of a cooling unit is shown in Figure 3.8.

Table 3.2 Details of chiller unit

Item	Specification
Electrical requirement	415V AC supply
Capacity of De-ionized water tank	5 Liters
Resistance of De-ionized water	$\geq 200 \text{ K}\Omega/\text{cm}$
Flow rate of De-ionized water	20 liters/min
operating temperature of De-ionized water	$24^\circ\text{C} \pm 1^\circ\text{C}$

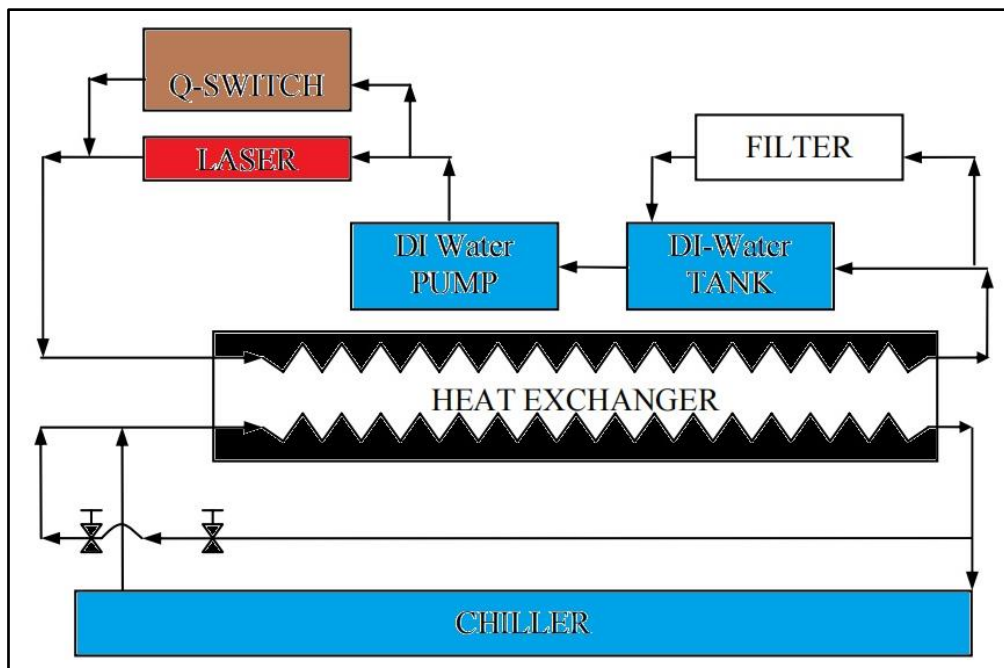


Figure 3.8 Schematic diagram of cooling unit

3.1.1.5 Work Holding Table and CNC Controller for X-Y-Z Axes Movement

For saw cutting and profile cutting operations, the work holding table can be adjusted in both X and Y directions. For proper workpiece retention during machining, many types of fixtures can be fitted to the X-Y table. The Z-axis movement of the focusing lens is also essential for focusing the laser beam on the task surface and utilizing the maximum energy of the beam. Motors are mounted to each axis and connected to a CNC controller unit called accupos to control X, Y, and Z axis movement. Table 3.3 shows the CNC table unit's hardware specifications [113]. Figure 3.9 shows the CNC-controlled working table.

Table 3.3 Specification of CNC table unit

Items	Description
Axis of travel (X-Y axis)	150mm × 150mm
Focusing vertical travel	50mm
Position accuracy	0.02 mm over travel 250 mm
Repeatability	0.01 mm over travel of 250 mm
Resolution	1 μm
Table working area	150mm ×150mm
Clamping	Using fixture
Control system	CNC open loop system

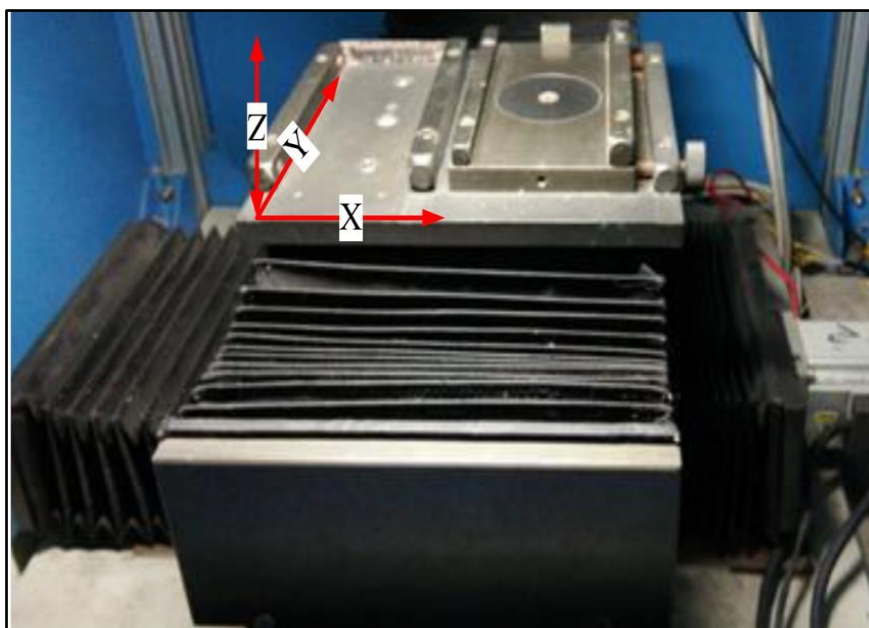


Figure 3.9 CNC controlled working table

3.1.2 Compressed Air Supply and Control Unit

For effective micro-cutting and drilling operations, assist gas must be delivered at a specific pressure. The quality of the machined surface can be improved by changing the pressure. Compressed air supply and control equipment has been designed and built with this aspect in mind. In the current laser machining technology, compressed air is used as an assist gas. The gas is mostly used to clear debris from the machining area. The moisture separator removes substantial moisture particles from compressed air when it comes out of the compressor. The pressure regulating valve is used to feed compressed air to the laser machining zone at varying pressures. The compressed air controlling mechanism is depicted schematically in Figure 3.10. For effective debris flushing from the job surface, compressed air can be delivered to the laser machining zone from two distinct directions in the compressed air supply setup.

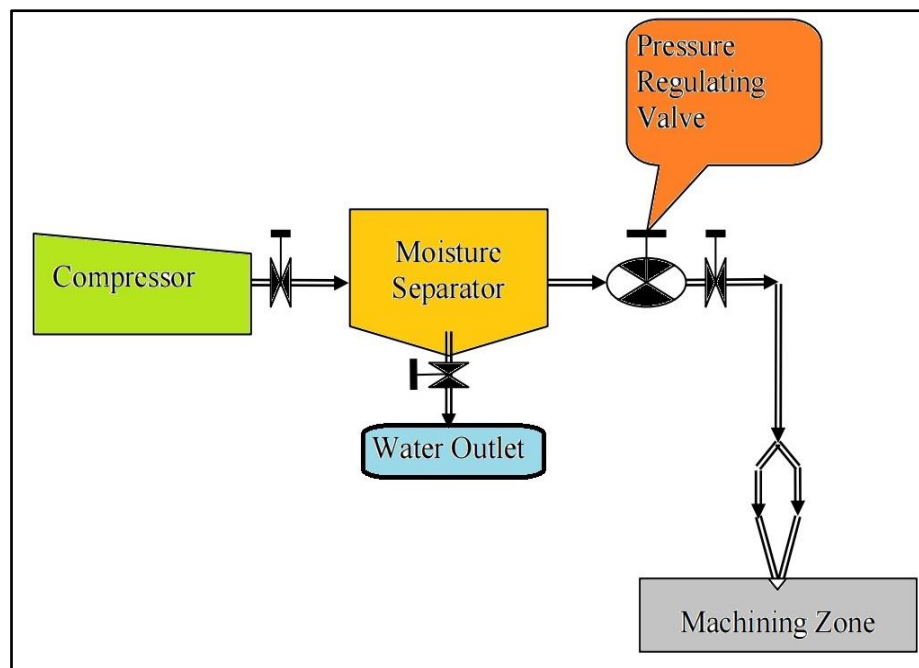


Figure 3.10 Schematic view of compressed air regulating system

3.2 Fiber Laser Micromachining System

Fiber lasers are the most versatile and rapidly expanding laser systems utilized in micromachining. Fiber lasers compete with the majority of high-power, bulk solid-state lasers, and gas lasers now on the market, primarily in the automotive and developing bio-medical domains. The manufacture of stents for biomedical applications is the most promising application of fiber lasers. Furthermore, fiber lasers

have a wide range of applications in automotive, aircraft, high-power applications and other fields.

M/S Sahajanand Laser Technology Limited's (Model: AKSHAR Fiber Pro-309) multi-diode pumped CNC-based Ytterbium (Yb^{3+}) doped 50 Watts fiber laser with a wavelength of 1064 nm and TEM_{00} mode of operation is used for a variety of laser micro-machining applications. The method for using fiber lasers is depicted in greater detail in Figure 3.11. An optical fiber laser system is comprised of three basic components: a) the laser generation unit; b) the optical fiber laser delivery system; and c) the assist air supply system. This unit also includes the following components: (i) optical fiber; (ii) silicate glass; (c) rare earth doped elements; (iv) fiber Bragg gratings; (v) laser diodes; (vi) fiber couplers; (vii) isolators; and, finally, (viii) fiber linked acousto-optic modulator (AOM). Among the subsystems in a fiber laser delivery system are the collimator, the beam bender, and the beam delivery unit, to name a few examples. Apart from that, the assist air supply unit and a CNC controller unit for the X-Z axis are other essential components of the fiber laser system. For the current system, the working table is transverse in the X-Y direction. The highest speed that may be achieved is 40 millimeters per second. The following Table 3.4 contains the technical specifications of the CNC pulsed fiber laser beam machining system. Figure 3.11 and Figure 3.12 shows the photographic view and schematic diagram of the CNC fiber laser beam machining system. The details of each system, as well as its subsystems, are examined in greater depth below.

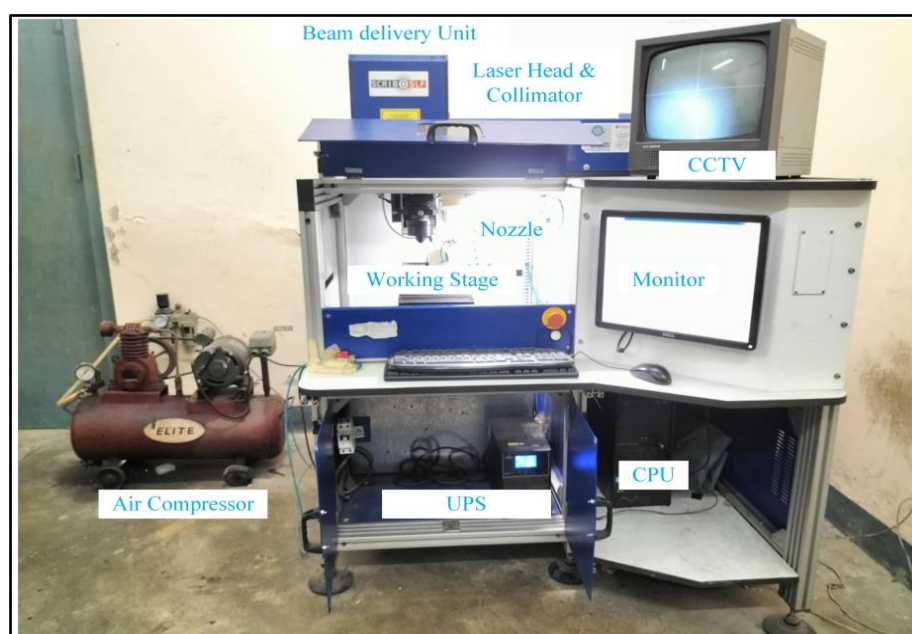


Figure 3.11 Photographic view of CNC pulsed fiber laser machining system

Table 3.4 Specification of fiber laser beam machining system

Description	
Laser	Multi diodes Pumped Fiber Laser
Spectral Characteristics	
Wavelength	1060± 10nm
Optical Characteristics	
Polarization Type	Linear/Random
Maximum Pulse Energy	>1mJ
Max. Peak Power	> 7.5 kW
Nominal Average Power	≥ 50 W
Power Tunability	10-100%
Pulse Repetition Rate	50-120 kHz
Pulse Duration	According to PRR/<120ns
Power Stability	>95%
Inbuilt Guide Laser	0.5-4.0 mW
Wall-plug Efficiency	>30%
Spot Diameter	21μm
Beam Characteristics	
Beam Quality (M^2)	<1.5
Beam Roundness	>90%
Controller & CNC system	
Axis Travel (X & Y)	≥150mm
Drive	Servo Control Drives
Vision system	CCTV Camera
Cooling	Integrated
Electrical	
Power Supply	230V/50 Hz-115V/60 Hz
Software	I mark, Gyro, Q-saw

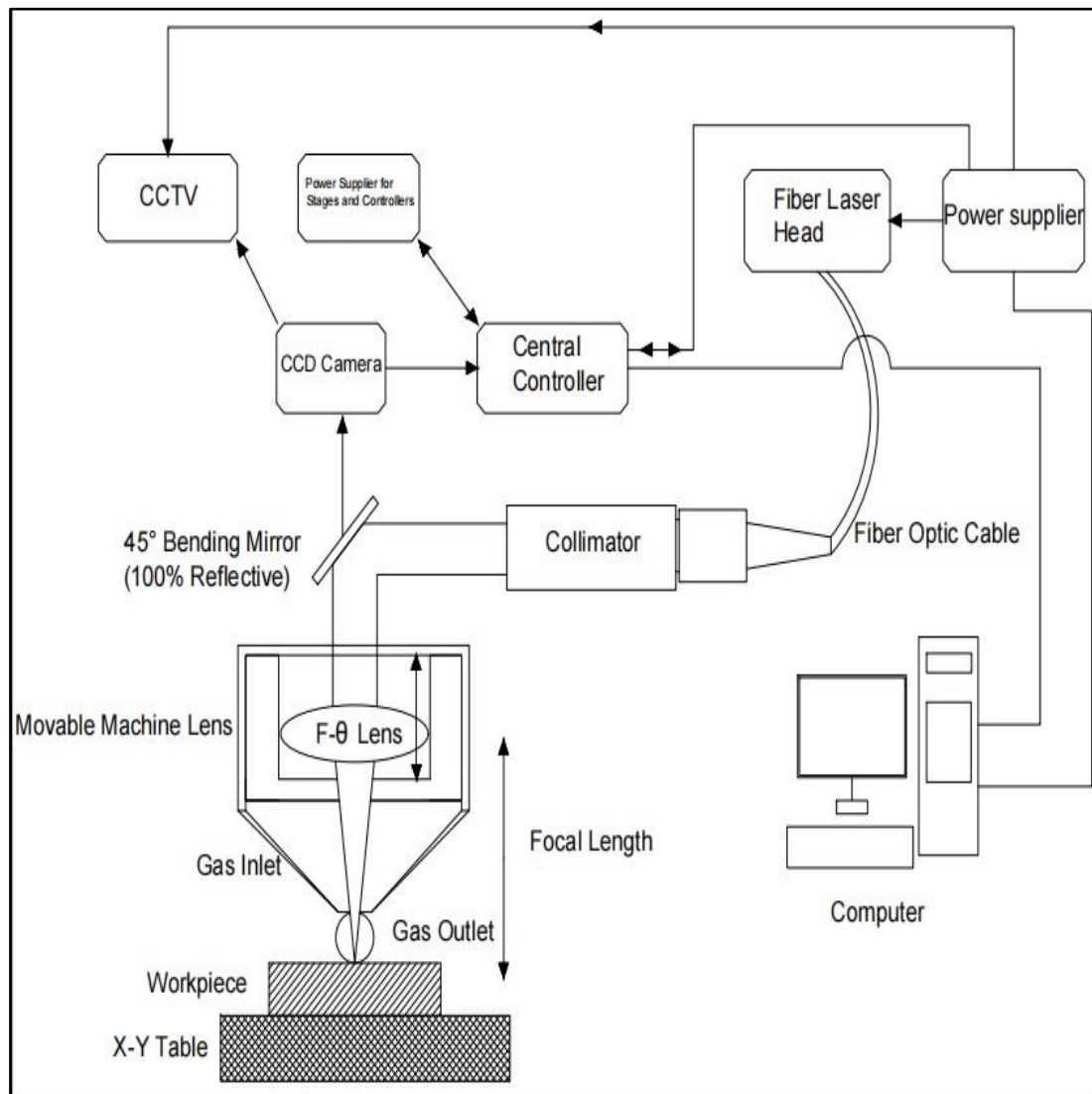


Figure 3.12 Schematic diagram of CNC fiber laser beam machining system

3.2.1 Fiber Laser Generation Unit

The optical fiber laser generation unit is made up of eight components: (i) optical fiber; (ii) silicate glass; (iii) rare earth doped elements; (iv) fiber Bragg gratings; (v) laser diodes; (vi) fiber couplers; (vii) isolators; and (viii) fiber linked acousto-optic modulator. Figure 3.13 is a photographic image of fiber laser generation equipment. A detailed description can be found below.



Figure 3.13 Photographic view of fiber laser generation unit

3.2.1.1 Optical Fiber

Optical fibers are the most important component of a fiber laser system. Figure 3.14 depicts an optical fiber made of silicate glass in its natural state. The fiber's core and cladding are both made of silicate glass, as is the rest of the fiber. The presence of doping in the fiber's core is required in order to raise the core's refractive index. Germanium is used to dope the fiber core, which is why it is added. The refractive index of silicate glass drops when fluorine and boron are used as dopants, on the other hand. Because the current fiber laser system runs at a wavelength of 1064 nm, the inherent loss within the fiber (measured in decibels per kilometer travelled) is quite substantial. The optical fiber used in this system has a length of three meters in this configuration. A layer of acrylic coating with a higher refractive index is applied to the glass surface in order to protect it from damage. Further, the coating applied to the fiber prevents the transmission of undesired light into the cladding glass.

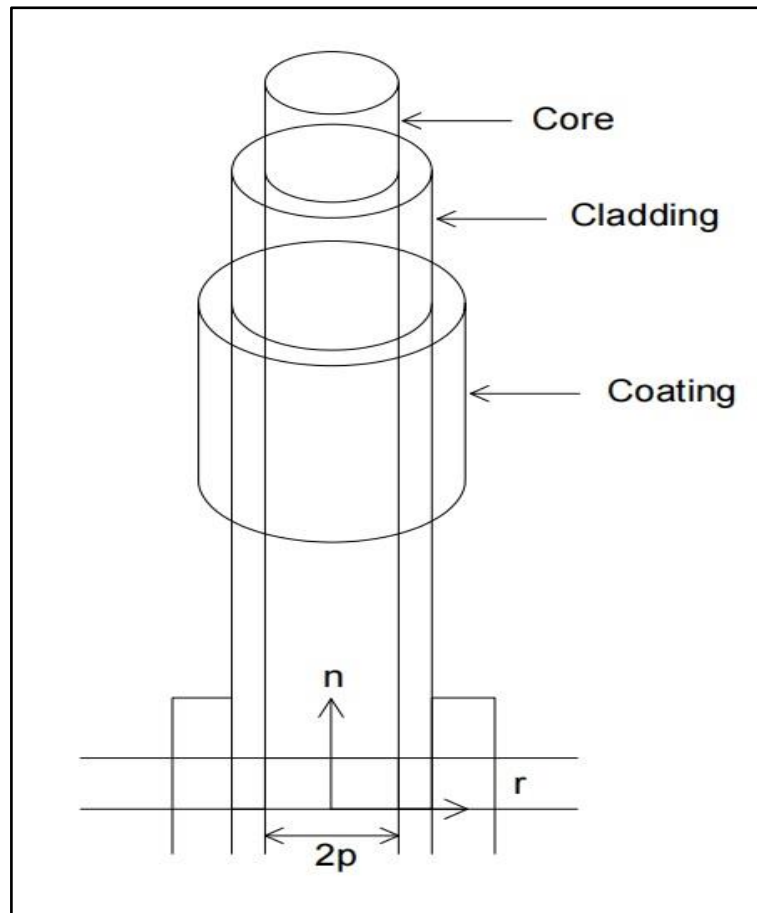


Figure 3.14 Optical fiber with refractive index distribution

3.2.1.2 Silicate Glass

A variety of low-power to high-power fiber laser applications employ silicate glass as their optical fiber, which has been most extensively utilized. Glass molecules, in contrast to crystals, are disordered but rigidly bound together. The structure of the glass is held together by a number of matrix molecules, such as $(\text{SiO}_4)^{4-}$ or $(\text{PO}_4)^{3-}$ in the case of silicate and phosphate glasses, respectively [115]. Additionally, the silicate glass has a wide range of optical transparency, which allows it to achieve the lowest possible loss of optical transmission. Silicate glass is a mechanically strong material that exhibits extraordinary resistance to bending when properly prepared. Silicate glass also exhibits a high degree of chemical resistance, which is another advantage.

3.2.1.3 Rare Earth Doped Elements

To absorb light, fiber amplifiers have laser-active rare earth ions doped in the fiber core. The light is amplified by these doped earth elements due to stimulated emission.

Ytterbium (Yb^{3+}), erbium (Er^{3+}), thulium (Tm^{3+}), and neodymium (Nd^{3+}) are examples of rare earth ions. In order to incorporate rare earth ions into the fiber core, the usual glass network must be disrupted. (a) passive optical fiber; (b) active mode area; (c) numerical aperture; (d) cut off length; (e) bend losses; (f) rare earth doping concentration; (g) wavelength-dependent effective absorption and emission cross sections; and (h) energy transfer speed are some of the critical factors leading to the characterization of rare earth doped fibers.

In the current method, ytterbium-doped rare earth ion fiber laser boosts are generated in the multimode regime of the fiber. For high-power fiber lasers, Yb^{3+} ions have recently become the dopant of choice. When compared to the regularly utilized Nd^{3+} ions, Yb^{3+} has various advantages as a laser-active ion in solids like crystals and glasses [115]. These advantages include:

- (i) A longer lifetime in the upper state.
- (ii) Absorption bands at 915 and 976 nm are broad and robust in Yb^{3+} -doped laser-active glasses.
- (iii) A little quantum flaw that causes a lower thermal load per unit of pump power.
- (iv) Up-conversion losses and absorption of the excited state are absent.
- (v) Room-temperature excited state lifetime is approximately 1 ms.

3.2.1.4 Fiber Bragg Gratings (FBGs)

Fiber Bragg gratings (FBGs) are essential for the development and commercialization of fiber lasers. The majority of fiber Bragg gratings are employed in single-mode fibers, and physical modeling of FBGs is frequently straightforward. The principle of operation of FBGs is the same as that of dielectric mirrors. Each periodic refraction of FBGs reflects a small amount of light. At room temperature, FBGs are shown to be quite stable. The wavelength and bandwidth are necessary for using FBGs in fiber lasers are in the range of 0.1–1 nm, with a centre wavelength control of ± 0.5 nm.

3.2.1.5 Laser Diodes

Laser diodes are used in fiber lasers for photon pumping. Five diodes are used for optical pumping in the current setup to provide 50W of average laser power. Single-

emitter optical pump sources are commonly connected into a 105/125 fiber, which has a 105 μm diameter core and a 125 μm diameter silica glass cladding. The average laser power of the laser varies depending on the number of diodes, the higher the number of diodes, the higher the average power. Multi-emitter pumps are commonly available commercially and consist of three, five, seven, or more laser diodes integrated into a single 105/125 delivery fiber, delivering 60–140 W depending on the power per emitter.

3.2.1.6 Fiber Couplers

Fiber couplers are one of the most important components of a fiber laser. Because most industry standard fibers have a core diameter of 105 μm or 200 μm , the delivery fibers are limited. Depending on the power distribution inside the fiber laser, fiber couplers join one or more input fibers with many output fibers.

3.2.1.7 Fiber Laser Isolators

During many stages of amplification with the help of a fiber amplifier, inter-stage optical isolation is necessary. Fiber-coupled isolators are low-cost components that eliminate back reflections by allowing only one path of light to pass. Commercially accessible 50 W fibers to free space isolators for output from a master oscillator power amplifier (MOPA) system are available [116]. In the case of fiber-to-fiber isolators, the current limit for commercially available high-power isolators is roughly 50 W. As a result, they're frequently used in nanosecond pulsed fiber amplifiers.

3.2.1.8 Fiber-Coupled Acousto-Optic Modulator

Pulsed fiber lasers with mill joule pulse energy and nanosecond pulse duration offer a wide range of applications in materials processing. Q-switching is commonly employed in oscillators to generate optical pulses, which are subsequently amplified in a MOPA arrangement to increase their power. An acoustic-optic modulator (AOM) is used to implement the Q-switch function, which can turn off a beam by deflecting it in a different direction. A travelling acoustic wave deflects the beam, which is controlled electrically by a radio frequency (RF) signal, usually at a few tens of MHz. AOM typically takes 5 to 100 ns to switch a beam on or off, which is roughly restricted by the acoustic wave's passage time across the beam. Electro-optic

modulators (EOMs) are commonly utilized when faster control is required. A commercially available fiber-coupled AOM Q-switch typically has a power handling capacity of 1 W and a peak power handling capacity of 30 kW. The AOM principle is shown in Figure 3.15. Figure 3.16 shows a schematic illustration of the ytterbium-doped fiber laser head.

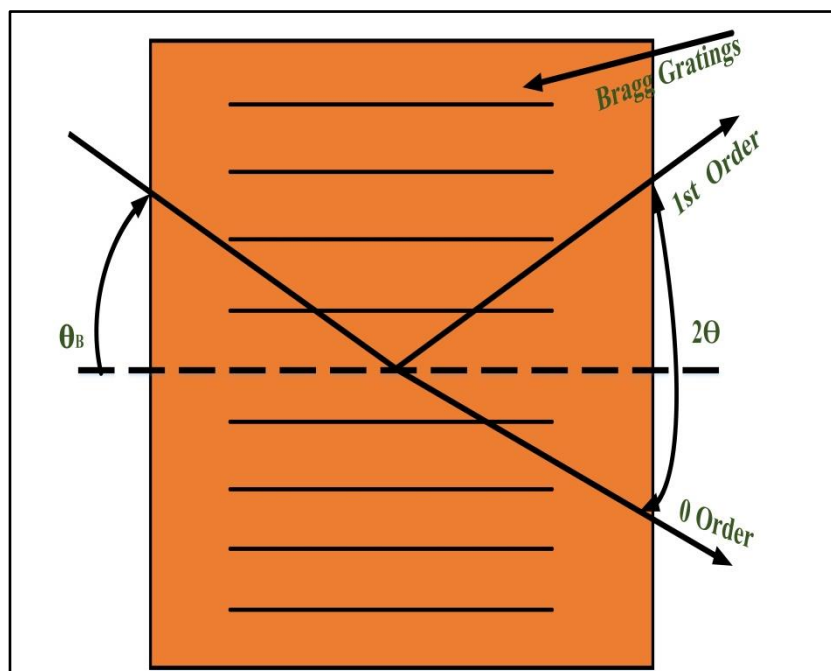


Figure 3.15 Principle of AOM

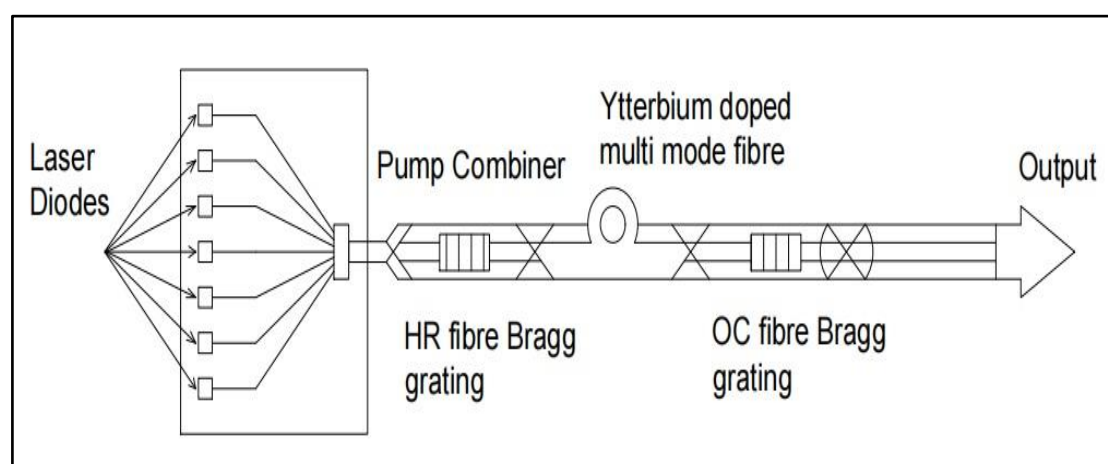


Figure 3.16 Schematic representations of ytterbium-doped fiber laser head

3.2.2 Fiber Laser Delivery System

An optical fiber laser delivery system is comprised of a collimator, an optical beam bender, an optical beam delivery device, and an optical focusing lens. The

specifications of each of the aforementioned units are addressed in greater detail in the following subsections.

3.2.2.1 Collimator

With the help of a collimator, it is possible to convert the light output from an optical fiber into a free-space collimated beam in which the fiber end is securely held at a distance between it and the lens that is nearly equal to the focal length. Fiber optic collimators are available in a variety of collimated beam sizes, which results in a variety of focal length values, i.e., larger collimated beams must be both longer and larger in diameter, as a result of the varying collimated beam sizes. When it comes to multimode fiber laser systems, the collimated beam size is determined by the launch parameters as well as how far the fiber is bent. Figure 3.17 depicts an image of the collimators taken from a different perspective. The diameter of the beam at the collimator end is 9 mm in the current configuration.

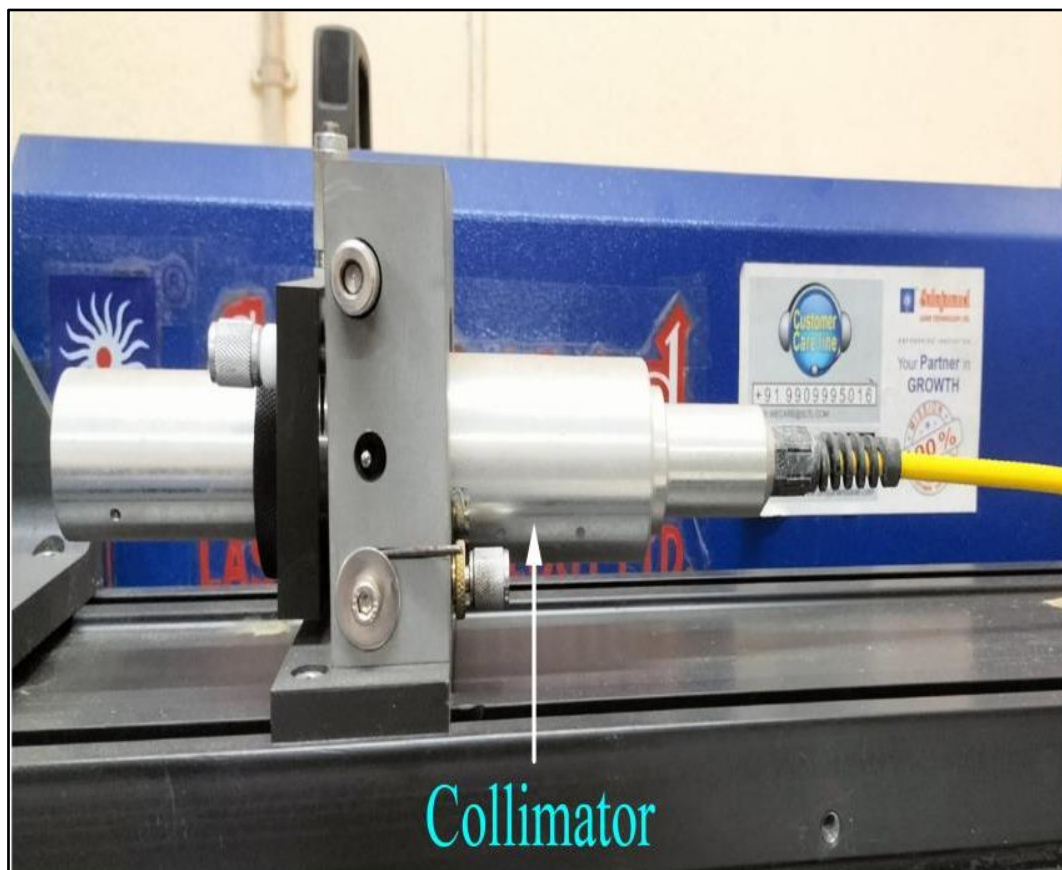


Figure 3.17 Photographic view of the collimator

3.2.2.2 Beam Bender

After the collimator, a 100% reflectivity beam bender is put at a 45° angle to the horizontal plane, allowing the laser to be perpendicular to the focus lens. A charge coupled device camera (CCD) is mounted on the top of the beam bender and is connected to a CCTV. The photographic perspective of a beam bender is illustrated in Figure 3.18.

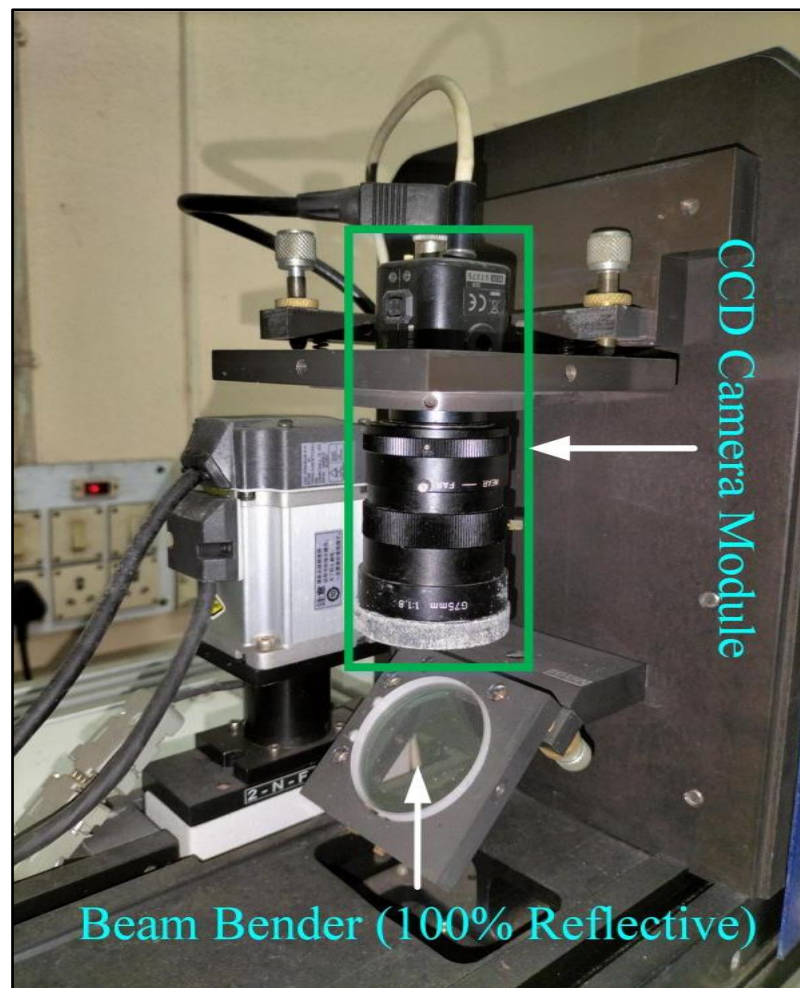


Figure 3.18 Photographic view of beam bender

3.2.2.3 Beam Delivery Unit and Focusing Lens

Before exiting through a nozzle, the laser is forced through an F- θ lens with a 71 mm diameter, which is insulated from dust and other contaminants. It is usual to find the F-mount lens in laser marking systems, as well as engraving and cutting equipment. The spot diameter of the fiber laser beam is 21 μm in diameter. The laser beam that falls on the surface of the focusing lens must be precise and well-aligned in order to

be effective. It is not linear if the centre of the lens does not correspond with the centre of the beam. This results in low energy for the laser beam and a lower micro-machining efficiency since the beam does not pass through the lens. There are two types of cameras that are used for focusing: closed-circuit television (CCTV) and charge-coupled device (CCD). The CCD camera is mounted on the top of the laser head in order to take images of the workpiece while the laser micro-machining is being performed. Furthermore, the beam should be focused on the surface in order to acquire the most efficient micro-machining operations possible. The CCTV system's primary role is to modify the position of the focused beam on the workpiece under inspection. In order to acquire a precise laser beam focusing condition, this device is attached to the CCD camera through a USB cable. The laser beam is precisely focused on the workpiece surface in order to maximize the efficiency with which the laser beam's energy is utilized. As a result, the laser beam's focal point position should be carefully adjusted. Within the experimental setup, a CNC-controlled arrangement is included in order to efficiently modify the focal point of control of the lens movement position along the Z axis as the experiment progresses. Figure 3.19 depicts the photographic view of beam delivery unit and working table.

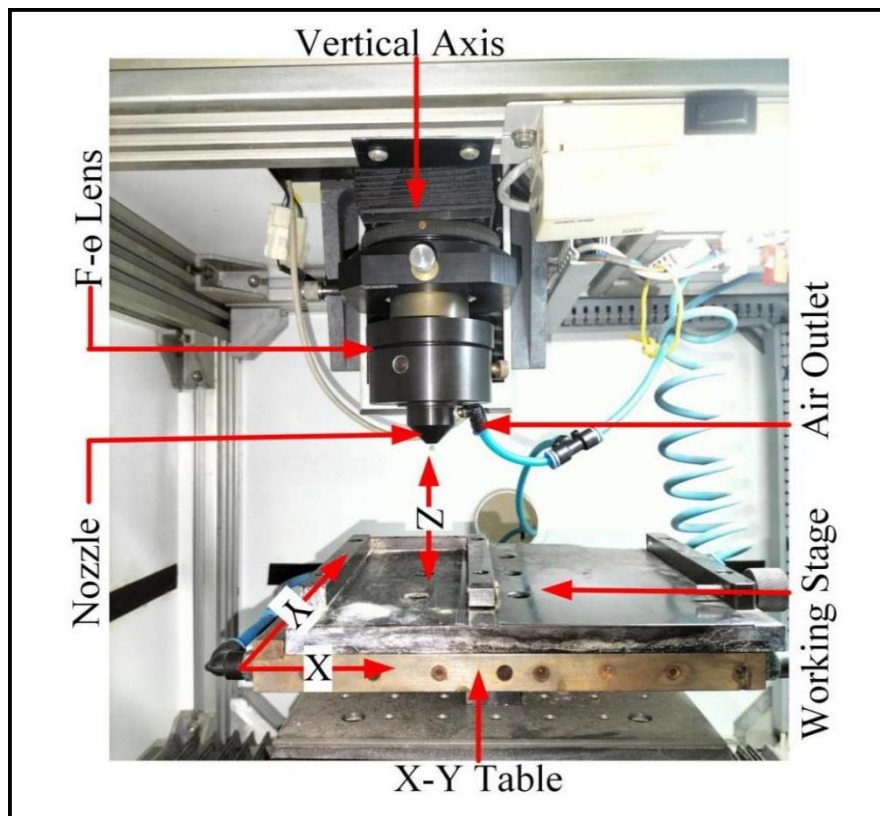


Figure 3.19 photographic views of beam delivery unit and working table

3.2.3 Assist Air Supply Unit

Depending on the micro-machining method and materials used in the micro-machining process, a co-axial nozzle coupled to the beam delivery system can feed inert gases such as nitrogen, argon, helium, and other inert gases, as well as compressed air. It is possible to partially overcome molten material resolidification in the micro-machining zone by using a jet flow of helping gas to assist in the evacuation of molten material from the ablated surface. If compressed air is needed, the supply line must first pass through a moisture separator before connecting to a pressure-regulating valve further down. As a result of this operation, a jet of dry, pressurized air is directed into the laser micro-machining zone. The laboratory setup can hold a workpiece with a thickness of up to 1 mm when compressed gas pressure is applied, thanks to a 6 kgf/cm^2 compressed gas pressure and a vacuum job fixture. A moisture separation unit is linked to the air compressor for the purpose of eliminating moisture from the gas. Figure 3.20 shows an image of an air compressor with a moisture separator.

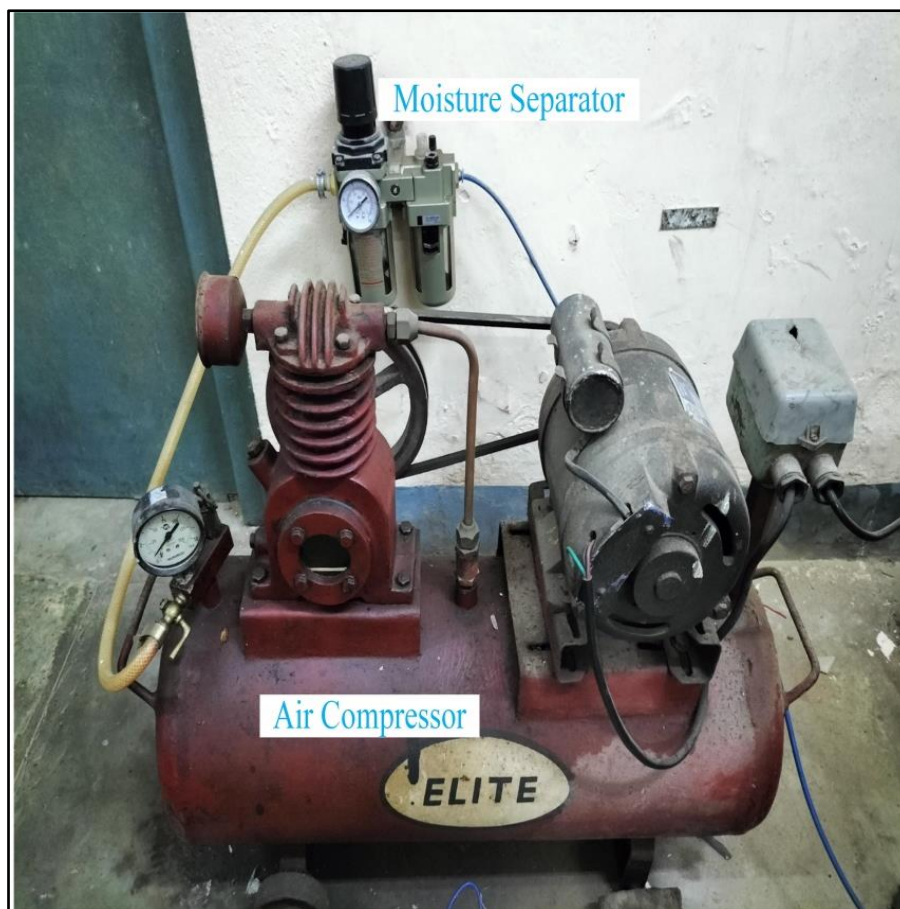


Figure 3.20 Photographic view of an air compressor with moisture separator

3.2.4 CNC Controller for X–Y–Z Movement

The movement of the worktable along the X-Y axis, as well as the movement of the laser nozzle along the Z axis, is controlled by a CNC controller unit. Each axis is driven by a servo motor, which is also connected to the servo interfacing unit. The axis motions of the X–Y worktable are controlled by this servo controller, which is coupled to the computer system (interface software-I mark plus). The computer system sends a command to the servo interfacing unit, which then receives a command to move the servo motors in the right direction. Depending on how the fiber laser system is used, the axis can be controlled by a CNC-based motor system or a galvanometer type motor system. A galvanometer system is perfect for marking and scribing applications. A CNC-based system, in contrast to the technique described above, is well-known for cutting, drilling, and various micro-machining applications.

The software that interfaces with the CNC laser system has features that allow you to coordinate the operation of the laser beam supply, workstation motion control, and more. I-mark, gyro, and Q-Saw software are used in the current system for various micro-machining operations, such as micro-cutting, micro-drilling, marking, surface texturing, and so on. The I-mark software is largely used for CNC programming, whilst the other two programmes mentioned above are utilized to set the cutting depth and angle.

3.3 Fixture of Workpiece Mounting Unit

In this investigation, micromachining was performed on a PMMA workpiece using an Nd: YAG laser and a fiber laser machining system. A device was used to accommodate various sizes of workpieces in both submerged and air-aided media. The schematic view and photographic picture of the fixture for the current research project are shown in Figures 3.21 and Figure 3.22. The fixture is made of acrylic polymer and was chosen to fit the space limits of the arrangement. Di-ionized water at room temperature (24°C-25°C) was used as the water medium due to its ease of availability and nonreactive nature to workpiece material even at higher temperatures. In each experiment, fresh water was used. The workpiece is held in position by the fixture's jammer, which prevents it from movement owing to water flow or pressure. To measure the water level, a scale has been attached to the fixture.

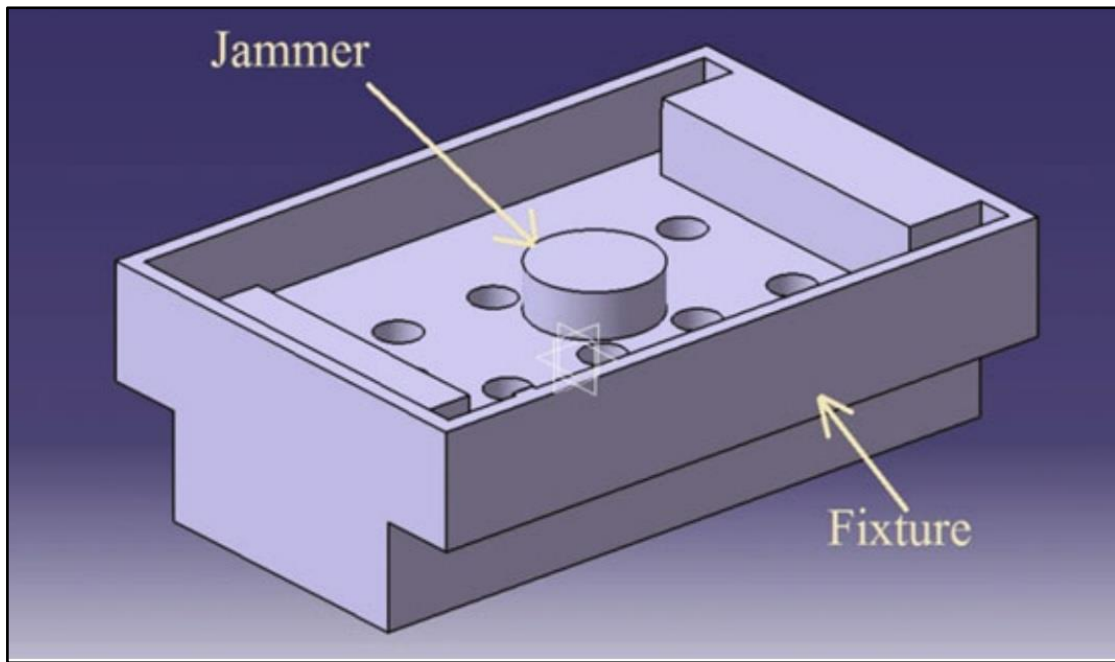


Figure 3.21 Schematic diagram of workpiece holding unit for laser transmission micromachining



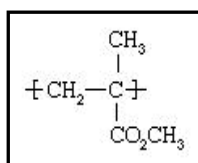
Figure 3.22 Photographic view of workpiece holding unit for laser transmission micromachining

Chapter 4

MATERIAL SPECIFICATIONS AND EXPERIMENTAL METHODOLOGY

4.1 Material Specification

Rowland Hill and John Crawford of Imperial Chemical Industries (ICI) in England discovered polymethyl methacrylate (PMMA) in the early 1930s. The product was given the trademark Perspex by ICI. Around the same time, chemist and industrialist Otto Rohm of Rohm and Haas AG in Germany experimented with polymerizing methyl methacrylate between two layers of glass to create safety glass. The polymer split from the glass in the form of a clear plastic sheet, which Rohm dubbed Plexiglas. In the late 1930s, Perspex and Plexiglas were both commercialized. E.I. du Pont de Nemours & Company (now DuPont Company) later introduced its own Lucite-branded product in the United States. During World War II, PMMA was used to make aeroplane windows and bubble canopies for gun turrets, which was the first major application of the new material. After the war, civilian applications began to flood in. PMMA (polymethyl methacrylate) is a synthetic resin made by polymerizing methyl methacrylate. PMMA is a translucent, hard plastic that is frequently used as a glass alternative in goods including shatterproof windows, skylights, illuminated signs, and aircraft canopies. Plexiglas, Lucite, and Perspex are some of the brand names for it. PMMA is a methacrylic acid ester ($\text{CH}_2=\text{C}[\text{CH}_3]\text{CO}_2\text{H}$) that belongs to the major acrylic resin family. Propylene, a chemical derived from the lighter portions of crude oil, is used mostly in modern manufacture. Cumene, or isopropylbenzene, is formed by combining propylene and benzene; cumene hydroperoxide is oxidised to cumene hydroperoxide, which is then treated with acid to generate acetone; acetone is then transformed to methyl methacrylate ($\text{CH}_2=\text{C}[\text{CH}_3]\text{CO}_2\text{CH}_3$), a flammable liquid, in a three-step process. Methyl methacrylate, in bulk liquid form or suspended as minute droplets in water, is polymerized (its molecules joined together in enormous numbers) to form solid PMMA under the effect of free radical initiators. The polymer repeating unit's structure is as follows:



The polymer chains are prevented from packing tightly and revolving freely around the carbon-carbon bonds in a crystalline manner by the presence of the pendant methyl (CH₃) groups. As a result, PMMA is strong and stiff plastic. It also has virtually perfect visible light transmission, and it is an excellent glass replacement since it retains these qualities even after years of exposure to ultraviolet radiation and weather [117]. The tensile and flexural characteristics of PMMA are outstanding. The impact resistance of this material is ten times that of glass. It has the highest surface hardness of any standard thermoplastic and is exceptionally scratch resistant. Its hardness and stiffness, as well as its inexpensive cost and ease of use, as well as its favourable thermal and chemical resistance, moulding temperature, and surface derivation features, make it the material of choice for a variety of applications.

PMMA is employed as the workpiece material in this study effort, and it has a thickness of 11.328 mm, which is ideal for micro-channel manufacturing. The parameters of the workpiece material PMMA are listed in Table 4.1 (Manufacturer details and properties listed from study of PMMA properties, Milena Koleva, Technical university of Gabrovo), and Figure 4.1 depicts a SEM image of PMMA taken under a scanning electron microscope before machining.

Table 4.1 Property table of PMMA

Molecular formula	(C ₅ H ₈ O ₂) _n
Density	1.15-1.19 gm/cm ³
Refractive Index	1.492
Max water absorption ratio	0.3-0.4% by weight
Melting point	160 °C (320 °F)
Mass density	1170-1200 MPa
Young's modulus	1800-3100 MPa
Poisson's ratio	0.35-0.40
Stiffness constants	2944 MPa (modulus of elasticity)
Tensile or fracture strength	48-76 MPa
Specific heat	1.46-1.47 J/g°C
Thermal conductivity	0.167-0.250 W/m-K
Electrical conductivity	1E-19 (inverse of resistivity)

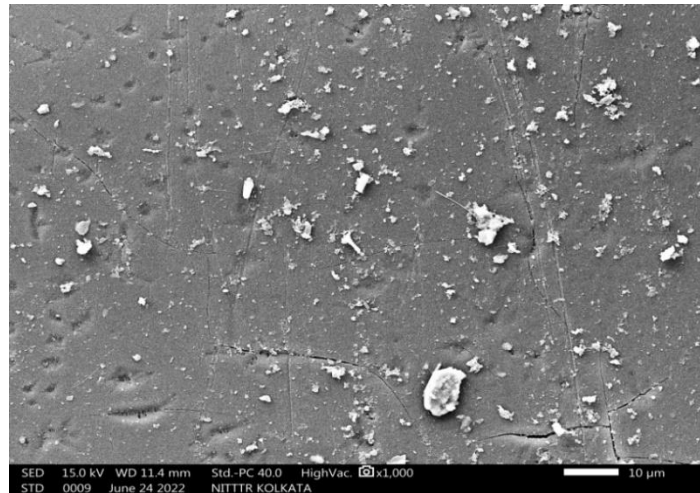


Figure 4.1 SEM view of PMMA (before machining)

4.1.1 XRD Test of PMMA (Before Machining and After Machining) and Sellotape

A crystal's atomic planes cause an incident beam of X-rays to interfere with each other as it leaves the crystal. X-ray diffraction is the name for this phenomenon. According to the current research work, the PMMA (workpiece) substrate and sellotape material are checked for conformity to their composition using an X-Ray Diffraction test. This is very important for estimating the chemical changes taking place in micro-channels in the workpiece during underwater laser beam transmission micromachining, which is very difficult to do without the use of an X-ray diffraction test. Figure 4.2 shows the image of the X-ray diffractometer machine.



Figure 4.2 X-RAY Diffractometer [RIGAKU, ULTIMA III, 40KV, 30mA (1.2kw)]
(Metallurgical and Material Engineering Department, JU)

All of the samples are taken as dust in order to determine the right composition of the various materials being tested. Three graphs for each of the three samples as a result of the XRD analysis. With the help of the Origin Pro 9 software are shown as follows:

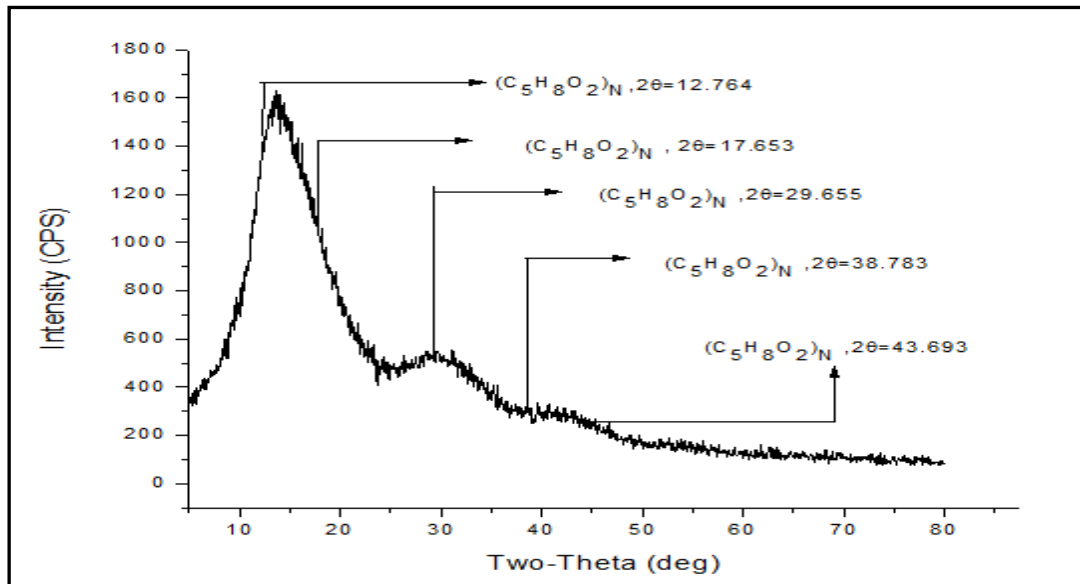


Figure 4.3 Intensity vs. Two-Theta (PMMA test before machining)

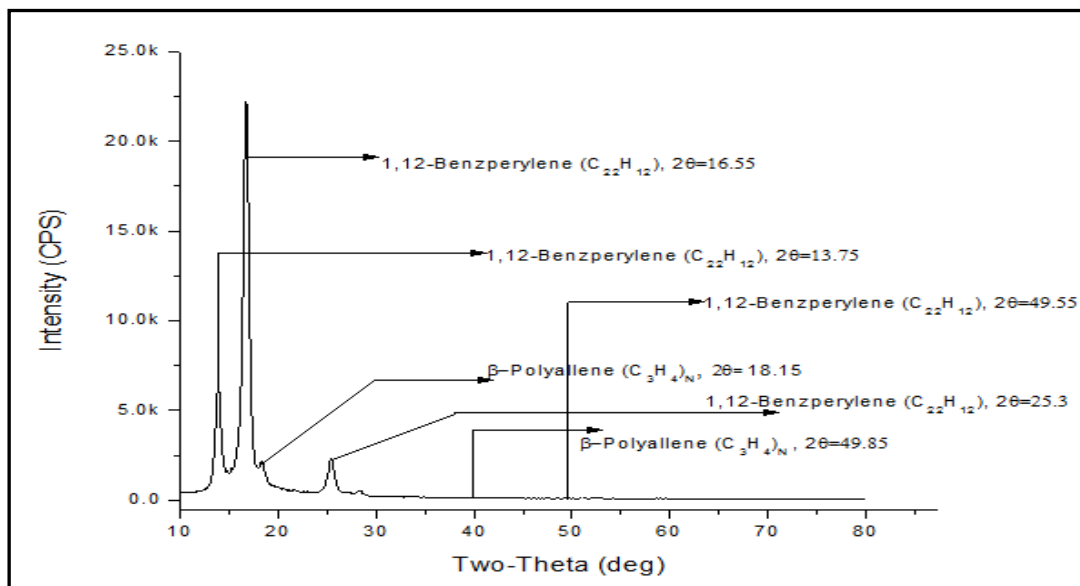


Figure 4.4 Intensity vs. Two-Theta (Sellotape material test)

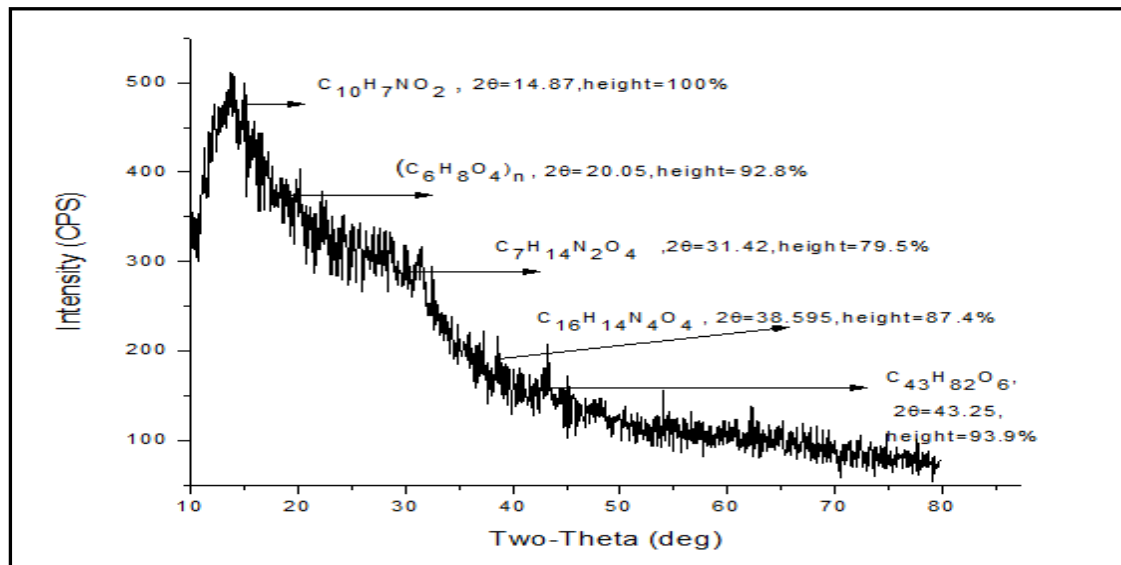


Figure 4.5 Intensity vs. Two-Theta (Micro-channel material test after machining)

Figure 4.3 clearly shows that the workpiece is made of polymethyl methacrylate, which is a strong indication of its composition (i.e., PMMA). In this case, the composition of all of the peaks is the same ($C_5H_8O_2$), which corresponds to the chemical formula of PMMA.

Figure 4.4 depicts the chemical composition of the black sellotape (coating substance) that was utilized during the experiment (as shown in the previous section). The XRD analysis indicated essentially two types of composition, namely 1, 12-Benzperylene ($C_{22}H_{12}$) and β -Pollyallene (C_3H_4)_n. It was also discovered that the sellotape material included the highest concentration of 1, 12-Benzperylene ($C_{22}H_{12}$). In the channeling operation performed on the workpiece material (PMMA) by underwater laser beam micro-machining, significant modifications were discovered in the workpiece material. By performing an XRD test on the material following the machining procedure, it was possible to determine these modifications, as well as the chemical composition of the material. Figure 4.5 shows that the material is mostly formed of five different types of chemicals, namely, $C_{10}H_7NO_2$, $(C_6H_8O_4)_n$, $C_7H_{14}N_2O_4$, $C_{16}H_{14}N_4O_4$, and $C_{43}H_{82}O_6$. The chemical $C_{10}H_7NO_2$ was determined to contain the greatest quantity of nitrogen. The test not only confirmed the chemical composition of the sellotape, which had been previously used for coating purposes, but it also unveiled the workpiece's high level of purity. The machining process was performed on a coated PMMA sample using random parametric settings (PF = 40 kHz, LC = 28 amps, CS = 1.00 mm/sec, and PW = 94%), under submerged conditions. This allowed

for a clear display of the depth of cut, kerf width, and HAZ width impressions. Furthermore, the sample was easily extracted from the micro-channel for XRD testing.

4.2 Experimental Methodology

4.2.1 Response Surface Methodology

Box and Draper (1987) developed RSM to model experimental responses, which have been used for numerical experiment modeling. RSM stands for response surface methodology, and it is a set of statistical and mathematical tools for designing, enhancing, and optimizing processes. RSM is a useful technique for constructing empirical mathematical models between input parameters and responses, as well as for analyzing the model. RSM's applications can be broadened to include new product design, development, and formulation, as well as improving existing product designs. It is used to create a functional relationship between a response of interest (y) and a set of associated control (or input) variables ($x_i, i = 1, 2, 3, \dots, n$).

The statistical technique is mostly used in research that contains input factors that may have an impact on some performance measure or quality attribute of the product or process under investigation. The reaction is a performance metric or quality feature. It is usually measured on a continuous scale, though it can also include attribute responses, ranks, and sensory responses. In most real-world RSM applications, the experimental research includes more than one response. For the purposes of a test or an experiment, the input variables are sometimes referred to as independent variables, and they are within the control of the engineer or scientist.

The experimental model can be expressed as polynomial function of appropriate form and order, selection specific to the concerned experimental design:

$$y = f(x_1, x_2, x_3, x_4) + e \dots \quad (\text{Eq}^n.4.1)$$

The independent variables (factors) are $x_1, x_2, x_3,$ and $x_4,$ on which the response y is dependent. The dependent variable y is a function of the experimental error term, represented as 'e,' and the independent variables $x_1, x_2, x_3,$ and $x_4.$ Any measurement error on the answer, as well as other types of changes not counted in the function $f,$ are represented by the error term 'e.' It is a statistical error that is expected to have a

normal distribution with a mean of zero and variance of s^2 . The true response function f is unknown in the majority of RSM issues. The researcher usually starts with a low-order polynomial across a small area of investigation in order to develop a proper approximation for f . The approximation function is a first-order model if the response can be characterized by a linear function of independent variables. The following is an example of a first-order model with two independent variables:

$$y = \beta_0 + \beta_1 x_1 + \beta_2 x_2 + \epsilon \dots \quad (\text{Eq}^n . 4.2)$$

If there is a curvature in the response surface, then a higher degree polynomial should be used. The approximating function with 2 variables is called a second-order model which can be expressed as:

$$y = \beta_0 + \beta_1 X_1 + \beta_2 X_2 + \beta_{11} X_{11}^2 + \beta_{22} X_{22}^2 + \beta_{12} X_{12} + \epsilon .. \quad (\text{Eq}^n . 4.3)$$

In general, all RSM use one of these models or a combination of the two. The levels of each element are independent of the levels of the other factors in each model. The right experimental design must be employed to collect data in order to acquire the most efficient outcome in the approximation of polynomials. The Least Square Method is used to estimate the parameters in the polynomials once the data has been collected. The fitted surface is used to perform the response surface analysis. The generalized first degree model of RSM is as follows:

$$y = \beta_0 + \sum_{i=1}^k \beta_i X_i + \epsilon \dots \quad (\text{Eq}^n . 4.4)$$

Generalized second degree model for RSM:

$$y = \beta_0 + \sum_{i=1}^k \beta_i X_i + \sum \sum_{i < j} \beta_{ij} X_i X_j + \sum_{i=1}^k \beta_{ij} X_i^2 + \epsilon \dots \quad (\text{Eq}^n . 4.5)$$

Where, x_1, x_2, \dots, X_i are controllable input variables, β is a vector of k unknown constant coefficients known as parameters, and ϵ is a random experimental error with a zero mean. For the reasons listed below, the second-order model is extensively employed in response surface methodology:

- a) The second-order model is quite versatile. It can be used to do a wide range of tasks.
- b) In the second-order model, estimating the parameters (β 's) is simple. This can be accomplished using the least squares method.

- c) There is a lot of evidence that second-order models are effective at solving real-world response surface problems.

Response surface designs are many sorts of response surface fitting designs. As a result, the goal of researching RSM can be achieved by:

- i) Recognizing the response surface's topography (local maximum, local minimum, ridge lines).
- ii) Identifying the region in which the best response occurs. The goal is to proceed quickly and efficiently along a path in order to reach a maximum or lowest reaction and maximize the answer.

One of the main goals of RSM is to discover the optimum values of the control variables that result in the maximum (or least) response over a specific area of interest (R).

Because such a model is to be used to calculate the value of the optimum, it must be a 'good' fitting model that provides an adequate representation of the mean response. The nature of the fitted model determines the optimization approaches utilized in RSM. The method of steepest climb (or descent) is a valid methodology for systematically working toward the best response for first-degree models. The second-degree model predicts parameter change as well as the best conditions for experimental study.

Many types of industrial challenges can be solved using response surface approach.

In general, these issues can be divided into three categories:

- a) Mapping a Response Surface between system responses and input variables.
- b) Optimization of the Response.
- c) Selection of Operating Conditions to Achieve Specifications and results of desired and optimum quality and design.

In this context, RSM is a significant branch of experimental design, is an important tool for establishing new processes, enhancing their efficiency, and improving the design and/or formulation of new goods. Because, the product design, process development, quality, manufacturing engineering, and operations professionals frequently work together in a team environment to use RSM, it is often an important

concurrent engineering technique. RSM can often be used directly to achieve quality improvement goals such as reduced variability and improved product and process performance.

4.2.1.1 Central Composite Design (CCD)

The Central Composite Design (CCD) aids in the efficient construction of second-degree models [118]. Factorial points, central points, and axial points make up the structure. To construct the second order model, more axial and center points are added to the first degree model. Analysis of variance was used to characterize the response surface in order to fit the data to the second-order.

4.2.1.2 Analysis of Variance (ANOVA)

The decomposition of the variance, also known as analysis of variance (ANOVA), can help to get a clearer sense of the relative effect of the various elements. The goal of ANOVA is to quantify the error variance and determine the relative size of each component on the objective function. ANOVA is also used in Robust Design to select the best quality attributes and S/N ratio for a given problem from a large number of options. ANOVA was utilized to see which machining parameters had a significant impact on the measured values. The ANOVA and the F-test were used to assess the experimental data in this study. The related meaning and equations are as follows:

$$S_m = \frac{(\sum \eta_i)^2}{q}, S_r = \sum \eta_i^2 - S_m \quad (\text{Eq}^n.4.6)$$

$$S_A = \frac{\sum \eta_{Ai}^2}{N} - S_m, S_E = S_T - \sum S_a \quad (\text{Eq}^n.4.7)$$

$$V_A = \frac{S_A}{f_A}, F_{AB} = \frac{V_A}{V_B} \quad (\text{Eq}^n.4.8)$$

Where,

S_m is the sum of square, based on the mean; S_T is the sum of square, based on total variation; S_A is the sum of square, based on parameter A; S_E is the sum of square, based on error; q is number of experiment; η_i is the mean value of each experiment ($i=1, \dots, q$); η_{Ai} is the sum of i^{th} level of parameter A ($i=1,2$ or $i=1,2,3$); N is the repeating number of each parameter A level; f_A is the freedom degree of parameter A;

V_A is the variation of parameter A; F_{AB} is the F-test value of parameter A; $F_{0.05, n_1, n_2}$ is as quoted from the “Table for Statisticians”. The contribution of the input; parameter is defined as significant if the calculated values exceed $F_{0.05, n_1, n_2}$.

4.2.1.3 Use of RSM Technique in the Present Study

Response surface methodology is a statistical and mathematical tool for designing, modifying, and optimizing processes. Employment of this technique ensures integrity of experimental design with valid mathematical acceptability and minimization of inherent and induced experimental errors. The reasons for selecting central composite design (CCD) technique of Response Surface Methodology for the present study are:

- a) It involves a moderate number of experimental runs which are not as high as in case of full factorial design and not too low as in case of Taguchi-based designs. As the channeling experiments have four input factors respectively each of five value levels this techniques provides manageable number of experimental runs.
- b) RSM based design of experiment involves repetition of parametric combination of input parameters which ensure accountability and predictability of inherent human and system errors which may creep in during performance of experiments.
- c) RSM based CCD technique also presents effect of variation of input parameters on output responses in form of graphs which helps effectively in analysis of impact and effect of these input parameters on output responses.
- d) The Analysis of Variance provided by RSM analysis indicates the significance of input factors and their effective parametric combinations in terms of the experimental data and regression analysis of data set based on inclusive algorithms.
- e) The technique allows developing a mathematical model to establish the essential relationships between output responses and input process factors based on the computed experimental data set.
- f) It also provides effective optimization for output responses for parametric combination of input factors which predicts the optimal desired output value at a mathematically predicted and approximated setting of input factors. It thereby predicts the best combination of input factors. This feature is not available in case of Taguchi-based techniques and Full Factorial designs.

- g) The RSM techniques also provide effective multi-parameter optimization for output responses in terms of same set of input parameters.
- h) The quality of machined features can be predicted, optimized and improved using the analysis and mathematical model as predicted by RSM based design.
- i) Most importantly this technique is evident to be widely used for designing experiments involving different machining processes, specially machining of polymers as inferred by references and journals.
- j) There are a wide range of techniques for designing experiments, but it is beneficial to use RSM technique, especially because of its simplicity, easier mathematical algorithm, and statistical interpretability and justified selection of experiments.

Chapter 5

PRELIMINARY DETAILS AND INVESTIGATION OF THE STUDY

5.1 Introduction

In this present study, Nd:YAG laser and fiber laser are used for experimentation. Both the lasers are of 1064 nm wavelength and 50 and 75 watt capacity respectively. Laser generation processes are different for Nd:YAG and fiber, which have been described in the previous chapters. For micro-channeling operation, different assisted mediums i.e., air and submerged in water medium in the present research. Deionised water has been used as it is chemically stable and does not chemically react during operation. Important and effective parameters of both types of lasers have been studied and chosen by the basic experimental study which helped to select the effective parameters and their ranges. According to the fundamental investigation, outcomes for both lasers are superior under submerged conditions. One of the basic experimental studies is discussed in this chapter.

5.2 Reason for Using Submerged Condition in Water

In a submerged environment, the actual machining operation has been carried out. In underwater processing, the presence of water has a significant impact on the material removal process. A concentrated laser beam removes the material from the bottom surface of the workpiece. Water acts as a barrier to the resolidification of materials that have been removed from the channel. The upper surface layer is irradiated when machined in the open air, losing its shine and smoothness; however, the bottom surface irradiates less energy when machined in submerged conditions, keeping the majority of its shine and smoothness. The removed part of the material gets trapped in the water. As a result, water helps to reduce the redeposition of material. However, the underlying mechanism of material removal, namely melting and evaporation stays the same. Because of the trapped material in the water, laser rays' diffraction occurs, resulting in lower channel quality at the end of the procedure.

5.3 Material Removal Technique

5.3.1 Laser Transmission Technique

The material which is being used for the present study is of transparent type. Henceforth whenever Nd: YAG laser transmits through the transparent material, machining operation does not take place. But, whenever any absorbing material is used on the bottom surface in conjunction with the transparent material, the machining phenomenon takes place. This micro-machining process is shown in Figure 5.1.

I. Enhance absorptivity

The material being utilized is transparent, and sellotape has been used to ensure that no energy passes through the substance. Since black absorbs energy the most, it has been employed as an absorbent to increase absorptivity.

ii. Focus on the bottom surface of the workpiece material

The workpiece material used i.e., PMMA is transparent; it can be easily focused on the bottom surface. Hence absorbent is attached to the bottom surface of the workpiece material so that the laser beam can be focused on the absorbent being used.

iii. Physical characteristics used in the removal mechanism

The physical characteristics setting used in the removal mechanism are listed in Table 5.1.

Table 5.1 Physical characteristics used in the removal mechanism

Characteristics	Remarks
Workpiece thickness	11.328 mm
Absorbent	Sellotape
Workpiece + Absorbent	11.368 mm
Absorbent thickness	0.040 mm
Absorbent colour	Black
Water level (the gap between the ground level of the underwater setup and the workpiece material)	3mm (in case of submerged condition in water)
Gap measuring tool	Sleeve gauge

Figure 5.2 (a, b) shows the without coated and gold coated micro-machined sample of transparent PMMA sample. Figure 5.2(b) shows that sample 11 is not machined because it is taken as the reference surface of the PMMA workpiece.

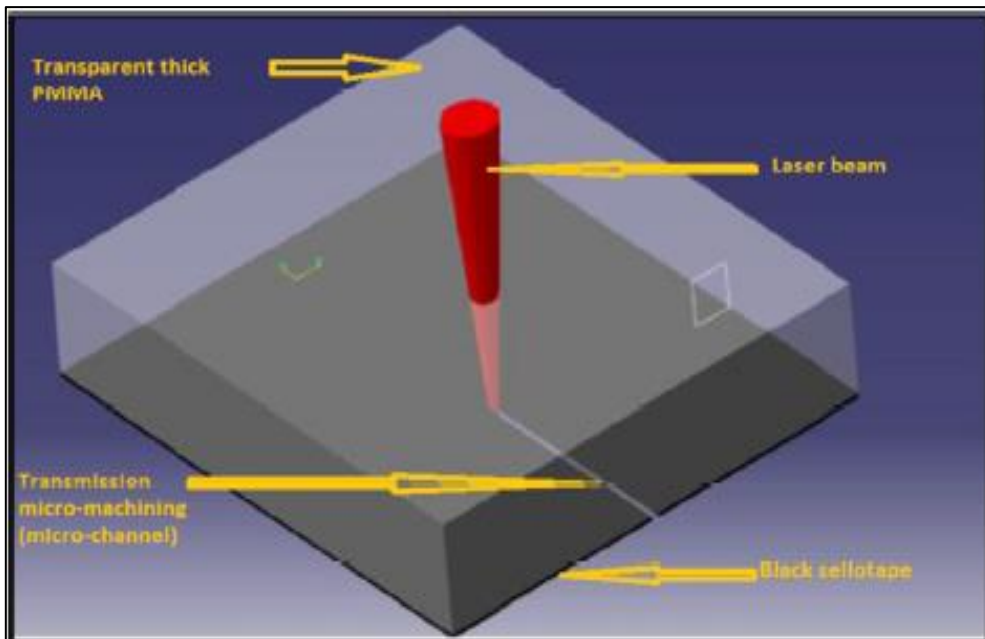


Figure 5.1 Schematic diagram of laser transmission micro-channeling process (absorbent material used as black sellotape)



(a)

(b)

Figure 5.2 (a) PMMA workpiece without coating; and (b) Machining slots coated with gold after machining

5.3.1.1 Advantages of this Novel Technique

- (i) The absence of micro-cracks along with low or no debris deposition on the formed micro-channel;
- (ii) The adverse effect of plasma shielding is not noticed here;
- (iii) The effect of water as a coolant gives proper edge line of the micro-channel by restricting thermo-gravitational flow due to low thermal conductivity of PMMA in the submerged condition;
- (iv) There is no laser power is absorbed by the water as the workpiece is not in fully submerged condition and the laser beam is not travel through it; and
- (v) Optical damage threshold is much less in water which presents at the machining zone and hence gets better quality characteristics of the micro-channel.

5.4 Identification of the Effective Process Parameters

5.4.1 Selection of the Process Parameters for Nd: YAG Laser

To analyze the geometry of Nd:YAG laser generated micro-channels on PMMA, various process parameters such as lamp current, pulse width or duty cycle, pulse frequency or pulse repetition frequency, cutting speed or scan speed, and number of passes are considered. The detail of each process parameter is as follows:

(i) Lamp Current: A solid state laser's primary parameter is lamp current. The YAG host is stimulated to emit photons by the krypton arc lamp. The intensity of lamp, which is only controlled by the lamp current, is directly involved in increasing the power density of the laser beam. Peak power can be attained using a pulsed Nd:YAG laser at a low pulse frequency since the period for accumulation per pulse is longer. As a result, high peak power may be generated at low pulse frequency and high lamp current.

(ii) Pulse Width (Duty Cycle): The time required to vaporize the substance is defined as pulse duration or pulse width. It should not be less than the penetration time of laser beam. It can be roughly calculated by using the relation [39]:

$$T_i < \frac{1}{2f_p} \quad [\text{Eq}^n 5.1]$$

Where, T_i = pulse duration,

f_p = pulse repetition frequency.

When, consider the continuous and smooth machined surface:

$$\frac{V}{f_p} < d(0) \quad [\text{Eq}^n 5.2]$$

Where, $d(0)$ = diameter of the focused spot,

V = cutting speed.

As the pulse energy increases with decrease in penetration time.

(iii) Pulse Frequency (Pulse Repetition Frequency): The mechanism of pulsed laser cutting differs from that of CW laser cutting because of the periodic nature of heating. Cutting action is the result of a sequence of single pulses acting in machining zone. Higher frequency minimizes the cut roughness by increasing the overlapping number. However, pulse repetition frequency has an upper limit beyond which the pulse duration is limited and the pulse approaches a continuous wave. The pulse period should be greater than the pulse duration, which is the inverse of the pulse frequency.

(iv) Cutting Speed (Scanning Speed): cutting speed is the rate at which the working table moves in the X and Y directions. The unit is measured in millimeters per second. The cutting speed is controlled by a CNC controller system.

(v) Number of Passes: The number of passes is a unit-less parameter that specifies how many times the laser beam impinges in a given length for a given geometrical feature.

5.4.2 Selection of the Process Parameters for Fiber Laser

To analyze the geometry of micro-channels on PMMA machined by fiber laser, various process parameters such as laser power, pulse width or duty cycle, pulse frequency, cutting speed or scan speed, and number of passes are considered. The detail of each process parameters is as follows:

- (i) **Working Power (Laser Power):** The instantaneous power irradiated on a specific workpiece for melting and evaporation of molten material is referred as laser power. It is usually the average power of the system.

- (ii) **Pulse Width (Duty Cycle):** The rise and fall of the laser pulse are combined in the time period. The width of the curve at half height is used to characterize the pulse length. The percentage of the cycle time is referred to as the duty cycle.
- (iii) **Pulse Frequency:** Pulse frequency is the number of pulses per second (s^{-1} or Hz) and is the inverse of temporal pulse spacing. The following equation (Eqⁿ 5.3) gives the relationship between laser power, peak power, duty cycle, and pulse frequency:

$$\text{Peak Power} = \frac{\text{Laser Power}}{\text{Pulse Frequency} \times \text{Duty Cycle}} \quad [\text{Eq}^n \text{ 5.3}]$$

- (iv) **Cutting Speed (Scanning Speed):** Scanning speed is defined by the speed at which the working table transverses along X and Y directions. The unit of scanning speed is mm/sec. Scan Speed is controlled by a CNC controller system for each of the axis.
- (v) **Number of Passes:** The number of passes is a unit less parameter that defines the number of times the laser beam moves to and fro in a specific length for a specific geometrical feature.

5.5 Procedural Steps for Measurement of Responses

All machining responses are measured in this set of experiments using an OLYMPUS STM6 measuring microscope (Figure 5.3) with a 5X optical lens. The measuring microscope employed has a 5X to 20X magnification range and is fitted with an x-axis, y-axis, and z-axis shift arrangement to ensure that the measured sample, surface, or subject is in perfect focus. All of the responses are measured three times in three different micro-channels, and then an average is calculated. To precisely quantify the collected images, OLYMPUS' proprietary programme GETIT is used. The thicknesses of the PMMA samples are measured using a digital vernier caliper with a resolution of 0.001 mm at various parts.

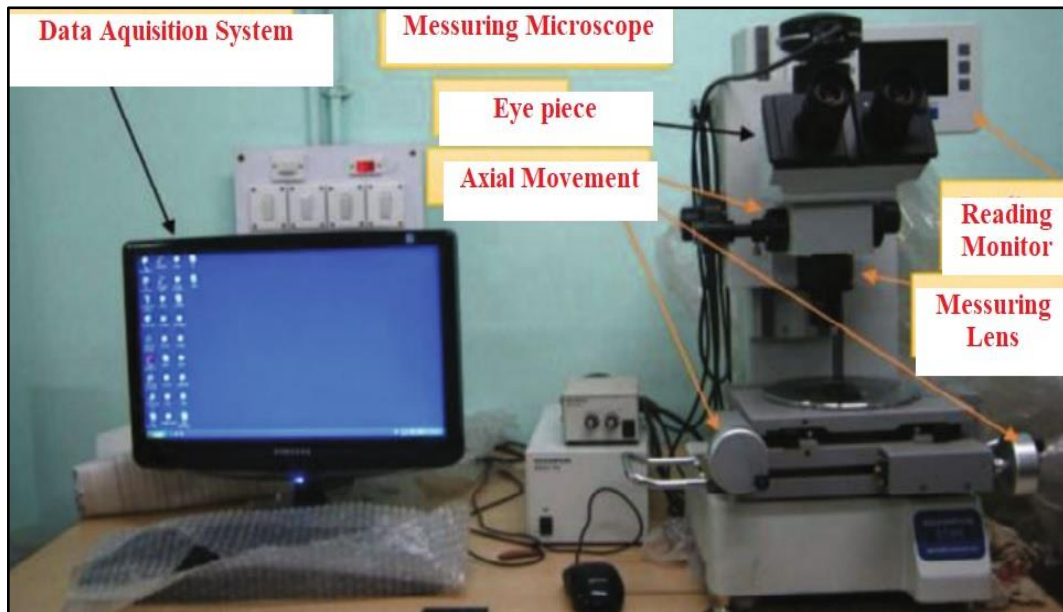


Figure 5.3 OLYMPUS STM6 measuring microscope

5.6 Primary Investigations

5.6.1 Preliminary Investigation for Micro-channeling on PMMA Using Laser Transmission Technique in Nd:YAG Laser

Basic experimental studies have been carried out after a hit and trial experiments. For Nd:YAG laser, the important and influencing parameters that have been taken into account were lamp current, pulse frequency, pulse width, and cutting speed. This basic experimental study has been carried out in submerged conditions in deionised water. The experimental details are described below,

Figure 5.4 shows the influence of lamp current on depth, kerf width, and HAZ width of the underwater Nd: YAG laser generated PMMA micro-channels, while other process parameters are kept constant such as pulse frequency of 40kHz, pulse width of 94%, and cutting speed of 1mm/sec. An increment of lamp current leads to an increase in average power as well as the peak power of the generated laser beam. In addition to this it also causes an increment in the energy input per area. Therefore, the conversion of optical energy to thermal energy directed on the workpiece improves significantly. The present research system is also boosted by nanosecond pulse regime (duty cycle) which further reduces the laser-material interaction time. As a consequence of the aforesaid phenomena, kerf width and depth of the PMMA micro-channels along with the HAZ width increases simultaneously. Therefore, controlling

of lamp current is an important aspect in order to reduce the kerf width along with HAZ width. Table 5.2 shows the influence of lamp current on the response criteria. Experimental data for various machining responses are shown below:

Table 5.2 Influence of lamp current on the response criteria

Lamp Current (amp)	Depth of Cut (μm)	Kerf Width (μm)	HAZ Width (μm)
24	59.57	127.88	81.65
25	69.13	163.76	94.74
26	71.57	204.7	123.28
27	80.67	219.76	169.57
28	93.47	242.42	189.29
Constant parameters	Cutting Speed = 1 mm/sec		
	Pulse Frequency = 40 kHz		
	Pulse Width = 94%		

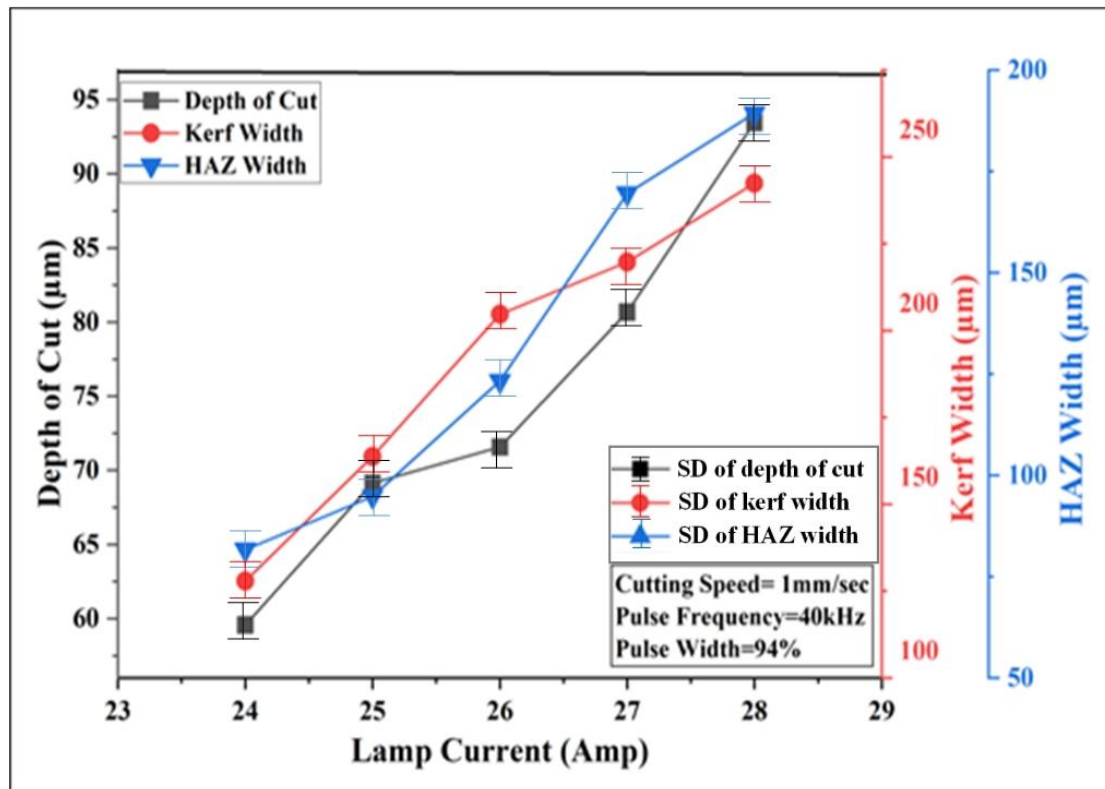


Figure 5.4 Effect of lamp current on kerf width, HAZ width and depth of cut

Figure 5.5 shows the influence of pulse frequency on depth, kerf width, and HAZ width of the underwater Nd: YAG laser generated PMMA micro-channels, while other process parameters kept constant such as lamp current of 24 amps, pulse width of 94%, and cutting speed of 1mm/sec. An increment in pulse frequency reduces peak power (when average power is constant). The aforesaid parametric combinations are chosen based on threshold energy to ablate the PMMA workpiece for the present system. Beyond this limit, the optical energy is not converted to the desired thermal energy to initiate micro-channeling operations. When pulse frequency is set at its low value, all the responses tend to increase owing to a high penetration rate (ablation rate). This phenomenon holds true up to 40 kHz of pulse frequency for the present set of experiments. This phenomenon reverts back to the increment of pulse frequency as the penetration rate decreases. It is interesting to note that at higher pulse frequencies, the number of laser pulses increases which further causes more spot overlapping and continuous profiles of the underwater laser fabricated micro-channels. However, as the cutting speed is relatively low during all the micro-channeling operations, laser-material interaction time was more, which may lead to re-solidification of the molten material at the micro-channel surfaces. Table 5.3 shows the influence of pulse frequency on the response criteria.

Table 5.3 Influence of pulse frequency on the response criteria

Pulse Frequency (kHz)	Depth of Cut (μm)	Kerf Width (μm)	HAZ Width (μm)
25	105	472.88	181.01
30	114.3	493.7	223.56
35	131.8	502.88	242.65
40	137	513.82	257.14
45	133.6	501.4	235.75
Constant parameters	Lamp Current = 24 amp		
	Pulse Width = 94%		
	Cutting Speed = 1 mm/sec		

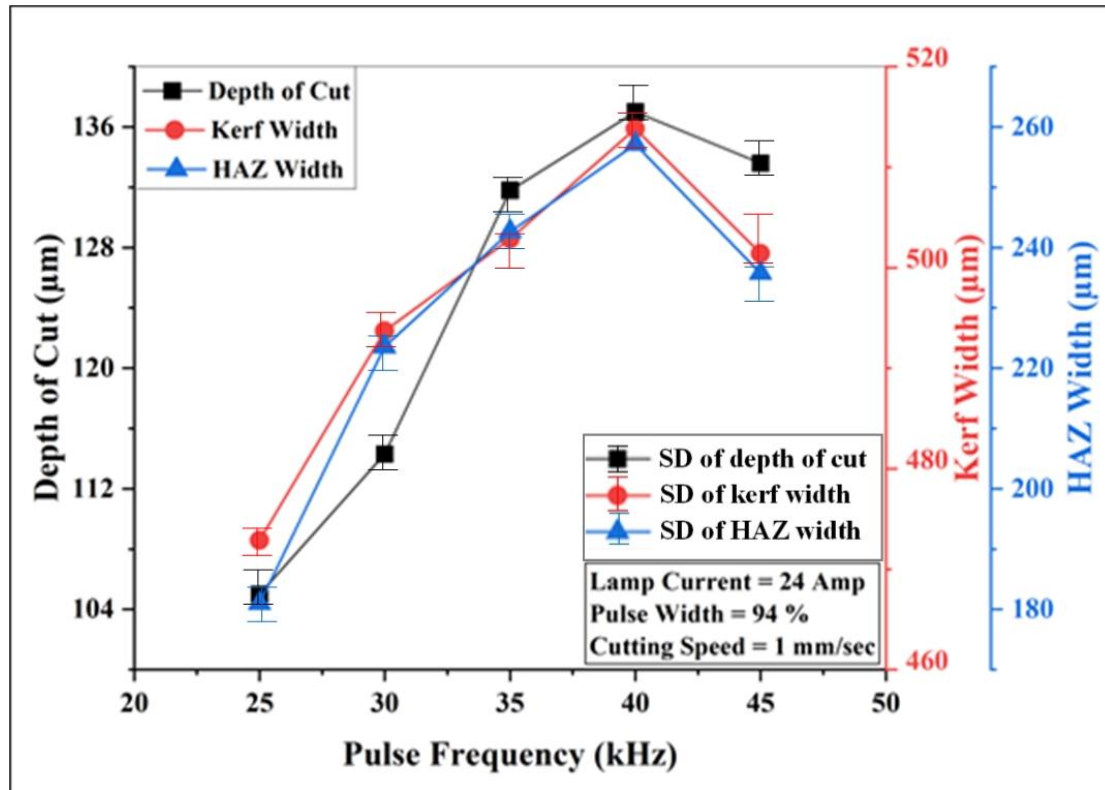


Figure 5.5 Effect of pulse frequency on kerf width, HAZ width and depth of cut

Figure 5.6 shows the influence of pulse width on depth, kerf width, and HAZ width of the underwater Nd: YAG laser generated PMMA micro-channels, while other process parameters are kept constant such as lamp current of 24 amps, pulse frequency of 40 kHz, and cutting speed of 1mm/sec. The range of pulse width is elevated (90-98% of the cycle time) for the present set of experiments so as to eliminate the burning factor during the micro-channeling operations. Some amount of HAZ width is obvious owing to photo-thermal ablation process as well as the low thermal conductivity of PMMA. When the pulse width is increased, the machining cycle time (in nano-second) is increased which further reduces the peak power and penetration rate simultaneously. No significant changes are observed in the response criteria as the penetration rate is sufficiently low. Although all the machining responses tend to decrease with the increment of pulse width after a certain period (94% of cycle time), the overall machining responses lead to uniformity and low sputtering of the molten material. Table 5.4 shows the influence of pulse width on the response criteria. Experimental data and responses are shown below:

Table 5.4 Influence of pulse width on the response criteria

Pulse Width (%)	Depth of Cut (μm)	Kerf Width (μm)	HAZ Width (μm)
90	15.3	189.5	109.83
92	33.2	196.83	115.56
94	37.1	209.76	128.8
96	34.4	199.97	120.105
98	32.6	196.88	117.11
Constant Parameters	Lamp Current = 24 amp		
	Pulse Frequency = 40 kHz		
	Cutting Speed = 1 mm/sec		

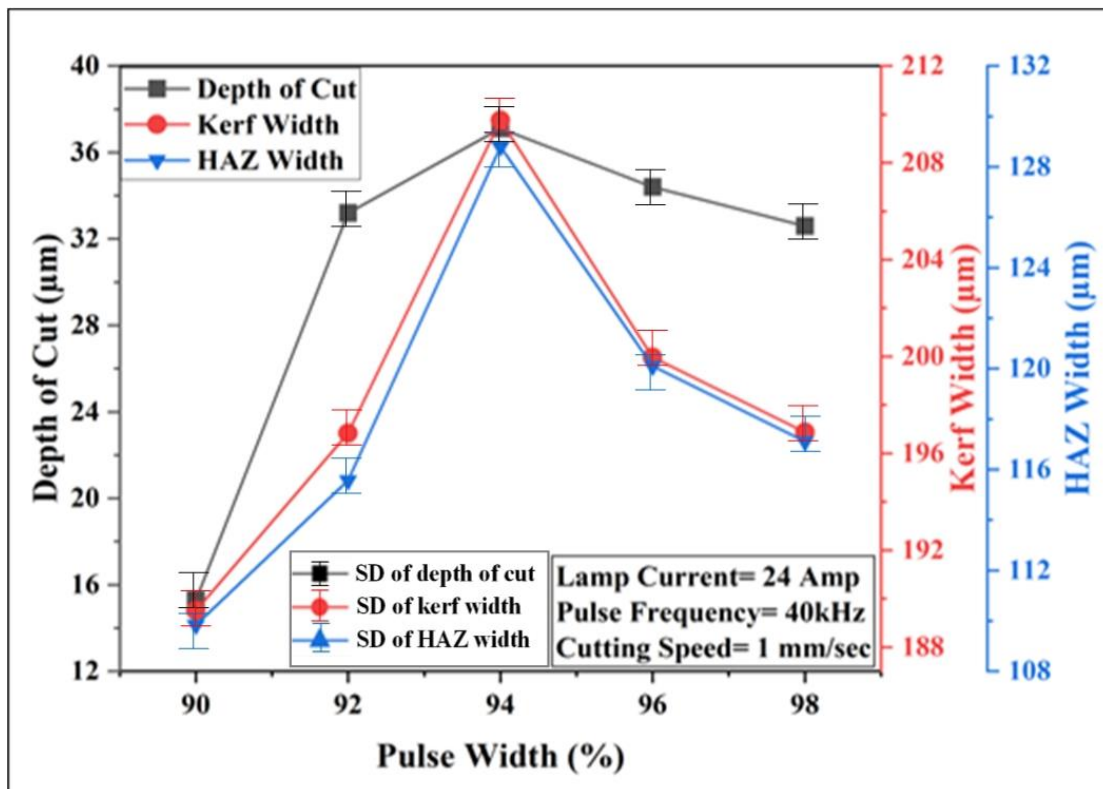


Figure 5.6 Effect of pulse width on kerf width, HAZ width and depth of cut

Figure 5.7 shows the influence of cutting speed on depth, kerf width, and HAZ width of the underwater Nd: YAG laser machined PMMA micro-channels, while other process parameters are kept constant such as lamp current of 24 amps, pulse frequency of 40 kHz, and pulse width of 94%. Cutting speed is the most crucial factor for determining the amount of HAZ during laser machining of a given material. Although, higher cutting speed reduces HAZ width but it is also characterized by poor surface quality and geometrical aspects of the laser generated micro-channels. These

phenomena occur due to low laser-material interaction time as well as low spot overlapping and penetration rate of the laser beam. As a consequence of which all the machining responses have a tendency to reduce significantly with the increment of cutting speed. However, as discussed in the above section, the micro-channel profiles are attributed by non-uniformity and sputtering of the molten material which further enhances the possibility of re-solidification of the molten material at the edges of the micro-channels. Hence, it is important to carefully design the process parameters in such a way that desired machining responses can be achievable. Table 5.5 shows the influence of cutting speed on the response criteria. Figure 5.4 to Figure 5.7 depict the standard deviations (SD) of the responses with respect to process parameters.

Table 5.5 Influence of cutting speed on the response criteria

Cutting Speed (mm/sec)	Depth of Cut (μm)	Kerf Width (μm)	HAZ Width (μm)
1.00	41.3	232.76	96.34
1.25	32.9	214.35	88.095
1.50	29.07	213.12	75.67
1.75	23.83	208.18	56.27
2.00	20.13	204.43	45.325
Constant parameters	Lamp Current = 24 amp		
	Pulse Frequency = 40 kHz		
	Pulse Width = 94%		

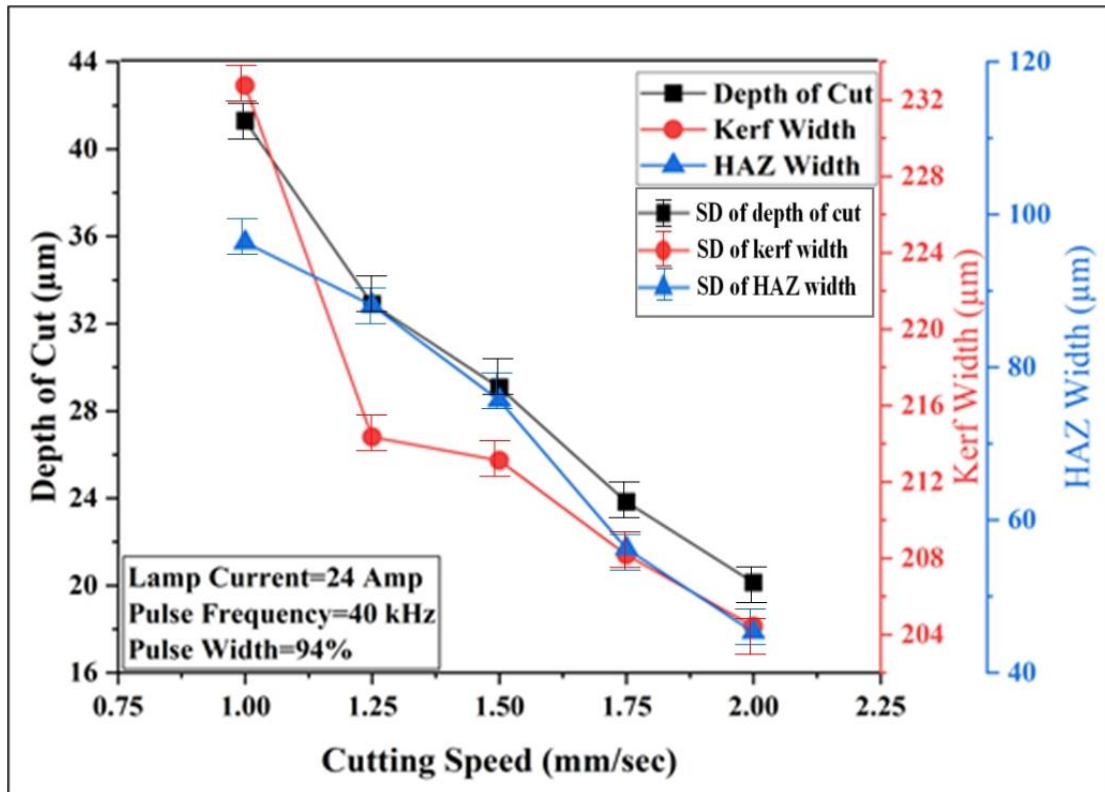


Figure 5.7 Effect of cutting speed on kerf width, HAZ width and depth of cut

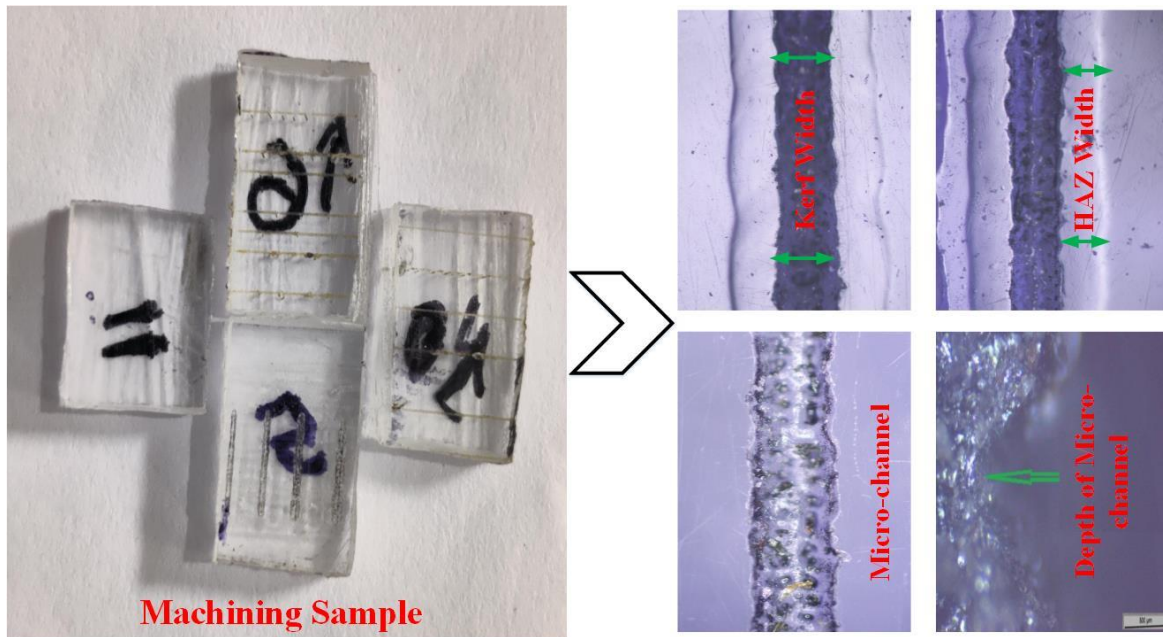


Figure 5.8 Machining samples and microscopic view of micro-channel characteristics

Machining sample and characteristics i.e., depth of cut, kerf width and HAZ width of the micro-channel has been shown the in Figure 5.8.

5.7 Outcomes

From the study, it may be concluded that the lamp current, pulse frequency, pulse width, and cutting speed are the major influencing parameters for transmission micro-channeling operation in Nd:YAG laser at both assisted mediums. It has also been found from the basic experimental study that the pulse frequency, working power, and cutting speed play a major role in influencing the experiments as effective parameters for transmission micro-channeling operation in fiber laser at different environments. The basic experimental studies have helped to decide the ranges of process parameters for detailed experimental study further. For Nd:YAG laser, the effective ranges of process parameters are, lamp current (24 to 28 amp), pulse frequency (25 to 45 kHz), cutting speed (1.00 to 2.00 mm/sec) and pulse width (90 to 98 %). For fiber laser, the effective ranges of process parameters are, pulse frequency (50 to 70 kHz), working power (13 to 17 %), cutting speed (0.10 to 0.60 mm/sec) and pulse width (91 to 99 %).

Chapter 6

EXPERIMENTAL INVESTIGATION INTO PULSED Nd: YAG LASER MICRO- CHANNELING OF PMMA

6.1 Introduction

Laser beam micro-channeling of thick PMMA plates has been demonstrated by a few researchers as found in the previous literature. Due to the creation of deep sub-surface micro-cracks caused by the burning and charring of polymeric chains in thick clear PMMA plates, it is extremely challenging to process it with Nd: YAG laser radiation. Laser transmission machining, one of the most technologically advanced forms of laser machining operation, may be effected used to overcome this difficulty. In this present research work, the feasibility of nanosecond laser transmission cutting of thick transparent PMMA in different environmental conditions (air and submerged in deionized water) has been studied. The effect of process parameters on machining responses has also been investigated during the study. An Nd:YAG laser with nanosecond pulses in the NIR region has been used to carry out the experiments based on response surface methodology (RSM). Depth of cut, kerf width, and HAZ width have been considered as machining characteristics, whereas pulse frequency, lamp current, and cutting speed are considered as process parameters. A second-order polynomial model has been developed to perform the statistical analysis with the help of MINITAB software. Single as well as multi-objective optimization has also been carried out to get the desired value of quality characteristics of machined micro-channels.

6.2 Background and Fundamentals

Nd:YAG laser machine is an indirect ablation process. Here, the laser beam is not coupled with workpiece material, in spite of which the laser beam is transmitted through the object and absorbed by an absorbent affixed on the backside of the workpiece. The absorbent material then transmits the heat to the workpiece using the

conduction method, which heats up the back end of the object. In this process, the back end above the object is considered as the machining zone. By this procedure, the material is removed from the intersection of the laser, absorbent material, and workpiece, and the cutting front is created. The backside of the workpiece sample which is to be machined is kept in both the environmental conditions, i.e., in air and underwater. Pure deionized (DI) water is used as the submerged medium, which acts as a coolant during machining.

6.3 Parametric Study Based on Response Surface Methodology for Laser Beam Transmission Micro-channeling of PMMA with Air as an Assist Medium

6.3.1 Experimental Details

Table 6.1 lists the constant and variable process parameter settings, as well as their levels. Pulse frequency, lamp current, and cutting speed were varied between 25 and 45 kHz, 24-28 amp, and 1.00-2.00 mm/sec respectively. During the experimentation, several additional parameters' influence on responses was kept constant.

Table 6.1 Process variables and their levels

Process Parameter	Unit	Symbol	Levels				
			-2	-1	0	1	2
Pulse Frequency (PF)	kHz	A	25	30	35	40	45
Lamp Current (LC)	amp	B	24	25	26	27	28
Cutting Speed (CS)	mm/sec	C	1.00	1.25	1.50	1.75	2.00
Constant Factors	Pulse Width = 94%						
	Number of passes = Single pass						

6.3.2 Results and Discussion

Laser transmission cutting in the air as the medium was used to carry out 20 sets of experiments. The experimental results are given in Table 6.2. Images of the PMMA substrate and the micro-channels fabricated by the laser transmission cutting in partially submerged conditions are given in Figure 6.1 and Figure 6.2, correspondingly.

Table 6.2 Experimental result

Experiment No.	Pulse Frequency (PF: kHz)	Lamp Current (LC: Amp)	Cutting Speed (CS: mm/sec)	Depth of Cut (μm)	Kerf Width (μm)	HAZ Width (μm)
1	-1	-1	-1	22.105	135.605	288.034
2	1	-1	-1	13.588	145.149	173.810
3	-1	1	-1	32.783	133.235	435.271
4	1	1	-1	32.016	156.126	457.439
5	-1	-1	1	34.504	122.836	221.892
6	1	-1	1	14.697	136.097	132.723
7	-1	1	1	21.907	133.859	392.968
8	1	1	1	12.151	160.080	448.435
9	-2	0	0	28.364	134.206	258.802
10	2	0	0	12.155	170.370	199.095
11	0	-2	0	15.331	116.524	105.176
12	0	2	0	27.374	140.316	556.983
13	0	0	-2	32.167	148.999	360.229
14	0	0	2	21.075	139.478	277.029
15	0	0	0	24.680	135.888	412.877
16	0	0	0	28.166	135.316	413.139
17	0	0	0	27.651	135.888	414.669
18	0	0	0	23.690	135.628	409.402
19	0	0	0	26.582	135.836	412.243
20	0	0	0	27.770	136.305	409.402

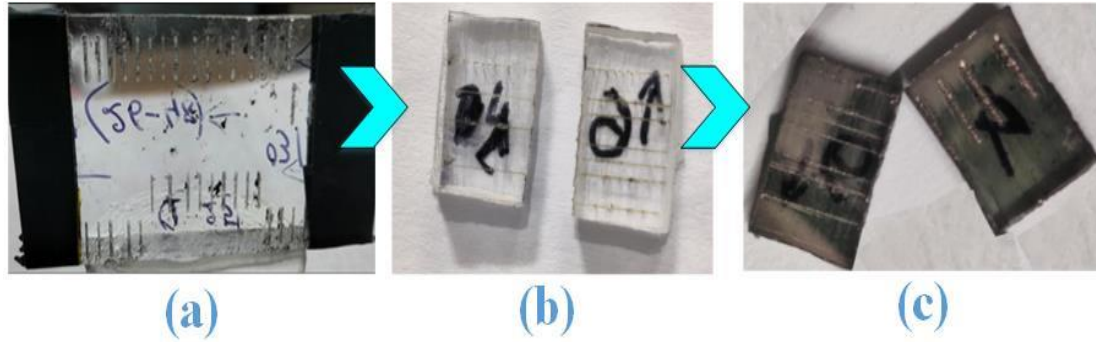


Figure 6.1 PMMA workpiece after Nd:YAG laser transmission cutting in air, (a) Parent sample, (b) Sliced micro-machined sample, (c) Gold coated micro-machined sample.

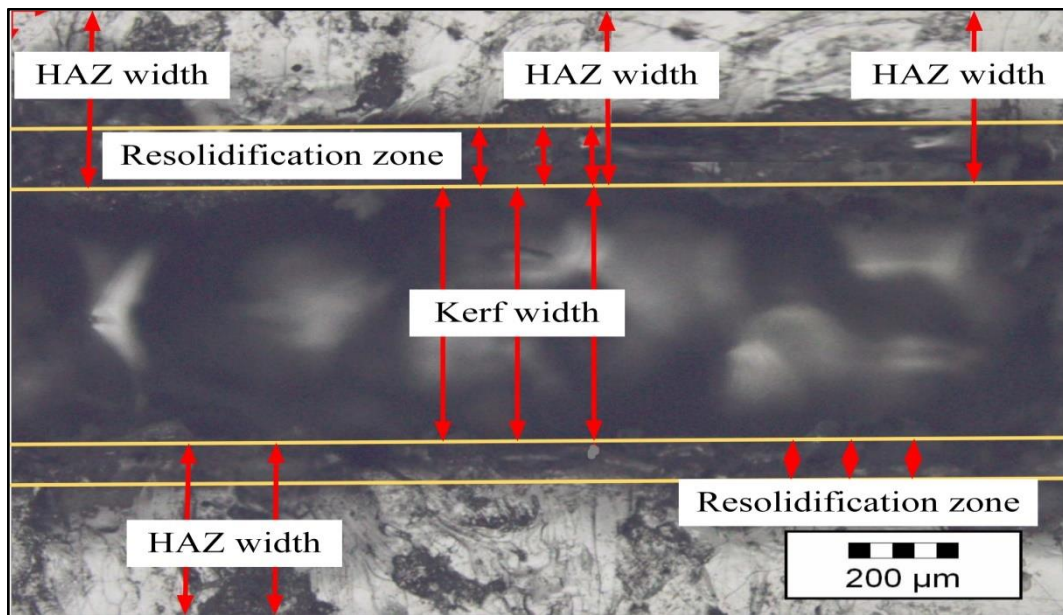


Figure 6.2 Microscopic view of the PMMA micro-channel.

6.3.2.1 Development of Second-order Polynomial Model

The mathematical relationship between the response and variable process parameters has been established using response surface modeling (central composite design). Below are the second-order polynomial equations in a coded manner.

Expression for Depth of cut

$$Y_{\text{Depth of cut}} = 26.297 - 4.454 A + 2.378 B - 2.464 C - 1.604 A^2 - 1.331 B^2 - 0.014 C^2 + 2.225 AB - 2.535 AC - 5.531 BC \quad (\text{Eq}^n.6.1)$$

Expression for Kerf Width

$$Y_{\text{Kerf Width}} = 135.844 + 9.015 A + 5.700 B - 2.268 C + 4.1362 A^2 - 1.8308 B^2 + 2.1238 C^2 + 3.288 AB + 0.881 AC + 3.300 BC \quad (\text{Eq}^n.6.2)$$

Expression for HAZ Width

$$Y_{\text{HAZ Width}} = 411.26 - 15.323 A + 113.829 B - 20.308 C - 46.100 A^2 - 20.567 B^2 - 23.680 C^2 + 35.13 AB + 7.29 AC + 6.99 BC \quad (\text{Eq}^n.6.3)$$

Where ‘A’ denotes pulse frequency (kHz), ‘B’ denotes lamp current (amp), and ‘C’ denotes cutting speed (mm/sec).

6.3.2.2 ANOVA of Machining Responses

Analysis of variance (ANOVA) and subsequent F- and p-value tests were conducted to assess the adequacy of the generated mathematical models for kerf width, depth of cut, and HAZ width. Tables 6.3, 6.4, and 6.5 show the results of an ANOVA analysis of the quadratic model with different adequacy measures R^2 , adjusted R^2 , and predicted R^2 .

Table 6.3 ANOVA results of depth of cut at air medium.

Source	DF	Adj SS	Adj MS	F-Value	P-Value
Model	9	938.072	104.230	34.53	0.000
Linear	3	505.009	168.336	55.77	0.000
A	1	317.423	317.423	105.15	0.000
B	1	90.481	90.481	29.97	0.000
C	1	97.106	97.106	32.17	0.000
Square	3	97.288	32.429	10.74	0.002
A ²	1	64.693	64.693	21.43	0.001
B ²	1	44.533	44.533	14.75	0.003
C ²	1	0.005	0.005	0.00	0.969
2-Way Interaction	3	335.775	111.925	37.08	0.000
A×B	1	39.613	39.613	13.12	0.005
A×C	1	51.405	51.405	17.03	0.002
B×C	1	244.757	244.757	81.08	0.000
Error	10	30.186	3.019		
Lack-of-Fit	5	13.291	2.658	0.79	0.601
Pure Error	5	16.895	3.379		
Total	19	968.259			
Model Summary		S	R ²	R ² (adj.)	R ² (pred.)
		1.73742	96.88%	94.08%	86.23%

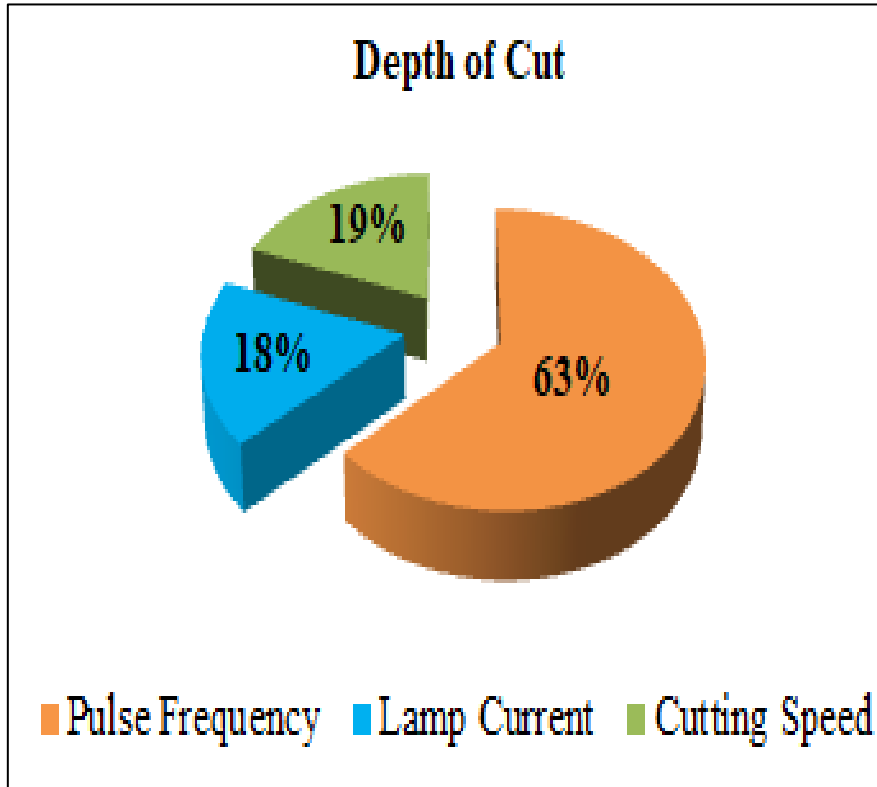


Figure 6.3 Contribution of parameters on depth of cut

The related p-value of the model is less than 0.05 (i.e., $\alpha = 0.05$, or 95 % confidence level) as shown in Table 6.3, indicating that the model terms are statistically significant. The model's lack-of-fit value implies non-significance, which is ideal. All of the input process factors, as well as the two-way interaction terms, are significant and influence machining reactions in some way. According to the table, pulse frequency (62.85 %) is the most important factor for depth of cut, followed by lamp current (17.91 %), and cutting speed (19.23 %). Other adequacy measures such as R^2 , adjusted R^2 , and forecast R^2 are in reasonable agreement and close to 100%, indicating that the model is adequate. The impact of parameters on depth of cut is depicted in Figure 6.3.

Table 6.4 ANOVA results of kerf width at air medium.

Source	DF	Adj SS	Adj MS	F-Value	P-Value
Model	9	2787.230	309.690	1629.78	0.000
Linear	3	1902.510	634.170	3337.37	0.000
A	1	1300.410	1300.410	6843.54	0.000
B	1	519.810	519.810	2735.52	0.000
C	1	82.290	82.290	433.05	0.000
Square	3	704.890	234.960	1236.52	0.000
A ²	1	430.150	430.150	2263.70	0.000
B ²	1	84.270	84.270	443.50	0.000
C ²	1	113.410	113.410	596.83	0.000
2-Way Interaction	3	179.830	59.940	315.45	0.000
A×B	1	86.510	86.510	455.25	0.000
A×C	1	6.210	6.210	32.67	0.000
B×C	1	87.110	87.110	458.44	0.000
Error	10	1.900	0.190		
Lack-of-Fit	5	1.370	0.270	2.55	0.164
Pure Error	5	0.540	0.110		
Total	19	2789.130			
Model Summary		S	R ²	R ² (adj.)	R ² (pred.)
		0.435913	99.93%	99.87%	99.57%

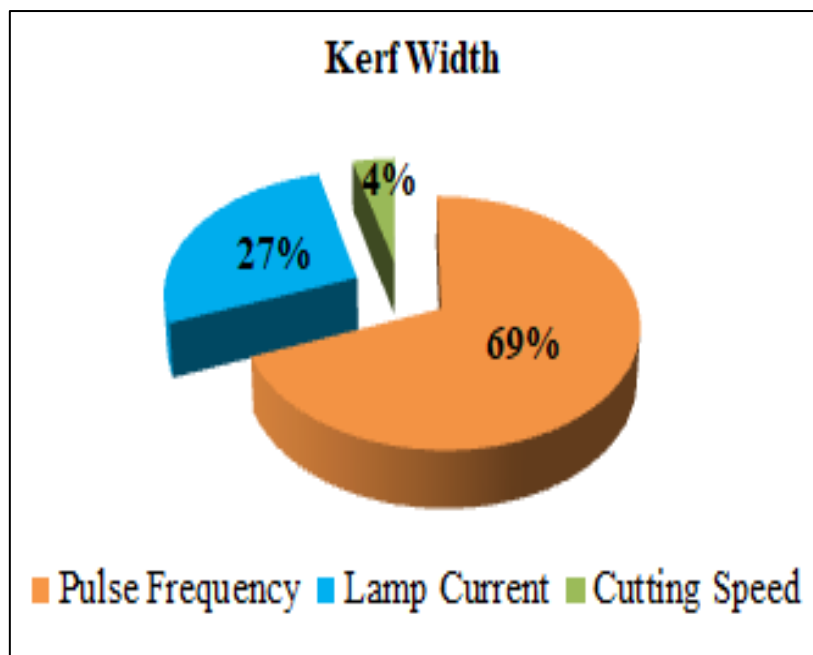


Figure 6.4 Contribution of parameters on kerf width

As can be seen in Table 6.4, the relevant p-value of the model has a value that is lower than 0.05, which indicates that the model terms have a degree of statistical significance that is equivalent to having a confidence level of 95 %. The value of the model's lack-of-fit indicates that it is not significant, which is the desired outcome. It was discovered that every single one of the input process factors, in addition to the two-way interaction terms, exerts a significant amount of influence over the machining responses. Pulse frequency (68.35 %) is the most dominant parameter for depth of cut, followed by lamp current (27.32 %), and cutting speed (4.32 %). It was noted that R^2 , adjusted R^2 , and forecast R^2 are in good agreement and close to 100%, which shows the adequacy of the model. Figure 6.4 depicts the influence of various parameters on kerf width.

Table 6.5 ANOVA results of HAZ width at air medium.

Source	DF	Adj SS	Adj MS	F-Value	P-Value
Model	9	288664	32074	2813.610	0.000
Linear	3	217669	72556	6364.880	0.000
A	1	3757	3757	329.560	0.000
B	1	207314	207314	18186.190	0.000
C	1	6599	6599	578.880	0.000
Square	3	60306	20102	1763.420	0.000
A ²	1	53434	53434	4687.390	0.000
B ²	1	10636	10636	933.000	0.000
C ²	1	14099	14099	1236.770	0.000
2-Way Interaction	3	10689	3563	312.550	0.000
A×B	1	9872	9872	866.010	0.000
A×C	1	426	426	37.340	0.000
B×C	1	391	391	34.290	0.000
Error	10	114	11		
Lack-of-Fit	5	91	18	4.010	0.077
Pure Error	5	23	5		
Total	19	288778			
Model Summary		S	R ²	R ² (adj.)	R ² (pred.)
		3.37632	99.96%	99.92%	99.74%

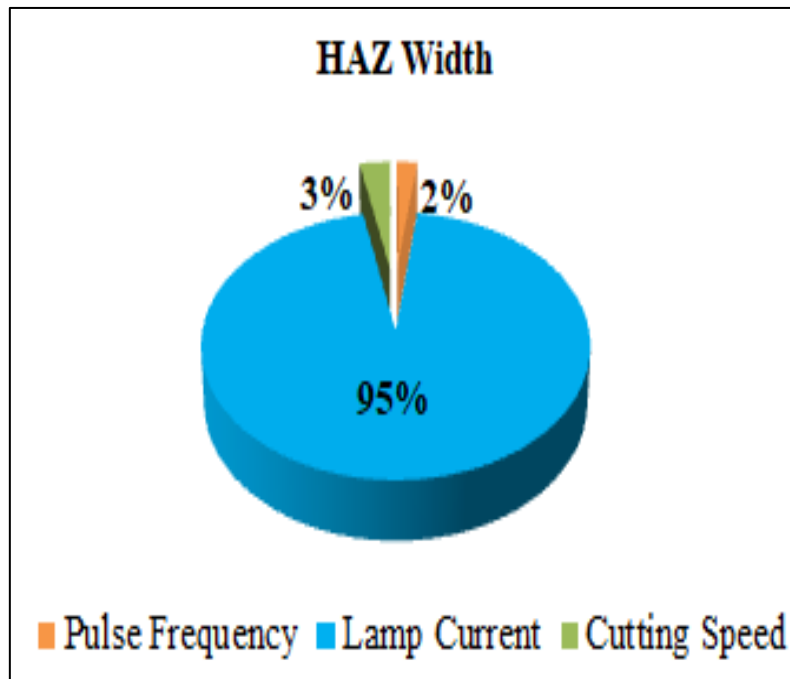


Figure 6.5 Contribution of parameters on HAZ width

Table 6.5 exhibits the related p-value of the model which is less than 0.05 (i.e., $\alpha = 0.05$, or 95 % confidence level), indicating the significance of the model terms. The lack-of-fit value implies non-significance, which is ideal. All of the input process factors, as well as the two-way interaction term, are significant and influence machining reactions in some way. According to the table, the most important component for depth of cut is lamp current (95.24 %), followed by cutting speed (3.03 %), and pulse frequency (1.73 %). Other adequacy measures R^2 , adjusted R^2 , and forecast R^2 are in reasonable agreement and close to 100%, indicating that the model is adequate. Figure 6.5 depicts the effect of several parameters on HAZ width.

6.3.2.3 Parametric Analysis of the Characteristics of Open-Air Laser Transmission Micro-channeling of PMMA

(i) Parametric Effects on Depth of Cut

It is a very challenging task to obtain a high and uniform depth of cut of micro-channel during laser transmission micro-channeling operation in air medium because laser machining is dependent on various process parameters. As a result, the effects of laser machining parameters such as lamp current, pulse frequency, and cutting speed on depth of cut on PMMA workpiece of thickness of 11.328mm during laser micro-channeling have been investigated.

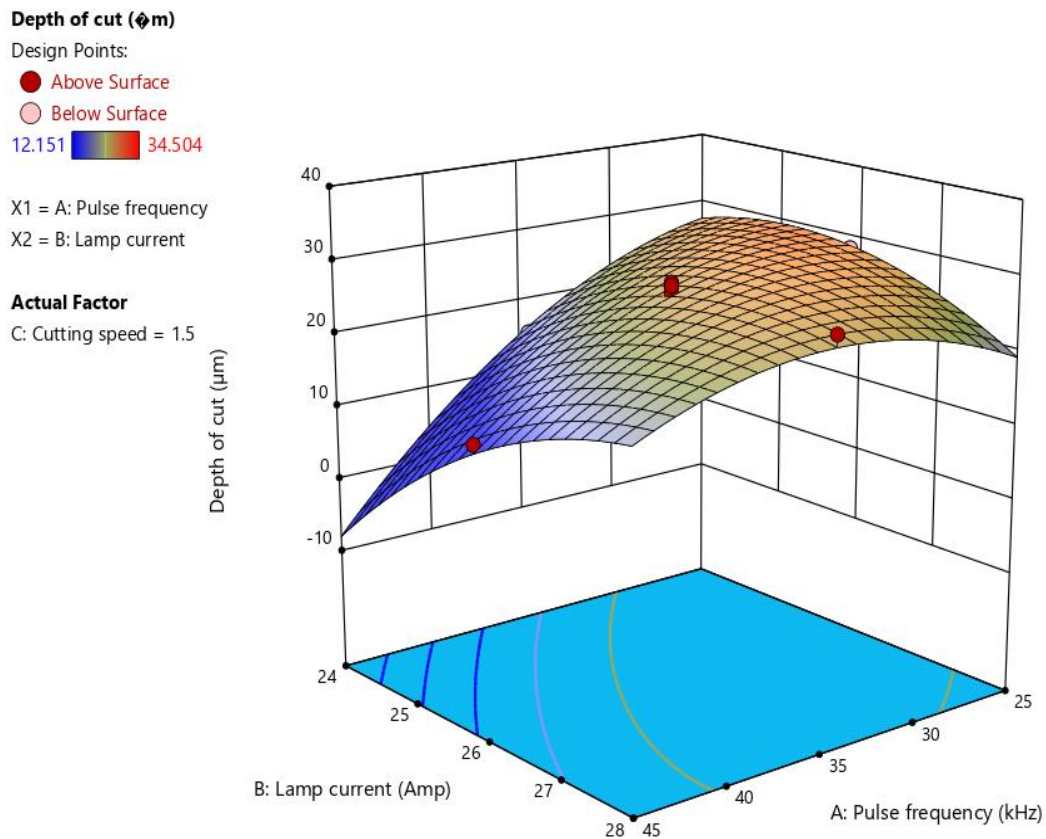


Figure 6.6 Surface plot of depth of cut versus lamp current and pulse frequency.

Figure 6.6 demonstrates the combined effects of lamp current and pulse frequency on depth of cut, holding cutting speed at 1.5 mm/sec. At higher lamp current with lower pulse frequency, the depth of cut increases but at lower lamp current with higher frequency shows the minimum depth of cut. This may be due to the fact that boosting of the lamp current at a low frequency produces high thermal energy and high quality laser beam, which increases the depth of cut and the results shows vice versa at a lower lamp current with a higher frequency. It is also observed from the surface plot that the depth of cut decreases with an increase in lamp current at lower pulse frequency. The reason behind this phenomenon may be due to the higher tendency of re-solidification of molten material. The melting of materials takes place due to the high heat generation in the machining zone. Resolidification of material might be the possible reason for the lower depth of cut of the micro-channel. The depth of cut gradually increases with an increase in lamp current at a higher level of pulse frequency because of higher rate of material removal due to generation of high thermal energy. The increase in pulse frequency deteriorates the quality of the laser beam leading to less thermal energy which in turn produces lower depth of cut. This phenomenon is significant at lower lamp current.

Depth of cut (μm)

Design Points:

● Above Surface

○ Below Surface

12.151  34.504

X1 = A: Pulse frequency

X2 = C: Cutting speed

Actual Factor

B: Lamp current = 26

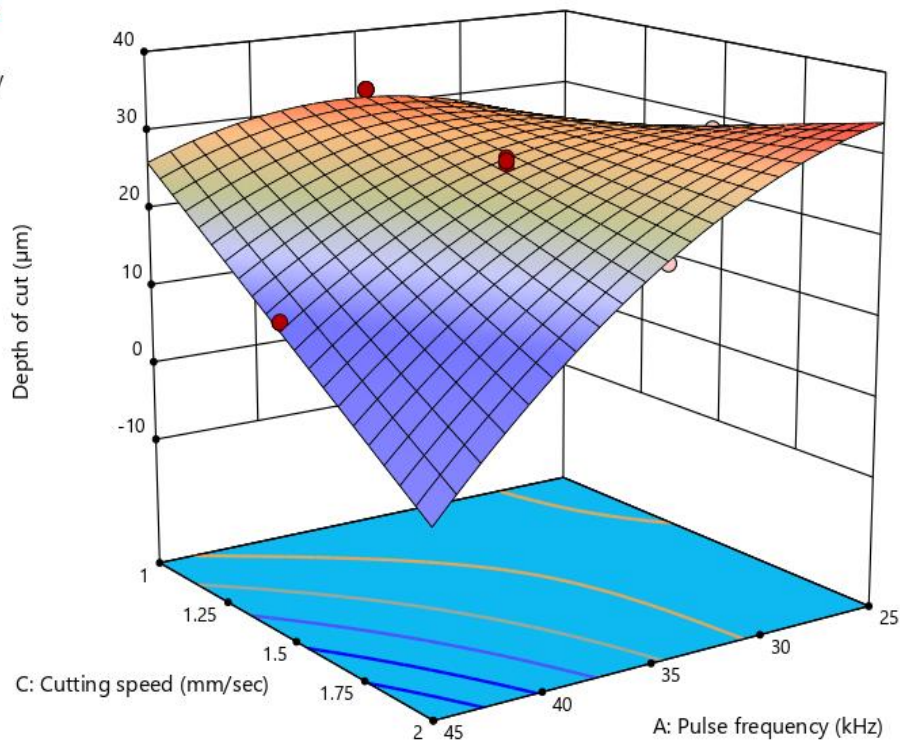


Figure 6.7 Surface plot of depth of cut versus cutting speed and pulse frequency.

The combined effects of cutting speed and pulse frequency on depth of cut keeping lamp current constant at 26 amps are shown in Figure 6.7. Initially, depth of cut increases a little bit with an increase in pulse frequency at lower cutting speed, then depth of cut decreases with an increase in pulse frequency. The number of pulses overlaps increases, leading to an improvement in the depth of cut. But with a further increase in pulse frequency at lower cutting speed results in less power of the incident beam, which produces a lower depth of cut. At higher cutting speeds, overlapping of laser pulses is reduced. An increase in pulse frequency produces lower laser power due to the fact that depth of cut decreases with an increase in pulse frequency at higher cutting speeds. At lower pulse frequency and minimum cutting speed, a very high amount of material removal takes place due to high heat generation and resolidification of material tends to increase at this combination of parameters, but with an increase in cutting speed, the tendency of resolidification of material decreases, which helps in improving the depth of cut.

Depth of cut (ϕm)

Design Points:

● Above Surface

○ Below Surface

12.151  34.504

X1 = B: Lamp current

X2 = C: Cutting speed

Actual Factor

A: Pulse frequency = 35

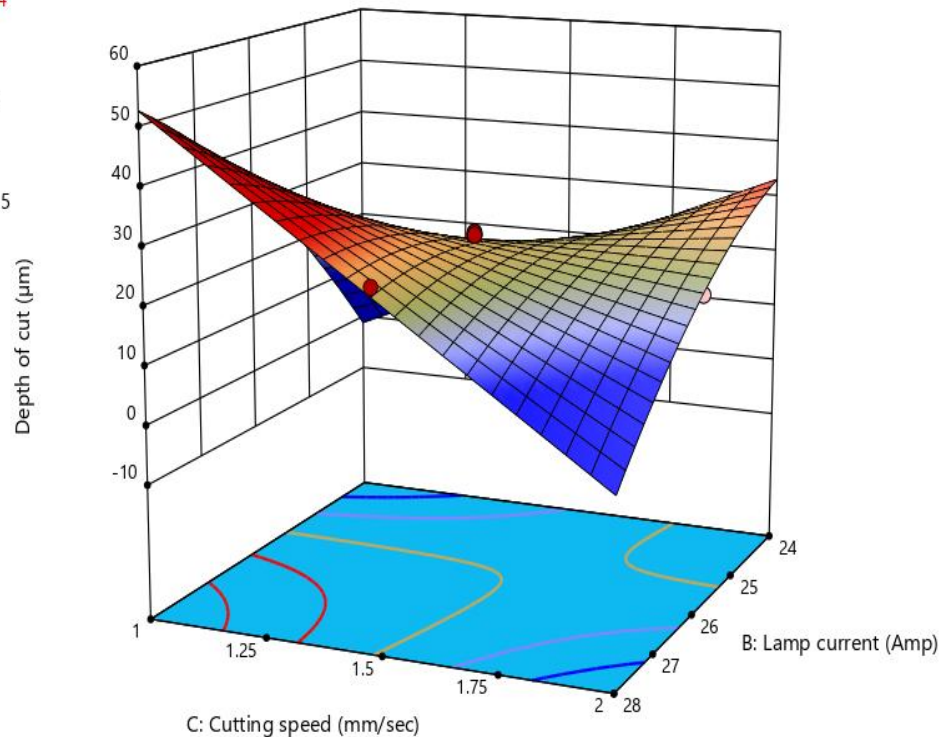


Figure 6.8 Surface plot of depth of cut versus cutting speed and lamp current.

The nature of curve shown in Figure 6.8 demonstrates the combined effects of lamp current and cutting speed on depth of cut when the pulse frequency is kept constant at 35 kHz. The depth of cut gradually increases with decrease in cutting speed at higher value of lamp current. The reason behind this phenomenon is higher rate of material removal due to generation of high thermal energy with high interaction time between workpiece and laser beam. It is the fact that power is a depending factor of energy of laser beam. High thermal energy is derived from high value of power for which the upper surface of work sample on which laser beam is focused gets melted. As a result, it vaporizes immediately and removal of a large volume of material from the top surface during penetration produces a high depth of cut. High cutting speed produces relatively low depth of cut. When the cutting speed is moderate to low, the interaction time of the laser beam with the material increases which results in material removal leading to higher depth of cut. The depth of cut decreases with decrease in lamp current at lower cutting speed, because of low material removal from workpiece due to low thermal energy where cutting speed is insignificant. Again, the depth of cut

gradually decreases with increase in lamp current at higher cutting speed. As the higher lamp current causes higher thermal energy but with higher cutting speed causes low interaction time between laser beam and workpiece, that parametric condition produces low depth of cut.

(ii) Parametric Effects on Kerf Width

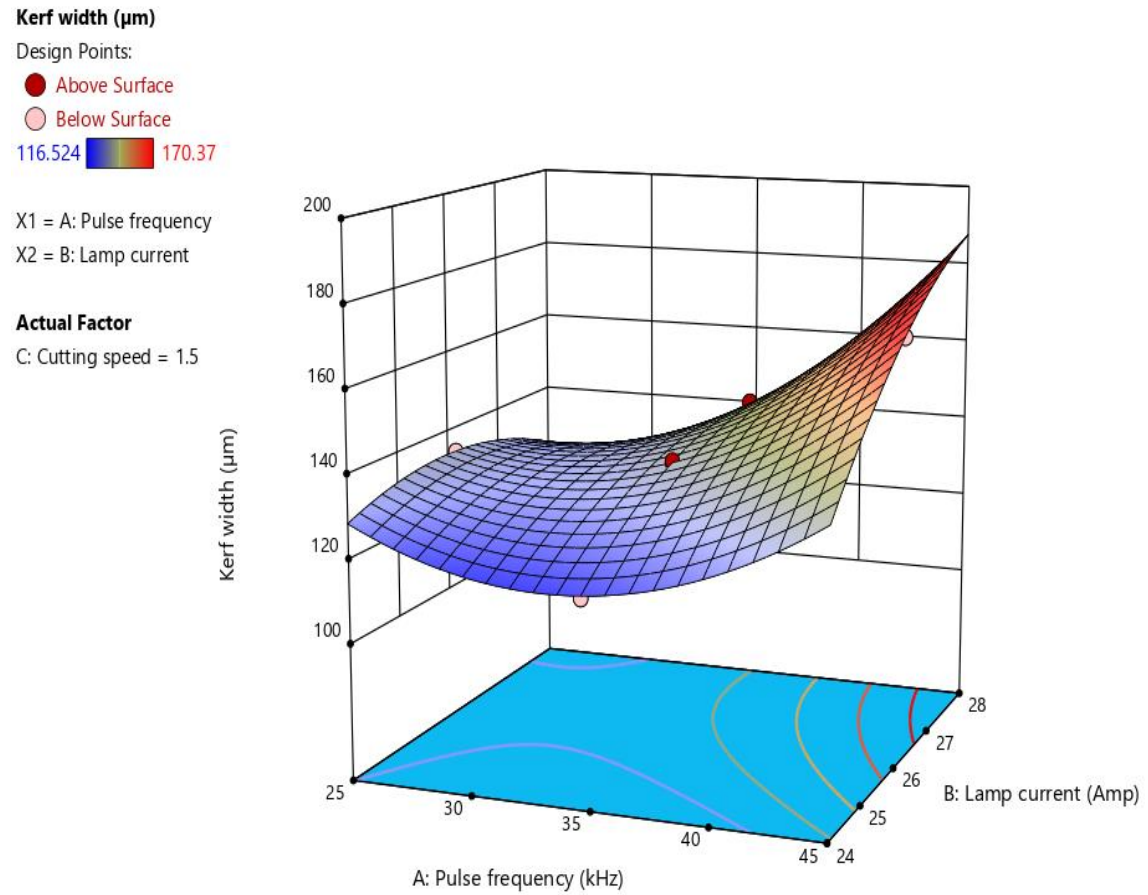


Figure 6.9 Surface plot of kerf width versus pulse frequency and lamp current.

The variation of kerf width with respect to pulse frequency and lamp current at constant cutting speed of 1.5 mm/sec is depicted in Figure 6.9. There is slightly decrement observed in kerf width with increase in lamp current at lower pulse frequency. At this parametric combination, higher temperature arises at the machining surface and generation of heat causes increment of bar formation and high HAZ zone, which may reduce the kerf width a little bit. Kerf width initially decreases over small span of pulse frequency then increases with increase in pulse frequency at entire range of lamp current. Number of pulses per unit time impinge on the surface of the material increases with increase in pulse frequency which in turn increases the kerf width. It is observed that kerf width increases almost linearly with an increase in lamp current at

a mid-to-high range of pulse frequency. An increase in lamp current increases the energy density at the machining zone, which is absorbed by the absorbent material and results in raising the temperature of the backside of PMMA. The material has only been removed from the tiny concentrating spot on the top surface of the work sample at extremely low pulse frequencies because of the delay between two successive incident beams is longer at these frequencies, despite the slightly higher beam intensity. This condition enhances the phase change process and increases the kerf width.

Kerf width (μm)

Design Points:

● Above Surface

○ Below Surface

116.524  170.37

X1 = A: Pulse frequency

X2 = C: Cutting speed

Actual Factor

B: Lamp current = 26

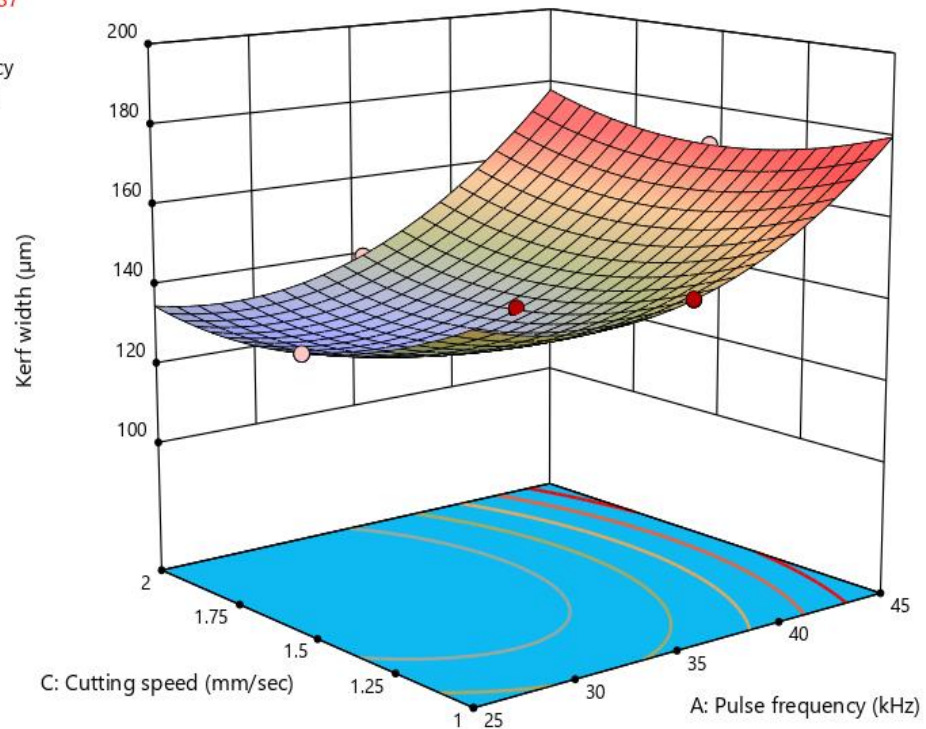


Figure 6.10 Surface plot of kerf width versus pulse frequency and cutting speed.

Figure 6.10 exhibits the combined effects of pulse frequency and cutting speed on kerf width when the lamp current value is held at 26 amps. The kerf width increases with increase in pulse frequency at all values of cutting speeds because of more overlapping of incident laser beams. Higher relative motion between the laser beam and workpiece is denoted by higher cutting speed, leading to less interaction between them and incomplete machining occurs. Due to higher cutting speed the molten debris is not properly removed from the machining zone because of the resolidification of

molten material at the wall or edge of the cutting front which may vary the kerf width; thus, this kind of surface plot is generated. The beam energy remains slightly higher when pulse frequency is very low. Time between two successive incident beams becomes more, as a result of which removal of material takes place only from the confined spot on top surface of the workpiece. So, the kerf width decreases with decrease in pulse frequency at lower cutting speed.

Kerf width (μm)

Design Points:

● Above Surface

○ Below Surface

116.524  170.37

X1 = B: Lamp current

X2 = C: Cutting speed

Actual Factor

A: Pulse frequency = 35

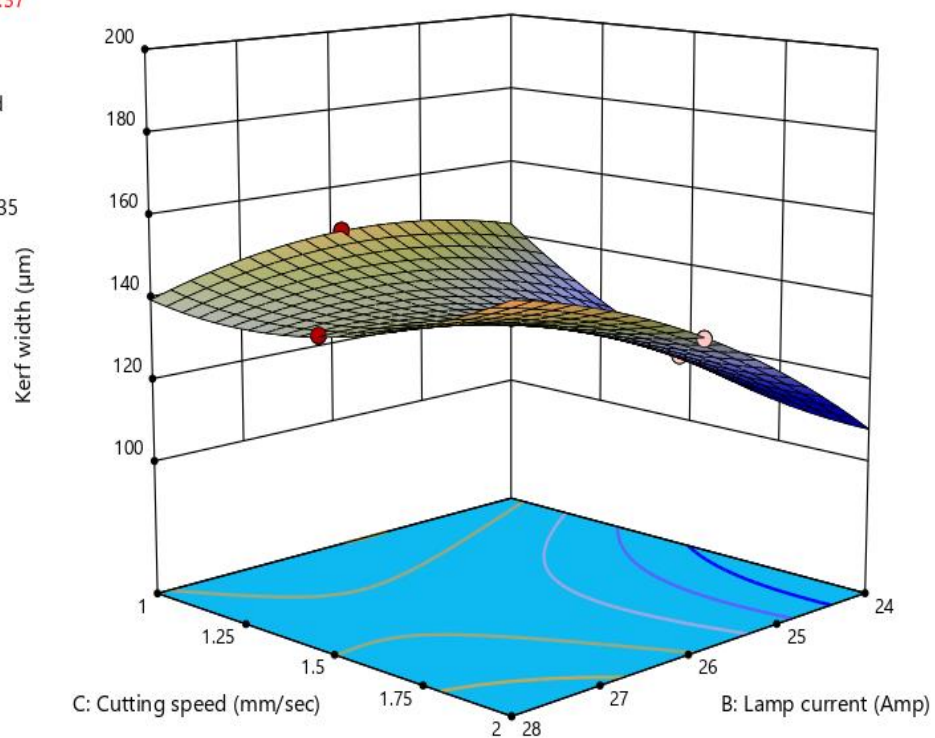


Figure 6.11 Surface plot of kerf width versus cutting speed and lamp current.

Figure 6.11 shows the combined effects of the lamp current and cutting speed on kerf width, keeping pulse frequency constant at 35 kHz. There is an insignificant changes observed in kerf width with decrease in cutting speed at higher lamp current and same is true in case of variation of kerf width with respect to lamp current at lower cutting speed. The kerf width gradually decreases with increase in cutting speed at lower value of lamp current. The kerf width linearly increases with increase in lamp current at higher cutting speed. The energy density at the machining zone is comparatively more at the aforesaid parameter settings which may lead to uniform material removal from the machining zone resulting in formation of even kerf edge. Higher relative

motion between the laser and workpiece is denoted by higher cutting speed, leading to less interaction between them and incomplete machining occurs. Higher lamp current helps to get more powerful energy to melt the top layer of workpiece.

(iii) Parametric Effects on HAZ Width

HAZ width (μm)

Design Points:

● Above Surface

○ Below Surface

105.176  556.983

X1 = A: Pulse frequency

X2 = B: Lamp current

Actual Factor

C: Cutting speed = 1.5

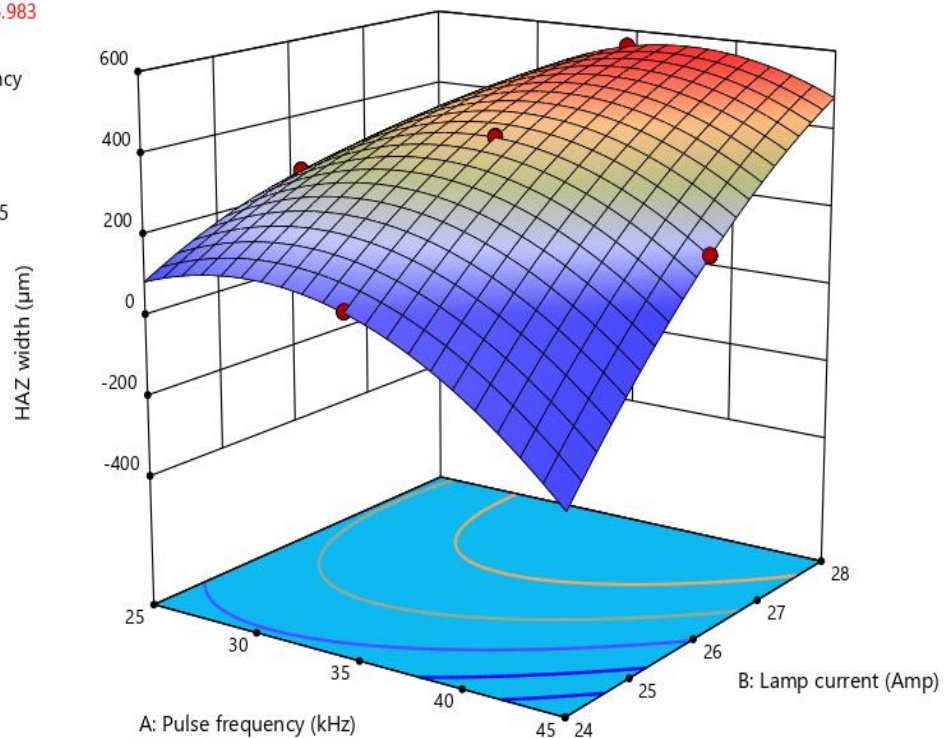


Figure 6.12 Surface plot of HAZ width versus pulse frequency and lamp current.

Figure 6.12 depicts the combined effects of pulse frequency and lamp current on HAZ width when the cutting speed is set to 1.5 mm/sec. The HAZ width increases with decrease in pulse frequency at lower lamp current. At lower lower lamp current, increase in pulse frequency deteriorates the quality of laser and produces less energy density. At higher level of lamp current the amount of thermal energy generated is high in addition, pulse repetition rate increases with increase in pulse frequency resulted a higher heat affected zone (HAZ) with respect to increase in pulse frequency at higher level of lamp current. This may be the reason for decrease in HAZ width with respect to pulse frequency at lower level of lamp current. The HAZ width increases with increase in lamp current at lower pulse frequency. High thermal energy is produced by the high value of lamp current, which results in a high HAZ width.

The laser beam's peak power is higher at low pulse frequencies. Increasing lamp current while maintaining a low frequency causes excessive material removal. As a result, the HAZ width grows with lamp current more quickly.

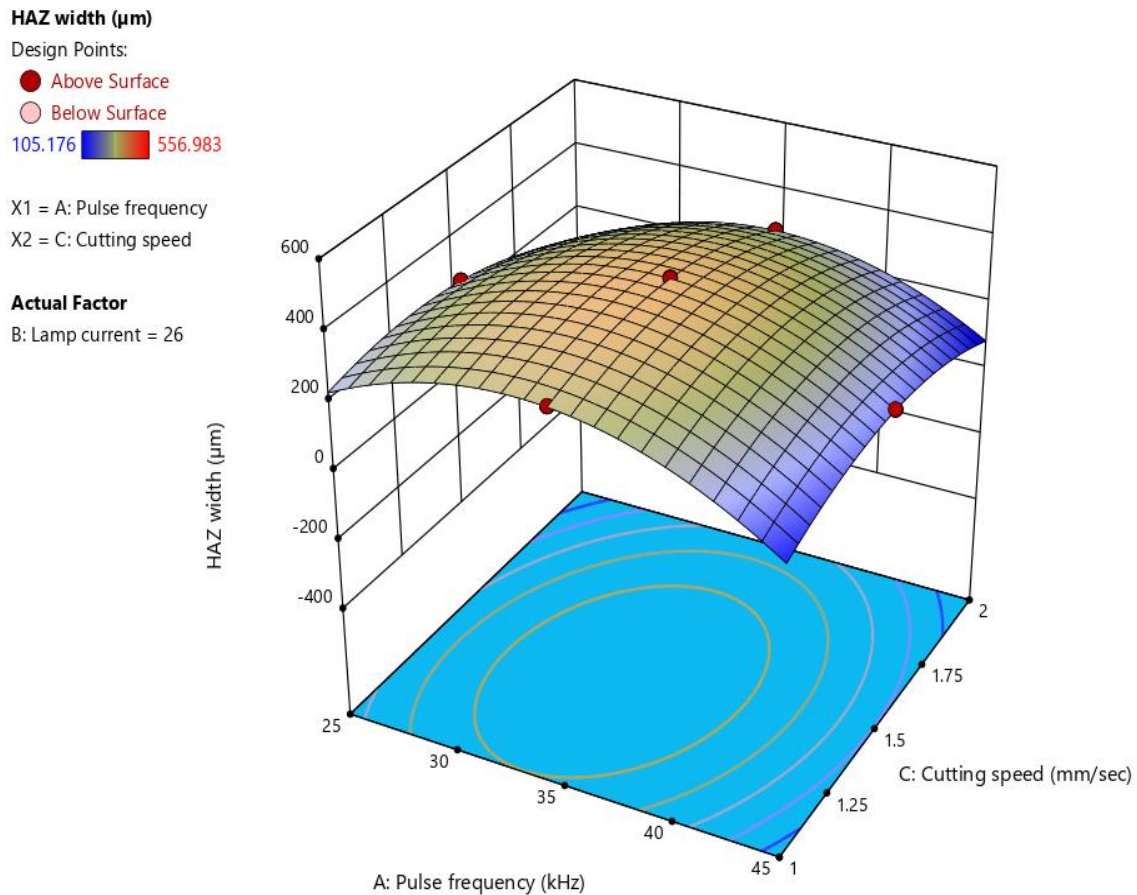


Figure 6.13 Surface plot of HAZ width versus pulse frequency and cutting speed

The surface plot shown in Figure 6.13 demonstrates the combined effects of pulse frequency and cutting speed on HAZ width when the lamp current is held constant at 26 amps. HAZ width initially increases a little bit and then decreases with increase in pulse frequency at lower cutting speed. Higher interaction time at lower cutting speed generates more heat in the machining zone causes the increment in HAZ width. But further increase in pulse frequency produces less energy density which results in reduction of HAZ width. This may be due to higher energy density (as the lamp current is fixed at 26 amp) with higher interaction time, which in turn more heat generation in the machining zone causes the increment in HAZ width. At a moderate level, heat generation causes the maximum HAZ width. HAZ width gradually decreases with increase in cutting speed at all values of pulse frequency. As the higher cutting speed leads to lower interaction time between workpiece and laser beam,

additionally the higher pulse frequency causes lower energy intensity, which may in turn reduce heat generation in the machining zone causes decrement of HAZ width.

HAZ width (μm)

Design Points:

● Above Surface

○ Below Surface

105.176  556.983

X1 = B: Lamp current

X2 = C: Cutting speed

Actual Factor

A: Pulse frequency = 35

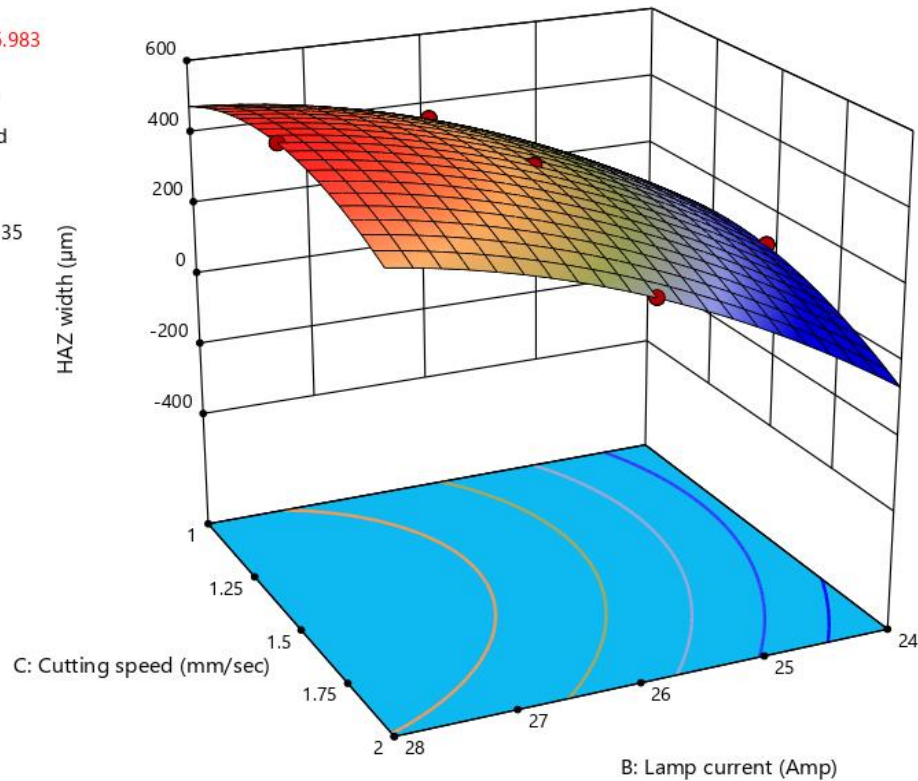


Figure 6.14 Surface plot of HAZ width versus cutting speed and lamp current.

The combined effects of lamp current and cutting speed on HAZ width keeping pulse frequency constant at 35 kHz is shown in Figure 6.14. There is a little bit increment observed in HAZ width with decrease in cutting speed at higher value of lamp current. This phenomenon may be caused by an increase in thermal energy density at the machining zone when lamp current is increased and lower cutting speed causes more interaction time, which in turn increases the heat on the machining zone causes the increment of HAZ width. HAZ width gradually decreases with decrease in lamp current at lower value of cutting speed. Lower lamp current produces low thermal energy at lower cutting speed, where cutting speed has no such impact on the machining zone. The said parametric combination produces lower HAZ width. HAZ width decreases a little bit with increase in cutting speed at lower lamp current. As the low lamp current produces low thermal energy at the machining area as well as higher

cutting speed decreases the interaction time between laser beam and workpiece, due to which HAZ width decreases. The HAZ width linearly increases with increase in lamp current at higher cutting speed. At higher cutting speed i.e., low interaction between laser beam and workpiece, which causes low HAZ width but at the same time the increase in lamp current causes higher thermal energy which may be the reason for increment of HAZ width.

6.3.2.4 Determination of Optimal Process Parameter Using Response Surface Methodology

(i) Single-Objective Optimization Analysis

To obtain the optimum values of different process variables optimization of machining characteristics has been conducted.

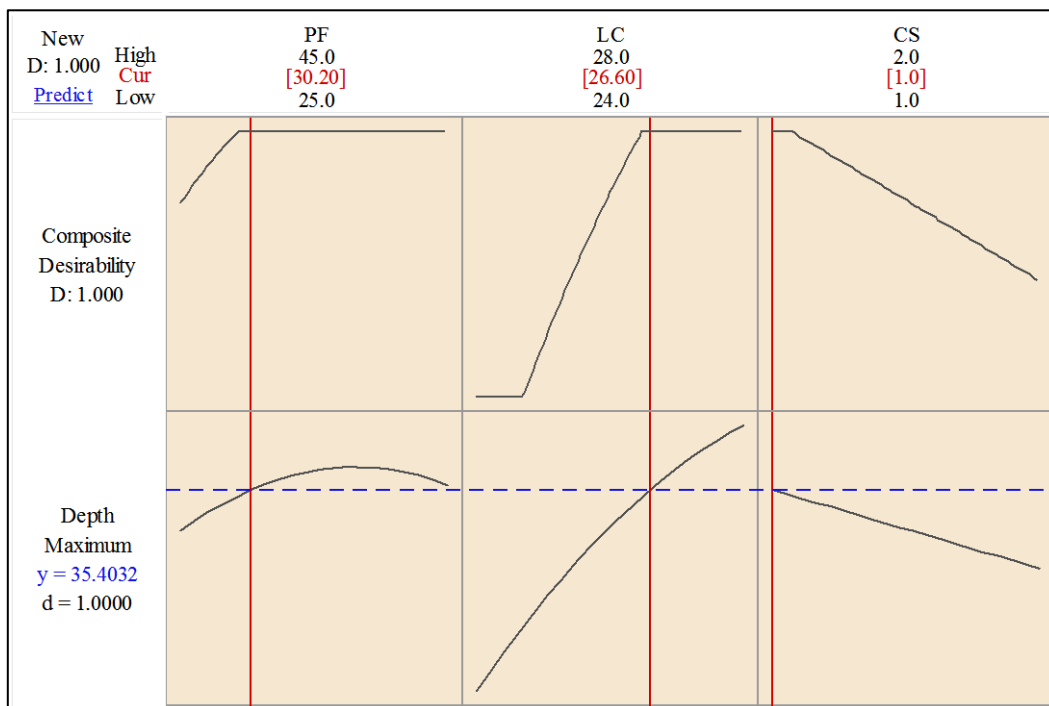


Figure 6.15 Single-objective optimization plot for the depth of cut of the micro-channel.

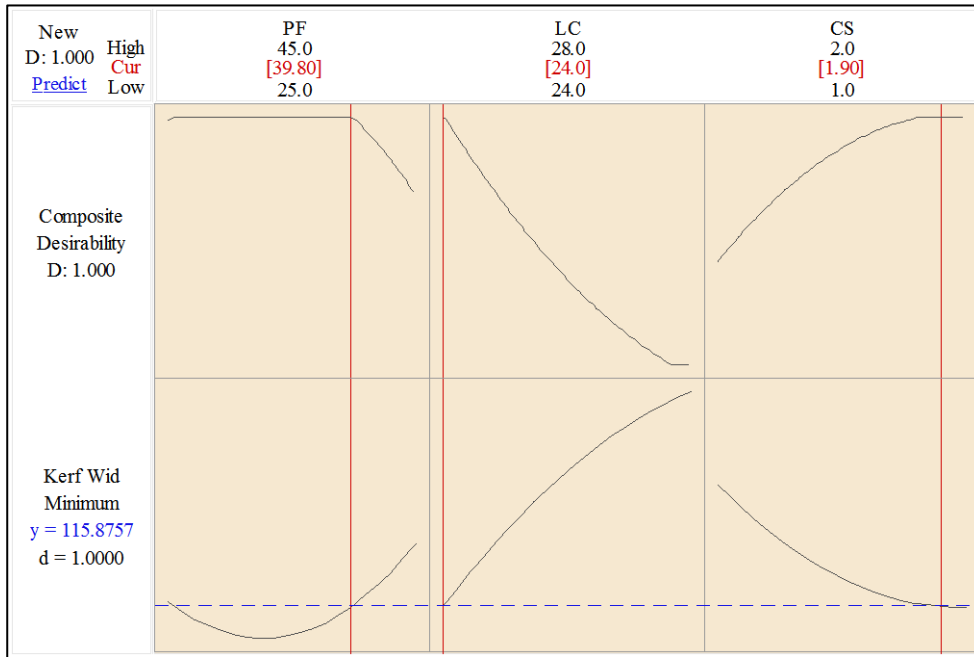


Figure 6.16 Single-objective optimization plot for the kerf width of the micro-channel.

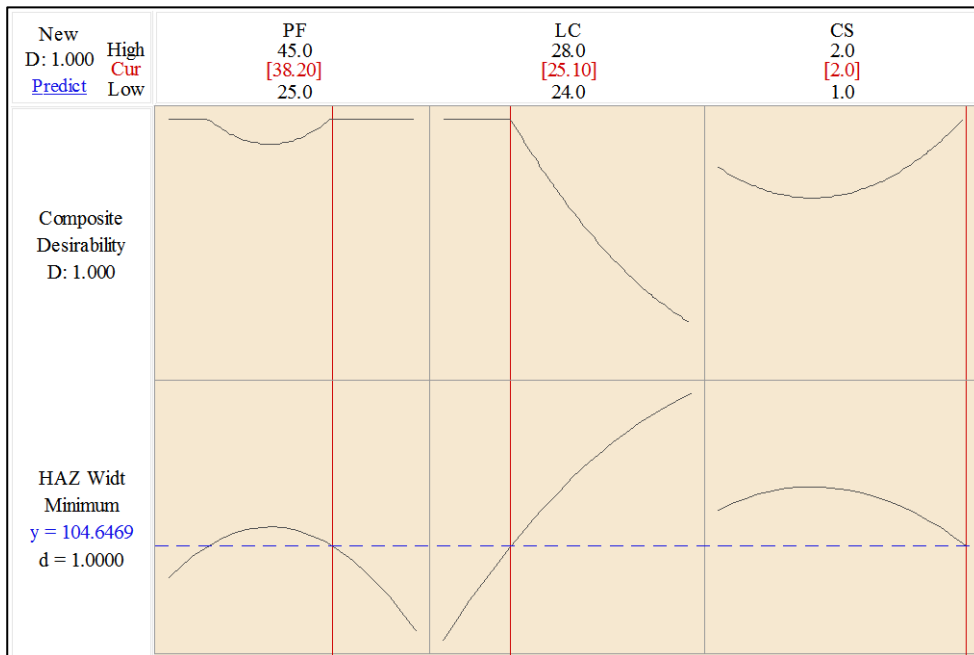


Figure 6.17 Single-objective optimization plot for the HAZ width of the micro-channel.

From Figure 6.15, it is shown that the optimal parametric conditions to obtain maximum depth of cut (35.4032 μm) are pulse frequency of 30.20 kHz, the lamp current of 26.60 amp, and cutting speed of 1 mm/s. From Figure 6.16, it is observed that the minimum kerf width (115.8757 μm) is obtained at pulse frequency of 39.80

kHz, lamp current of 24 amp, and cutting speed of 1.90 mm/s. It is evident from the Figure 6.17, the optimal settings of process variables to get minimum HAZ width (104.6469 μm) are pulse frequency of 38.20 kHz, the lamp current of 25.10 amp, and cutting speed of 2 mm/s.

(ii) Multi-Objective Optimization Analysis

All of the goals are merged into a single desirability function in multi-objective optimization. The multi-objective optimization results are shown in Figure 6.18. All of the responses have been optimized to achieve the best possible result. Each column of the graph in Figure 6.18 represents a factor.

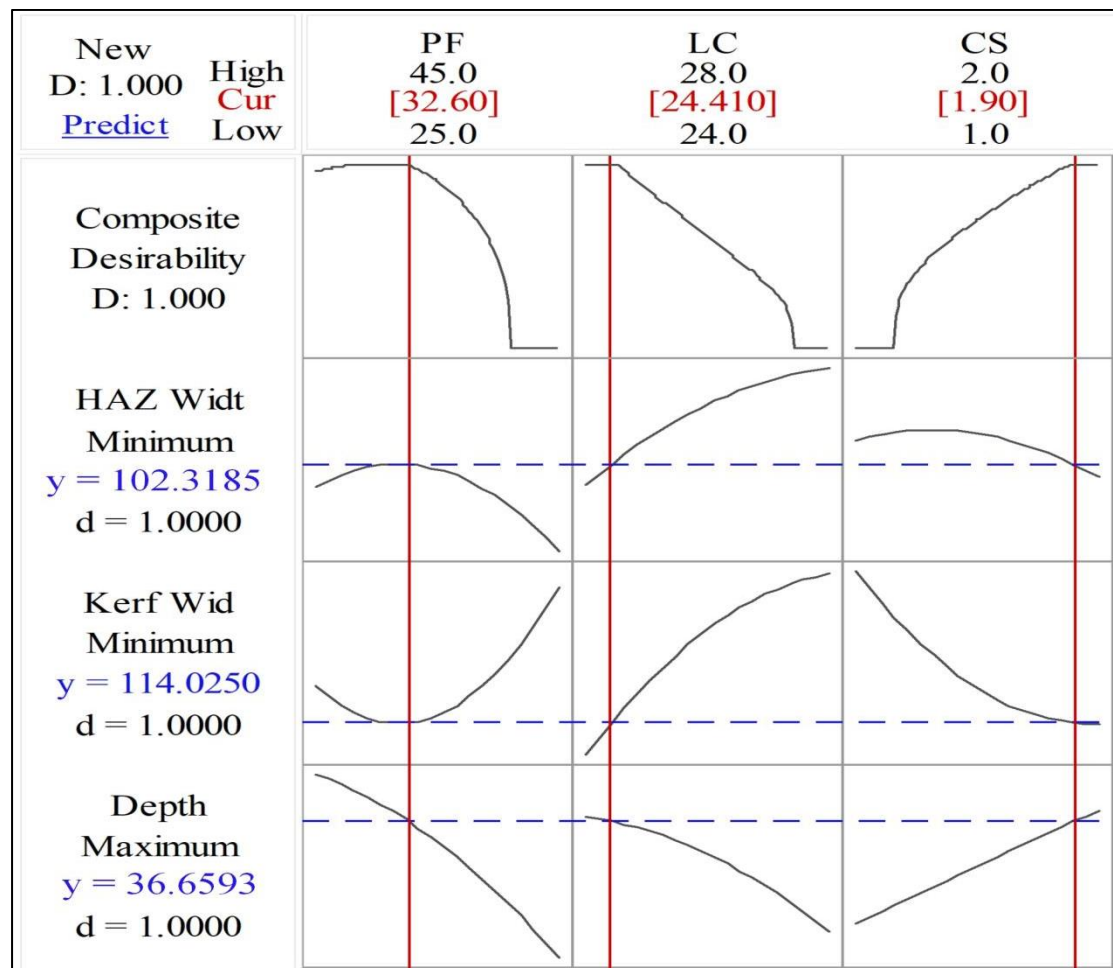


Figure 6.18 Multi-objective optimization plot for the micro-channels.

A response variable is represented by each row of the graph. Each graph cell illustrates the change in one of the response variables as a function of one of the factors, while the other factors remain constant. At the top of the column, the current factor level settings, as well as the high and low values of factors, are presented. To

the left of each row, the response goal, expected response, y , at current factor settings, and individual desirability score are listed. Figure 6.18 shows that the response value of the HAZ width of 102.319 μm , kerf width of 114.0250 μm , and depth of cut of 36.659 μm can be reached with the pulse frequency of 32.60 kHz, lamp current of 24.410 amp, and cutting speed of 1.90 mm/s.

6.3.2.5 Confirmation Test

To validate the results at the optimum condition, 5 additional experiments have been conducted as per the obtained optimum condition and the average is taken. It was observed that the experimental results are fairly close to the predicted results. Average of experimental results are taken into account for confirmation test and given below in Table 6.6 and Figure 6.19 shows the microscopic image and SEM image of the micro-channel.

Table 6.6 Confirmation test of laser micromachining at air medium

Optimal parameter settings	Machining responses	Predicted value at Optimal parametric settings	Experimental value Optimal parametric settings	% of error
PF=32.60 kHz; LC=24.41 amp; CS=1.90 mm/sec	Depth of cut (μm)	36.6593	35.1513	4.11
	Kerf width (μm)	114.0250	111.2612	2.42
	HAZ width (μm)	102.3185	107.2313	4.80

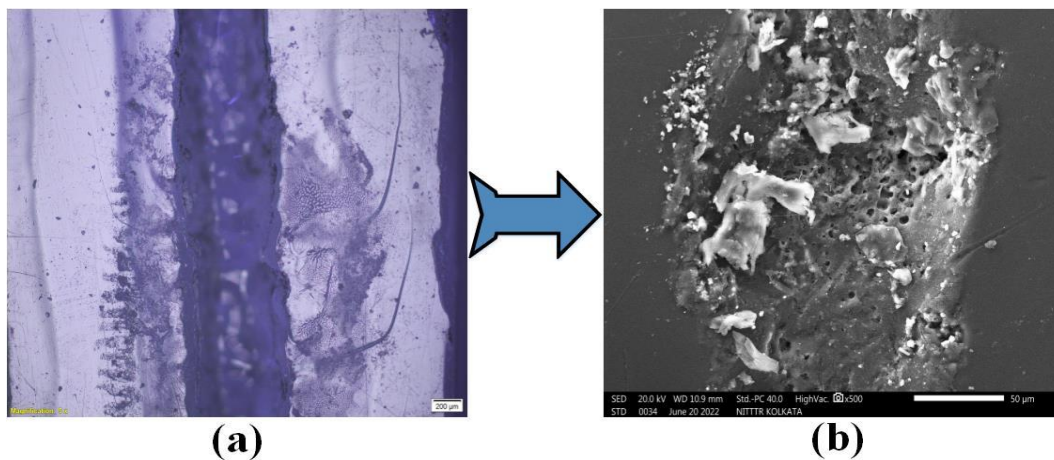


Figure 6.19 (a) Microscopic image of the micro-channel, (b) SEM micrograph

6.3.3 Outcomes

The current study utilized an Nd: YAG laser system to carry out an experimental investigation on polymethyl methacrylate (PMMA) to create micro-channels using the laser transmission technique. Micro-channel operations were conducted in air medium. The coated material that absorbs the energy first, is black tape (absorbent material). During the machining process, the main goals were to increase the depth of cut, decrease the heat affected zone (HAZ), and keep the kerf width remain same. The lamp current, the pulse frequency, and the cutting speed were the process parameters considered during the experiment. The ‘depth of cut’, ‘kerf width’, and ‘HAZ width’ of machined micro-channels were then measured and analyzed. The mathematical correlations between the process parameters that went in and the outcome were obtained using response surface methodology (RSM). The adequacy of the model was tested using analysis of variance (ANOVA). The tests are planned using the three-factor central composite design (CCD) technique of response surface methodology (RSM). From the analysis of variance (ANOVA), it can be concluded that all of the process variables are statistically important. A parametric study has also been done. Optimization has been done to find out the best parameter settings for each process variable to obtain the maximum depth of cut, the smallest kerf width, and the smallest heat-affected zone (HAZ) width.

Also, a multi-objective optimization is done to obtain the best results for depth of cut, kerf width, and HAZ width, which are, 36.6593 μm , 114.0250 μm , and 102.3185 μm respectively. The best settings are for the pulse frequency to be 32.60 kHz, the lamp current to be 24.41 amps, and the cutting speed to be 1.90 mm/sec. At optimal conditions, the error between predicted values and actual test result was found to be very less, within the tolerance limit. This proves that the prediction analysis of Nd:YAG laser transmission micro-channeling of thick PMMA is in good agreement and may be used effectively for research and industrial need.

6.4 Parametric Study Based on Response Surface Methodology for Laser Beam Transmission Micro-channeling of PMMA at Submerged Condition of Water Medium

6.4.1 Experimental Details

Table 6.7 shows the constant and variable process parameter settings, as well as their levels. Pulse frequency, lamp current, and cutting speed are varied between 25 and 45 kHz, 24-28 amp, and 1.00-2.00 mm/sec. During the experimentation, the influence of several additional parameters on responses may be kept constant.

Table 6.7 Process variables and their levels

Process Parameter	Unit	Symbol	Levels				
			-2	-1	0	1	2
Pulse Frequency (PF)	kHz	A	25	30	35	40	45
Lamp Current (LC)	amp	B	24	25	26	27	28
Cutting Speed (CS)	mm/sec	C	1.00	1.25	1.50	1.75	2.00
Constant Factors	Pulse Width = 94%						
	Number of Passes = 1						

6.4.2 Experimental Results and Discussion

Laser transmission cutting operations in partially submerged condition were used to carry out 20 sets of experiments. The experimental results are given in Table 6.8. Images of the PMMA substrate and the micro-channels fabricated by the laser transmission cutting in partially submerged conditions are exhibited in Figure 6.20 and Figure 6.21, respectively.

Table 6.8 Experimental result

Experiment No.	Pulse Frequency (PF: kHz)	Lamp Current (LC: Amp)	Cutting Speed (CS: mm/sec)	Depth of Cut (μm)	Kerf Width (μm)	HAZ Width (μm)
1	-1	-1	-1	70.323	206.526	185.235
2	1	-1	-1	43.227	221.062	111.777
3	-1	1	-1	104.293	202.917	279.923
4	1	1	-1	101.853	237.780	295.179
5	-1	-1	1	105.769	187.079	142.699
6	1	-1	1	46.756	207.276	85.354
7	-1	1	1	69.692	203.867	252.718
8	1	1	1	38.656	243.802	288.389
9	-2	0	0	90.235	204.396	166.436
10	2	0	0	38.669	259.474	128.038
11	0	-2	0	48.772	176.466	68.639
12	0	2	0	87.084	213.701	358.196
13	0	0	-2	102.334	226.925	231.663
14	0	0	2	67.046	212.425	178.157
15	0	0	0	78.514	206.957	265.521
16	0	0	0	89.605	206.086	265.690
17	0	0	0	87.966	206.957	266.674
18	0	0	0	75.364	206.561	263.286
19	0	0	0	84.564	206.878	265.113
20	0	0	0	88.344	207.593	263.286

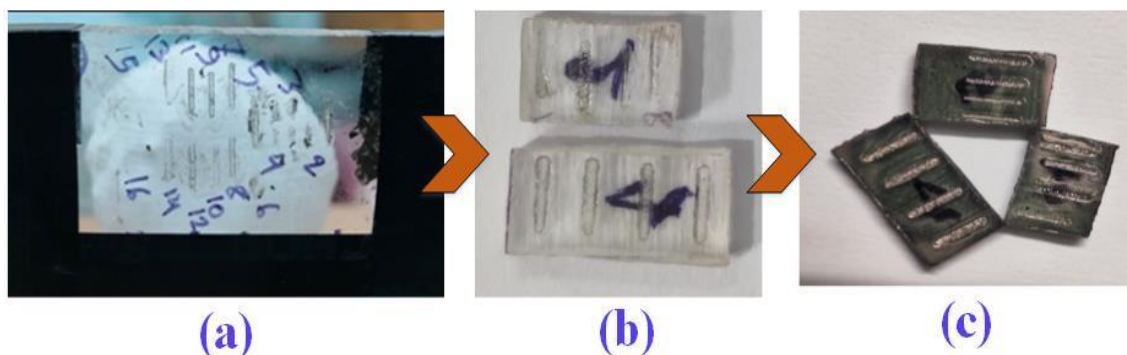


Figure 6.20 PMMA workpiece after Nd:YAG laser transmission cutting in water medium, (a) Parent sample, (b) Sliced micro-machined sample, (c) Gold coated micro-machined sample.

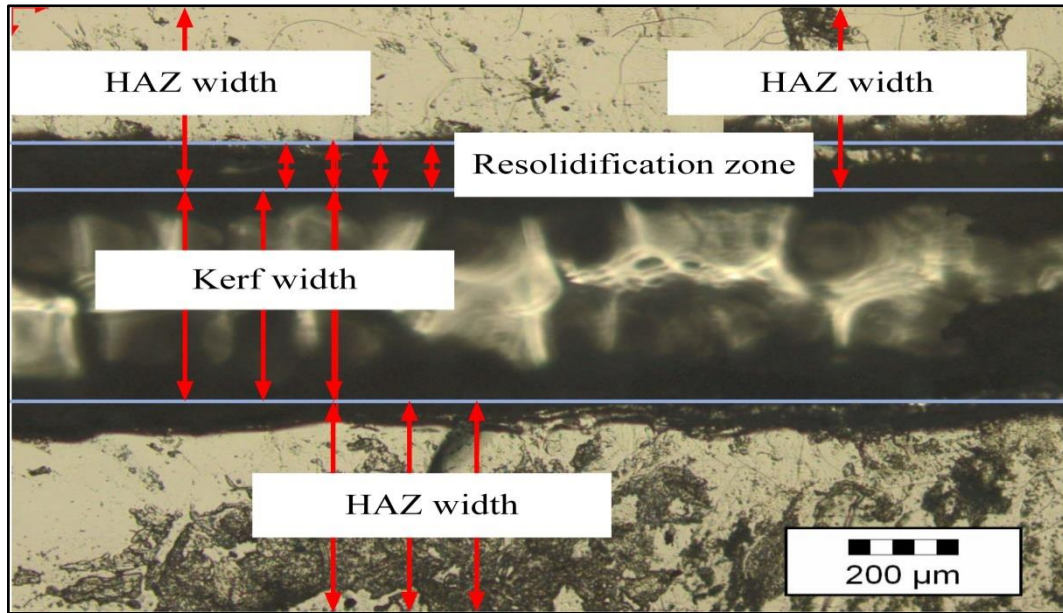


Figure 6.21 Microscopic view of the PMMA micro-channel.

6.4.2.1 Development of Second-Order Polynomial Model

The mathematical relationship between the response and variable process parameters is established using response surface modeling (central composite design). Below are the second-order polynomial equations.

Expression for Depth of cut

$$Y_{\text{Depth of cut}} = 83.57 - 13.92 A + 7.82 B - 8.09 C - 5.15 A^2 - 4.28 B^2 - 0.09 C^2 + 6.58 AB - 7.56 AC - 17.10 BC \quad (\text{Eq}^n.6.4)$$

Expression for Kerf Width

$$Y_{\text{Kerf Width}} = 206.912 + 13.730 A + 8.806 B - 3.454 C + 6.311 A^2 - 2.902 B^2 + 3.246 C^2 + 5.008 AB + 1.342 AC + 5.026 BC \quad (\text{Eq}^n.6.5)$$

Expression for HAZ Width

$$Y_{\text{HAZ Width}} = 264.480 - 9.792 A + 73.141 B - 13.123 C - 29.647 A^2 - 13.102 B^2 - 15.229 C^2 + 22.716 AB + 4.566 AC + 4.370 BC \quad (\text{Eq}^n.6.6)$$

Where 'A' denotes pulse frequency (kHz) 'B' denotes lamp current (amp), and 'C' denotes cutting speed (mm/sec).

6.4.2.2 ANOVA of Machining Responses

Analysis of variance (ANOVA) and subsequent F- and p-value tests were conducted to assess the adequacy of the generated mathematical models for kerf width, depth of cut, and HAZ width. Tables 6.9, 6.10, and 6.11 show the results of an ANOVA analysis of the quadratic model with different adequacy measures like R^2 , adjusted R^2 , and predicted R^2 .

Table 6.9 ANOVA results of depth of cut at submerged condition.

Source	DF	Adj SS	Adj MS	F-Value	P-Value
Model	9	9266.01	1029.56	36.81	0.000
Linear	3	5123.92	1707.97	61.06	0.000
A	1	3100.18	3100.18	110.83	0.000
B	1	977.23	977.23	34.94	0.000
C	1	1046.51	1046.51	37.41	0.000
Square	3	999.73	333.24	11.91	0.001
A ²	1	666.42	666.42	23.83	0.001
B ²	1	460.44	460.44	16.46	0.002
C ²	1	0.20	0.20	0.01	0.935
2-Way Interaction	3	3142.36	1047.45	37.45	0.000
A×B	1	346.28	346.28	12.38	0.006
A×C	1	457.73	457.73	16.36	0.002
B×C	1	2338.36	2338.36	83.60	0.000
Error	10	279.72	27.97		
Lack-of-Fit	5	108.73	21.75	0.64	0.684
Pure Error	5	170.99	34.20		
Total	19	9545.73			
Model Summary		S	R ²	R ² (adj.)	R ² (pred.)
		5.28882	97.07%	94.43%	88.11%

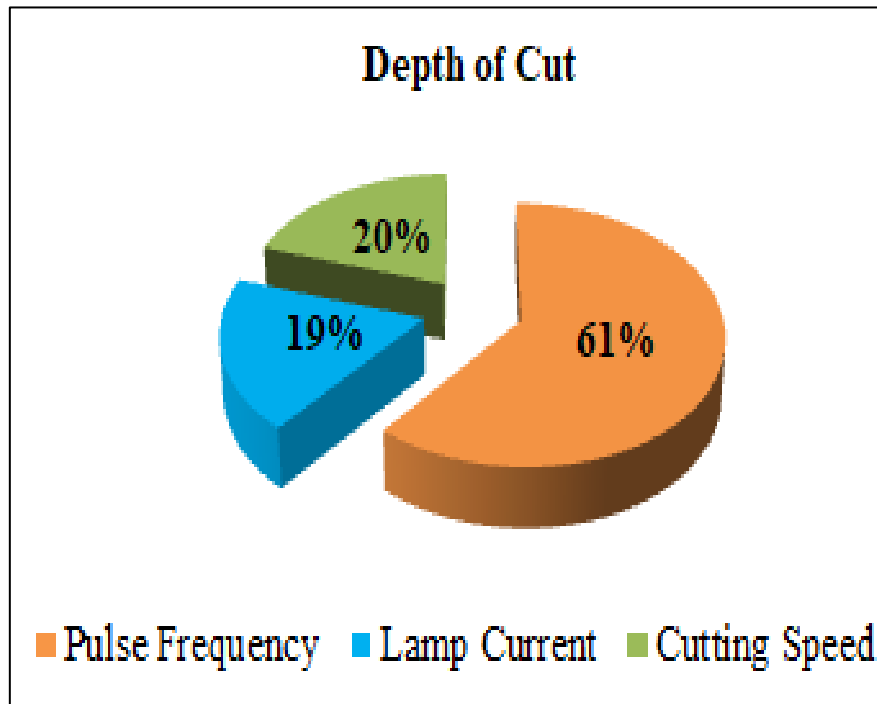


Figure 6.22 Contribution of parameters on depth of cut

Table 6.9 shows that the model's p-value is less than 0.05, indicating that its terms are statistically relevant. Ideal model 's lack-of-fit value implies non-significance. All process inputs and the two-way interaction term influence machining responses. It is exhibited from the Table 6.9, the most important element for depth of cut is pulse frequency (60.50 %), followed by cutting speed (20.42 %), and lamp current (19.08 %). Other adequacy measures R^2 , adjusted R^2 , and predicted R^2 are in reasonable agreement and close to 100%, indicating that the model are adequate. Figure 6.22 is depicted the impact of factors on depth of cut.

Table 6.10 ANOVA results of kerf width at submerged condition.

Source	DF	Adj SS	Adj MS	F-Value	P-Value
Model	9	6533.59	725.95	1109.38	0.000
Linear	3	4447.94	1482.65	2265.73	0.000
A	1	3016.40	3016.40	4609.56	0.000
B	1	1240.68	1240.68	1895.96	0.000
C	1	190.86	190.86	291.67	0.000
Square	3	1668.55	556.18	849.94	0.000
A ²	1	1001.39	1001.39	1530.30	0.000
B ²	1	211.73	211.73	323.56	0.000
C ²	1	264.91	264.91	404.83	0.000
2-Way Interaction	3	417.11	139.04	212.47	0.000
A×B	1	200.65	200.65	306.63	0.000
A×C	1	14.40	14.40	22.01	0.001
B×C	1	202.06	202.06	308.77	0.000
Error	10	6.54	0.65		
Lack-of-Fit	5	5.30	1.06	4.27	0.069
Pure Error	5	1.24	0.25		
Total	19	6540.14			
Model Summary		S	R ²	R ² (adj.)	R ² (pred.)
		0.808937	99.90%	99.81%	99.30%

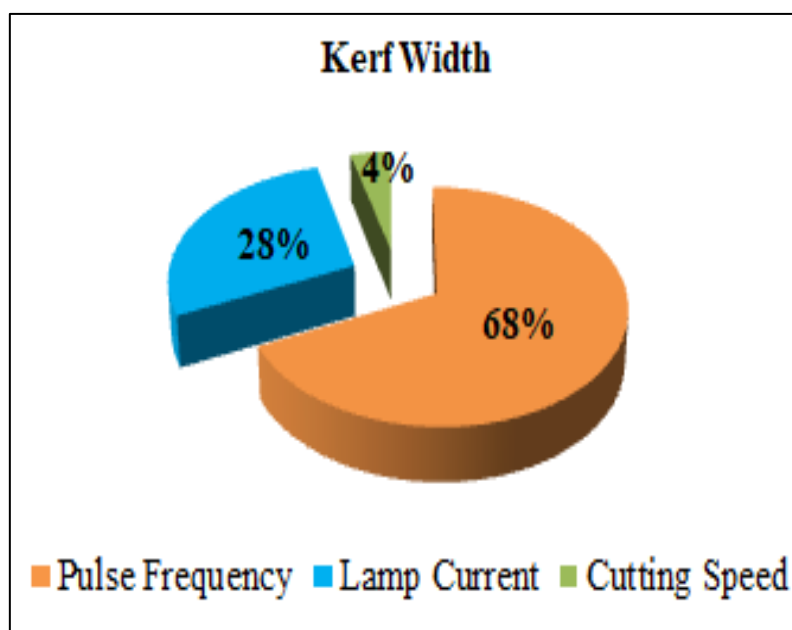


Figure 6.23 Contribution of parameters on kerf width

From the Table 6.10, the model's relevant p-value is less than 0.05 (i.e., $\alpha = 0.05$, or 95 percent confidence level), showing that the model terms are statistically significant. The lack-of-fit value of the model implies non-significance, which is ideal. All of the input process parameters, as well as the two-way interaction term, are relevant and have some effect on machining responses. According to the table, pulse frequency (67.82 %) is the most important component for depth of cut, followed by lamp current (27.89 %), and cutting speed (4.29 %). Other adequacy measures R^2 , adjusted R^2 , and forecast R^2 are in reasonable agreement and close to 100%, indicating that the model are adequate. Figure 6.23 depicts the influence of several parameters on kerf width.

Table 6.11 ANOVA results of HAZ width at submerged condition.

Source	DF	Adj SS	Adj MS	F-Value	P-Value
Model	9	119237	13248.50	2710.42	0.000
Linear	3	89883	29961.20	6129.54	0.000
A	1	1534	1534.10	313.86	0.000
B	1	85594	85594.00	17511.06	0.000
C	1	2755	2755.40	563.70	0.000
Square	3	24906	8301.80	1698.41	0.000
A ²	1	22099	22098.90	4521.06	0.000
B ²	1	4316	4315.90	882.96	0.000
C ²	1	5831	5830.90	1192.90	0.000
2-Way Interaction	3	4448	1482.60	303.32	0.000
A×B	1	4128	4128.20	844.56	0.000
A×C	1	167	166.80	34.12	0.000
B×C	1	153	152.80	31.26	0.000
Error	10	49	4.90		
Lack-of-Fit	5	39	7.90	4.20	0.071
Pure Error	5	9	1.90		
Total	19	119286			
Model Summary		S	R ²	R ² (adj.)	R ² (pred.)
		2.21088	99.96%	99.92%	99.73%

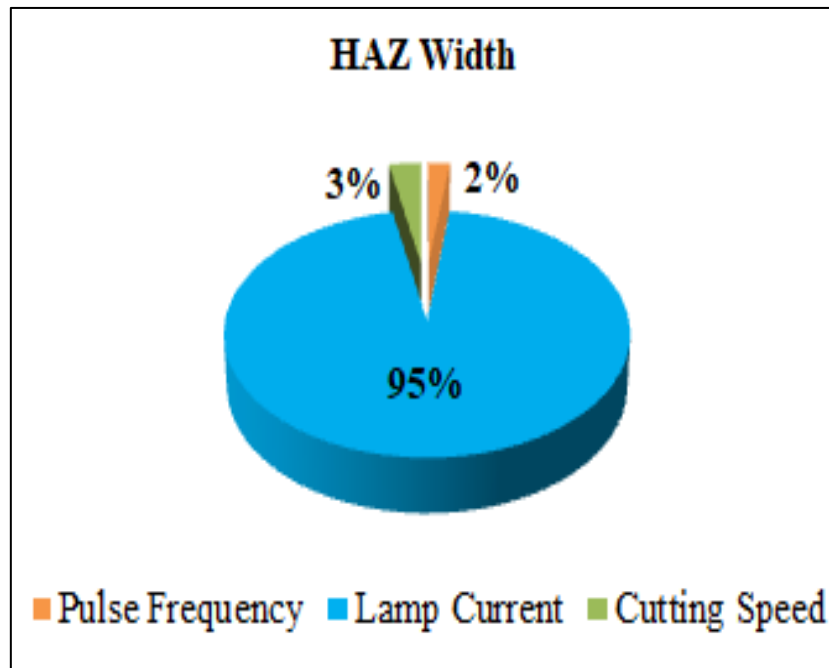


Figure 6.24 Contribution of parameters on HAZ width

As shown in table 6.11, the model's related p-value is less than 0.05 (i.e., $\alpha = 0.05$, or 95 % confidence level), which means that the model terms are statistically significant. The model's lack-of-fit value suggests that it is not significant, which is ideal. All of the input process variables and the two-way interaction term are important and have some impact on the machining responses. The table shows that lamp current (95.23%) is the most important factor for depth of cut, followed by cutting speed (3.06%) and pulse frequency (1.71%). Other measures of the model's adequacy, R^2 , adjusted R^2 , and forecast R^2 , are close to 100% and agree on most things, which shows that the model is appropriate. Figure 6.24 shows that various factors influenced the HAZ width.

6.4.2.3 Parametric Analysis of the Characteristics of Underwater Laser Transmission Micro-channeling of PMMA

(i) Parametric Effects on Depth of Cut

Increment of depth of cut is very challenging task in submerged condition underwater laser transmission micro-channeling operation. In the present study, influence of the laser machining parameters, i.e., lamp current, pulse frequency, pulse width and cutting speed on depth of cut phenomena during laser micro-channeling of 11.328mm thick PMMA workpiece has been analyzed.

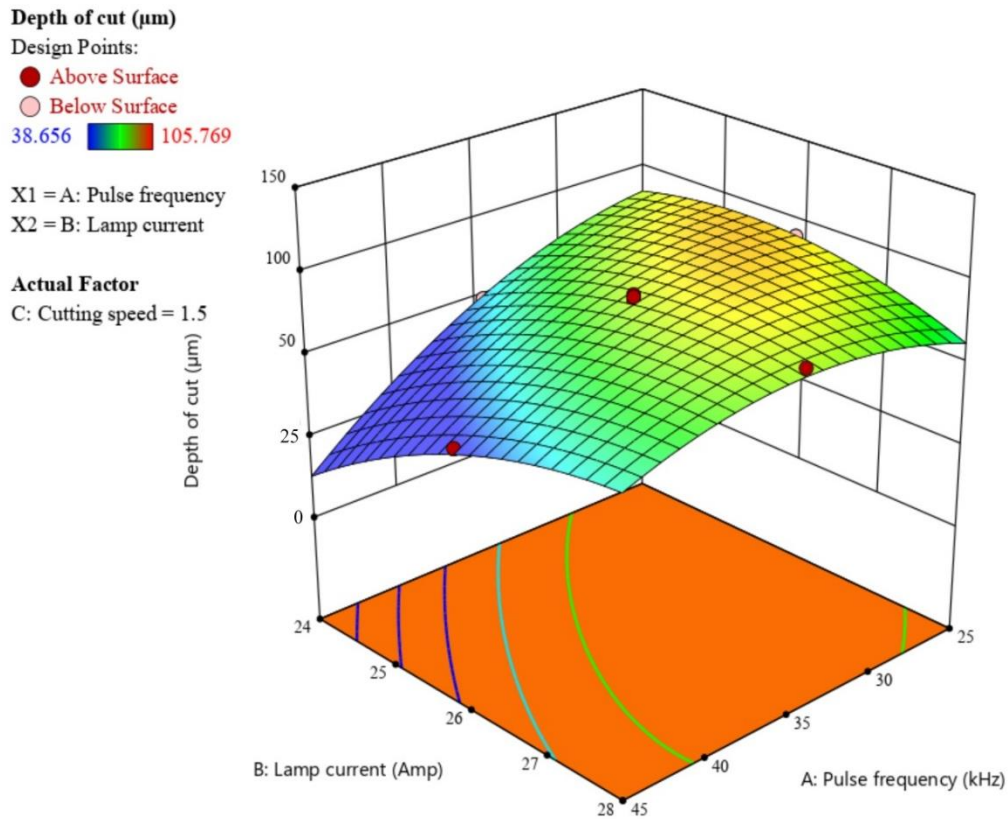


Figure 6.25 Surface plot of depth of cut versus pulse frequency and lamp current.

Figure 6.25 shows the combined effects of lamp current and pulse frequency on the depth of cut when cutting speed is kept constant at 1.5 mm/sec. The graph shows that as lamp current is increased, the depth of cut increases at low pulse frequencies but reduces slightly as pulse frequencies increase. As the lamp current is increased at a low pulse frequency, the thermal energy and quality of the laser beam increase, allowing for a much deeper cut. With additional increases in lamp current, the depth of cut reduces, which may be related to the resolidification of molten material at extremely high energy densities for the same reason and high pulse repetition rate. Conversely, at high levels of pulse frequency, the depth of cut steeply increases with lamp current increases. With increase in pulse frequency, comparatively less energy is generated which cannot interact with workpiece material at moderate value of energy due to loss of energy during contact with water on account of the Beer–Lambert's law on the workpiece surface. This causes less material to be removed from the machining zone, leading to lower cuts, and prevents the laser beam from reaching the ablation threshold limit at the bottom of the cut region. For the same reason, the pulse frequency has a greater impact on the cutting depth across the whole lamp current range.

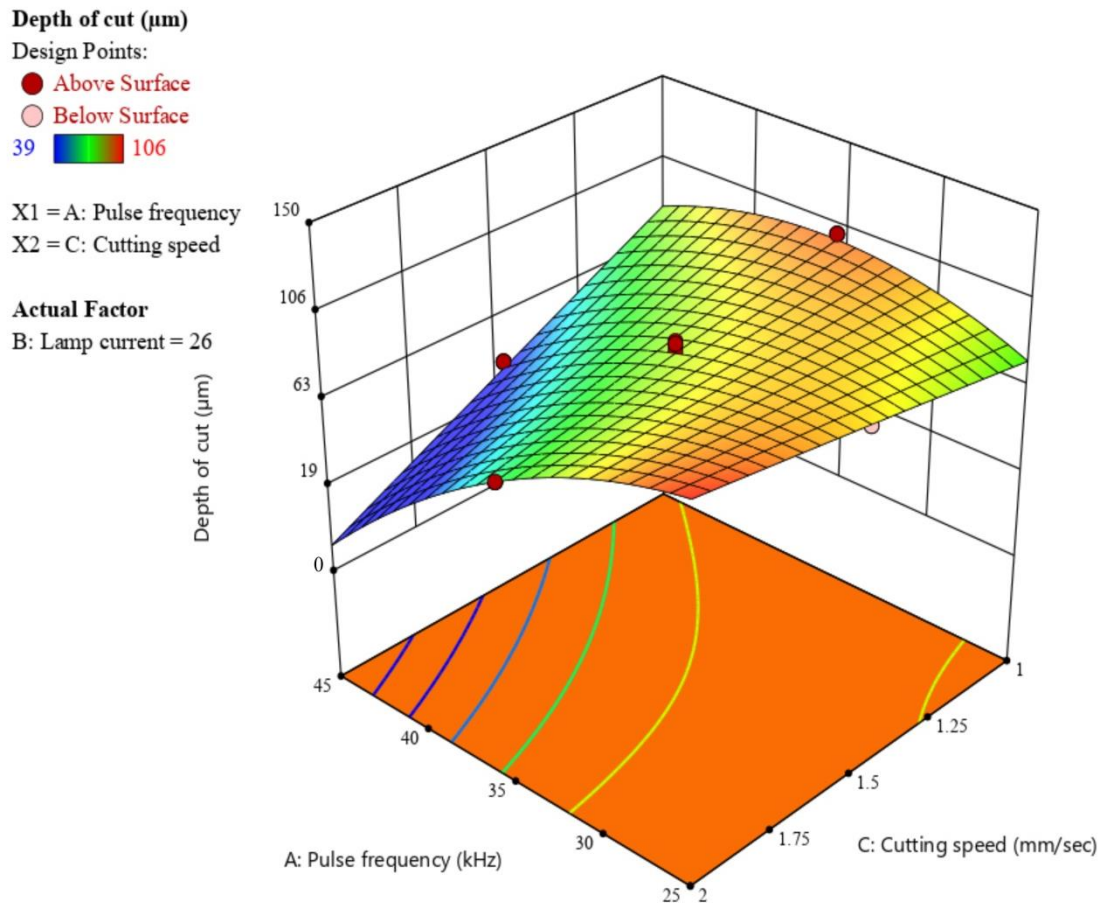


Figure 6.26 Surface Plot of depth of cut versus pulse frequency and cutting speed.

The combined effects of the pulse frequency and cutting speed on the depth of cut when the lamp current is kept constant at 26 amps is shown in Figure 6.26. The figure shows that the highest depth of cut is achieved when the pulse frequency and cutting speed are both low. Spot overlapping is related to the ratio between pulse frequency and cutting speed. Reduced cutting speeds cause a greater amount of laser spot overlap, and reduced pulse frequencies enhance energy density, both of which result in a higher depth of cut. The depth of cut is diminished because of the difficulty in removing the cutting front of molten material as the cutting speed rises. When the laser beam is submerged, the refraction effect causes the diameter of the laser spot to decrease, increasing the shear force along the work surface and decreasing the penetration force along the generation of a water wave. As a result of the focused laser beam and the longest possible contact time between the laser beam and the work substrate at the slowest cutting speed, the energy density at the spot in the submerged condition reaches its maximum at the aforementioned parametric parameters. When

the pulse frequency is raised, the cutting speed also rises, leading to a deeper cut. Uneven machining on the workpiece's surface may have resulted from a bubble bursting in the machining zone. Because of the low quality of the laser beam at high pulse frequency combined with the shorter contact time as cutting speed increases, depth of cut reduces at higher values of pulse frequency.

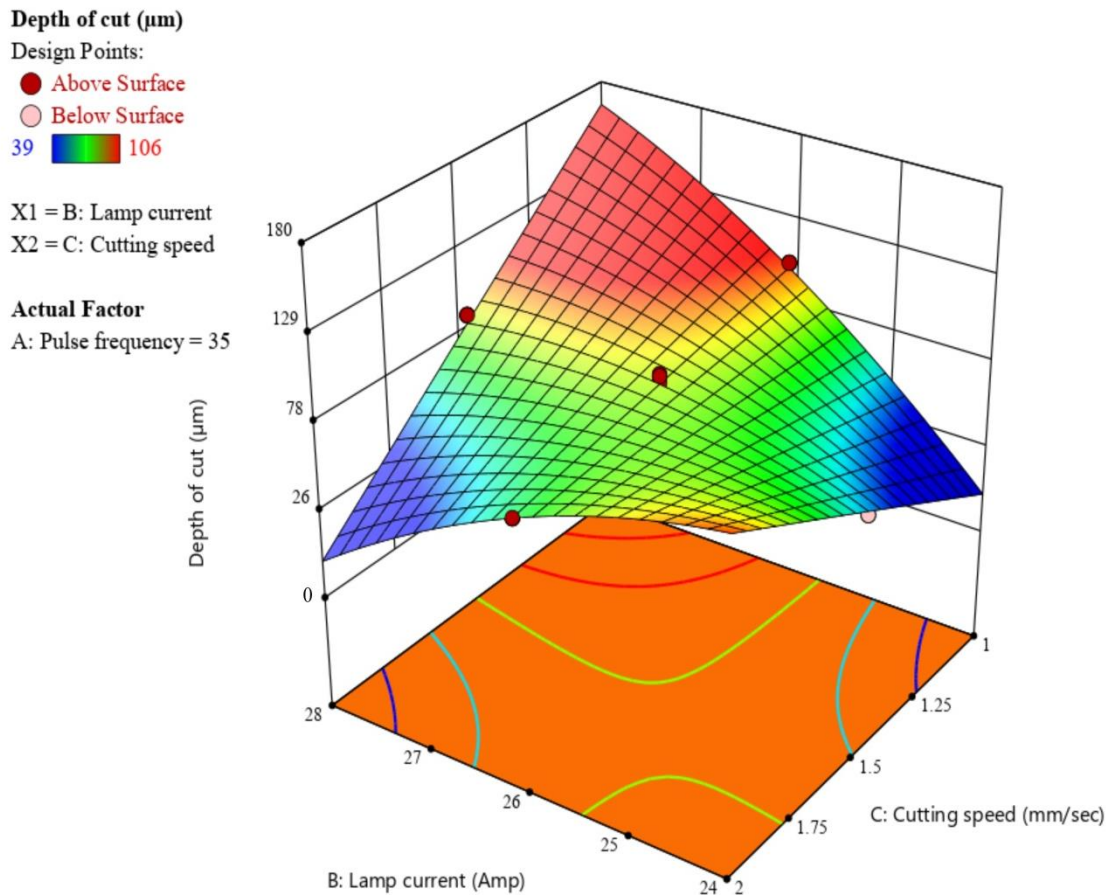


Figure 6.27 Surface plot of depth of cut versus lamp current and cutting speed.

Surface plots shown in Figure 6.27 demonstrates the combined effects of the lamp current and cutting speed on depth of cut when the pulse frequency is kept constant at 35 kHz. It has been noted that cutting depth increases sharply when lamp current increases at slower cutting speeds. The increase in lamp current causes the generated laser beam's average and peak powers to increase at a slower cutting speed, causing a longer interaction time with a higher penetration rate, which results in more material being removed from the surface. The depth of cut therefore increases. Furthermore, it has been observed that, at lower lamp currents, cutting speed has little impact on depth of cut, however at higher energy densities, cutting speed causes depth of cut to decrease. Low lamp current and the laser's power being absorbed by water as a result

of deflection result in a very weak laser beam that would not be able to remove material from the workpiece's surface. When the lamp current is higher, the time required for the laser to engage with the material decreases as the cutting speed increases, and vice versa. This is because less time is spent interacting, which results in less heat being generated in the cutting zone and a lower depth of cut. When cutting at a faster rate, the depth of cut initially rises before falling as lamp current rises. The machining zone may have experienced uneven machining as a result of bubble formation. With increased lamp current at low cutting speed, the depth of cut increases significantly. This may be because slower cutting speeds result in longer laser-material interactions and greater thermal energy production as lamp current increases.

(ii) Parametric Effects on Kerf Width

The quality of kerf width is an important aspect of laser beam micro-channeling operations. A shorter kerf width along with the high depth of channels causes the high aspect ratio (width/depth) micro-channels.

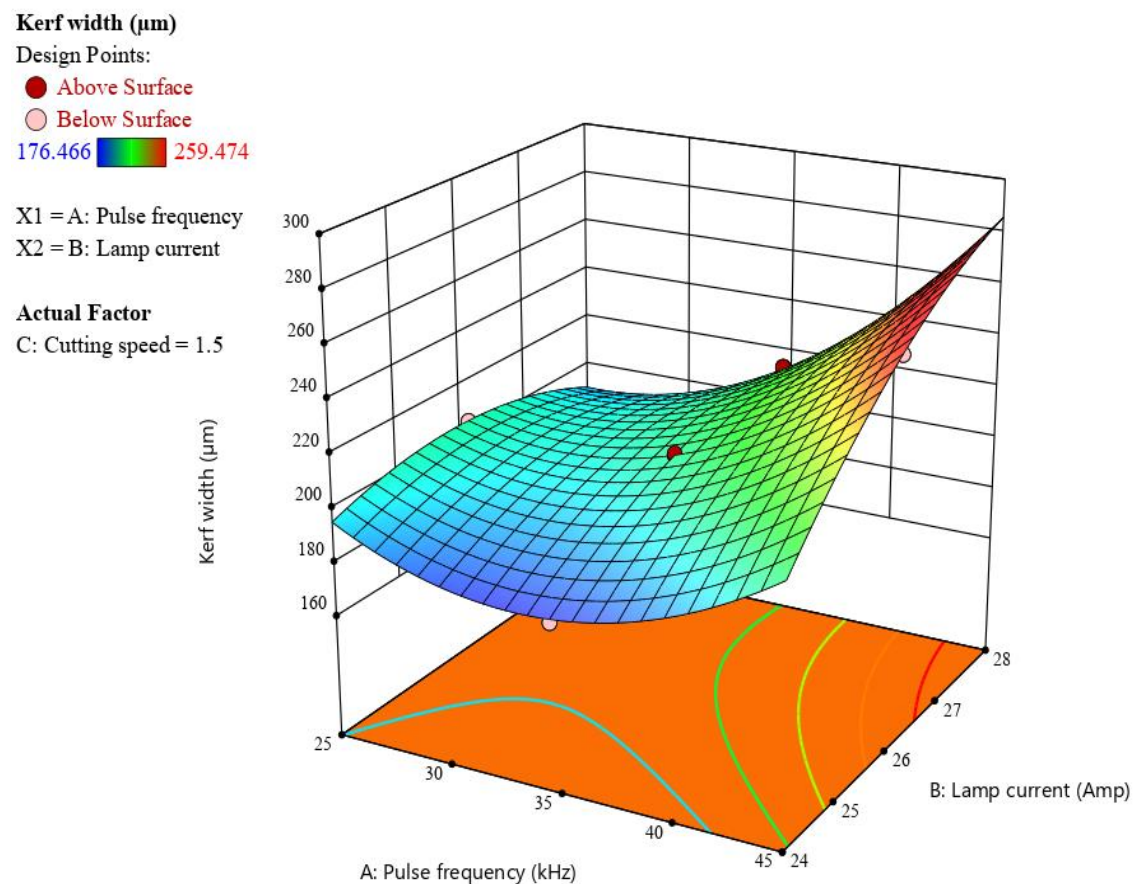


Figure 6.28 Surface plot of kerf width versus pulse frequency and lamp current.

The variation of kerf width with respect to the combined effects of pulse frequency and lamp current on kerf width keeping cutting speed is kept constant at 1.5 mm/sec is shown in Figure 6.28. At entire range of pulse frequency, the kerf width increases as the lamp current increases. This is caused by an increase in energy density in the machining zone that is absorbed by the absorbent material, and this excess energy contributes to raising the temperature of the PMMA's backside. This circumstance quickens the phase change process and increases the kerf width. Similar to this, at all levels of lamp current, kerf width initially reduces and subsequently grows with an increase in pulse frequency. The pulse repetition rate increases with an increase in pulse frequency, but the kerf width decreases due to the resolidification of molten material on the edges of the cut front under submerged conditions. After a certain range, the kerf width increases as the pulse frequency continues to rise, resulting in higher pulse repetition rates, which leads to more material removal from the workpiece's top surface.

Kerf width (μm)

Design Points:

● Above Surface

○ Below Surface

176.466  259.474

X1 = A: Pulse frequency

X2 = C: Cutting speed

Actual Factor

B: Lamp current = 26

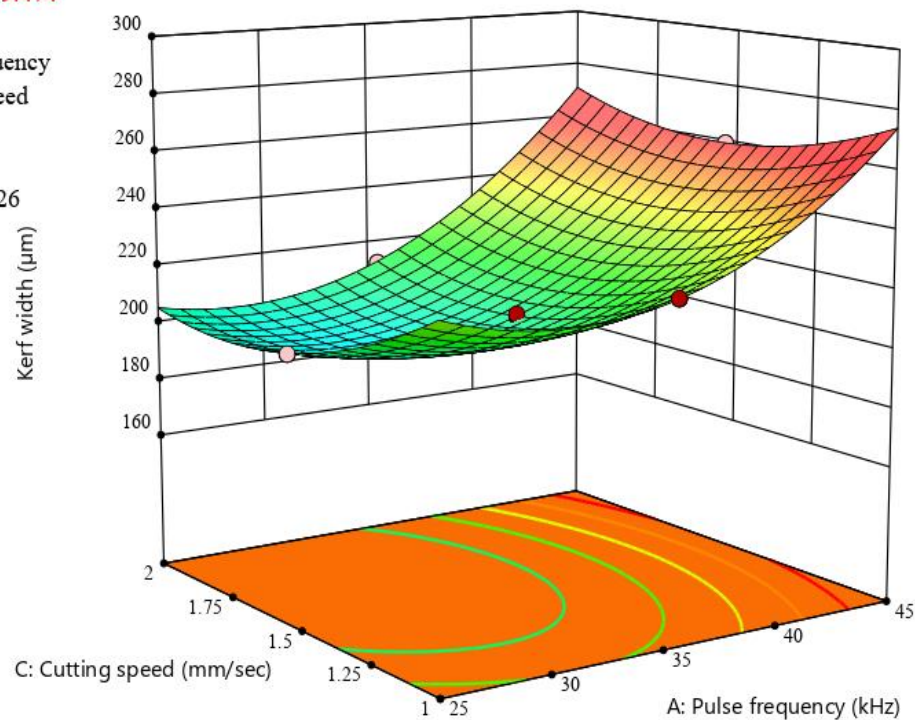


Figure 6.29 Surface Plot of Kerf Width Versus Pulse Frequency and Cutting Speed.

The surface plot as shown in Figure 6.29, exhibits the combined effects of pulse frequency and cutting speed on kerf width at lamp current of 26 amps. Pulse width and number of passes are held constants at 94% and 1 respectively. In slower cutting speeds, it is observed that the kerf width grows steeply with increase in pulse frequency. Since there is more time for the incident laser beam to overlap in the machining zone at a slower cutting speed, the kerf width increases. When cutting at lower pulse frequencies, the kerf width reduces as cutting speeds increase because not enough heat is being transferred to the work substrate. When the cutting speed and pulse frequency are both increased, a wider kerf width is produced. Since the lower pulse frequency produces a higher energy density at the point of irradiation, which aids in the formation of more melt pools. Increasing the cutting speed may not be enough to remove all of the molten debris from the machining zone, which can result in a wider kerf width at some points along the laser's path of travel.

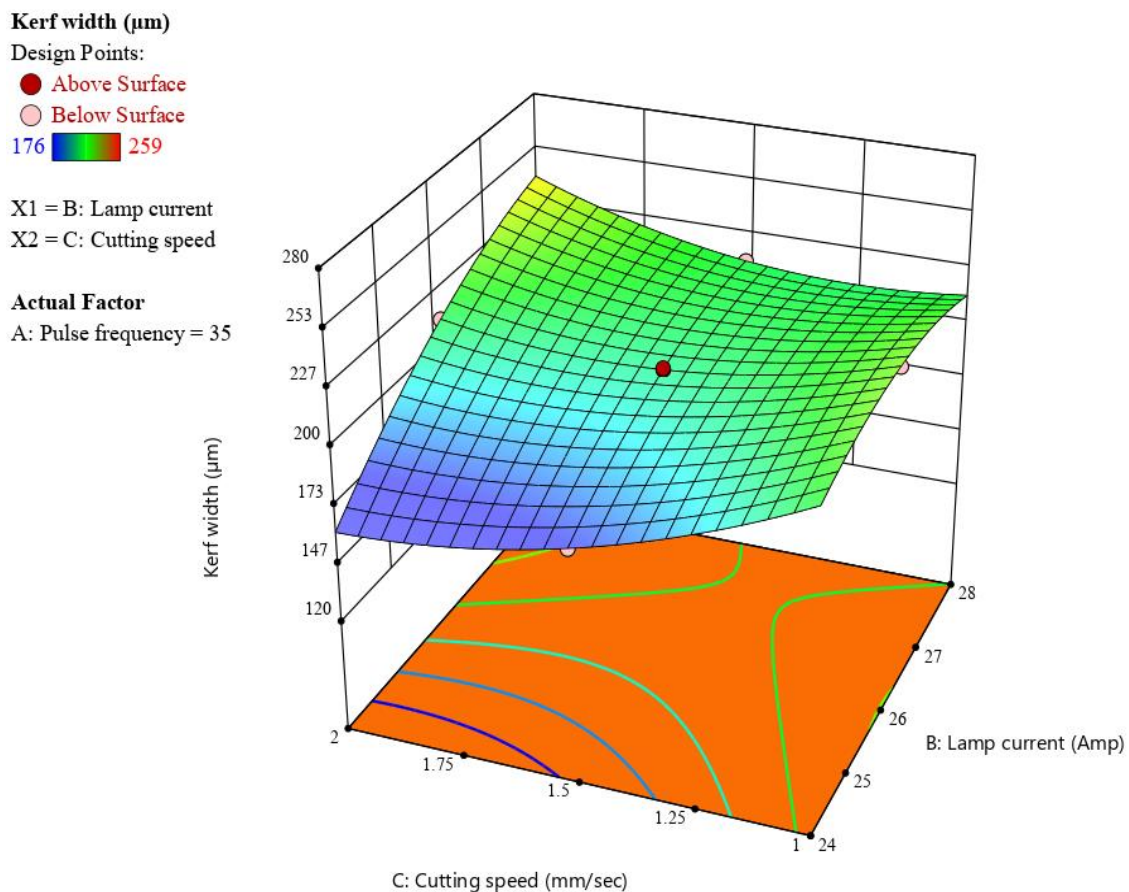


Figure 6.30 Surface plot of kerf width versus lamp current and cutting speed.

Figure 6.30 shows the nature of variation of kerf width with respect to lamp current and cutting speed when the pulse frequency and pulse width are kept constant at 35 kHz and 94%, respectively. In the figure, as lamp current increases across the entire range of cutting speed, the kerf width initially rises and then reduces. Increases in lamp current result in higher energy densities, which in turn raise kerf width at first, but too much of a boost in lamp current leads to spattering and resolidification of the molten material, which in turn reduces the kerf width. The kerf width variation is insignificant across the whole lamp current range. Higher cutting speeds have little impact on kerf width because they reduce the amount of heat energy transferred to the work substrate's reverse side during the cutting process.

(iii) Parametric Effects on HAZ Width

Figure 6.31 shows the combined effects of pulse frequency and lamp current on HAZ width keeping the cutting speed constant at 1.5 mm/sec. The surface plot clearly shows that the HAZ width reduces as the pulse frequency rises at lower lamp current. Due to the longer settling times of the debris removed from the cut zone, the laser beam's thermal energy is scattered and absorbed more widely during underwater laser beam machining, which results in a narrower HAZ width. At higher lamp currents, HAZ width grows as pulse frequency increases as well. High energy density at high lamp current and high repetition rate of incident laser beam with increase in pulse frequency generates very high amount of thermal energy on the surface of the workpiece, which causes the HAZ width to grow. However, at very high pulse frequencies, the laser beam quality degrades because of lower peak power and produces narrower HAZ width. At lower frequencies, HAZ width goes up at first, then goes down after a certain range as working power goes up. Whereas in a submerged condition, when the refractive index varies linearly, less heat is applied to the workpiece's top surface. Because of this, the HAZ width may be reduced when submerged in water. Moreover, an increase in lamp current causes the HAZ width to increase at higher pulse frequencies. Due to the high lamp current and high thermal energy output, a large HAZ width is produced.

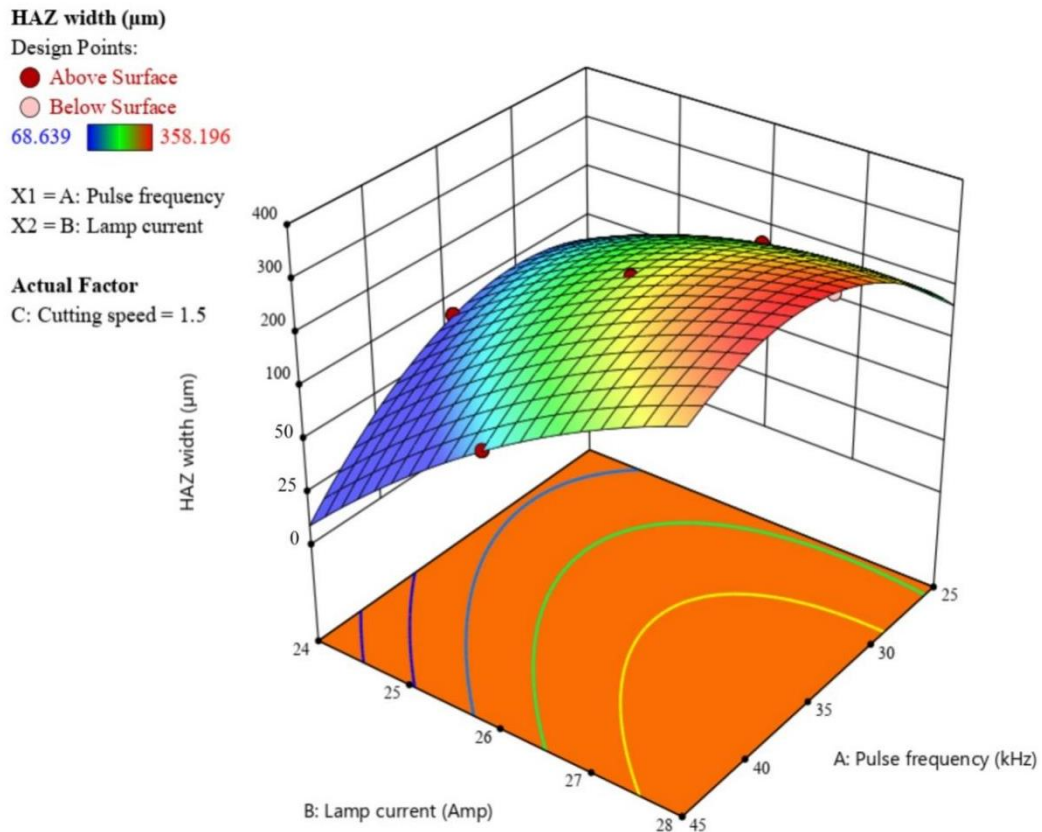


Figure 6.31 Surface plot of HAZ width versus pulse frequency and lamp current.

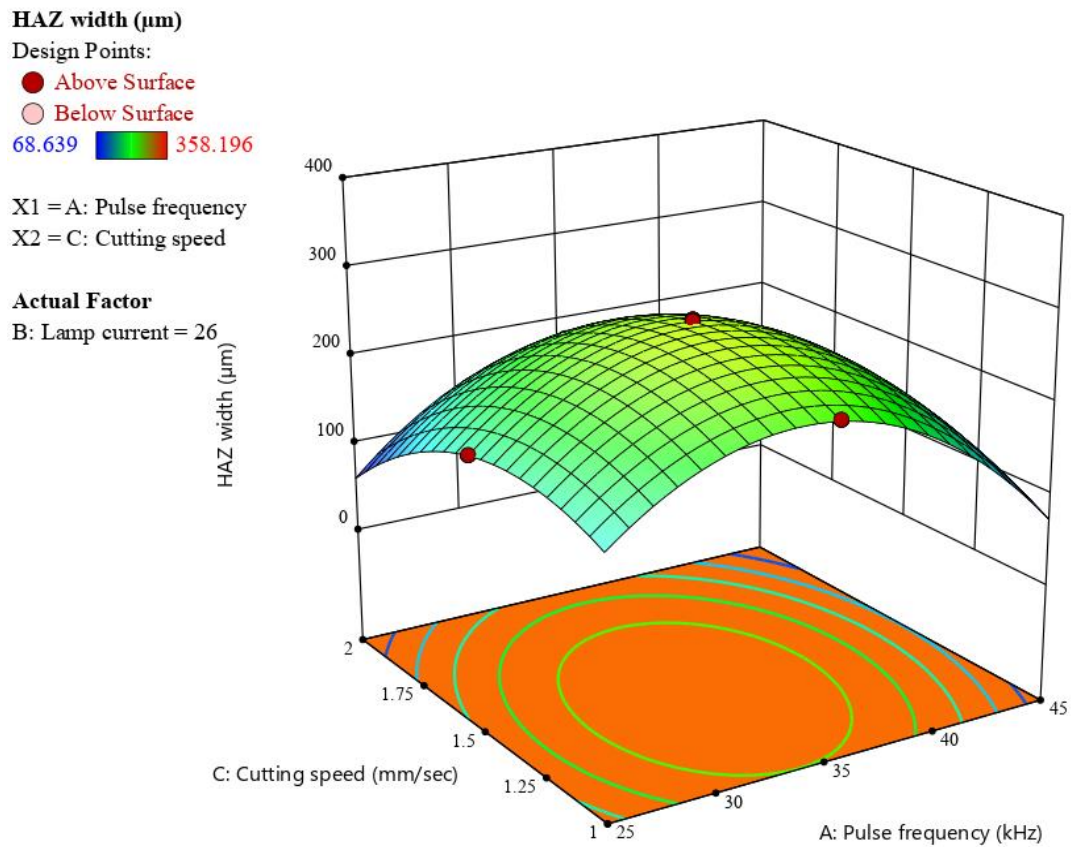


Figure 6.32 Surface plot of HAZ width versus pulse frequency and cutting speed.

The combined effects of pulse frequency and cutting speed on HAZ width is shown in Figure 6.32, keeping lamp current constant at 26 amps. The HAZ width increases at low pulse frequencies and subsequently decreases as the pulse frequency increases; this trend is true across the whole range of cutting speeds. When the pulse repetition rate is increased, more heat is generated in the machining zone, leading to an increase in the HAZ width during the initial stages of the process. However, the HAZ width is decreased by the water effect and further increases in pulse frequency. As cutting speed is increased, the HAZ width is found to decrease gradually; further increases in cutting speed result in lower HAZ width for all values of pulse frequencies after a certain range. Increased heat generation in the machining zone may occur due to the 26 amps lamp current setting and the combination of higher peak power at lower pulse frequency. With this parameter settings, increased cutting force with increase in cutting speed enhances spatter formation and subsequently increases the HAZ width. However, as cutting speed increases, the amount of time a laser spends interacting with its material decreases. Simultaneously, the water medium results in less energy being used and less heat being created, which could minimize the thermal effect in the machining zone and reduce the HAZ.

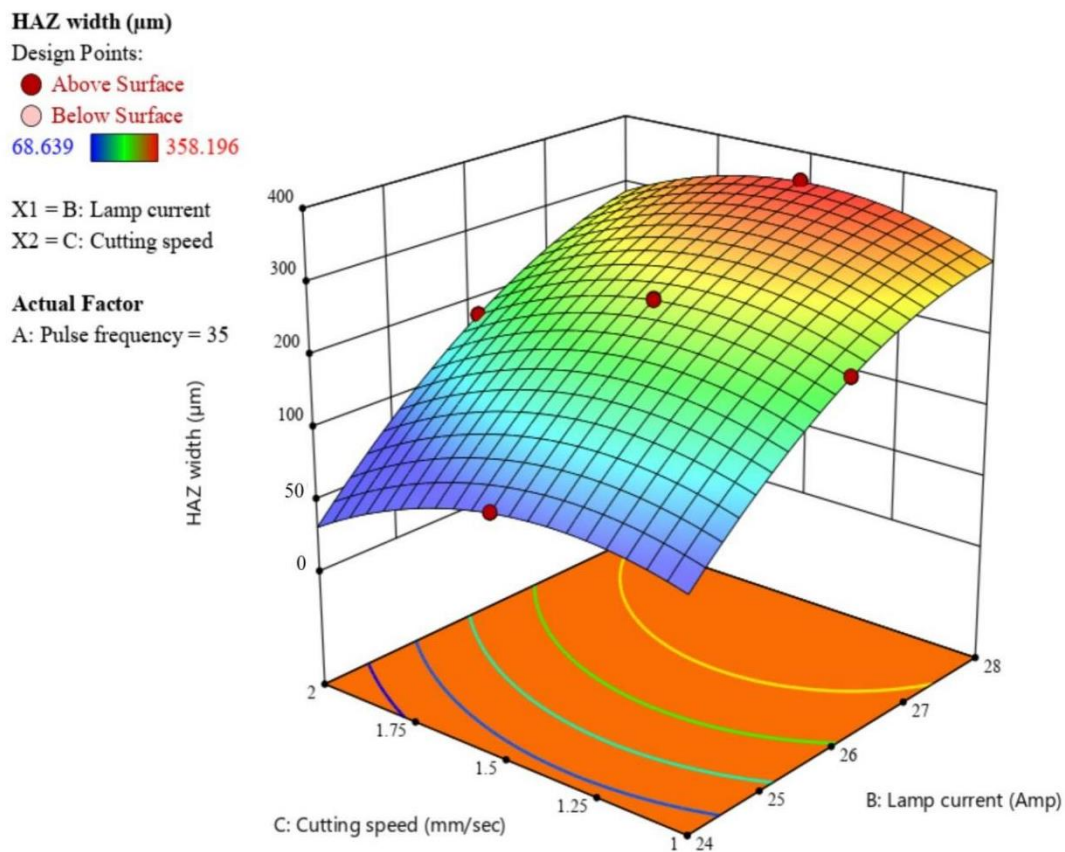


Figure 6.33 Surface plot of HAZ width versus lamp current and cutting speed.

The variation of HAZ width with respect to the combined effects of lamp current and cutting speed is shown in Figure 6.33. It observed from the figure that the HAZ width grows significantly as lamp current increases across the whole range of cutting speeds. This might be because as lamp current increases, the machining zone experiences an increase in thermal energy, resulting in a wider HAZ. In contrast, the HAZ width reduces as cutting speed increases at lower lamp current. A decrease in operating power results in less thermal energy being produced, whereas an increase in scanning speed reduces contact time and reduces the HAZ width. Increased power settings result in excessive material removal. When cutting at a higher lamp current, it is found that the HAZ width first increases slightly with increased cutting speed, but it thereafter gradually reduces with higher cutting speed. In reality, higher scanning speeds let heat to spread through the workpiece sample over a longer period of time, minimizing cut surface damage in terms of HAZ width.

6.4.2.4 Determination of Optimal Process Parameter Using Response Surface Methodology

(I) Single-Objective Optimization Analysis

Optimization of machining characteristics has been conducted to find out the optimum values of different process variables.

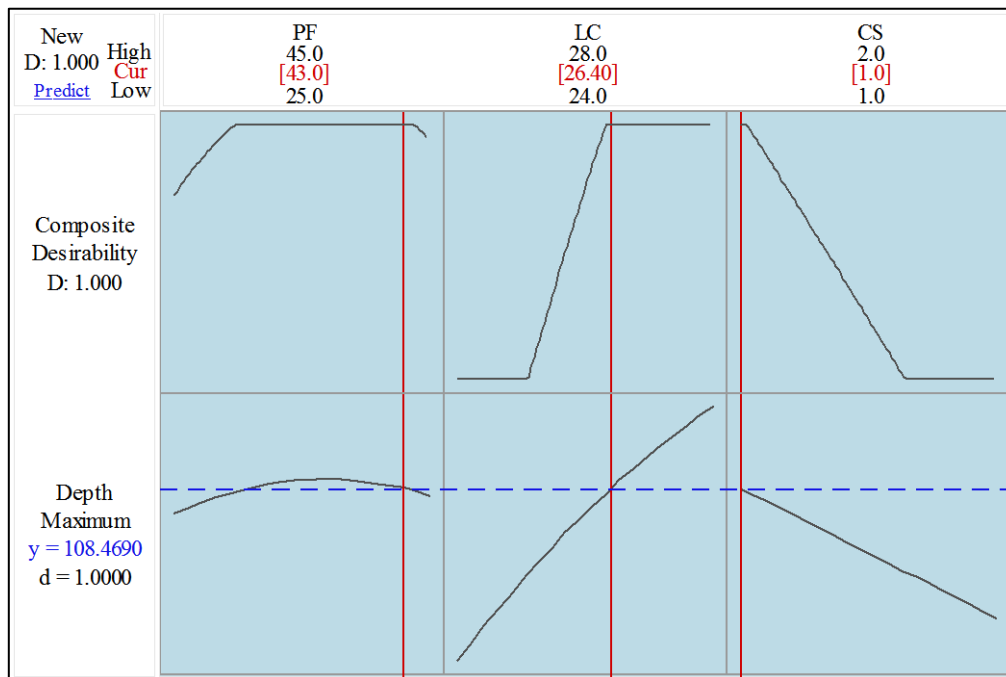


Figure 6.34 Single-objective optimization plot for the depth of cut of the micro-channel.

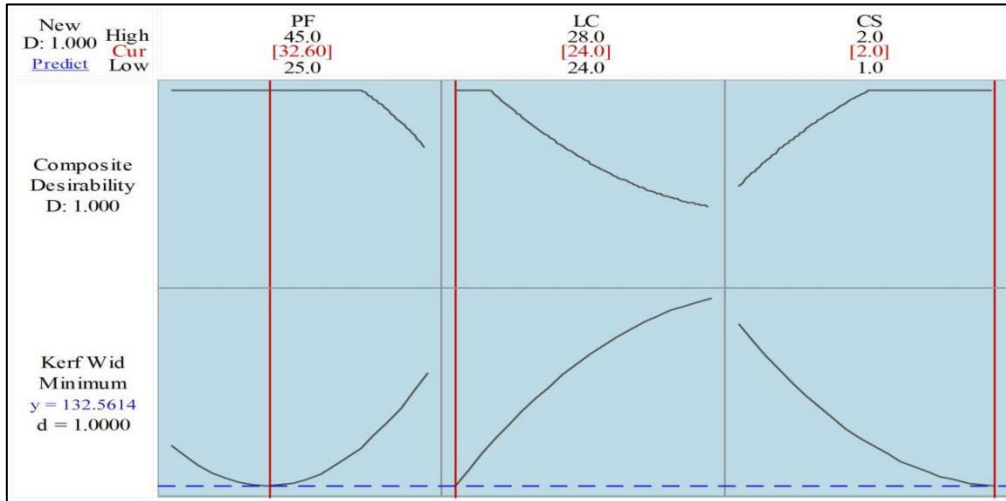


Figure 6.35 Single-objective optimization plot for the kerf width of the micro-channel.

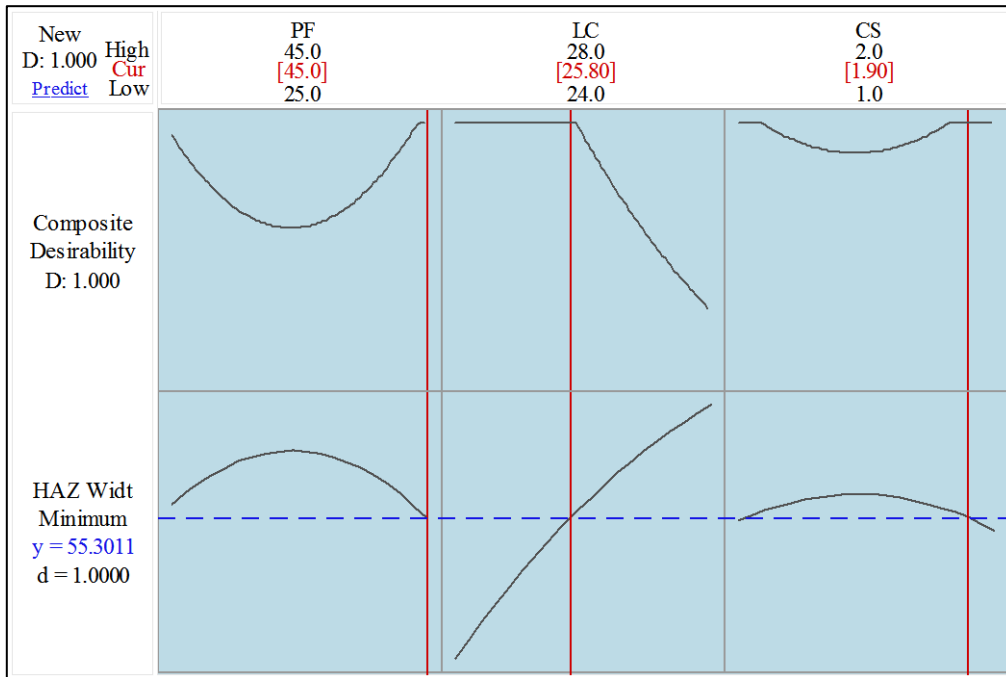


Figure 6.36 Single-objective optimization plot for the HAZ width of the micro-channel.

From Figure 6.34, it is shown that the optimal parameters to achieve maximum depth of cut (91.8020 μm) are lamp current of 26.60 amp, the pulse frequency of 35 kHz, the pulse width of 98.00%, and cutting speed of 1 mm/s. From Figure 6.35, shows that the optimal conditions obtained are lamp current of 25 amp, the pulse frequency of 25 kHz, the pulse width of 96.00%, and cutting speed of 2 mm/s to achieve minimum kerf width (57.5017 μm). Figure 6.36 exhibits the optimal settings of process

variables for minimum HAZ width (53.3851 μ m) which are lamp current of 25 amp, the pulse frequency of 30 kHz, the pulse width of 92.00% and cutting speed of 2 mm/s.

(ii) Multi-Objective Optimization Analysis

The goals of individual responses are merged into a single desirability function for multi-objective optimization. Figure 6.37 shows the multi-objective optimization results of the considered responses together. Each column of the graph in Figure 6.37 corresponds to a process variable.

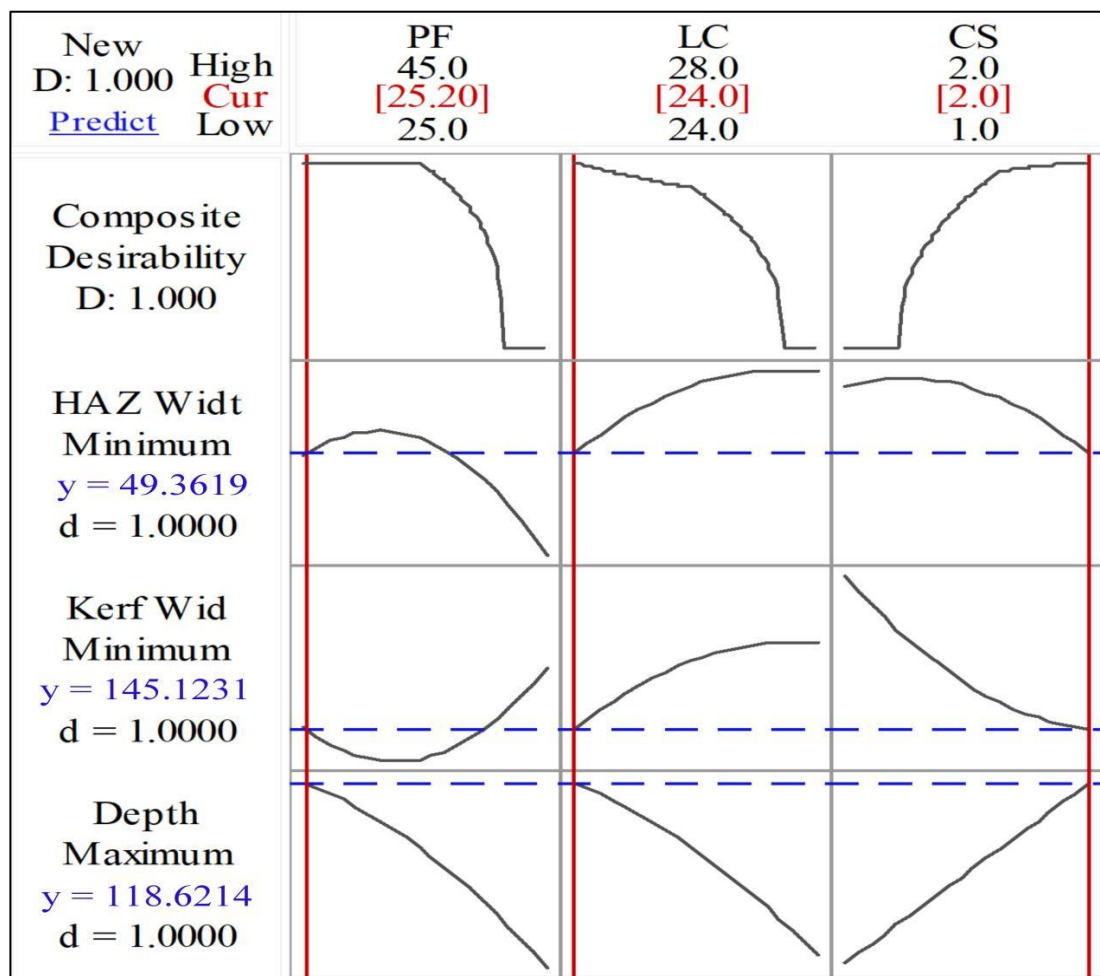


Figure 6.37 Multi-objective optimization plot for the micro-channels.

The responses are represented by each row as shown in figure. Each graph cell depicts how one of the response variables changes as a function of one of the factors, while the other factors remain constant. The current factor level settings, as well as the high and low values of factors, are displayed at the top of the column. The goal for the

responses, predicted responses, y , at current factor settings, and individual desirability scores are listed to the left of each row. The response value of the HAZ width obtained is $49.3619 \mu\text{m}$, kerf width of $145.1231 \mu\text{m}$, and depth of cut of $118.6214 \mu\text{m}$ can be reached with the parameter settings of pulse frequency of 25.20 kHz , lamp current of 24.0 amp , and cutting speed of 2 mm/sec .

6.4.2.5 Confirmation Test

Five additional validation experiments have been conducted as per the optimum condition and the average is then taken. It was observed that the experimental results are fairly close to the predicted results. Averages of experimental results are taken into account for confirmation test and results of the same is shown below in Table 6.12 and Figure 6.38 depicts the microscopic image and SEM micrograph of the micro-channel profile.

Table 6.12 Confirmation test of laser micromachining at submerged medium

Optimal parameter settings	Machining responses	Predicted value at Optimal parametric settings	Experimental value Optimal parametric settings	% of error
PF=25.20 kHz; LC=24.0 amp; CS=2.0 mm/sec	Depth of cut (μm)	118.6214	113.1217	4.64
	Kerf width (μm)	145.1231	140.8619	2.94
	HAZ width (μm)	49.3619	51.6391	4.61

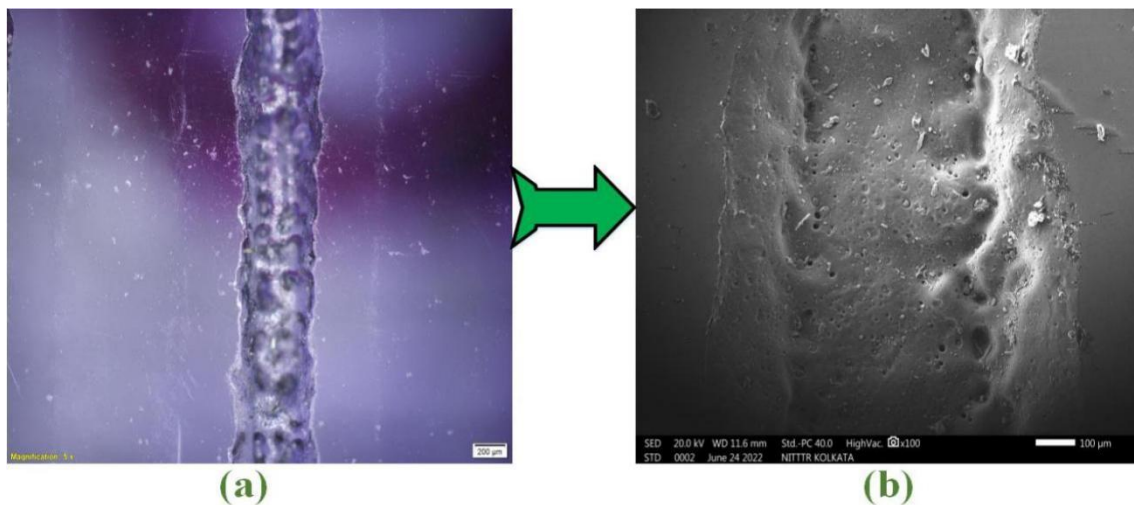


Figure 6.38 (a) Microscopic image of the micro-channel, (b) SEM micrograph

6.4.3 Outcomes

In the present research work, an Nd: YAG laser system has been used to conduct an experimental investigation on polymethyl methacrylate (PMMA). The micro-channels were using the laser transmission technique. The micro-channel operation was carried out in the presence of water. As the absorbent substance, black tape is employed. During the machining process, the key goals were to increase the depth of cut, limit the heat affected zone (HAZ), and keep the kerf width constant. During the experimentation, the process parameters considered were lamp current, pulse frequency, and cutting speed. The characteristics of the machined micro-channels, such as depth of cut, kerf width, and HAZ width, were then measured and studied. The RSM has been used for mathematical correlations between the input process parameters and output responses. The approach of analysis of variance (ANOVA) was used to test the adequacy of the model. Response surface methodology's (RSM) three-factor central composite design (CCD) technique is used to design the tests. It is found that all process variables are statistically significant. A parametric study has also been performed, to illustrate the observed phenomena in detail. It may be concluded from the study that the presence of water and a duty cycle nearer to 100% regarding pulse width play a vital role in achieving the desired machining characteristics during laser transmission ablation conducted in a water environment. Optimization has been conducted to obtain the optimum process variable settings to get the maximum depth of cut and minimum kerf width with the least possible heat affected zone (HAZ) width.

Further, a multi-objective optimization is carried out to achieve the optimal responses like in depth of cut, kerf width, and HAZ width, which are 118.6214 μm , 145.1231 μm , and 49.3619 μm , respectively. The optimal parameter settings are pulse frequency of 25.20 kHz, lamp current of 24.0 amp, and cutting speed of 2.0 mm/sec. The percentage of error obtained from the predicted and actual experimental results at optimal conditions is found to be very low, which signifies good acceptability of prediction analysis of Nd:YAG laser transmission micro-channeling of thick PMMA.

This research can also be used to determine the range of Nd:YAG laser process parameters, which is crucial for producing a uniform, smooth, and high aspect ratio micro-channel on PMMA. The study can be further utilized as a technical guideline for Nd:YAG laser micro-channeling of PMMA based on the findings. With the help

of Nd:YAG laser micro-machining operations, complex shapes of micro-channels on PMMA can also be accomplished with the utmost precision.

6.5 Experimental Investigation of Varying Laser Pass on Micro-channel Characteristics of Thick PMMA by Laser Transmission Micromachining

In this research work, the incident laser beam travelled through the thick transparent PMMA plate with no or minimal absorption which is inadequate to perform any kind of machining on the said plate. Whenever an absorbent is added at the bottom surface of the workpiece, that absorbs the thermal energy from the laser beam and heats up the adjacent zone of the workpiece through conduction as well as by transmission. The temperature of the adjacent zone may be increased with more absorption and subsequently the machining may take place. This laser machining process is known as laser transmission process or laser backside etching. In absence of adequate literature on laser transmission machining of thick PMMA, an experimental investigation on laser transmission machining on thick PMMA has been carried out. Laser working power, pulse frequency, pulse width and cutting speed are taken as input parameters whereas depth of micro-channel and heat affected zone (HAZ) width are chosen as machining responses. Passes are varying for this experiment during the machining operation to find out the changes in the output responses. Response surface methodology has been used to perform the micro-channeling operations. Three sets of experiments (i.e., 31 experiments for each set) have been carried out to understand and analyze the effects of process variables on responses.

Table 6.13 Range for Input Parameters of laser beam transmission micro-channeling

Process Parameters & Symbol	Low	High
Lamp current (amp) (A)	24	28
Pulse frequency (kHz) (B)	25	45
Pulse width (%) (C)	90	98
Cutting speed (mm/sec) (D)	1	2

The Olympus-STM-6, optical microscope has been used to capture the images of machined samples for subsequent measurement of the output responses. Depth and heat affected zone (HAZ) width for all the experiments have been measured at three

different locations along the micro-channel and the average is taken for further analysis.

6.5.1 Experimental Result and Discussion

The experimental values of depth of cut and HAZ width with varying laser passes are documented in Table no.2.

Table 6.14 Experimental results of single pass, double pass and triple pass for depth and HAZ width of the micro-channels

Sl. No.	Single Pass			Double Pass			Triple Pass		
	Depth of cut (µm)	Kerf width (µm)	HAZ width (µm)	Depth of cut (µm)	Kerf width (µm)	HAZ width (µm)	Depth of cut (µm)	Kerf width (µm)	HAZ width (µm)
1	58.37	185.8	133.81	65.83	145.36	149.96	70.57	189.49	81.78
2	53.2	233.22	151.57	92.77	217.08	142.325	65.23	214.25	111.6
3	54.73	172.04	161.92	89.63	146.74	111.89	89.07	175.74	111.44
4	58.8	237.36	192.64	98.63	218.04	117.755	89.53	232.76	116.61
5	44.57	172.04	118.22	89.67	154.56	130.87	85.17	192.73	100.92
6	52.6	210.68	156.27	100.5	222.82	125.03	89.87	233.24	122.82
7	36.73	170.66	122.02	107.87	175.26	131.64	93.23	176.89	130.29
8	58.17	216.44	161.82	105.67	251.37	134.765	96.37	249.78	121.18
9	51.5	163.3	83.67	109.3	170.66	122.82	89.27	201.88	88.02
10	40.53	219.88	58.13	130.27	226.71	141.255	98.43	251.23	114.27
11	50.9	172.5	114.48	122.83	172.5	83.03	101.6	195.3	93.01
12	44.5	239.82	116.76	123.47	223.49	113.925	116.2	246.1	95.28
13	23.4	169.74	100.74	125.83	173.88	84.58	98.73	191.82	98.67
14	27.37	209.3	103.04	132.07	225.86	109.225	116.5	250.7	112.01
15	17.57	184.66	116.28	124.53	189.39	93.765	100.17	181.7	100.05
16	29.43	240.26	137.23	116.7	229.54	127.88	118.13	244.26	90.85
17	24.7	122.6	110.97	146.23	158.14	85.84	101.53	187.22	86
18	31.4	227.24	138.035	156.05	267.26	112.24	109.8	285.91	113.64
19	19.93	180.68	96.42	124.13	220.2	118.11	98.03	235.98	97.05
20	20.37	196.88	141.68	129.83	219.42	103.13	117.17	218.04	97.29
21	94.8	241.5	149.27	69.67	184	142.34	85.3	227.24	89.01
22	62.27	227.98	147.06	82.13	203.32	129.72	101.4	232.76	110.55
23	87.9	208.28	158.42	52.23	159.26	154.6	56.33	162.72	139.66
24	54.23	209.08	76.4	106.43	166.06	116.38	93.13	177.56	105.04
25	66.13	260.6	116.35	35.27	181.24	131.375	99.83	194.12	140.1
26	65.33	259.1	111.49	32.8	182.62	130.45	103.33	206.54	140.32
27	63	260.9	113.56	30.7	181.24	125.57	99.17	195.04	137.59
28	70.1	263.24	117.77	35.2	189.98	124.81	97.37	201.94	140.32
29	74.8	265.08	112.73	32.63	186.76	127.02	103.53	202.86	141.19
30	75.07	264.74	118.26	35.9	179.28	128.025	105.33	196.76	135.41
31	71.97	262.16	117.96	32.17	173.42	129.06	99.7	202.06	136.17

6.5.1.1 For Depth of Cut

Figure 6.39, Figure 6.40, Figure 6.41, and Figure 6.42 illustrates the influence of lamp current, pulse frequency, pulse width, and cutting speed on the depth of cut at three different laser passes. In figures depth (1), depth (2), and depth (3) represent single pass, double pass, and triple pass respectively. Figures (6.39, 6.40, 6.41, and 6.42) demonstrate the variation of depth of cut with a number of passes.

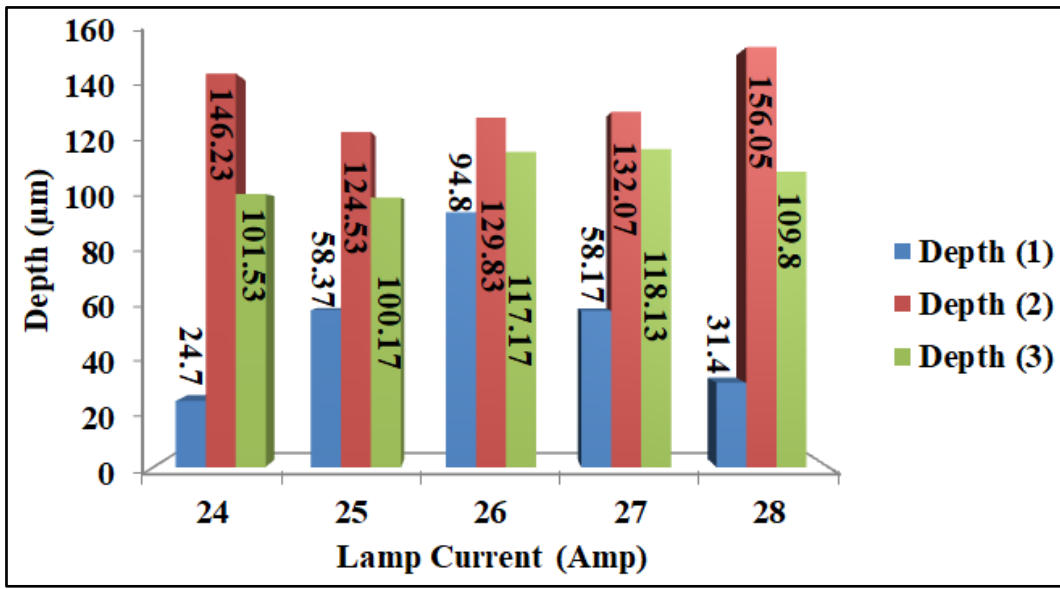


Figure 6.39 Lamp current vs depth (1), depth (2) and depth (3)

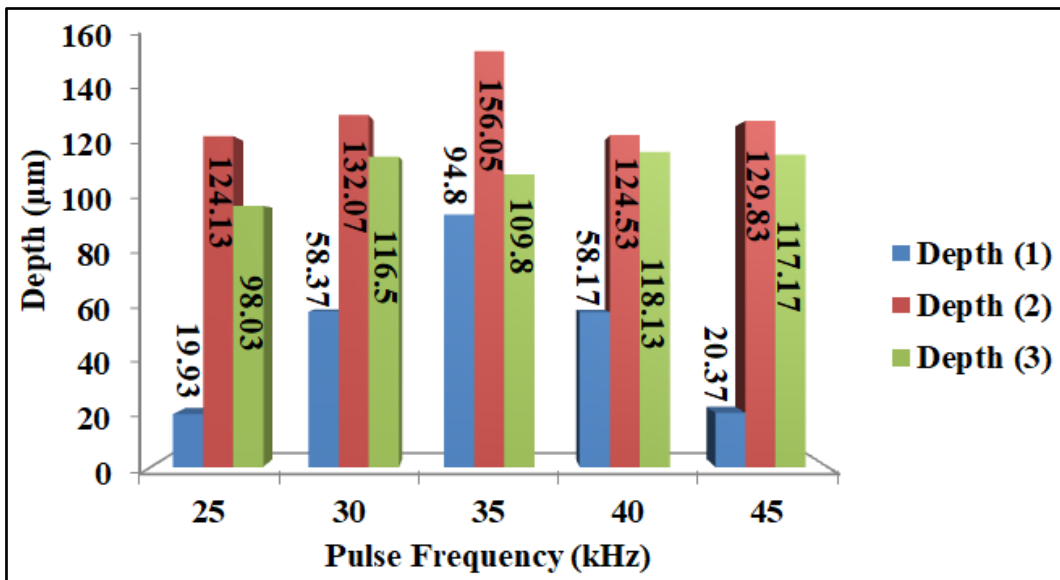


Figure 6.40 Pulse frequency vs depth (1), depth (2) and depth (3)

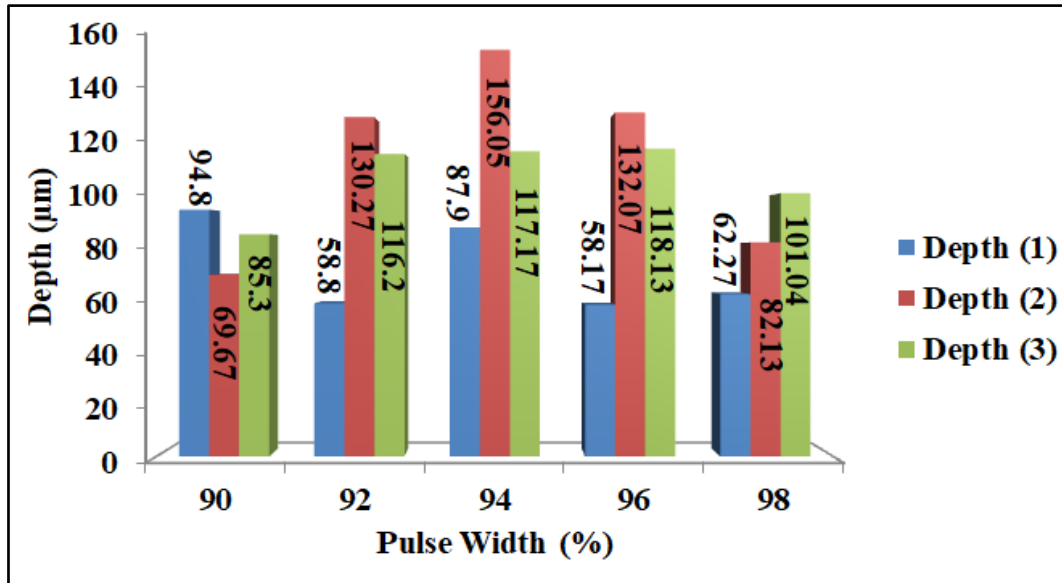


Figure 6.41 Pulse width vs depth (1), depth (2) and depth (3)

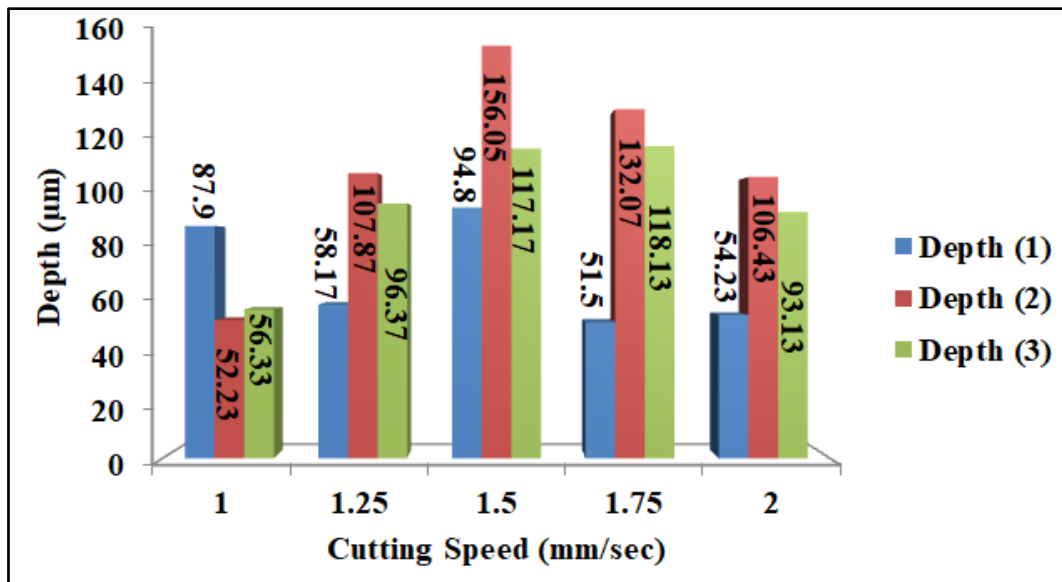


Figure 6.42 Cutting speed vs depth (1), depth (2) and depth (3)

It is found from the Figure 6.39 that the micro-channel depth is increased up to double pass and after that, it decreases with increase in laser pass along with varying laser lamp current. From the Figures (6.40, 6.41, 6.42) it is also noticed that when passes are varying with the respective parameters (i.e., pulse frequency, pulse width and cutting speed respectably), depth of cut also changes in the same way. In all the above cases, the depth of cut decreases after double passes. It is observed that at higher laser power with more number of laser passes, comparatively more thermal energy is absorbed and transmitted to the targeted region which helps to get more depth of cut.

But it is also noticed that depth of cut is comparatively less after 3rd consecutive pass than the experiments conducted with two laser passes. Presence of debris at machining zone in submerged conditions and cumulative time factor may affect the material removal for which this kind of phenomenon may be observed. The presence of debris in the water not only influences the material removal by affecting the surface tension force acting on the machining zone but also vary the rate of absorption leading to the production of adequate thermal energy required to conduct the transmission machining operation.

6.5.1.2 For Kerf Width

The influence of lamp current, pulse frequency, pulse width and cutting speed on kerf width is shown in Figure 6.43, Figure 6.44, Figure 6.45 and 6.46. Kerf width (1), Kerf width (2) and Kerf width (3) represent the value of kerf width with respect to one, two and three passes respectively. By keeping other parameters constant, passes are being varied here. Figures (6.43, 6.44, 6.45 and 6.46) show the variation of kerf width with number of passes.

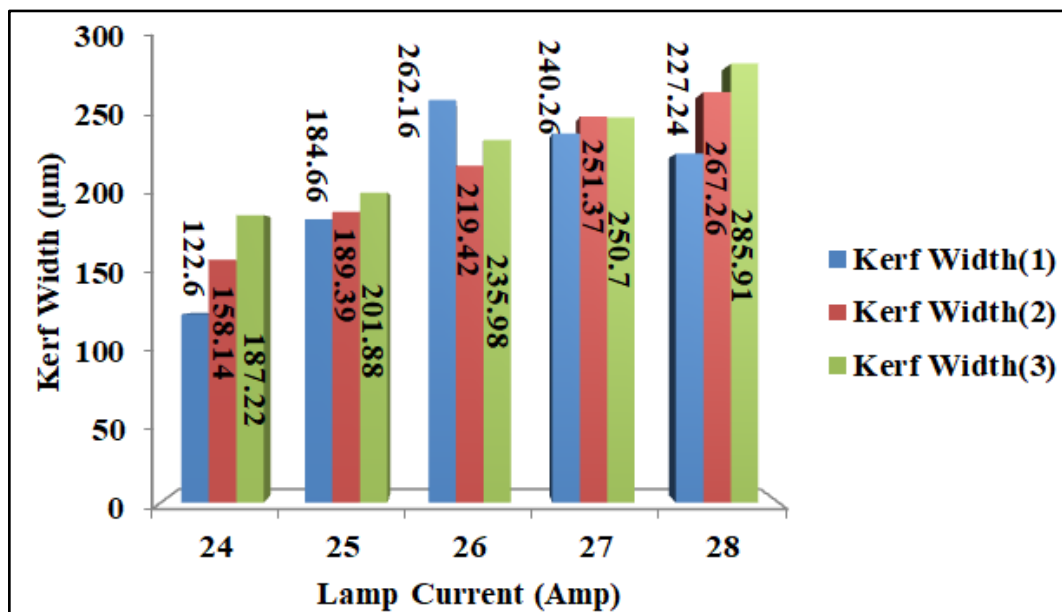


Figure 6.43 Lamp current vs kerf width (1), kerf width (2) and kerf width (3)

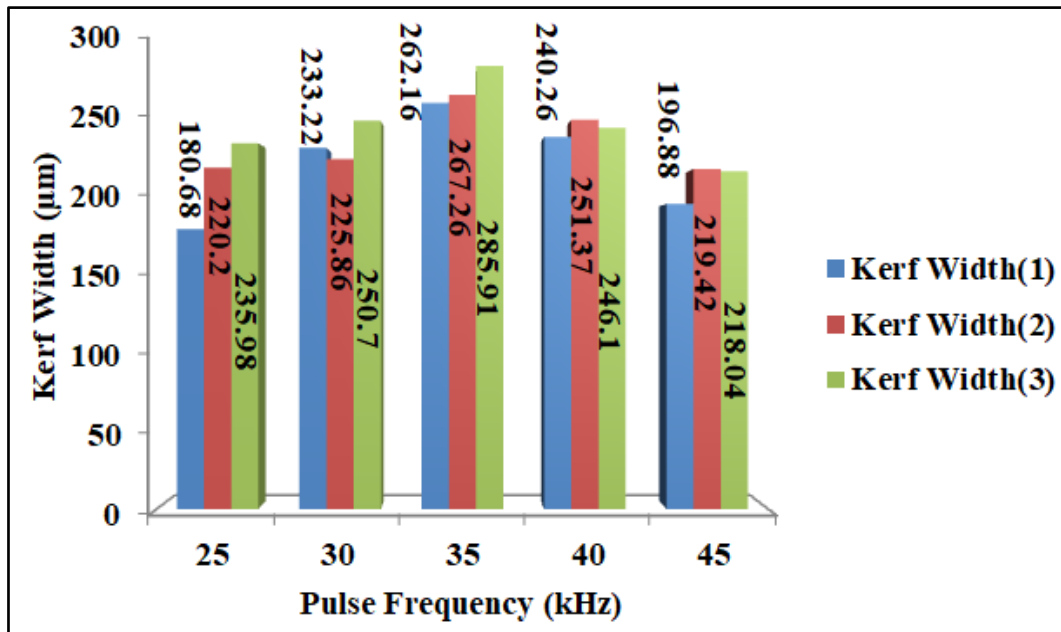


Figure 6.44 Pulse frequency vs kerf width (1), kerf width (2) and kerf width (3)

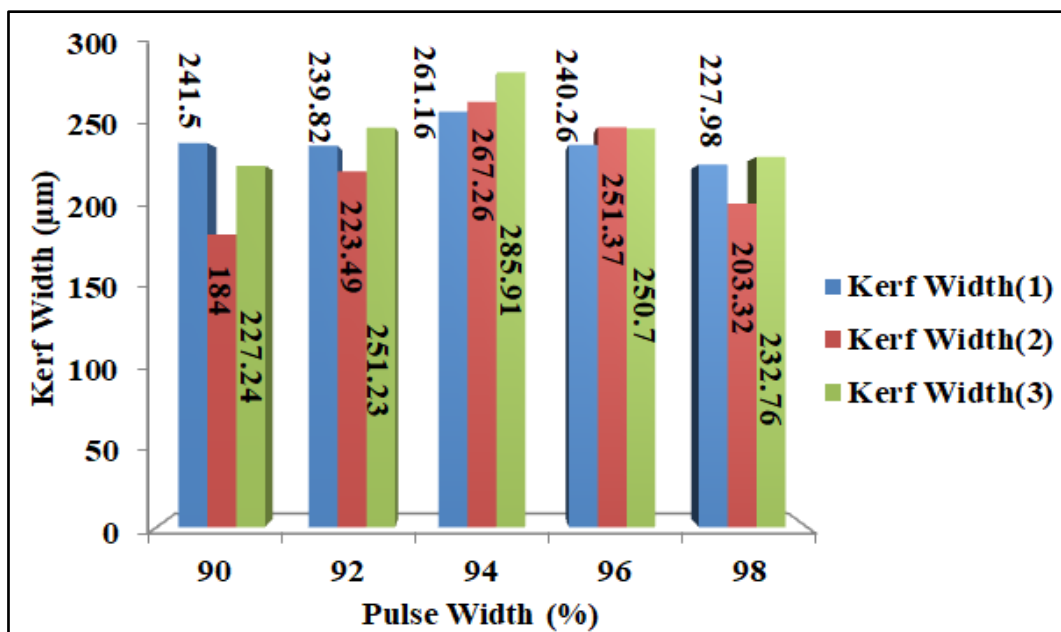


Figure 6.45 Pulse width vs kerf width (1), kerf width (2) and kerf width (3)

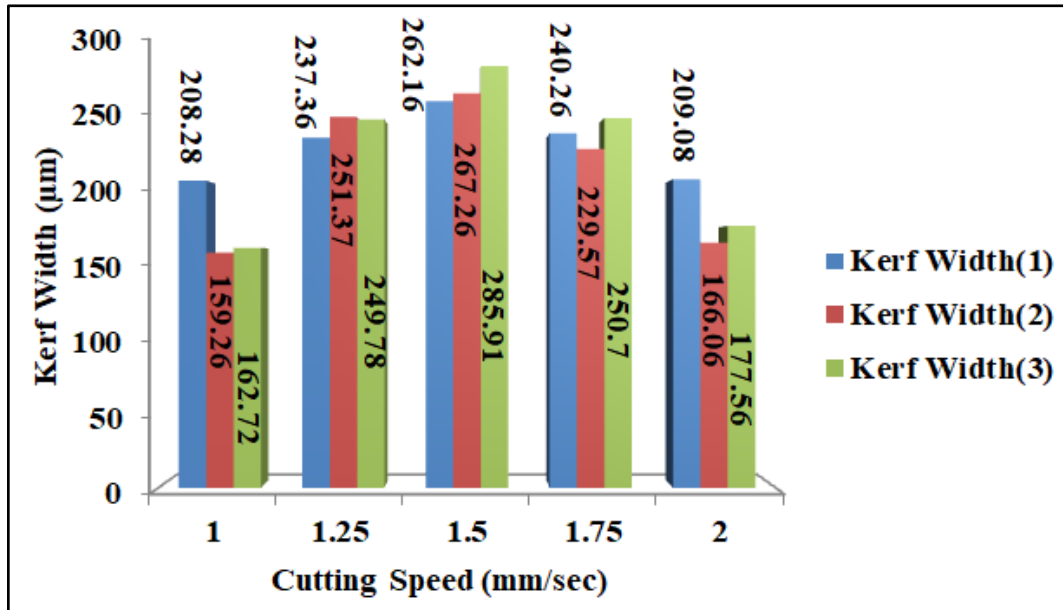


Figure 6.46 Cutting speed vs kerf width (1), kerf width (2) and kerf width (3)

6.5.1.3 For HAZ width

Figure 6.47, Figure 6.48, Figure 6.49 and Figure 6.50 show the influence of laser lamp current, pulse frequency, pulse width and cutting speed on HAZ width. HAZ width (1), HAZ width (2) and HAZ width (3) represents the measured HAZ width at single pass, double pass, and triple pass respectively.

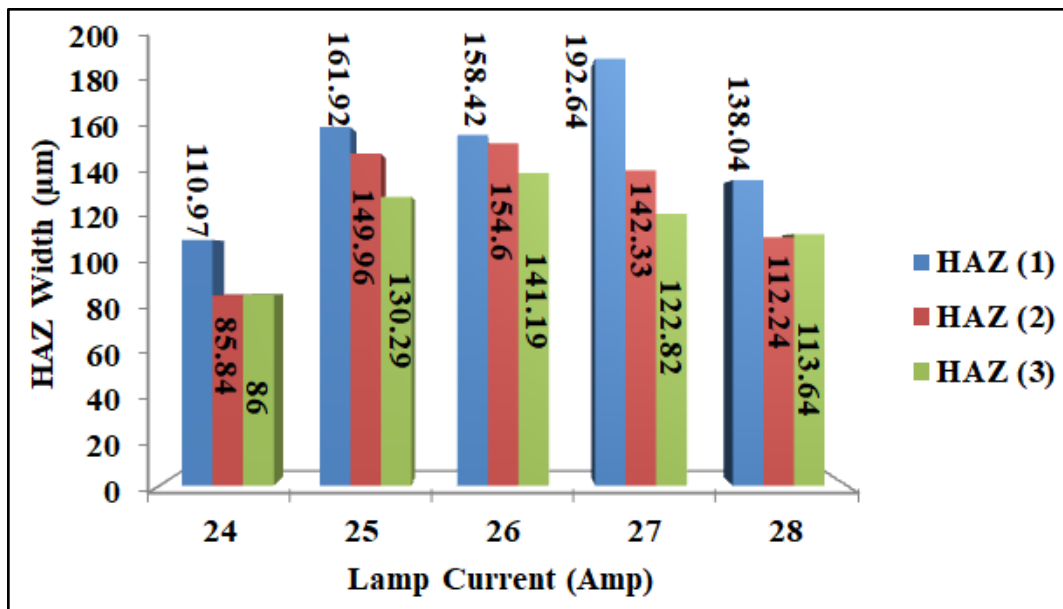


Figure 6.47 Lamp current vs HAZ width (1), HAZ width (2) and HAZ width (3)

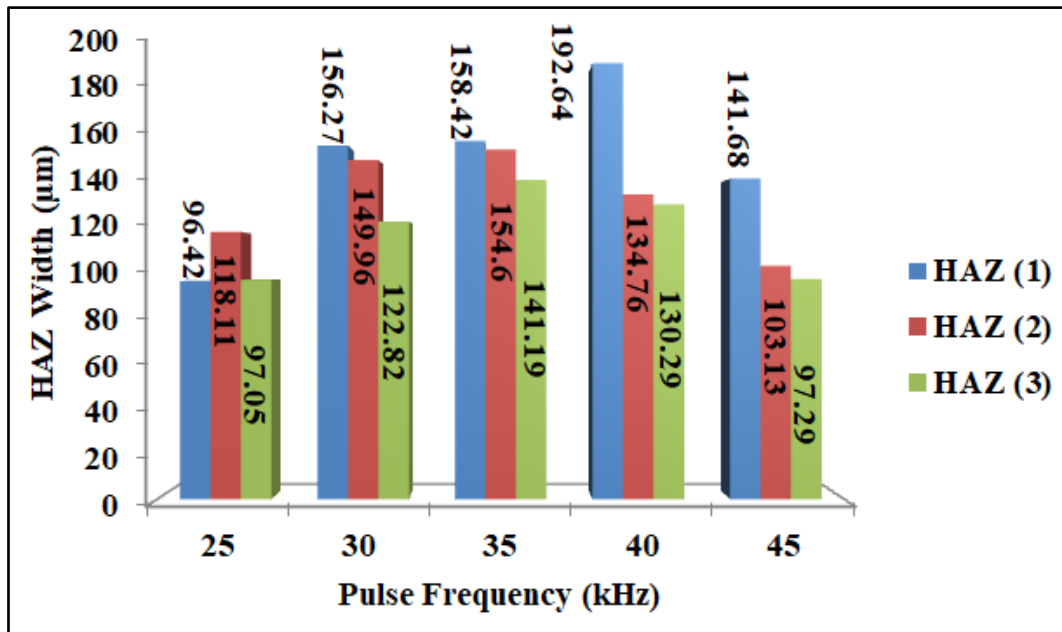


Figure 6.48 Pulse frequency vs HAZ width (1), HAZ width (2) and HAZ width (3)

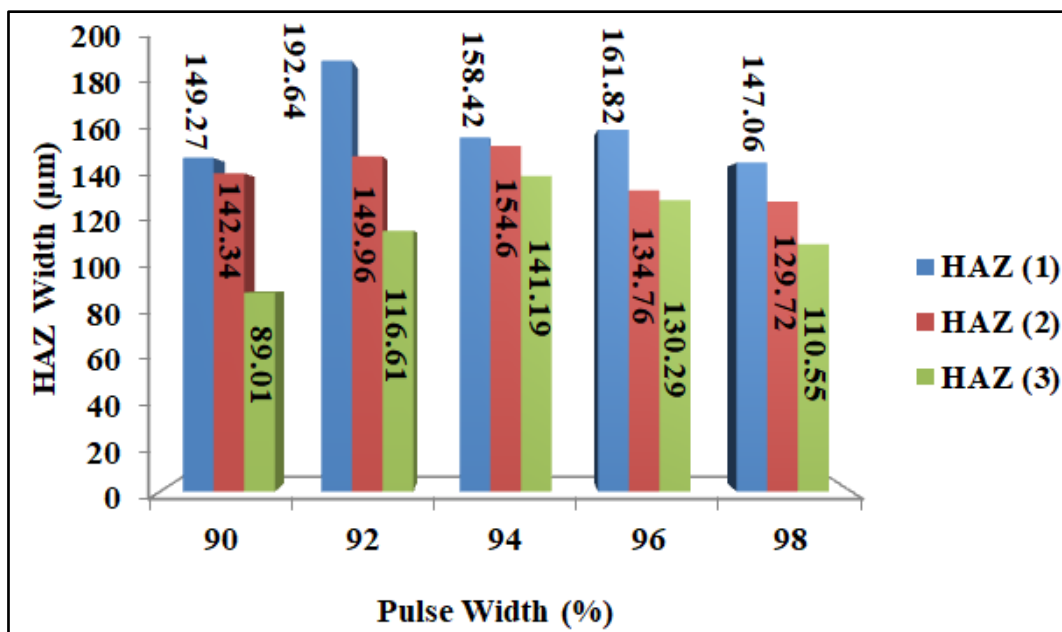


Figure 6.49 Pulse width vs HAZ width (1), HAZ width (2) and HAZ width (3)

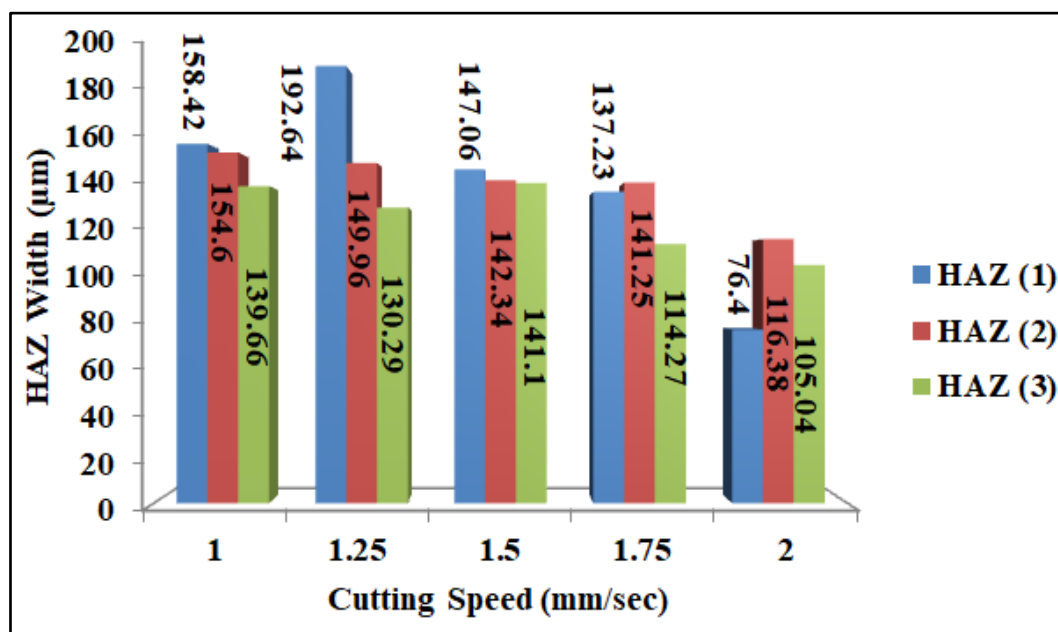


Figure 6.50 Cutting speed vs HAZ width (1), HAZ width (2) and HAZ width (3)

Thermal energy density on the machining zone is comparatively more at higher laser lamp current and higher pulse frequency which helps to get more HAZ width and vice versa. From the Figures (6.48, 6.49, 6.50), it is also noticed that when number of passes are varying with respected parameters (i.e., pulse frequency, pulse width and cutting speed respectably), HAZ width also changes in the similar way. With the increase in passes the HAZ width decreases significantly. Due to cumulative time factor and the presence of water at machining zone. Presence of water in the machining zone helps to restrict the thermal affects on the neighbouring zone by rapid cooling. Formation and collapse of the bubbles after two passes, in and around the machining zone not only carry out the debris from machining zone but also make a turbulence on the machining zone which extracts the heat and cool down the machining zone.

6.5.2 Outcomes

Laser transmission micro-machining technique is successfully employed in this study. Laser passes were varied for each set of experiment to observe and analyze the process outcome. It is found that the experimental results are significantly changed with the varying laser passes. From the Figures 6.39 to Figure 6.50, it can be concluded that the depth of cut changes significantly with the change in passes upto a certain limit, i.e., no significant changes are observed after double pass. The

significant change of depth of cut is found at 28 amps of lamp current, 35 kHz of pulse frequency at, 94% of pulse width and 1.5mm/sec of cutting speed. It is evident from the figures (6.47, 6.48, 6.49 and 6.50) that the passes play a vital role in controlling the HAZ width. The most significant change of HAZ width is found at lamp current of 24 amps, pulse frequency of 25 kHz, pulse width of 90% and cutting speed of 2 mm/sec respectably. From the study it can be concluded that within the specific parametric range, number of laser pass is a dominant factor along with the other process variables up to a certain limit. It is also observed that increase in number of laser pass during each experiment from two to three have a good effect on HAZ width but adverse effect on depth of cut.

Chapter 7

EXPERIMENTAL INVESTIGATION INTO DIODE PUMPED FIBER LASER MICRO- CHANNELING OF PMMA

7.1 Introduction

Some research has shown that thick PMMA plates can be micro-channelled by a laser beam. As a result of the burning and charring of polymeric chains, deep subsurface micro-cracks in thick clear PMMA plates are created, making processing with near-infrared (NIR) wavelength fiber laser radiation extremely difficult. Diode-pumped fiber laser transmission machining procedure may provide a solution to this problem. The practicality of diode pump fiber laser transmission cutting of thick transparent PMMA in various environmental circumstances (air and submerged in deionized water) was investigated in this research. During the research, the effect of process factors on machining responses was also studied. Experiments based on the response surface methodology (RSM) approach were carried out using a fiber laser with nanosecond pulses in the NIR band. Machining characteristics such as depth of cut, kerf width, and HAZ width have been evaluated, whereas process parameters such as pulse frequency, working power, and cutting speed have been considered. With the help of MINITAB software, a second-order polynomial model was created to do the statistical analysis. To determine the best value for micro-channels, single- and multi-objective optimization has been carried out.

7.2 Background and Fundamentals

This is a method of indirect ablation. Despite the fact that the laser beam is not associated with the workpiece material, it is transmitted through the object and absorbed by an absorbent attached to the workpiece's backside. The heat is subsequently transferred from the absorbent material to the workpiece via conduction, heating the object's backside. The machining zone is the back end of the object in this procedure. The material from the intersection of the laser, absorbent material, and

workpiece is removed, and the cutting front is formed. Both environmental conditions are maintained on the backside of the workpiece sample to be machined. Pure deionized (DI) water is employed as the submerged medium.

7.3 Parametric Study Based on Response Surface Methodology for Laser Beam Transmission Micro-channeling of PMMA with Air as an Assist Medium

7.3.1 Experimental Details

The process parameter settings and their levels are shown in Table 7.1. Three main input factors such as pulse frequency, working power, and cutting speed are varied from 50-70 kHz, 13-17%, and 0.02-0.06 mm/sec. Some other parameters that may have effects on responses were kept constant during the experimentation.

Table 7.1 Process parameters levels

Process Parameter	Unit	Symbol	Levels				
			-2	-1	0	1	2
Pulse Frequency (PF)	kHz	P	50	55	60	65	70
Working Power (WP)	%	Q	13	14	15	16	17
Cutting Speed (CS)	mm/sec	R	0.2	0.3	0.4	0.5	0.6
Constant Factors	Pulse Width = 99%						
	Number of passes = Single pass						

7.3.2 Results and Discussion

Laser transmission cutting in the air medium was used to carry out 20 sets of experiments. The experimental results are given in Table 7.2. Images of the PMMA substrate and the micro-channels fabricated by the laser transmission cutting in partially submerged conditions are given in Figure 7.1 and Figure 7.2, correspondingly.

Table 7.2 Experimental results

Experiment No.	Pulse Frequency (PF: kHz)	Working Power (WP: %)	Cutting Speed (CS: mm/sec)	Depth of Cut (μm)	Kerf Width (μm)	HAZ Width (μm)
1	-1	-1	-1	5.580	26.450	14.305
2	1	-1	-1	3.430	27.900	8.953
3	-1	1	-1	9.790	25.610	18.910
4	1	1	-1	7.577	30.010	20.931
5	-1	-1	1	8.710	24.380	10.734
6	1	-1	1	3.710	26.160	6.173
7	-1	1	1	5.530	25.730	17.981
8	1	1	1	2.310	30.770	20.519
9	-2	0	0	7.160	25.220	11.842
10	2	0	0	2.311	31.890	9.110
11	0	-2	0	3.870	24.320	6.050
12	0	2	0	6.910	27.740	24.702
13	0	0	-2	8.120	28.640	16.483
14	0	0	2	5.320	26.810	12.676
15	0	0	0	6.230	26.120	18.892
16	0	0	0	7.110	26.010	18.904
17	0	0	0	6.980	26.120	18.974
18	0	0	0	5.980	26.070	18.733
19	0	0	0	6.710	26.110	18.863
20	0	0	0	7.010	26.200	18.733

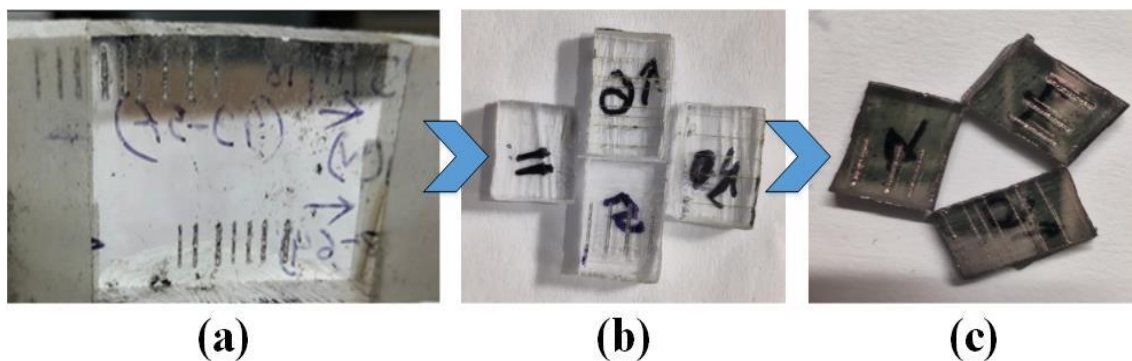


Figure 7.1 PMMA workpiece after fiber laser transmission cutting in air medium, (a) Parent sample, (b) Sliced micro-machined sample, (c) Gold coated micro-machined sample.

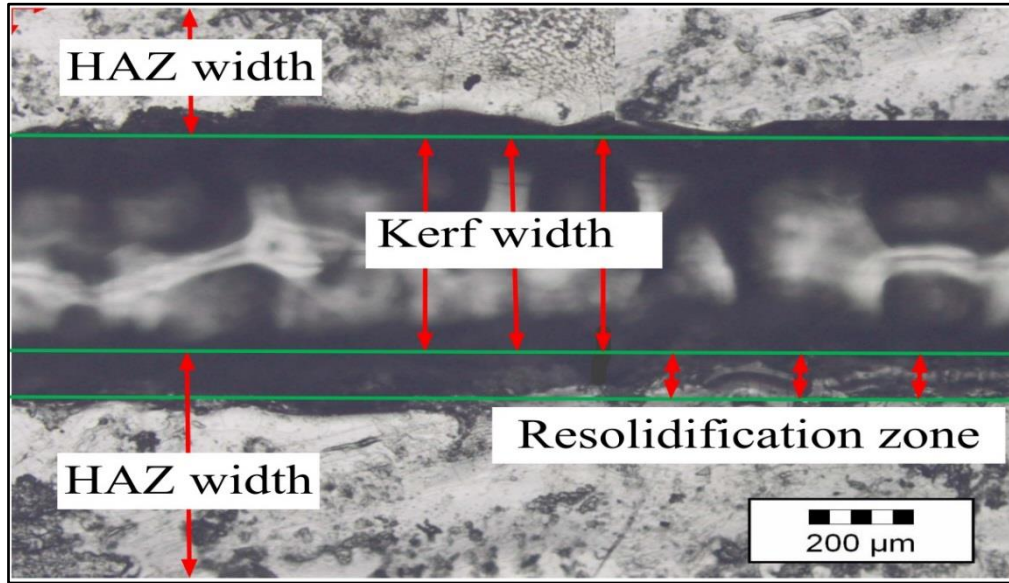


Figure 7.2 Microscopic view of the PMMA micro-channel.

7.3.2.1 Development of Second-Order Polynomial Model

Response surface modeling (central composite design) has been used to establish the mathematical relationship between the response and variable process parameters. The second-order polynomial equations are as follows.

Expression for Depth of cut

$$Y_{\text{Depth of cut}} = 6.661 - 1.393 P + 0.616 Q - 0.732 R - 0.4881 P^2 - 0.3245 Q^2 + 0.0080 R^2 + 0.215 PQ - 0.482PR - 1.617 QR \quad (\text{Eq}^n.7.1)$$

Expression for Kerf Width

$$Y_{\text{Kerf Width}} = 26.1091 + 1.6256 P + 0.8794 Q - 0.4119 R + 0.6145 P^2 - 0.0167 Q^2 + 0.4070 R^2 + 0.7763 PQ + 0.1213 PR + 0.5862 QR \quad (\text{Eq}^n.7.2)$$

Expression for HAZ Width

$$Y_{\text{HAZ Width}} = 18.8485 - 0.6761 P + 4.7175 Q - 0.9566 R - 2.0941 P^2 - 0.8691 Q^2 - 1.0682 R^2 + 1.8090 PQ + 0.1635 PR + 0.6262 QR \quad (\text{Eq}^n.7.3)$$

Where P, Q, and R indicate coded values of the process parameters, e.g., pulse frequency, working power, and cutting speed, respectively.

7.3.2.2 ANOVA of Machining Responses

The adequacy of the produced mathematical models for Kerf width, depth of cut, and HAZ width were evaluated using ANOVA and subsequent F- and p-value tests. The findings of an ANOVA investigation of the quadratic model with varied adequacy measures R^2 , adjusted R^2 , and predicted R^2 are shown in Tables 7.3, 7.4, and 7.5.

Table 7.3 ANOVA result of depth of cut at air medium

Source	DF	Adj SS	Adj MS	F-Value	P-Value
Model	9	76.7174	8.5242	35.81	0.000
Linear	3	45.6807	15.2269	63.97	0.000
P	1	31.0277	31.0277	130.36	0.000
Q	1	6.0725	6.0725	25.51	0.000
R	1	8.5805	8.5805	36.05	0.000
Square	3	7.8879	2.6293	11.05	0.002
P ²	1	5.9901	5.9901	25.17	0.001
Q ²	1	2.6472	2.6472	11.12	0.008
R ²	1	0.0016	0.0016	0.01	0.936
2-Way Interaction	3	23.1488	7.7163	32.42	0.000
P×Q	1	0.3685	0.3685	1.55	0.242
P×R	1	1.8596	1.8596	7.81	0.019
Q×R	1	20.9207	20.9207	87.90	0.000
Error	10	2.3802	0.2380		
Lack-of-Fit	5	1.3036	0.2607	1.21	0.419
Pure Error	5	1.0766	0.2153		
Total	19	79.0976			
Model Summary		S	R ²	R ² (adj.)	R ² (pred.)
		0.487869	96.99%	94.28%	85.06%

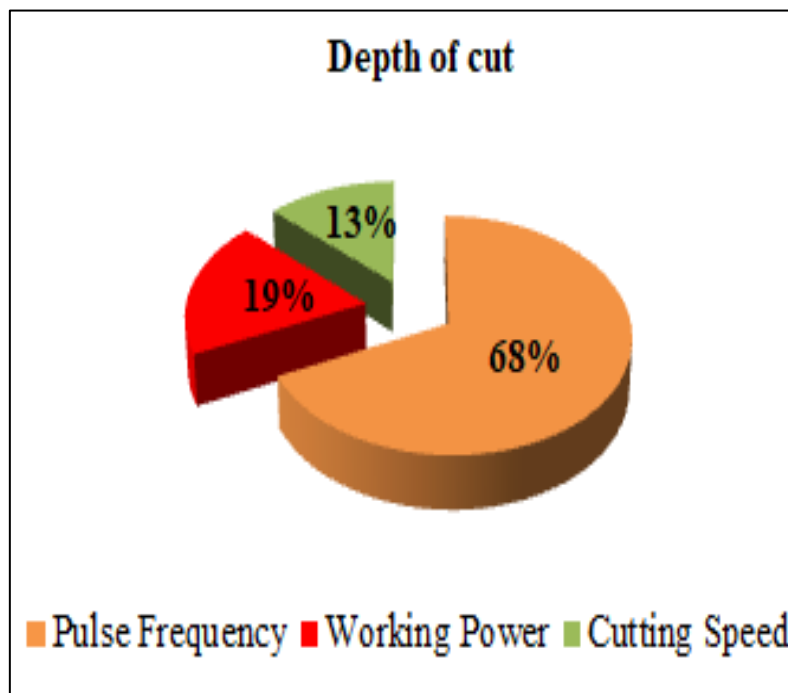


Figure 7.3 Contribution of parameters on depth of cut

The model has a statistically significant p-value of less than 0.05, as shown in Table 7.3. (i.e., 95 % confidence level). Because of the model's lack of fit value, the model's non-significance is ideal. All input process parameters, including the two-way interaction term, influence machining reactions to some extent. According to the table, pulse frequency (67.92 %) is the most important component for cutting depth, followed by working power (18.78 %), and cutting speed (13.29 %). Other adequacy measures R^2 , adjusted R^2 , and predicted R^2 are in reasonable agreement and close to 100%, indicating that the model is adequate. Figure 7.3 depicts the impact of several settings on the depth of cut.

Table 7.4 ANOVA result of kerf width at air medium

Source	DF	Adj SS	Adj MS	F-Value	P-Value
Model	9	77.6064	8.6229	822.48	0.000
Linear	3	57.3696	19.1232	1824.03	0.000
P	1	42.2825	42.2825	4033.04	0.000
Q	1	12.3728	12.3728	1180.16	0.000
R	1	2.7143	2.7143	258.89	0.000
Square	3	12.5492	4.1831	398.99	0.000
P ²	1	9.4956	9.4956	905.72	0.000
Q ²	1	0.0070	0.0070	0.67	0.432
R ²	1	4.1658	4.1658	397.35	0.000
2-Way Interaction	3	7.6876	2.5625	244.42	0.000
P×Q	1	4.8205	4.8205	459.80	0.000
P×R	1	0.1176	0.1176	11.22	0.007
Q×R	1	2.7495	2.7495	262.26	0.000
Error	10	0.1048	0.0105		
Lack-of-Fit	5	0.0851	0.0170	4.31	0.067
Pure Error	5	0.0197	0.0039		
Total	19	77.7112			
Model Summary		S	R ²	R ² (adj.)	R ² (pred.)
		0.10239	99.87%	99.74%	99.07%

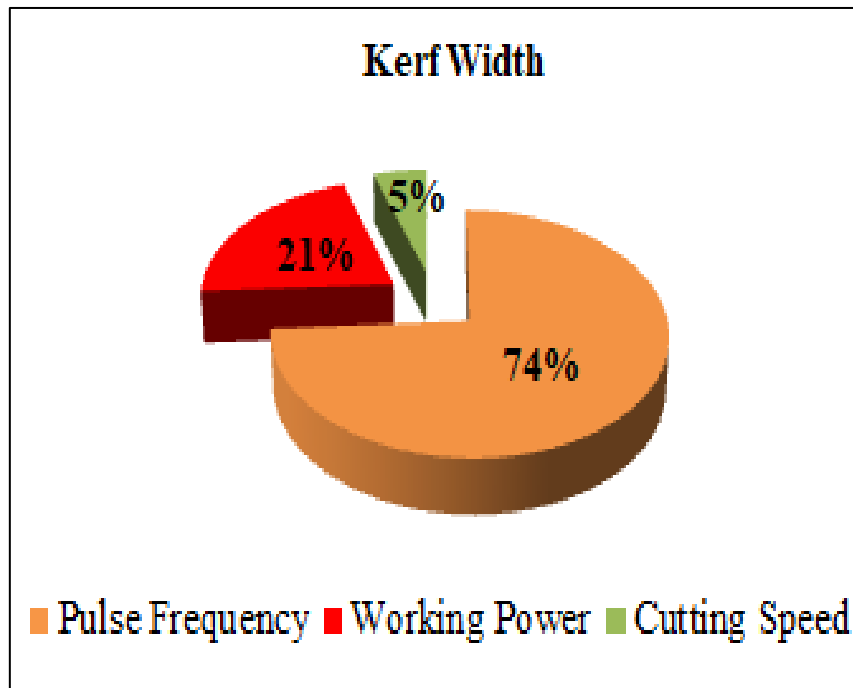


Figure 7.4 Contribution of parameters on kerf width

As shown in Table 7.4, the model's related p-value is less than 0.05 (i.e., $\alpha = 0.05$, or 95% confidence level), which means that the model terms are statistically significant. The model's lack-of-fit value implies non-significance, which is ideal. All of the input process factors and the two-way interaction term are important and have some effect on the machining reactions. Based on the table, pulse frequency (73.70%) is the most important factor for depth of cut, followed by working power (21.57%) and cutting speed (4.73%). Other measures of the model's adequacy, R^2 , adjusted R^2 , and predicted R^2 , are close to 100% and agree on most things, which shows that the model is good. Figure 7.4 shows how different parameters affect the kerf width.

Table 7.5 ANOVA result of HAZ width at air medium

Source	DF	Adj SS	Adj MS	F-Value	P-Value
Model	9	530.568	58.952	5568.50	0.000
Linear	3	378.033	126.011	11902.80	0.000
P	1	7.314	7.314	690.90	0.000
Q	1	356.077	356.077	33634.43	0.000
R	1	14.642	14.642	1383.07	0.000
Square	3	123.003	41.001	3872.89	0.000
P ²	1	110.258	110.258	10414.80	0.000
Q ²	1	18.991	18.991	1793.89	0.000
R ²	1	28.691	28.691	2710.08	0.000
2-Way Interaction	3	29.531	9.844	929.82	0.000
P×Q	1	26.180	26.180	2472.91	0.000
P×R	1	0.214	0.214	20.20	0.001
Q×R	1	3.138	3.138	296.36	0.000
Error	10	0.106	0.011		
Lack-of-Fit	5	0.058	0.012	1.22	0.415
Pure Error	5	0.048	0.010		
Total	19	530.673			
Model Summary		S	R ²	R ² (adj.)	R ² (pred.)
		0.102892	99.98%	99.96%	99.90%

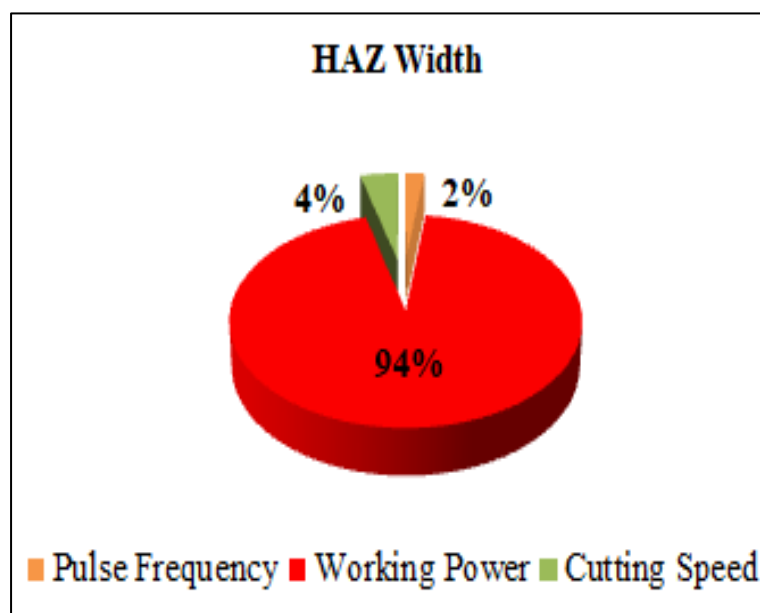


Figure 7.5 Contribution of parameters on HAZ width

As indicated in Table 7.5, model terms are statistically significant when the p-value is less than 0.05. This is the 95% level of confidence at which the p-value is less than 0.05. The model's perfect fit-to-data value suggests non-significance. All input process parameters, including the two-way interaction term, have some impact on machining reactions. Working power (95.22 %) is statistically the most important component for depth of cut, followed by cutting speed (3.32 %), and pulse frequency (1.46 %). Other adequacy measures R^2 , adjusted R^2 , and predicted R^2 are in reasonable agreement and close to 100%, indicating that the model is adequate. Figure 7.5 depicts the effect of several parameters on HAZ width.

7.3.2.3 Parametric Analysis

(i) Parametric Effects on Depth of Cut

The augmentation of depth of cut during laser transmission micro-channeling operation in the air is a difficult task as it is dependent on the laser machining process parameters. Thus, the effects of pulse frequency, working power, and cutting speed on depth of cut phenomena during laser micro-channeling of 11.328 mm thick and transparent PMMA workpiece have been examined.

Figure 7.6 shows the combined effects of pulse frequency and working power on depth of cut when cutting speed is kept constant at 0.4 mm/sec. Pulse width and number of passes are taken as constant at 99% and 1 respectively. Depth of cut is increased at higher working power and lower pulse frequency and decreased at lower working power and higher frequency. The results reveal the opposite when the working power is lowered with a higher frequency, which may be owing to the fact that doing so generates a lower-quality laser beam with less thermal energy and a lower depth of cut. As can be seen in the surface plot, the depth of cut decreases as the working power is increased at lower pulse frequencies. It's possible that the increased tendency of molten material to re-solidify is responsible for this phenomenon. High temperatures generated in the machining zone cause materials to melt. The reduced depth of the micro-channel may have been caused by the material resolidifying. Due to the increased rate of material removal caused by the generation of high thermal energy, the depth of cut grows in parallel with the working power at increasing levels of pulse frequency. As the pulse frequency rises, the laser beam quality decreases, resulting in less thermal energy and thus a lower depth of cut. For lower working power, this effect becomes more apparent.

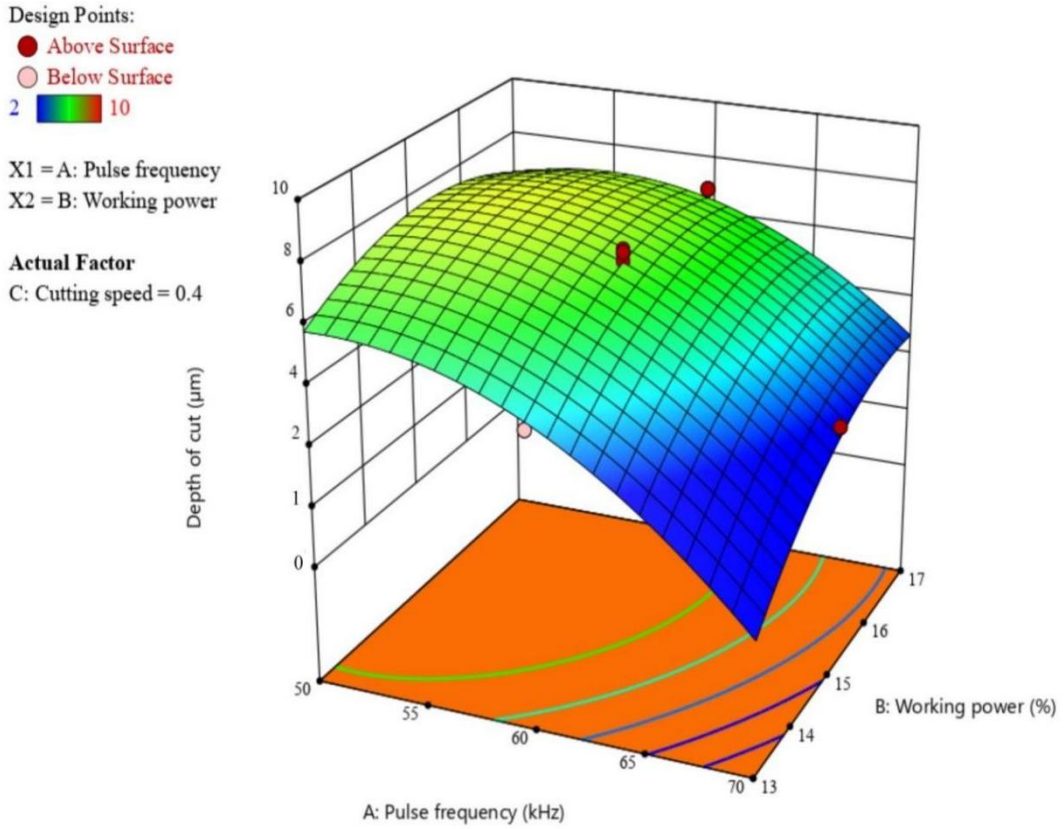


Figure 7.6 Surface plot of depth of cut versus pulse frequency and working power.

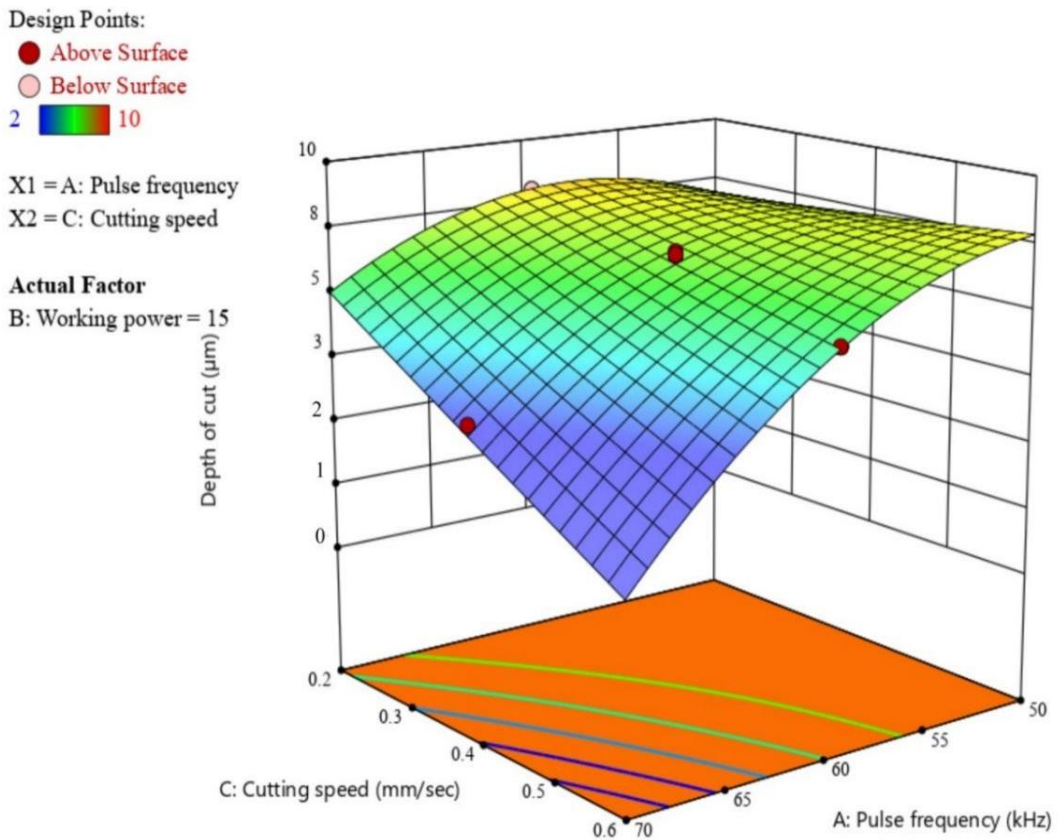


Figure 7.7 Surface plot of depth of cut versus pulse frequency and cutting speed.

The combined effect of pulse frequency and cutting speed on depth of cut at constant working power of 15 % is shown in Figure 7.7. At lower cutting speeds, increasing the pulse frequency somewhat enhances the depth of cut, but when the cutting speed is increased, the depth of cut decreases. Increases in the number of overlapping pulses improve cutting depth. However, increasing the pulse frequency at a slower cutting speed leads to a weaker incident beam and a lower depth of cut. Laser pulses are less likely to overlap while cutting at greater rates. Since the depth of cut reduces with increasing pulse frequency at higher cutting speeds, the result is less laser power. Although a large amount of material is removed at low pulse frequency and low cutting speed due to high heat generation and resolidification of material at this combination of parameters, the tendency to resolidify the material decreases with an increase in cutting speed, which aids in improving the depth of cut.

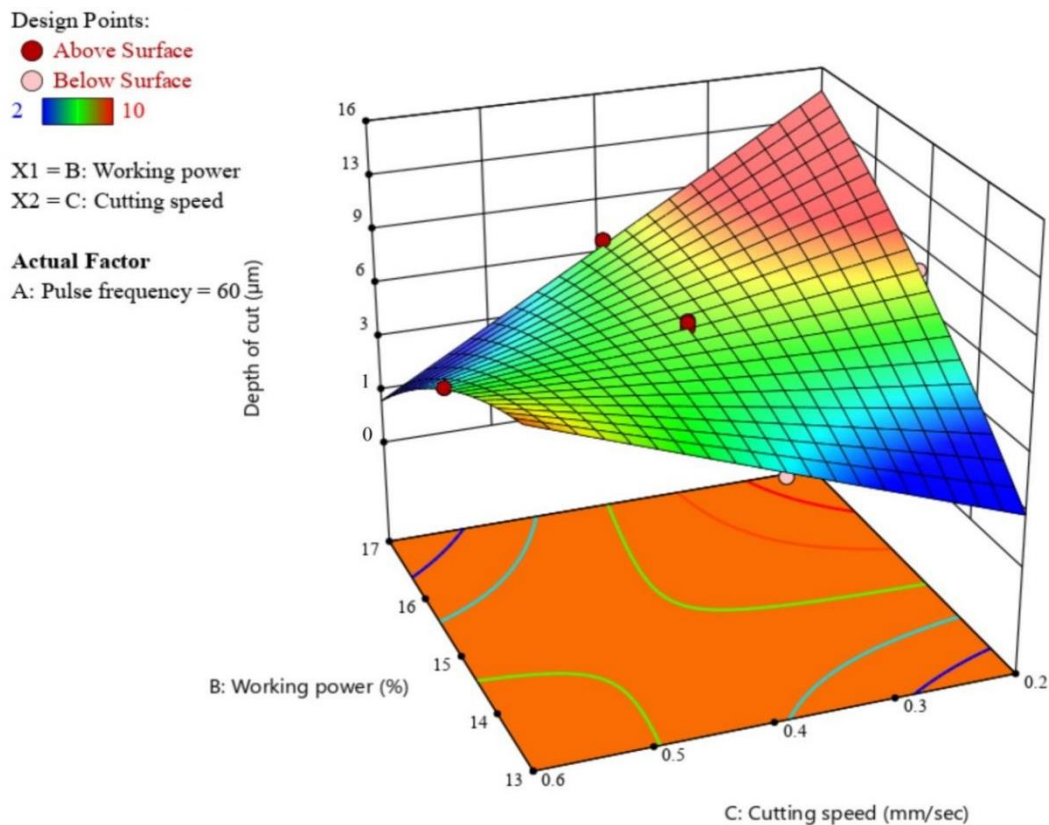


Figure 7.8 Surface plot of depth of cut versus working power and cutting speed.

The integrated impacts of working power and cutting speed on the depth of cut at a constant pulse frequency value of 60 kHz is illustrated in Figure 7.8. Both the pulse width and the number of passes are assumed to be constant at 99 and 1, respectively. Once the working power is raised, the depth of cut increases while cutting speed

decreases. When the laser beam interacts with a workpiece for a long enough period of time, enough heat is generated to cause a rapid removal of material. The energy of a laser beam is directly proportional to its power. A high value of power generates a lot of heat, which melts the top of the work sample under the laser's focus. So it evaporates instantly, and the significant depth of cut is a result of the removal of a lot of material from the top surface during penetration. When the cutting speed is high, the depth of cut is low. Moderate to low cutting speeds allow the laser beam to engage with the material for longer, resulting in more material being removed and a greater depth of cut. Because of the low material removal from the workpiece due to low thermal energy at lower cutting speeds, the depth of cut reduces with decrease in working power. Again, when the cutting speed increases and the working power rises, the depth of cut falls. Because increased working power leads to more heat energy, increased cutting speed causes a shorter interaction time between the laser beam and the workpiece, resulting in a lower depth of cut.

(ii) Parametric Effects on Kerf Width

Figure 7.9 shows the combined effects of pulse frequency and working power on kerf width when cutting speed value held at 0.4 mm/sec. Pulse width and number of passes are kept constant at 99% and 1 respectively. When working power increases at a lower pulse frequency, a slight decrease in kerf width is seen. In this parametric combination, the machining surface's temperature rises, increasing the production of bars and high HAZ regions, which may slightly reduce the kerf width. When the pulse frequency is increased throughout the complete range of working power, the kerf width initially reduces over a limited range of pulse frequency and subsequently increases. With an increase in pulse frequency, more pulses per unit of time impinge on the material's surface, which also increases the kerf width. At a mid-to-high range of pulse frequency, it has been found that kerf width grows almost linearly with an increase in working power. The energy density at the machining zone rises with an increase in working power; this energy is then absorbed by the absorbent substance, boosting the temperature of the PMMA's backside. At extremely low pulse frequencies, despite the slightly increased beam strength, the material has only been taken from the tiny focusing region on the top surface of the work sample. This is because at these frequencies, the time interval between two successive incident beams is longer. This circumstance improves the phase change process and increases the kerf width.

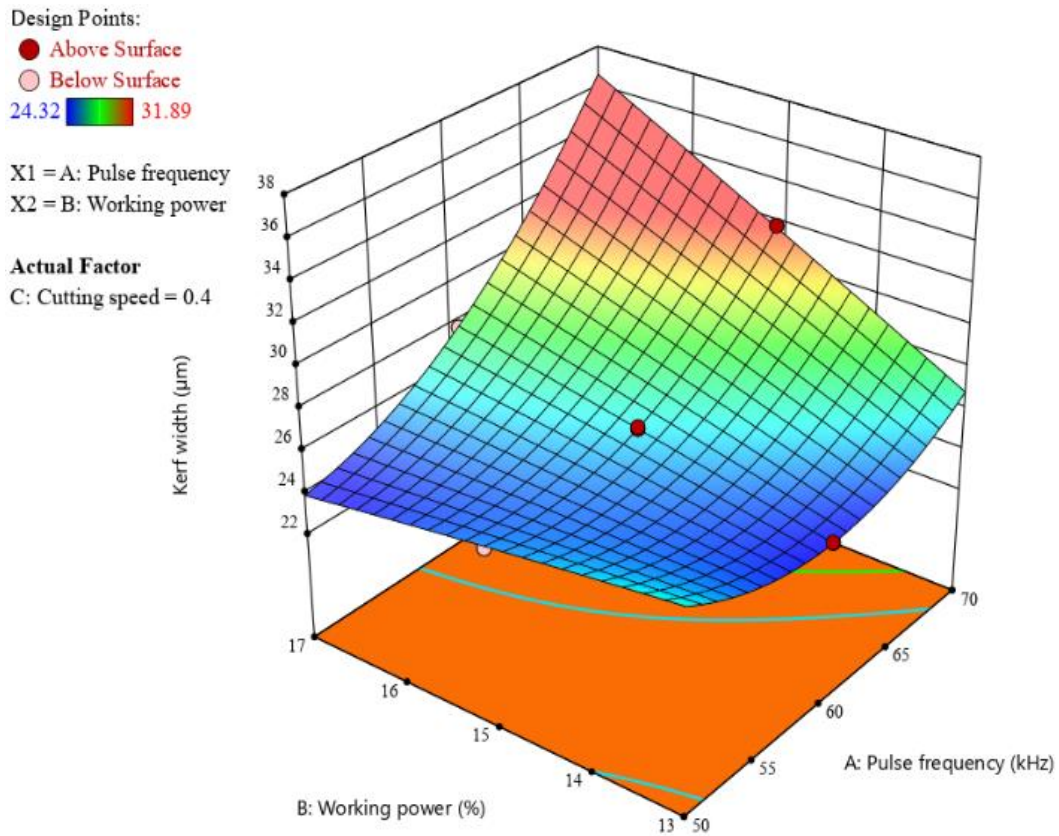


Figure 7.9 Surface plot of kerf width versus working power and pulse frequency.

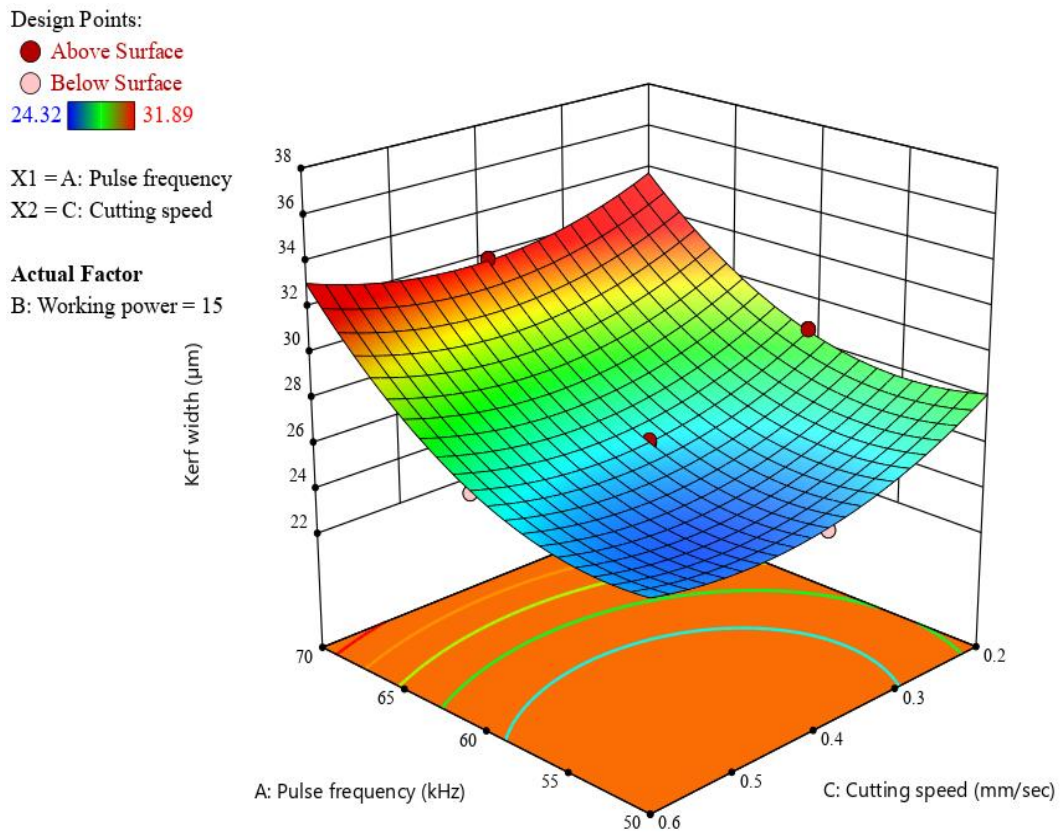


Figure 7.10 Surface plot of kerf width versus pulse frequency and cutting speed.

At a working power of 15%, the combined effects of pulse frequency and cutting speed are shown in Figure 7.10. The pulse width and the number of passes are fixed at 99 % and 1 respectively. Due to higher overlapping of incident laser beams, the kerf width increases with increasing pulse frequency at all values of cutting speeds. Higher cutting speed indicates greater relative movement between the laser beam and workpiece, which results in less interaction and incomplete machining. Due to the resolidification of molten material at the wall or edge of the cutting front, which may influence the kerf width, greater cutting speeds cause the molten debris to not be properly removed from the machining zone, leading to the generation of this type of surface plot. When the pulse frequency is extremely low, the beam energy stays slightly higher. More time passes between two successive incident beams, which limits the amount of material that can be removed from the workpiece's top surface. As a result, at lower cutting speeds, the kerf width decreases as the pulse frequency decreases.

Design Points:

● Above Surface

○ Below Surface

24.32  31.89

X1 = B: Working power

X2 = C: Cutting speed

Actual Factor

A: Pulse frequency = 60 (μm)

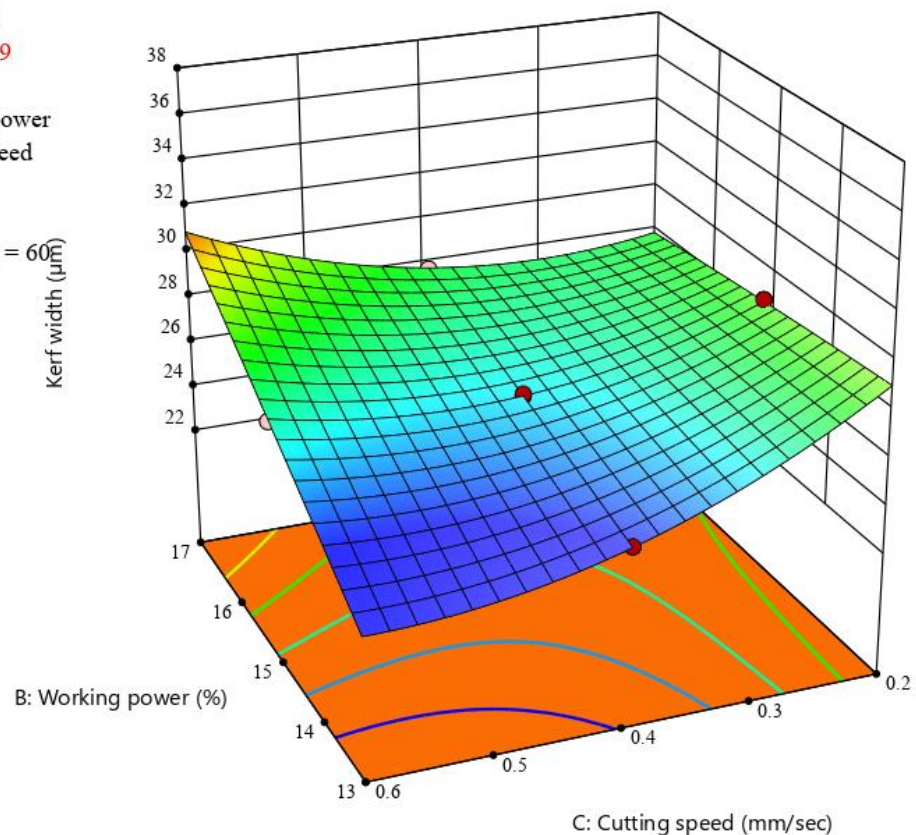


Figure 7.11 Surface plot of kerf width versus working power and cutting speed.

The effect of working power of different mediums on kerf width is shown in Figure 7.11. Pulse width and number of passes are taken as constant at 99% and 1 respectively. At a lower cutting speed and a higher working power, the kerf width varies insignificantly, and the opposite is true when cutting at a slower speed and a lower working power. With an increase in cutting speed at a lower value of working power, the kerf width gradually decreases. At increasing cutting speeds, the kerf width grows linearly as working power increases. At the aforementioned parameter settings, the energy density at the machining zone is relatively higher, which could result in uniform material removal from the machining zone and the production of an even kerf edge. Higher cutting speed indicates greater relative motion between the laser and workpiece, which results in less interaction and incomplete machining. Higher working power aids in obtaining more potent energy to melt the workpiece's top layer.

(iii) Parametric Effects on HAZ Width

Figure 7.12 shows the combined effects of pulse frequency and working power on HAZ width at a constant cutting speed of 0.4 mm/sec. The HAZ width gets wider as the pulse frequency goes down at lower working power. At lower working power, increasing the pulse frequency lowers the quality of the laser beam and makes it produce less energy density. At higher levels of working power, the amount of thermal energy produced is high, and the pulse repetition rate goes up as the pulse frequency increases. This means that as the pulse frequency increases, the heat affected zone (HAZ) grows wider. This may be the reason the HAZ width gets smaller as the pulse frequency goes down at lower levels of working power. When the pulse frequency is low and the working power goes up, the HAZ width gets higher. When the working power is high, it creates a lot of heat, which in turn HAZ width increases. The peak power of the laser beam is greater when the pulse frequency is low. Increasing working power while keeping the frequency low causes too much material removal. So, the HAZ width grows faster as the working power increases.

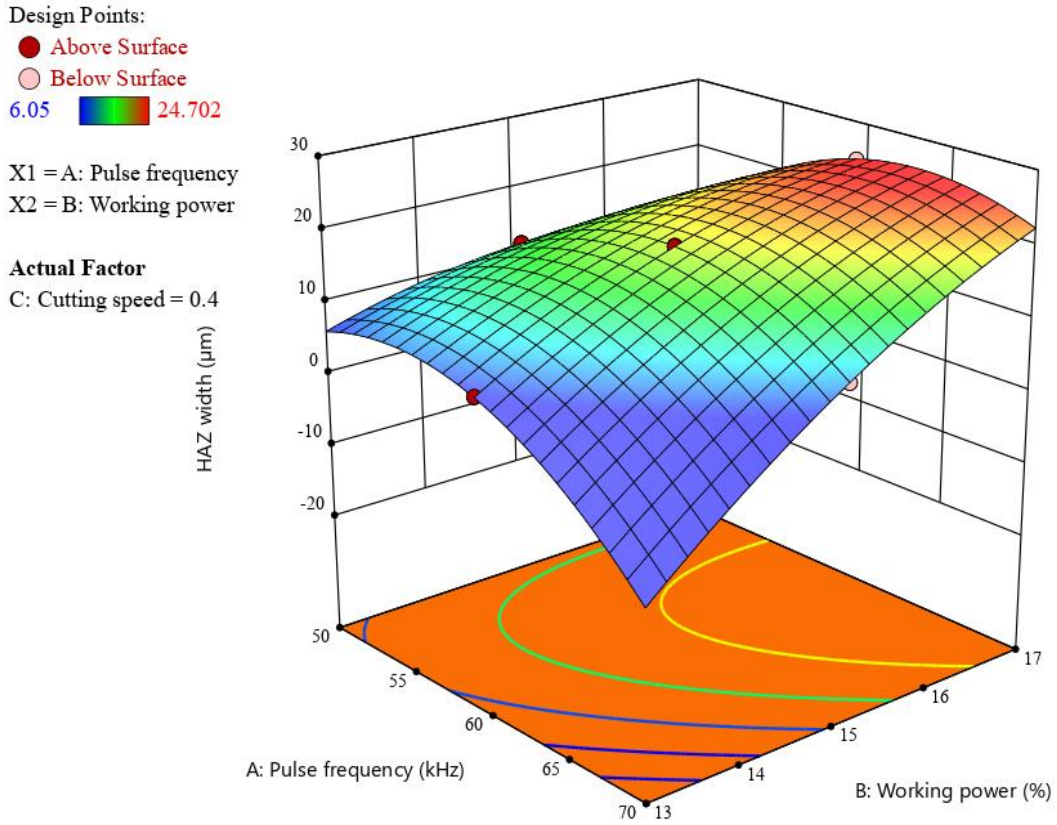


Figure 7.12 Surface plot of HAZ width versus pulse frequency and working power.

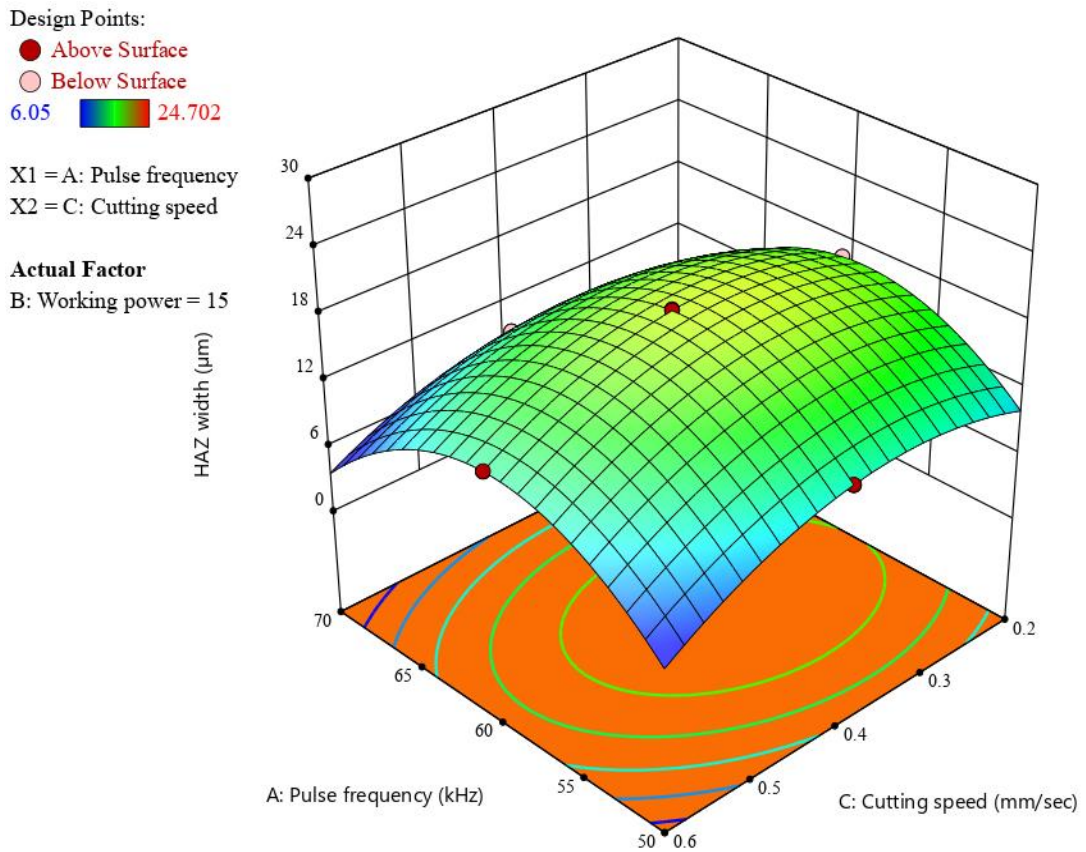


Figure 7.13 Surface plot of HAZ width versus pulse frequency and cutting speed.

The surface plot as shown in Figure 7.13 illustrates the effects of pulse frequency and cutting speed on HAZ width at fixed working power of 15%. As the pulse frequency is increased while the cutting speed is kept low, the HAZ width first grows slightly before decreasing again. With a longer contact time and slower cutting speed, more heat is produced in the machining zone, leading to a wider HAZ. But if the pulse frequency is increased even further, the energy density decreases, and the HAZ width reduces. Higher interaction times lead to greater energy density, which leads to increased heat generation in the machining zone, which in turn causes the HAZ width to increase. This is because the working power is fixed at 15%. Heat production causes the widest HAZ width at a moderate level. HAZ width is found to be progressively reduced with increasing cutting speed across the whole range of pulse frequencies. A lower HAZ width may be the result of less heat being generated in the machining zone as a result of the higher cutting speed leading to less time for the workpiece to interact with the laser beam.

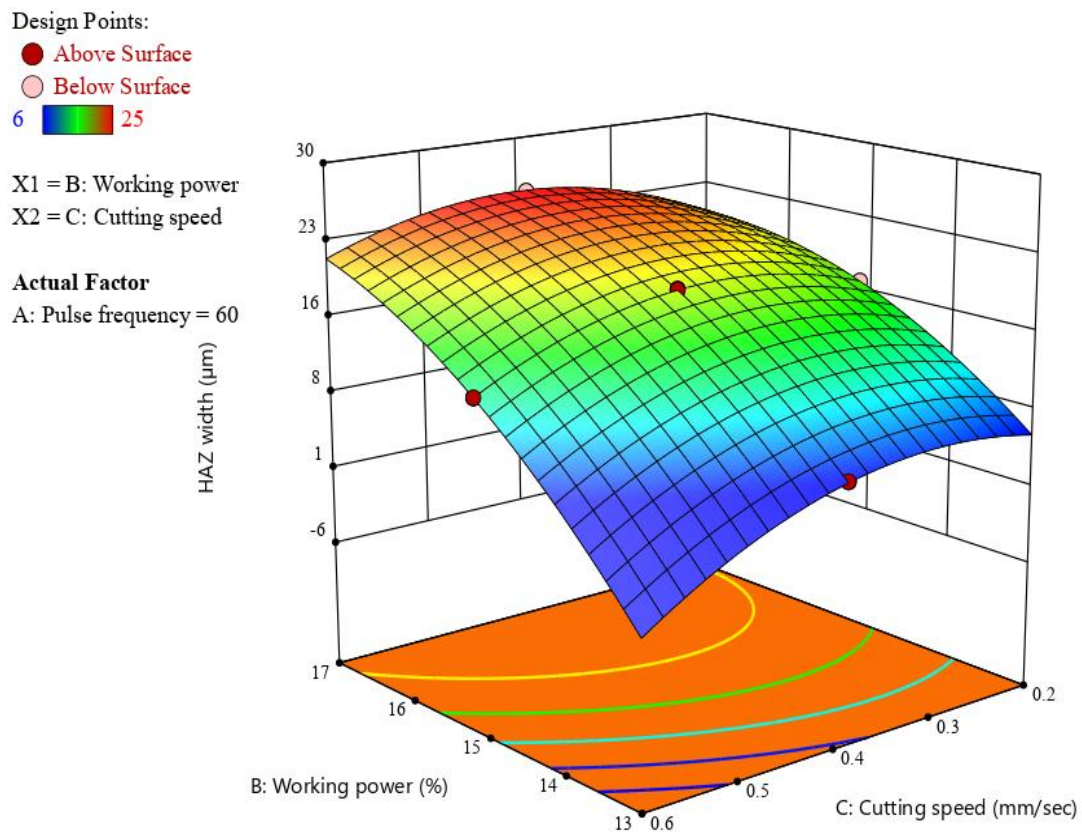


Figure 7.14 Surface plot of HAZ width versus working power and cutting speed.

The variation of HAZ width with working power and cutting speed at a constant pulse frequency of 60 kHz is exhibited in Figure 7.14. HAZ width is found to slightly increase with slower cutting speeds and higher working power. An increase in

working power and a decrease in cutting speed both increase the amount of time spent interacting, which in turn raises the temperature in the machining zone and causes the HAZ width to grow wider. The HAZ width progressively reduces as the working power is reduced for a lower value of cutting speed. When the cutting speed is low, less heat is produced by the lower working power. However, the cutting speed has no effect on the machining zone. The smaller HAZ width is a result of the aforementioned parameter combination. Increasing the cutting speed at a lower working power results in a slight decrease in HAZ width. As the cutting speed increases, the interaction time between the laser beam and the workpiece decreases, resulting in a smaller HAZ width. This is because the low working power creates minimal thermal energy in the machining area. At higher cutting speeds, increasing the working power causes the HAZ width to increase linearly. Increases in working power result in more thermal energy, which may be the cause of increasing HAZ width at high cutting speeds despite the fact that less interaction between the laser beam and the workpiece results in smaller HAZ width.

7.3.2.4 Determination of Optimal Process Parameter Using Response Surface Methodology

(i) Single-Objective Optimization Analysis

The machining characteristics have been optimized to find the best values of various process factors.

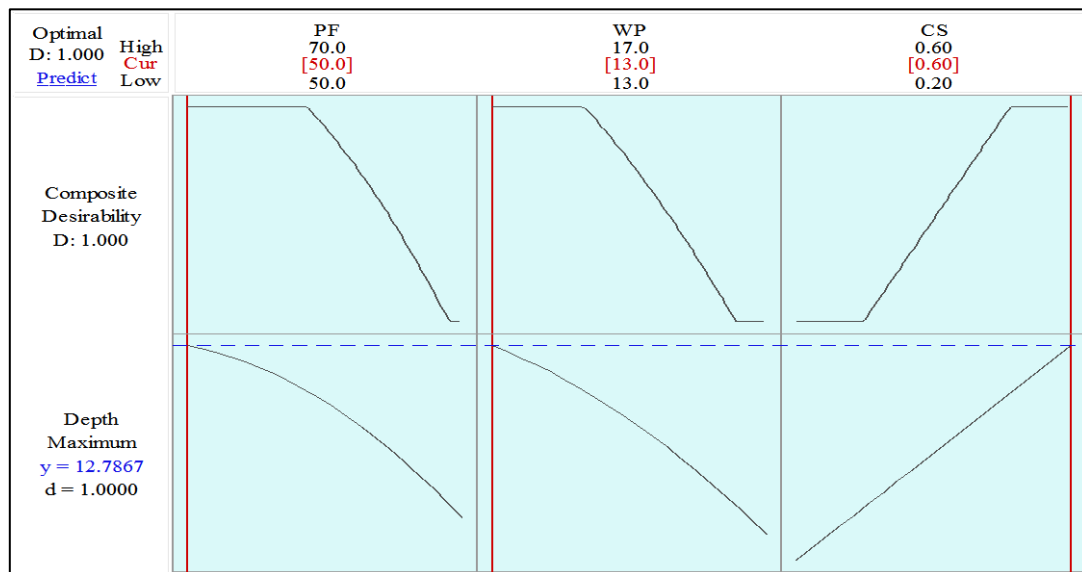


Figure 7.15 Single-objective optimization plot for the depth of cut of the micro-channel.

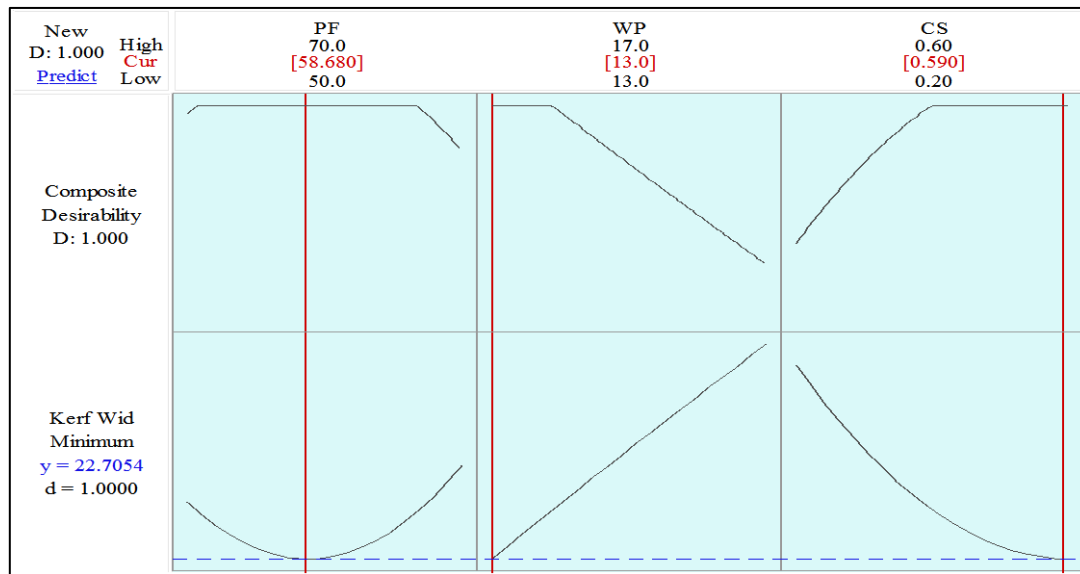


Figure 7.16 Single-objective optimization plot for the kerf width of the micro-channel.

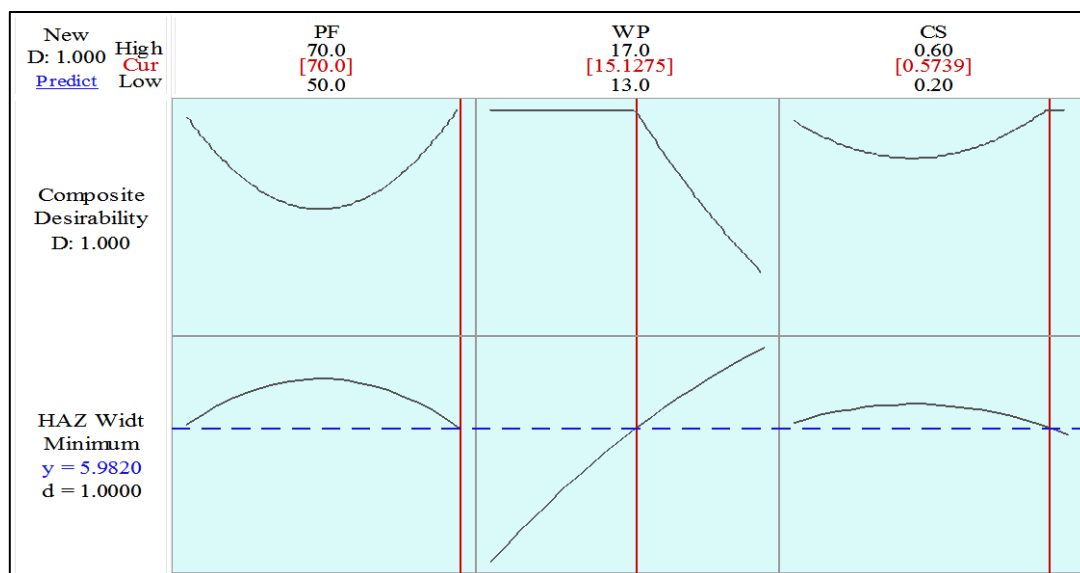


Figure 7.17 Single-objective optimization plot for the HAZ width of the micro-channel.

From figure 7.15, it is shown that the optimal conditions to get maximum depth of cut ($12.7867 \mu\text{m}$) are the pulse frequency of 50 kHz, the working power of 13 % and cutting speed of 0.06 mm/s. From figure 7.16, the optimal settings of process variables to get minimum Kerf width ($22.7278 \mu\text{m}$) are the pulse frequency of 57.70 kHz, the working power of 13 % and cutting speed of 0.60 mm/s. From figure 7.17, the optimal settings of process variables to get minimum HAZ width ($6.0535 \mu\text{m}$) are

the pulse frequency of 69.60 kHz, the working power of 15.15 % and cutting speed of 0.60 mm/s.

(ii) Multi-Objective Optimization Analysis

In multi-objective optimization, all of the goals are combined into a single desirability function. Figure 7.18 depicts the multi-objective optimization results. All of the responses have been optimized for the greatest potential outcome.

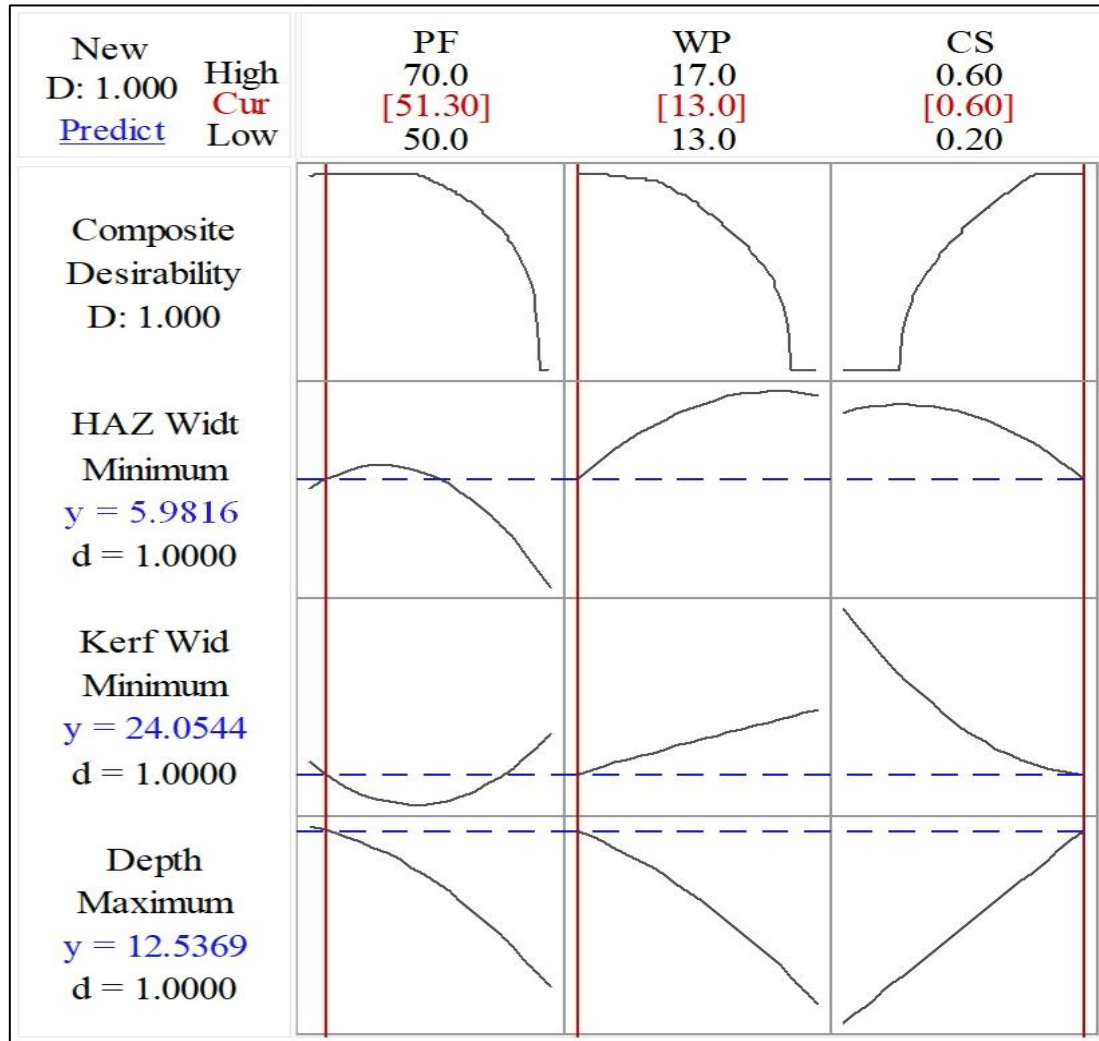


Figure 7.18 Multi-objective optimization plot for the micro-channels.

Each column of the graph in Figure 7.18 corresponds to a factor. A response variable is represented by each row of the graph. Each graph cell depicts how one of the response variables changes as a function of one of the factors, while the other factors remain constant. The current factor level settings, as well as the high and low values of factors, are displayed at the top of the column. The goal for the responses, predicted responses, y, at current factor settings, and individual desirability scores are

listed to the left of each row. It can be concluded from Figure 7.18 that a pulse frequency of 51.30 kHz, a working power of 13%, and a cutting speed of 0.60 mm/s may be used to attain desired response value like depth cut of 12.5369 μm , kerf width of 24.0544 μm , and HAZ width of 5.9816 μm can be attained.

7.3.2.5 Confirmation Test

Additional experiments have been conducted to validate the obtained optimum condition. Five experiments have been conducted and then the average of measured responses was taken into consideration. It was observed that the experimental results are fairly close to the predicted results, given below in Table 7.6 and Figure 7.19 shows the microscopic and SEM image of the micro-channel.

Table 7.6 Confirmation test of laser micromachining at air medium

Optimal parameter settings	Machining responses	Predicted value at Optimal parametric settings	Experimental value at Optimal parametric settings	% of error
PF=51.30 kHz; WP=13.0 %; CS=0.60 mm/sec	Depth of cut (μm)	12.5369	12.1124	3.39
	Kerf width (μm)	24.0544	23.0121	4.33
	HAZ width (μm)	5.9816	5.4538	8.82

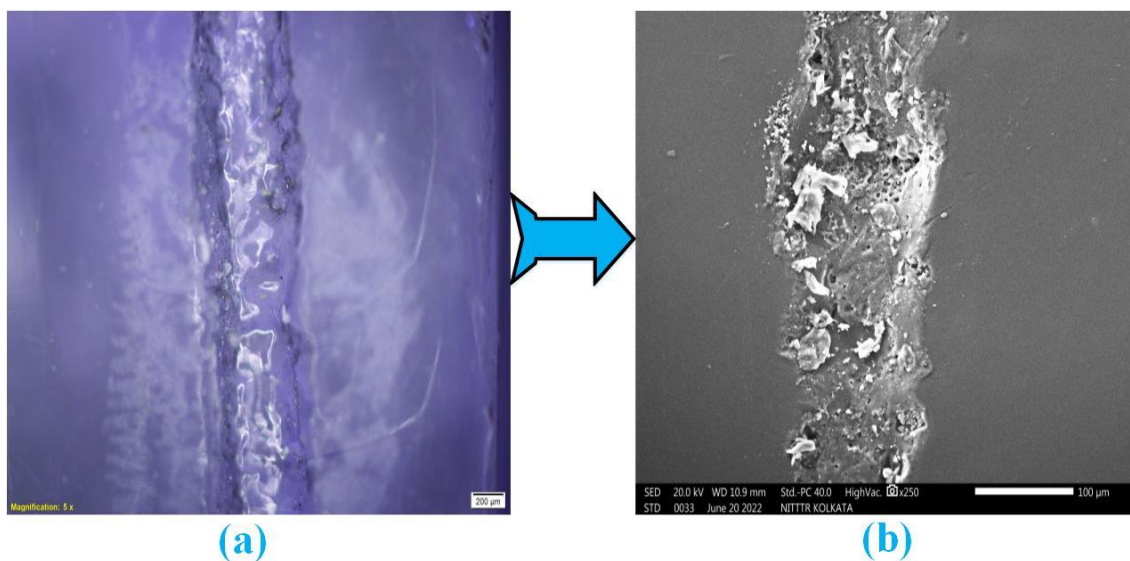


Figure 7.19 (a) Microscopic image of the micro-channel, (b) SEM micrograph

7.3.3 Outcomes

In the present study, an experimental investigation on polymethyl methacrylate (PMMA) to generate micro-channels using a fiber laser system and the laser transmission technique has been carried out. The micro-channel operations were conducted in presence of air. The absorbent substance is black tape. The primary goal of the machining operation was to maximize the depth of cut, minimize the heat affected zone (HAZ), and keep the kerf width constant. Pulse frequency, working power, and cutting speed were considered as process factors whereas, the depth of cut, kerf width, and HAZ width of the produced micro-channels were measured and analysed as responses. To correlate the input process parameters and output responses, the Response surface methodology (RSM) based technique was used. The analysis of variance (ANOVA) method was used to assess model adequacy. The tests are designed using the response surface methodology's three-factor central composite design (CCD) strategy. Based on the analysis of variance (ANOVA), it is possible to infer that all process variables are statistically significant. A parametric investigation was also carried out, and the rationale for the observed phenomena was broadly illustrated. The ideal process variable settings were determined to provide the maximum depth of cut and minimum kerf width with the smallest possible heat impacted zone (HAZ) width.

A multi-objective optimization is then performed to obtain the best results of responses depth of cut, kerf width, and HAZ width, of 12.5369 μm , 24.0544 μm , and 5.9816 μm , respectively. It was observed that the combination of 51.30 kHz pulse frequency, 13% operating power, and 0.60 mm/sec cutting speed may be considered as the best parameter setting to achieve the desired responses. The percentage of error between projected and actual experimental results at optimal conditions is found to be within the tolerance limit, indicating that the prediction analysis of fiber laser transmission micro-channeling of thick PMMA is acceptable.

7.4 Parametric Study Based on Response Surface Methodology for Laser Beam Transmission Micro-channeling of PMMA at Submerged Condition of Water Medium

7.4.1 Experimental Details

Table 7.7 shows the constant and variable process parameter settings, as well as their levels. The pulse frequency, working power, and cutting speed all varied from 50-70 kHz, 13-17 %, and 0.2-0.6 mm/sec, respectively. Some other parameters' effects on responses may be kept constant during the experiment.

Table 7.7 Process Parameter Levels

Process Parameter	Unit	Symbol	Levels				
			-2	-1	0	1	2
Pulse Frequency (PF)	kHz	P	50	55	60	65	70
Working Power (WP)	%	Q	13	14	15	16	17
Cutting Speed (CS)	mm/sec	R	0.2	0.3	0.4	0.5	0.6
Constant factors	Pulse Width = 99%						
	Number of passes = Single pass						

7.4.2 Experimental Results and Discussion

Laser transmission cutting in the partially submerged condition was used to carry out 20 sets of experiments. The experimental results are given in Table 7.8. Microscopic views of the PMMA substrate and the micro-channels fabricated by the laser transmission cutting in partially submerged conditions are given in Figure 7.20 and Figure 7.21, respectively.

Table 7.8 Experimental results

Experiment No.	Pulse Frequency (PF: kHz)	Working Power (WP: %)	Cutting Speed (CS: mm/sec)	Depth of Cut (μm)	Kerf Width (μm)	HAZ Width (μm)
1	-1	-1	-1	25.180	32.500	12.401
2	1	-1	-1	14.230	46.240	7.761
3	-1	1	-1	31.270	42.390	16.540
4	1	1	-1	23.670	57.070	18.260
5	-1	-1	1	18.370	34.960	9.451
6	1	-1	1	16.230	33.190	5.615
7	-1	1	1	19.170	45.350	15.433
8	1	1	1	21.700	43.120	17.910
9	-2	0	0	26.190	39.290	10.525
10	2	0	0	15.280	54.613	8.200
11	0	-2	0	13.550	25.470	5.001
12	0	2	0	22.570	42.110	20.699
13	0	0	-2	26.980	48.180	14.475
14	0	0	2	19.680	38.220	11.235
15	0	0	0	23.620	41.950	16.525
16	0	0	0	22.980	42.320	16.535
17	0	0	0	24.110	43.330	16.595
18	0	0	0	23.980	42.980	16.390
19	0	0	0	23.540	43.540	16.500
20	0	0	0	24.010	43.690	16.390

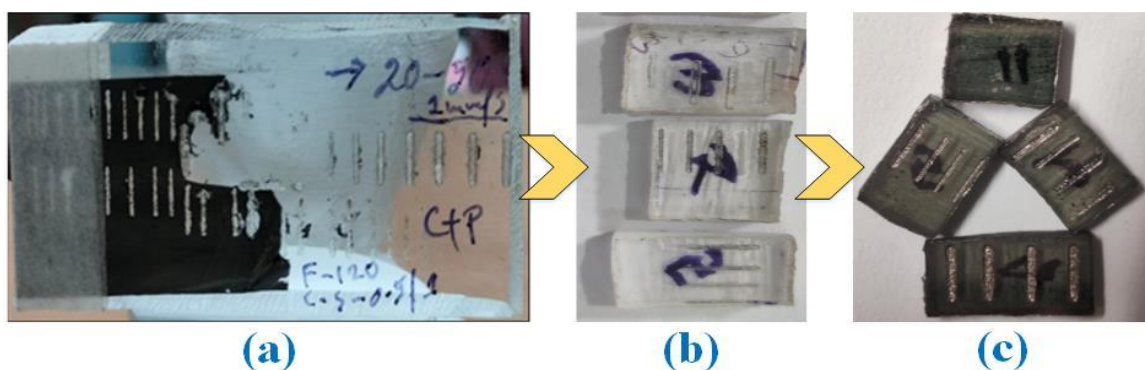


Figure 7.20 PMMA workpiece after fiber laser transmission cutting in water medium, (a) Parent sample, (b) Sliced micro-machined sample, (c) Gold coated micro-machined sample.

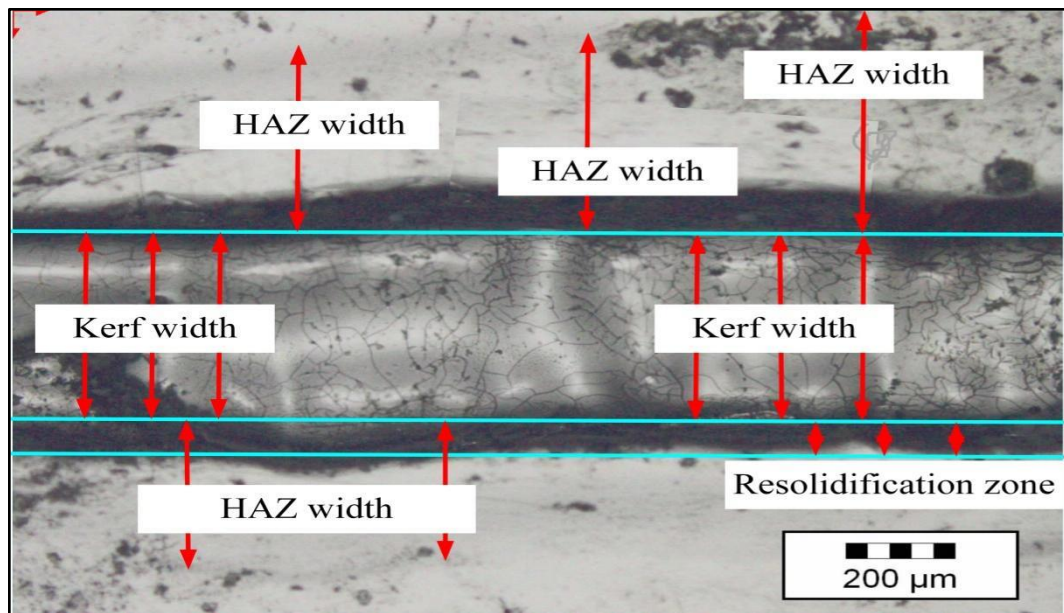


Figure 7.21 Microscopic view of the PMMA micro-channel.

7.4.2.1 Development of Second-Order Polynomial Model

The mathematical relationship between the response and variable process parameters is established using response surface modeling (central composite design). The second-order polynomial equations for all responses considered are as follows.

Expression for Depth of cut

$$Y_{\text{Depth of cut}} = 23.665 - 2.499 P + 2.490 Q - 2.093 R - 0.764 P^2 - 1.433 Q^2 - 0.115 R^2 + 1.002 PQ + 2.367 PR - 1.158 QR \quad (\text{Eq}^n.7.4)$$

Expression for Kerf Width

$$Y_{\text{Kerf Width}} = 42.991 + 3.442 P + 4.645 Q - 2.594 R + 1.007 P^2 - 2.283 Q^2 + 0.069 R^2 + 0.060 PQ - 4.053 PR - 0.050 QR \quad (\text{Eq}^n.7.5)$$

Expression for HAZ Width

$$Y_{\text{HAZ Width}} = 16.4950 - 0.5581 P + 4.0194 Q - 0.8146 R - 1.7787 P^2 - 0.9069 Q^2 - 0.9056 R^2 + 1.5841 PQ + 0.1951 PR + 0.4549 QR \quad (\text{Eq}^n.7.6)$$

Where P, Q, and R indicate coded values of the process parameters, e.g., pulse frequency, working power, and cutting speed, respectively.

7.4.2.2 ANOVA of Machining Responses

F ratio value and P value of analysis of variance (ANOVA) result may validate the developed regression models. The calculated F-ratio value should be higher than critical P ratio and the considered significant level should be higher than P-value. Tables 7.9, 7.10, and 7.11 show ANOVA results of depth of cut, kerf width, and HAZ width respectively. The critical F ratio at the 95% confidence level remains to be lower than the calculated F ratio values of source regression for considered responses. For all considered responses P values of source regression remain to be less than 0.05. Tables 7.9, 7.10, and 7.11 show the results of an ANOVA study of the quadratic model with different adequacy measures R^2 , adjusted R^2 , and predicted R^2 . To predict response values developed regression model equations for all characteristics remain to be adequate.

Table 7.9 ANOVA result of depth of cut at submerged condition

Source	DF	Adj SS	Adj MS	F-Value	P-Value
Model	9	391.881	43.5423	103.48	0.000
Linear	3	269.159	89.7195	213.22	0.000
P	1	99.900	99.9000	237.41	0.000
Q	1	99.202	99.2016	235.75	0.000
R	1	70.057	70.0569	166.49	0.000
Square	3	59.123	19.7078	46.83	0.000
P ²	1	14.671	14.6705	34.86	0.000
Q ²	1	51.603	51.6027	122.63	0.000
R ²	1	0.333	0.3332	0.79	0.394
2-Way Interaction	3	63.599	21.1996	50.38	0.000
P×Q	1	8.040	8.0400	19.11	0.001
P×R	1	44.840	44.8404	106.56	0.000
Q×R	1	10.718	10.7185	25.47	0.001
Error	10	4.208	0.4208		
Lack-of-Fit	5	3.315	0.6630	3.71	0.088
Pure Error	5	0.893	0.1785		
Total	19	396.089			
Model Summary		S	R ²	R ² (adj.)	R ² (pred.)
		0.648686	98.94%	97.98%	92.77%

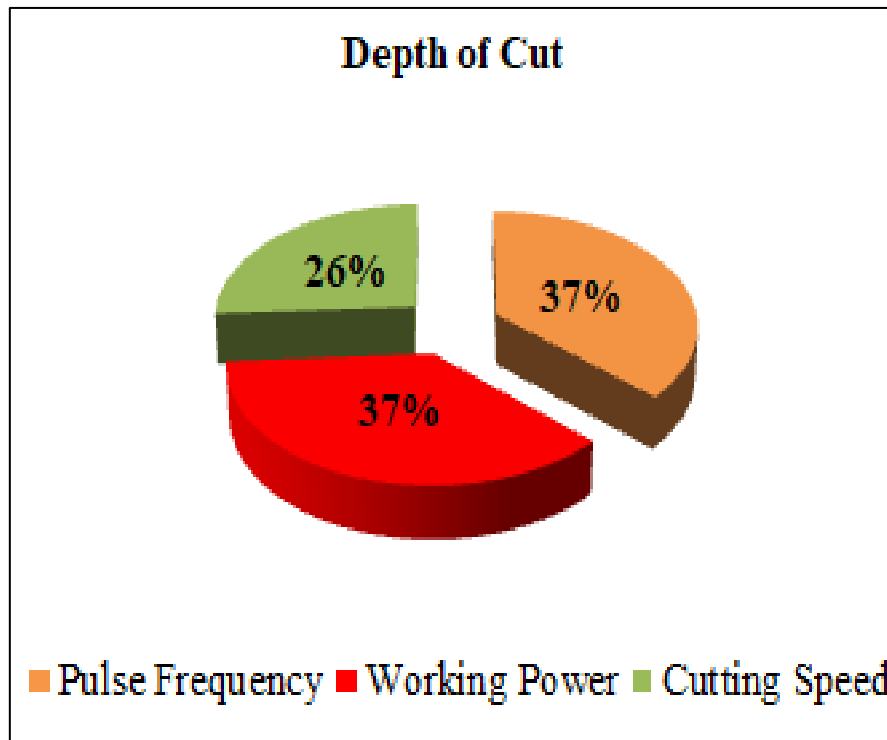


Figure 7.22 Contribution of parameters depth of cut

According to Table 7.9, the model's associated p-value is less than 0.05 (i.e., $\alpha = 0.05$, or 95% confidence level), indicating that the model terms are statistically significant. The ideal result is implied by the model's lack-of-fit value, which is non-significance. The two-way interaction term and each of the input process variables are important and have an impact on the machining responses in some way. As indicated in table, pulse frequency (37.12 %) is the most important element for depth of cut, followed by working power (36.86 %), and cutting speed (26.03 %). Other adequacy measures R^2 , adjusted R^2 , and predicted R^2 have reasonable agreement and are close to 100%, indicating that the model is adequate. Figure 7.22 depicts the impact of various settings on depth of cut.

Table 7.10 ANOVA result of kerf width at submerged condition

Source	DF	Adj SS	Adj MS	F-Value	P-Value
Model	9	966.246	107.361	117.88	0.000
Linear	3	642.374	214.125	235.10	0.000
P	1	189.517	189.517	208.09	0.000
Q	1	345.216	345.216	379.04	0.000
R	1	107.641	107.641	118.19	0.000
Square	3	192.442	64.147	70.43	0.000
P ²	1	25.504	25.504	28.00	0.000
Q ²	1	131.072	131.072	143.91	0.000
R ²	1	0.121	0.121	0.13	0.723
2-Way Interaction	3	131.431	43.810	48.10	0.000
P×Q	1	0.029	0.029	0.03	0.862
P×R	1	131.382	131.382	144.25	0.000
Q×R	1	0.020	0.020	0.02	0.885
Error	10	9.108	0.911		
Lack-of-Fit	5	6.672	1.334	2.74	0.146
Pure Error	5	2.436	0.487		
Total	19	975.354			
Model Summary		S	R ²	R ² (adj.)	R ² (pred.)
		0.954339	99.07%	98.23%	93.95%

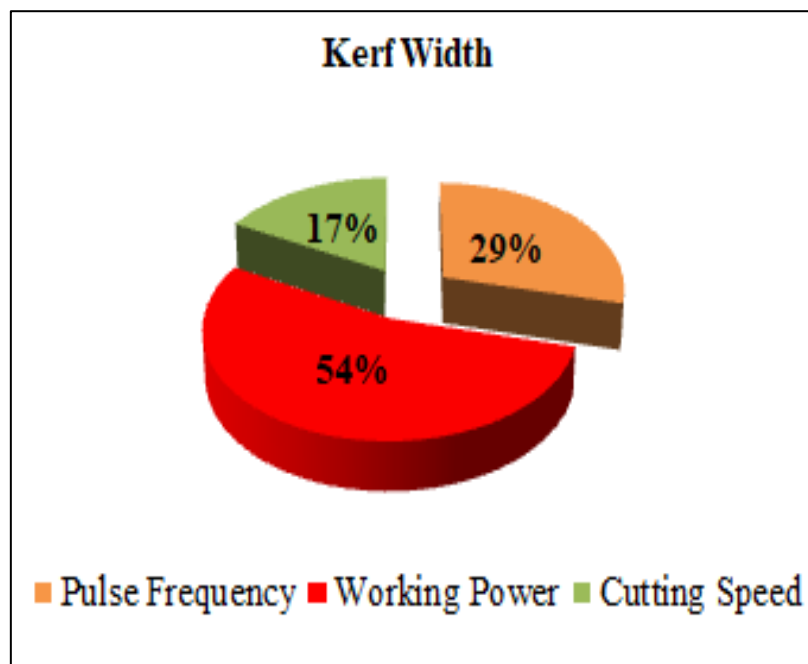


Figure 7.23 Contribution of parameters on kerf width

Table 7.10 shows that the model's p-value is less than 0.05 (i.e., $\alpha = 0.05$, or 95 % confidence level), indicating that its terms are statistically significant. The model's lack-of-fit value implies non-significance, which is ideal. All of the input process factors, as well as the two-way interaction term, are significant and influence machining reactions in some way. According to the table, working power (53.74 %) is the most important component for cutting depth, followed by pulse frequency (29.50 %), and cutting speed (16.76 %). Other adequacy measures R^2 , adjusted R^2 , and predicted R^2 are in reasonable agreement and close to 100%, indicating that the model is adequate. Figure 7.23 depicts the influence of several parameters on kerf width.

Table 7.11 ANOVA result of HAZ width at submerged condition

Source	DF	Adj SS	Adj MS	F-Value	P-Value
Model	9	388.030	43.114	2241.82	0.000
Linear	3	274.093	91.364	4750.66	0.000
P	1	4.983	4.983	259.10	0.000
Q	1	258.494	258.494	13440.87	0.000
R	1	10.616	10.616	552.01	0.000
Square	3	91.902	30.634	1592.86	0.000
P ²	1	79.550	79.550	4136.34	0.000
Q ²	1	20.678	20.678	1075.17	0.000
R ²	1	20.621	20.621	1072.20	0.000
2-Way Interaction	3	22.035	7.345	381.93	0.000
P×Q	1	20.076	20.076	1043.87	0.000
P×R	1	0.305	0.305	15.84	0.003
Q×R	1	1.655	1.655	86.07	0.000
Error	10	0.192	0.019		
Lack-of-Fit	5	0.158	0.032	4.60	0.060
Pure Error	5	0.034	0.007		
Total	19	388.223			
Model Summary		S	R ²	R ² (adj.)	R ² (pred.)
		0.138679	99.95%	99.91%	99.65%

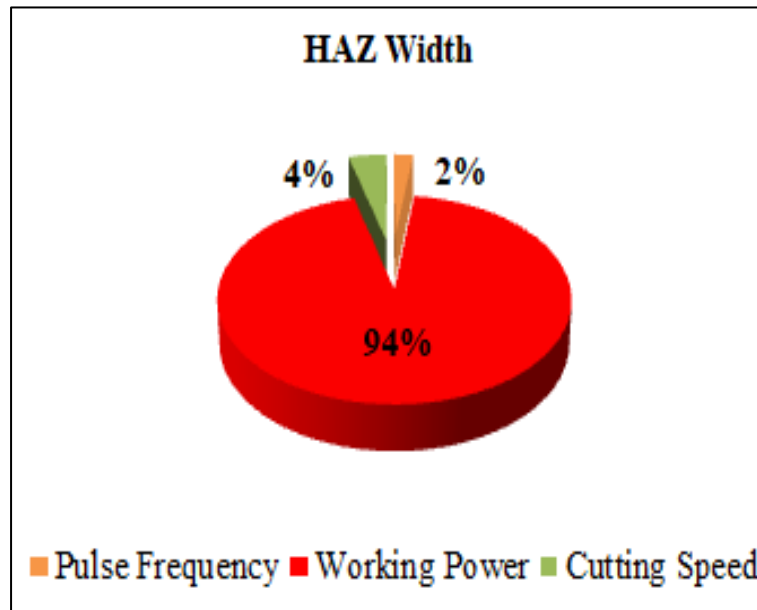


Figure 7.24 Contribution of parameters on HAZ width

As shown in Table 7.11, the model's related p-value is less than 0.05 (i.e., $\alpha = 0.05$, or 95 % confidence level), which means that the model terms are statistically significant. The model's lack-of-fit value implies non-significance, which is ideal. All of the input process factors and the two-way interaction term are important and have some effect on the machining reactions. Working power (95.22 %) is statistically the most important component for depth of cut, followed by cutting speed (3.32 %), and pulse frequency (1.46 %). Other adequacy measures R^2 , adjusted R^2 , and predicted R^2 are in reasonable agreement and close to 100%, indicating that the model is adequate. Figure 7.24 depicts the effect of various parameters on HAZ width.

7.4.2.3 Parametric Analysis

(i) Parametric Effects on Depth of Cut

Laser transmission micro-channeling operation, keeping the workpiece in submerged condition underwater has been conducted. Obtaining the depth of cut in laser micro-machining is always a challenging task as it is influenced by a number of laser machining process parameters. The influence of the laser machining parameters, i.e., pulse frequency, working power, and cutting speed on the depth of cut phenomena during laser micro-channeling of 11.328 mm thick PMMA workpieces has been analyzed.

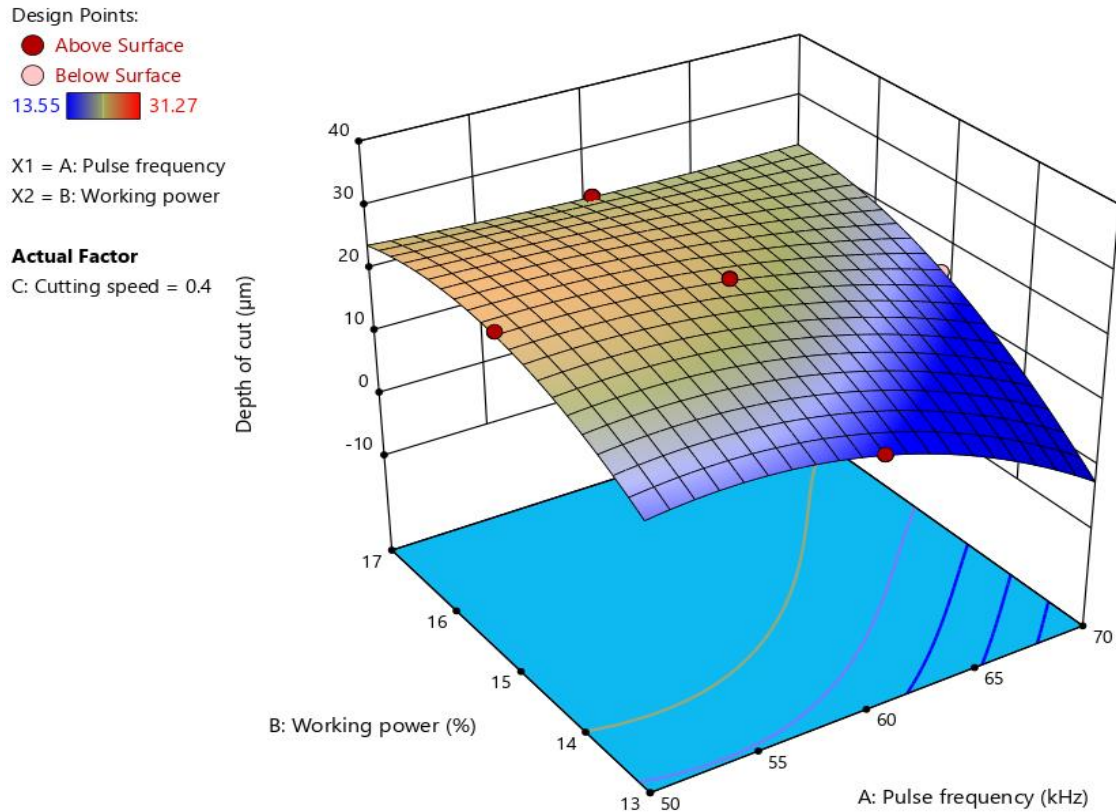


Figure 7.25 Surface plot of depth of cut versus working power and pulse frequency. Figure 7.25 shows the combined effects of pulse frequency and working power on depth of cut when cutting speed value is kept constant at 0.4 mm/sec. It is evident from the plot that depth of cut increases with the increase in working power, at low pulse frequency, and it gradually decreases a little bit with a further increase in working power. An increase in the working power at low pulse frequency, high thermal energy, and high quality of laser beam is generated which significantly increases the depth of cut. The depth of cut decreases with further increase in working power, which may be attributed due to the re-solidification of molten material at very high energy density because of the same reason and high pulse repetition rate depth of cut steeply increases with increase in working power at a high level of pulse frequency. With an increase in pulse frequency, comparatively less energy is generated which cannot interact with workpiece material at moderate value of energy due to loss of energy during contact with water on account of the Beer–Lambert's law on the workpiece surface. Due to this reason, laser beam cannot yield the ablation threshold limit at the bottom of cut region resulting in less material removal from the machining zone generating a low depth of cut and vice versa. Due to the same reason, the depth of cut decreases with increase in pulse frequency at entire range of working power.

Design Points:

● Above Surface

○ Below Surface

13.55  31.27

X1 = A: Pulse frequency

X2 = C: Cutting speed

Actual Factor

B: Working power = 15

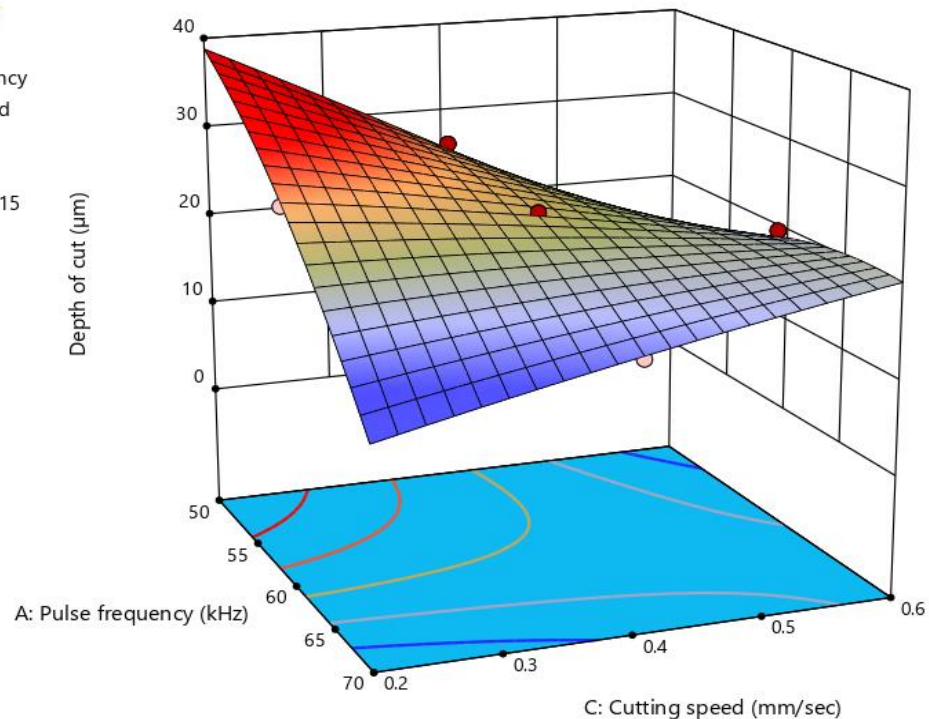


Figure 7.26 Surface plot of depth of cut versus pulse frequency and cutting speed.

Figure 7.26 shows the influence of pulse frequency and cutting speed on depth of cut when working power value is kept constant at 15%. It is found from the plot that the depth of cut reaches maximum at a lower pulse frequency in combination with the low cutting speed. The quantity of spot overlapping varies depending on the pulse frequency and cutting speed combination. Low cutting speed results in a higher number of laser spot overlapping and low pulse frequency produces higher energy density, which contributes to an increase in depth of cut. However, as the cutting speed increases, the heat available for cutting decreases, making the removal of molten material from the cutting front difficult which in turn reduces the depth of cut. Due to the refraction effect at submerged conditions, laser spot diameter decreases which results in the enhancement of shear force along the work surface and a decrease in penetration force along the formation of water waves during laser beam machining. At the said parametric settings, the energy density on the spot in submerged conditions reaches the highest level because of a focused laser beam in combination with the highest value of interaction time between the laser beam and with work substrate at the lowest cutting speed. At higher pulse frequency, with an increase in cutting speed, the depth of cut increases. It may be due to bubble burst in the

machining zone, which causes uneven machining to occur on the workpiece surface. With an increase in cutting speed at a higher value of pulse frequency, depth of cut decreases because of poor quality of laser beam at high pulse frequency in combination with less interaction time with increase in cutting speed.

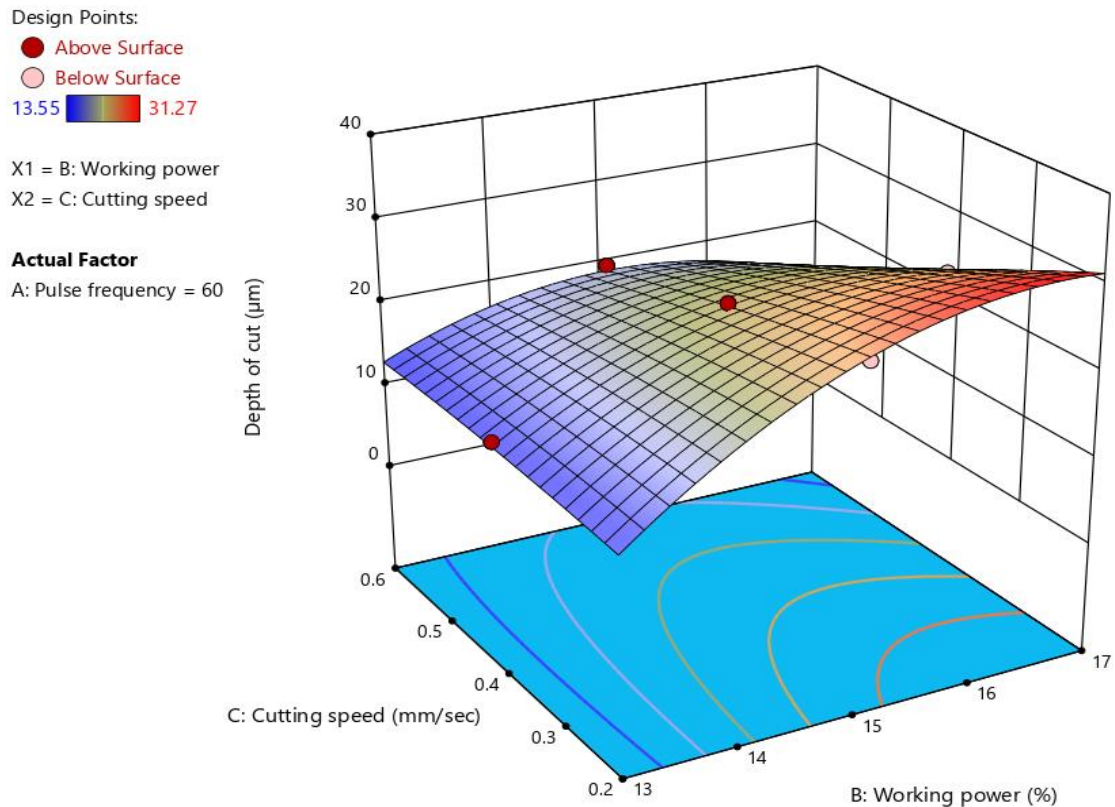


Figure 7.27 Surface plot of depth of cut versus working power and cutting speed. Figure 7.27 illustrates the combined effects of the working power and cutting speed on depth of cut when the pulse frequency is kept constant at 60 kHz. It is observed that the depth of cut increases with an increase in working power sharply at a lower cutting speed. The increment of working power leads to an increase in average power as well as the peak power of the generated laser beam at a lower cutting speed, resulting in higher material interaction time with a high penetration rate which causes higher material removal from the surface. As a result of which the depth of cut increases. It is also found that depth of cut does not vary significantly with cutting speed at lower working power but it decreases with an increase in cutting speed at high energy density. At low working power and because of absorption of laser power by water caused by deflection produce very weak laser beam which may not be able

to remove material from the surface of the workpiece. At higher working power, laser material interaction time decreases with an increase in cutting speed which subsequently decreases the depth of cut and vice versa. This is due to lower interaction time causing lower heat generation at machining zone leading to a lower depth of cut. At higher cutting speed, depth of cut initially increases and then decreases with an increase in working power. It may be due to bubble formation which causes uneven machining to occur in the machining zone. The depth of cut significantly increases with an increase in working power at low cutting speed. This may be due to the fact that lower cutting speed results in higher laser material interaction time and higher thermal energy generation with an increase in working power.

(ii) Parametric Effects on Kerf Width

Kerf width quality is a significant consideration in the laser beam micro-channeling approach. A lower kerf width combined with a high depth of cut results in micro-channels with a high aspect ratio (width/depth). The combined effect of pulse frequency and working power on kerf width at a constant cutting speed of 0.4 mm/sec is depicted in Figure 7.28. Kerf width increases with the increase in working power at entire range of pulse frequency. This is due to rise in energy density at machining zone which is absorbed by the absorbent material, and this excess energy helps to increase the temperature of the backside of PMMA. This condition accelerates the phase transformation procedure and increases the kerf width. Similarly, with an increase in pulse frequency, kerf width initially decreases and then increases at all levels of working powers. With an increase in pulse frequency, the pulse repetition rate increases but re-solidification of molten material on the edges of the cut front takes place in a submerged condition which reduces the kerf width. After a certain range, the kerf width increases with a further increase in pulse frequency causing a higher pulse repetition rate results in higher material removal from the top surface of the workpiece.

Design Points:

- Above Surface
- Below Surface
- 25.47  57.07

X1 = A: Pulse frequency
X2 = B: Working power

Actual Factor
C: Cutting speed = 0.4

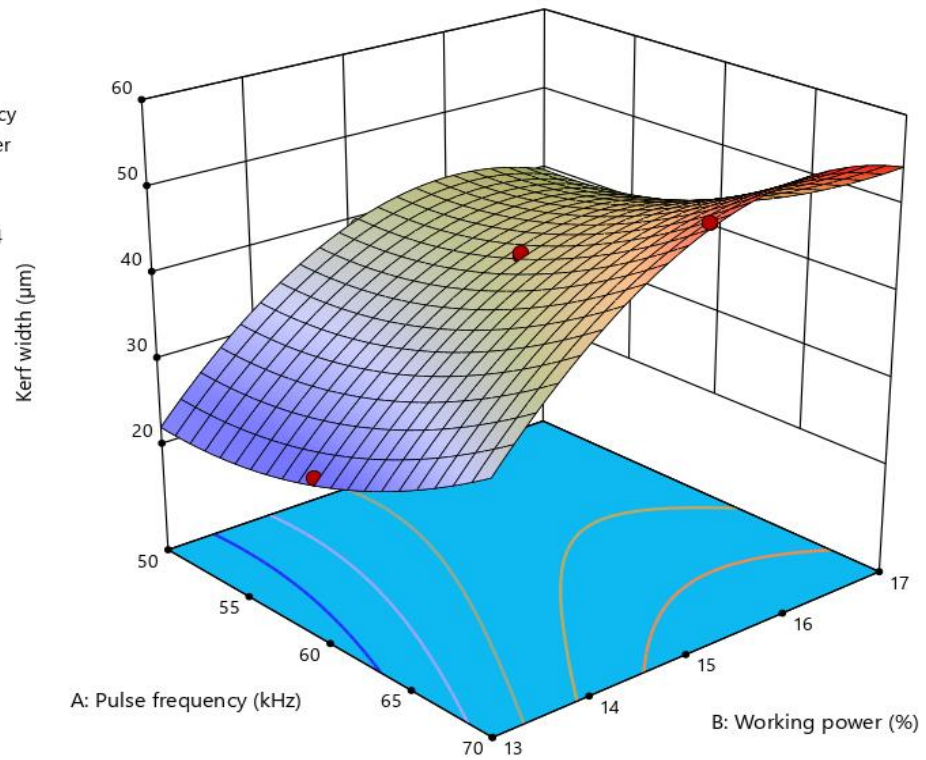



Figure 7.28 Surface plot of kerf width versus pulse frequency and working power.

Design Points:

- Above Surface
- Below Surface
- 25.47  57.07

X1 = A: Pulse frequency
X2 = C: Cutting speed

Actual Factor
B: Working power = 15

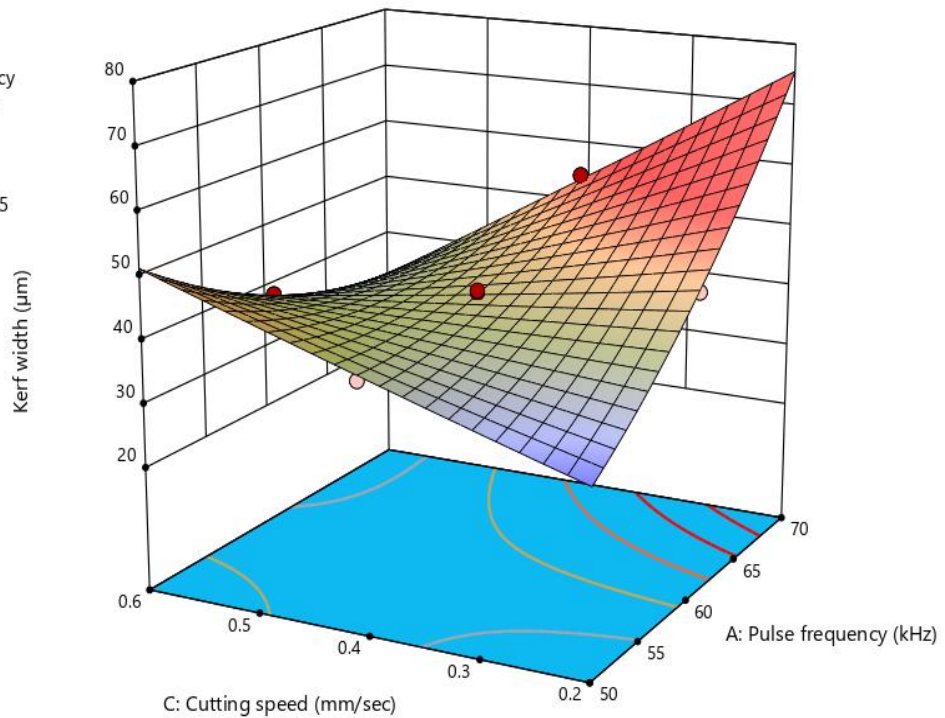


Figure 7.29 Surface plot of kerf width versus pulse frequency and cutting speed.

Figure 7.29 illustrates the combined effects of pulse frequency and cutting speed on kerf width at working power value of 15%. It is noticed that the kerf width increases steeply with increase in pulse frequency at lower cutting speed. The lower cutting speed produces more overlapping of incident laser beam in the machining zone, which causes wider kerf width. Kerf width decreases with the increase in cutting speed at lower pulse frequency due to insufficient thermal energy transmission to the work substrate. Kerf width increases with increase in cutting speed at higher pulse frequency. As the lower pulse frequency comparatively generates higher value of energy density at the spot of irradiation which helps to form more melt pool. This excess amount of molten debris may not properly remove from the zone of machining by higher cutting speed leading to non-uniform kerf width along the travel path of laser, which may cause increment of kerf width due to uneven machining.

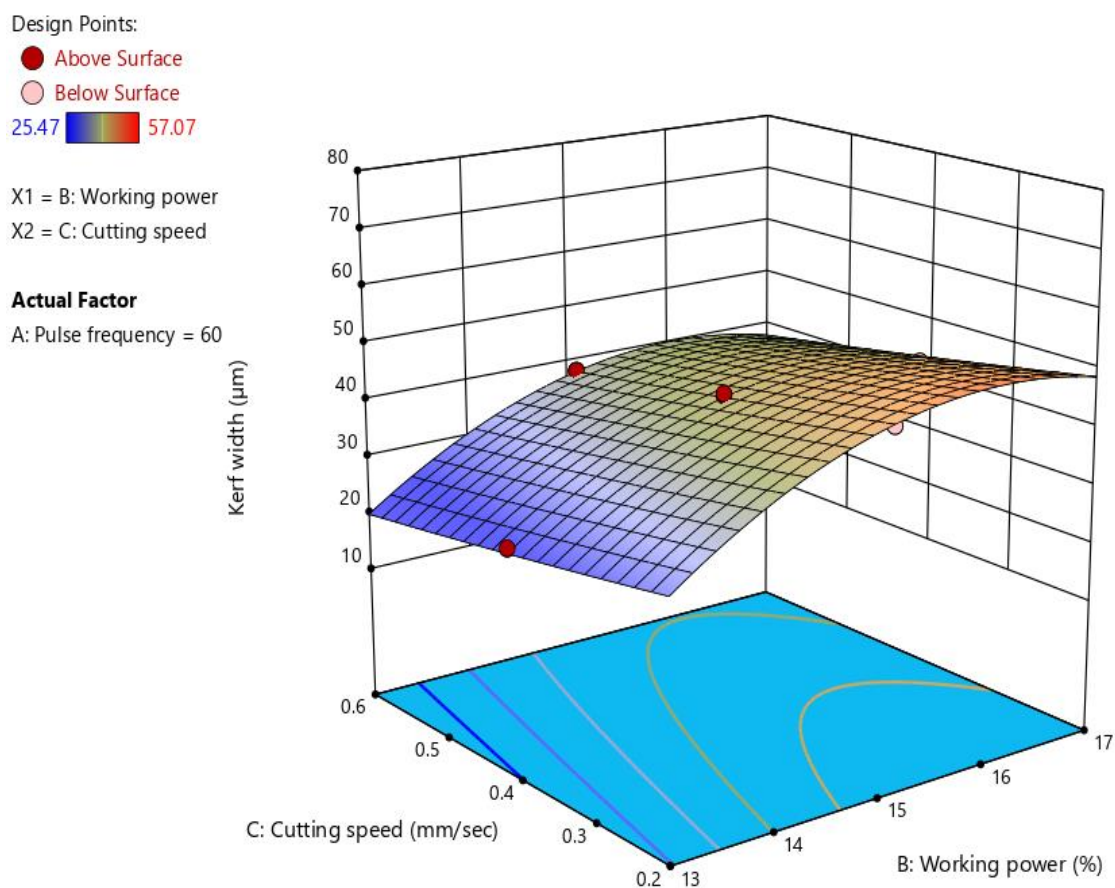


Figure 7.30 Surface plot of kerf width versus working power and cutting speed.

The nature of curve shown in Figure 7.30 demonstrates the combined effects of cutting speed and working power on depth of cut when the pulse frequency is kept constant at 60 kHz. In the plot, the kerf width initially increases and then decreases

with an increase in working power at the entire range of cutting speed. An increment of working power leads to increase in energy density which causes an initial increment of kerf width but further increase in working power causes excessive energy density resulting in spattering and resolidification of molten material which in turn reduces kerf width. At the entire range of working power, the variation of kerf width is insignificant. The fact that less interaction time at a higher cutting speed produces less thermal energy on the back surface of the work substrate does not have a predominant effect on kerf width.

(iii) Parametric Effects on HAZ Width

Figure 7.31 depicts the influence of pulse frequency and working power on HAZ width at a constant cutting speed of 0.4 mm/sec. It is evident from the surface plot that the HAZ width decreases with an increase in pulse frequency at lower working power. During underwater laser beam machining, the settling time of the debris material removed from the cut zone is much for which the scattering and absorption of thermal energy of laser beam are more which in turn produces lower HAZ width. HAZ width increases with an increase in pulse frequency at higher working power. High energy density at high working power coupled with a high repetition rate of incident laser beam with an increase in pulse frequency generates a very high amount of thermal energy on the workpiece surface resulting in an increment in HAZ width. But, at very high pulse frequencies, the quality of the laser beam deteriorates due to less peak power and produces less HAZ width. At lower frequencies, HAZ width initially increases and then decreases after a certain range with an increase in working power. Whereas in submerged conditions the refractive index changes linearly resulting in less heat input to the top surface of the workpiece. For that reason, HAZ width may be decreased in water-submerged conditions. Also, an increase in working power results in an increase in HAZ width at a higher pulse frequency. A wide HAZ width is produced by the high working power due to the generation of high thermal energy.

The variation of HAZ width versus pulse frequency and cutting speed when working power is kept constant at 15% is shown in Figure 7.32. HAZ width first grows slightly and then shrinks as pulse frequency rises and a similar variation of HAZ width is seen at the entire range of cutting speeds. HAZ width initially increases as a result of longer contact times because of a higher pulse repetition rate which produces more heat in the machining zone. However, a further rise in pulse frequency results in a lower energy density and, when combined with the water effect, reduces HAZ width.

Design Points:

- Above Surface
- Below Surface
- 5.001  20.699

X1 = A: Pulse frequency
X2 = B: Working power

Actual Factor

C: Cutting speed = 0.4

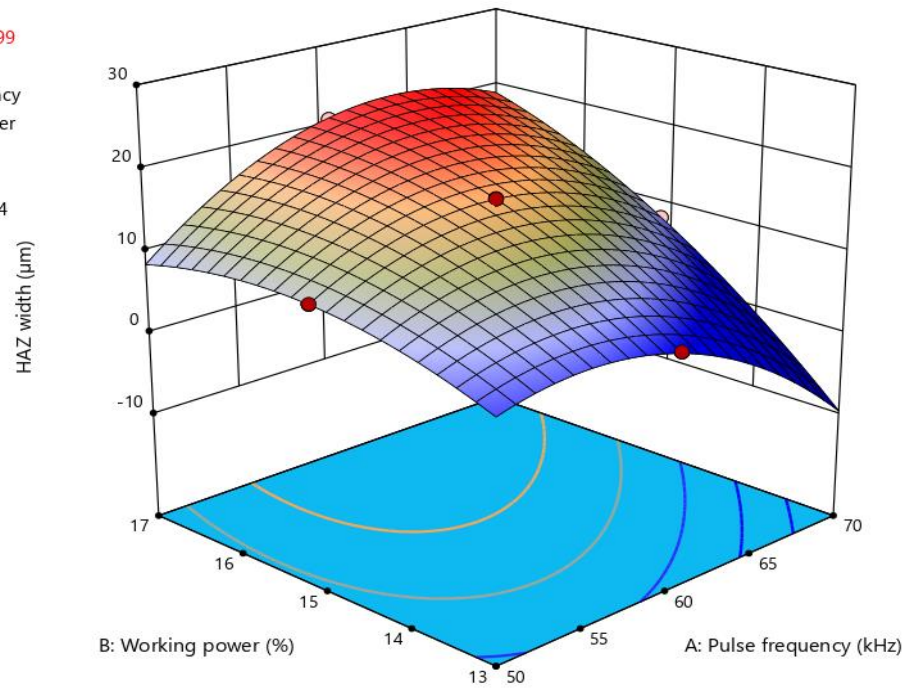


Figure 7.31 Surface plot of HAZ width versus working power and pulse frequency.

Design Points:

- Above Surface
- Below Surface
- 5.001  20.699

X1 = A: Pulse frequency
X2 = C: Cutting speed

Actual Factor

B: Working power = 15

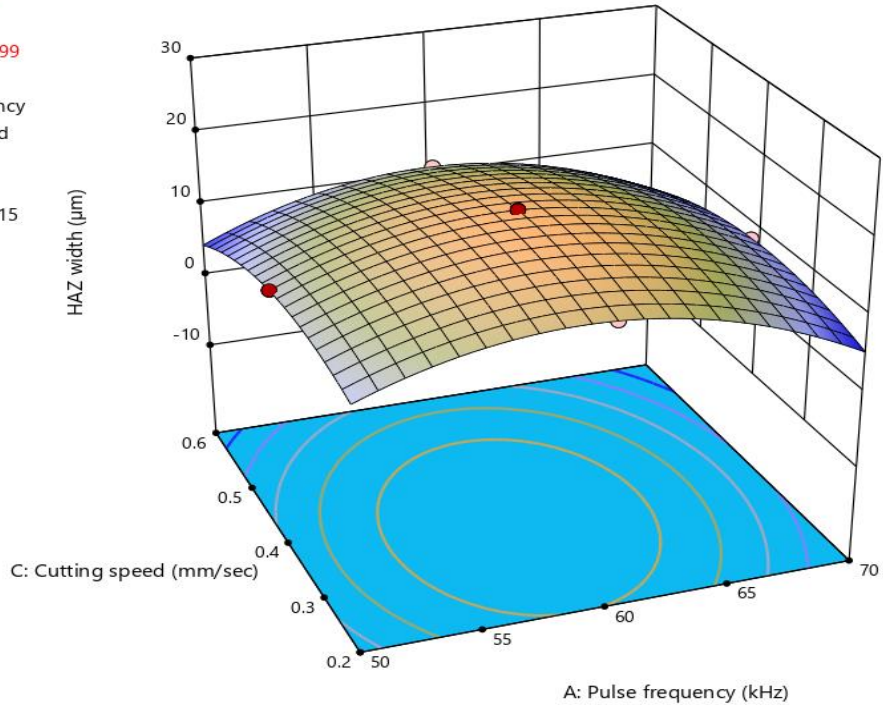


Figure 7.32 Surface plot of HAZ width versus pulse frequency and cutting speed.

Also, a gentle reduction of HAZ width is observed with an increase in cutting speed, and after a certain range, HAZ width decreases with a further increase in cutting

speed at all values of pulse frequency. Since, the working power is set at 15%, higher energy density may be produced, which when coupled with higher peak power at lower pulse frequency results in more heat generation in the machining zone. With these parameter settings, increased cutting force with an increase in cutting speed enhances spatter formation and subsequently increases the HAZ width. But, with further increases in cutting speed, laser material interaction time gets reduced. At the same time, the water medium causes less energy to be used and less heat to be produced; this may reduce the thermal effect in the machining zone and decreases the HAZ width.

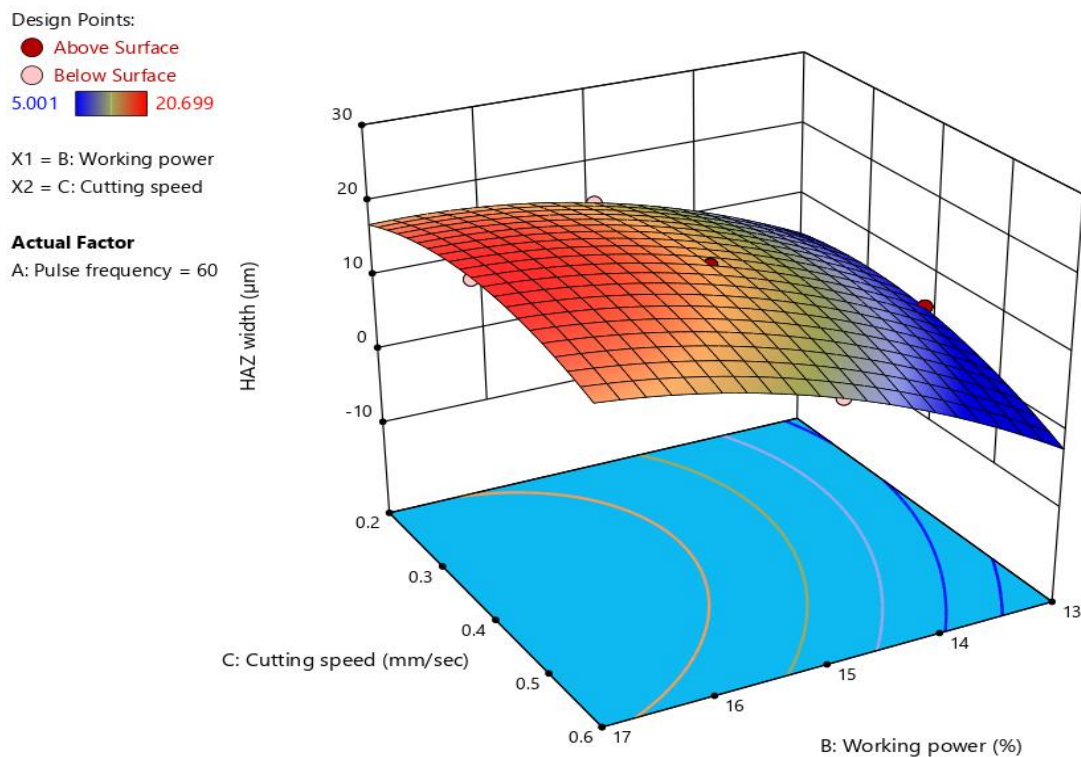


Figure 7.33 Surface plot of HAZ width versus working power and cutting speed.

The integrated effects of working power and cutting speed on HAZ width holding pulse frequency at 60 kHz are shown in Figure 7.33. It may be noted that the HAZ width increases steeply with an increase in working power at the entire range of cutting speed. This may be due to the fact that when working power goes up, there is more thermal energy in the machining zone, and produces more HAZ width. Whereas, the HAZ width decreases with an increase in cutting speed at lower working power. Lower working power generates less thermal energy and an increase in the scanning speed results in lower interaction time and develops lower HAZ width. An increase in power setting causes excessive removal of material. It is observed that the

HAZ width initially enhances slightly with an increase in cutting speed at higher working power but later on it decreases a little bit with a further increase in cutting speed. Actually, at a faster scanning speed, the propagation of heat in the workpiece sample is achieved in a longer span of time, causing minimization of the cut surface damage in terms of HAZ width.

7.4.2.4 Determination of Optimal Process Parameter Using Response Surface Methodology

(i) Single-Objective Optimization Analysis

Optimization of machining characteristics has been done to find the best values for the different process variables.

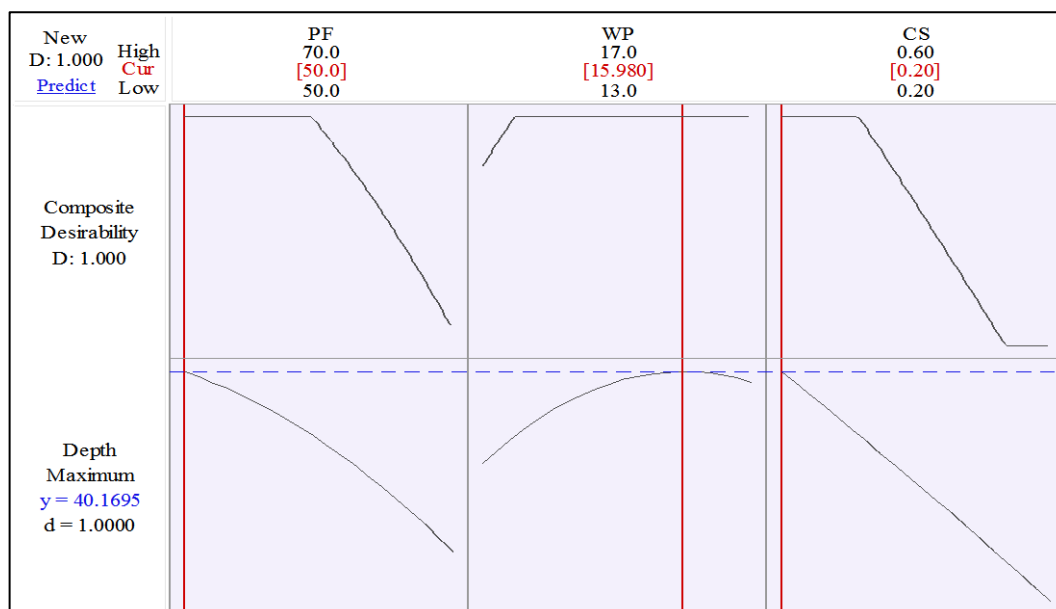


Figure 7.34 Single-objective optimization plot for the depth of cut of the micro-channel.

The best parameters for achieving the maximum depth of cut ($40.1693\mu\text{m}$) are a pulse frequency of 50 kHz, a working power of 15.9899 %, and a cutting speed of 0.20 mm/s, as shown in Figure 7.34. From Figure 7.35, the optimal settings of process variables to get minimum Kerf width ($23.0870\mu\text{m}$) are the pulse frequency of 54.0255 kHz, the working power of 13.4262 %, and cutting speed of 0.20 mm/s. From Figure 7.36, the optimal settings of process variables to get minimum HAZ width ($5.0881\mu\text{m}$) are the pulse frequency of 50 kHz, the working power of 15.1093 %, and cutting speed of 0.5851 mm/s.

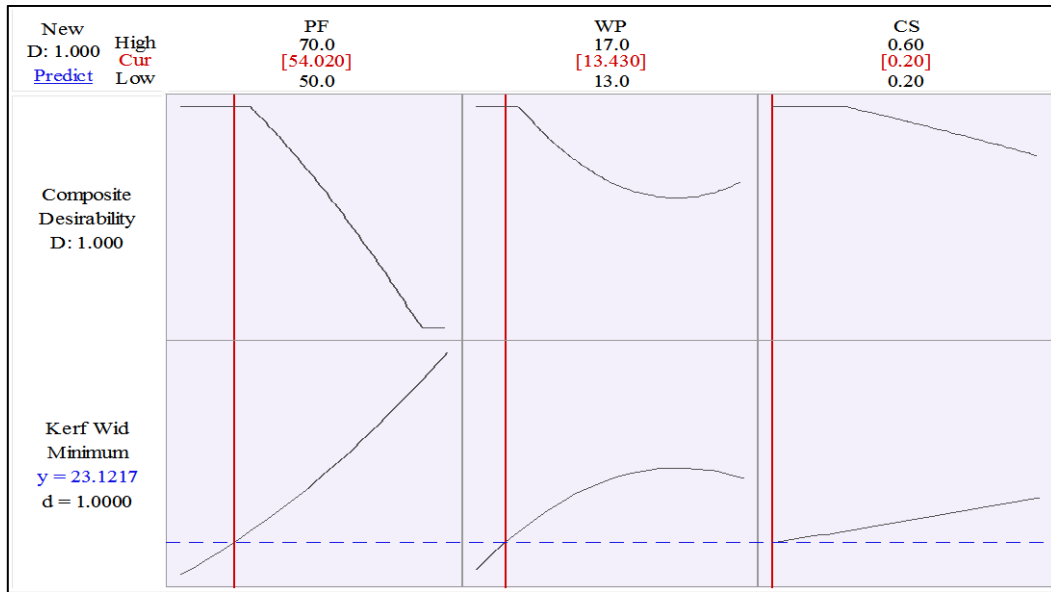


Figure 7.35 Single-objective optimization plot for the kerf width of the micro-channel.

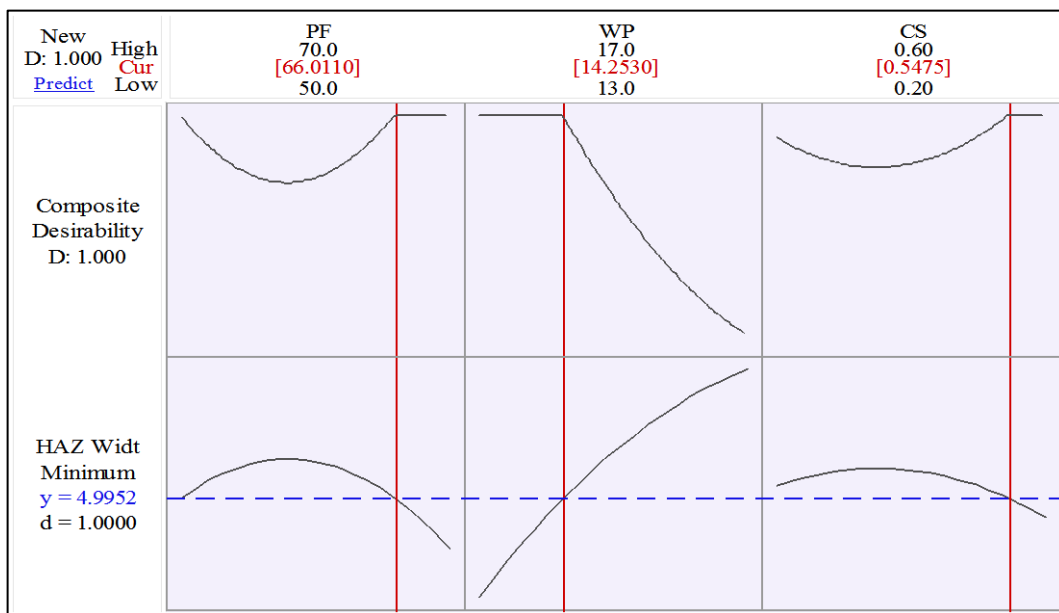


Figure 7.36 Single-objective optimization plot for the HAZ width of the micro-channel.

(ii) Multi-Objective Optimization Analysis

In multi-objective optimization, all of the goals are combined into a single desirability function. Figure 7.37 depicts the multi-objective optimization results. All of the responses have been optimized for the greatest potential outcome.

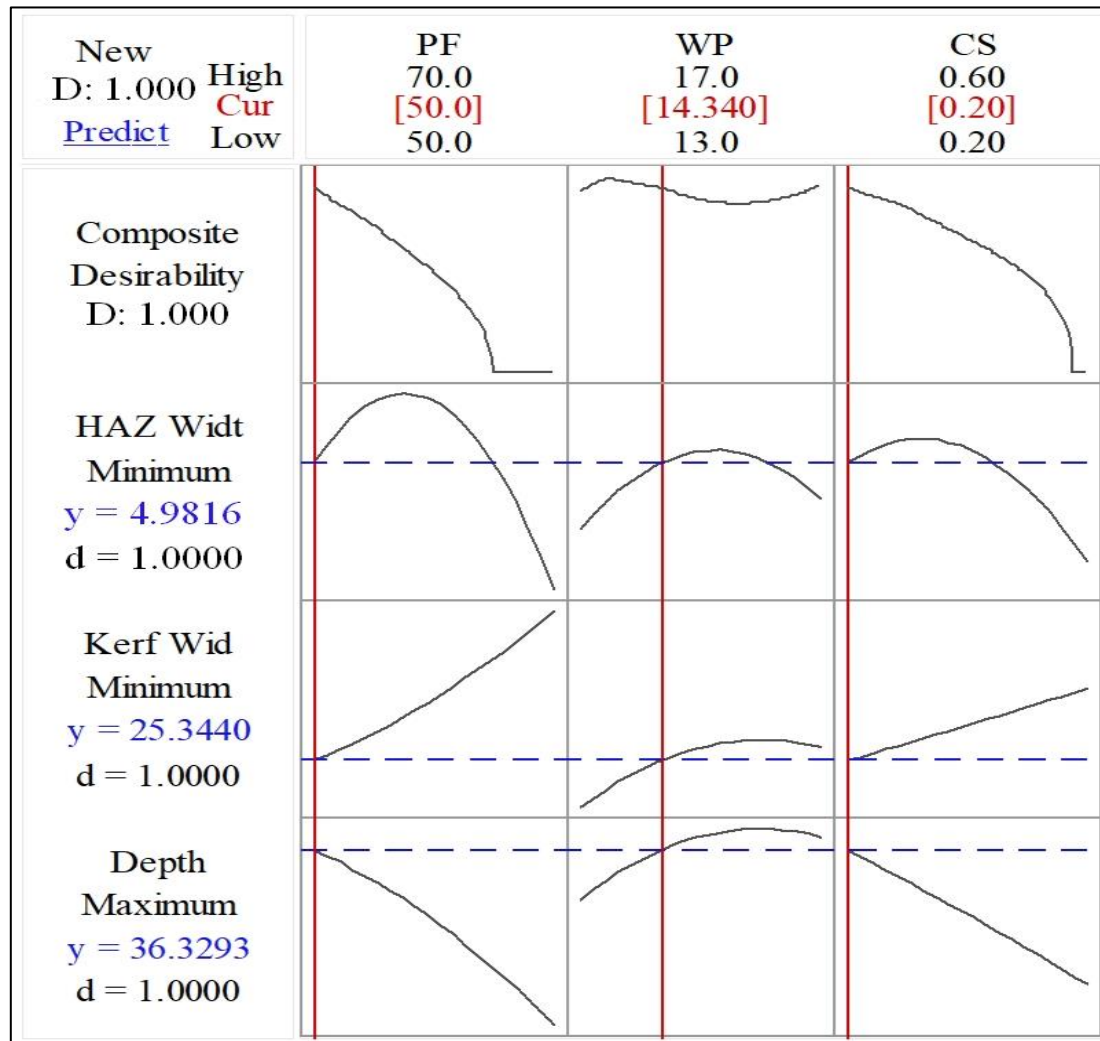


Figure 7.37 Multi-objective optimization plot for the micro-channels.

Figure 7.37 shows a graph with each column representing a factor. Each row of the graph represents a response variable. Each graph cell represents how one of the response variables changes as a result of one of the factors, while the others remain constant. At the top of the column, the current factor level settings, as well as the high and low values of factors, are presented. To the left of each row, the response goal, expected response, y , at current factor settings, and individual desirability score are listed. Figure 7.37 shows that with a pulse frequency of 50 kHz, a working power of 14.340 %, and a cutting speed of 0.20 mm/s, a response value of 36.3293 μm , 25.3440 μm , and 4.9816 μm for the depth of cut, kerf width, and HAZ width can be reached.

7.4.2.5 Confirmation Test

In order to verify that the results were obtained under the optimal circumstances, an additional 5 tests were carried out under such conditions, and their average was then

determined. It has been noticed that the outcomes of the experiments are quite similar to the results that were predicted. The confirmation test takes into account the average of the experimental results, which are presented in table 7.12 below and Figure 7.38 exhibits the microscopic image and SEM micrograph of the micro-channel.

Table 7.12 Confirmation test of laser micromachining at underwater medium

Optimal parameter settings	Machining responses	Predicted value at Optimal parametric settings	Experimental value at Optimal parametric settings	% of error
PF=50.0 kHz; WP=14.34 %; CS=0.20 mm/sec	Depth of cut (μm)	36.3293	34.9565	3.93
	Kerf width (μm)	25.3440	23.0334	9.12
	HAZ width (μm)	4.9816	4.7915	3.82

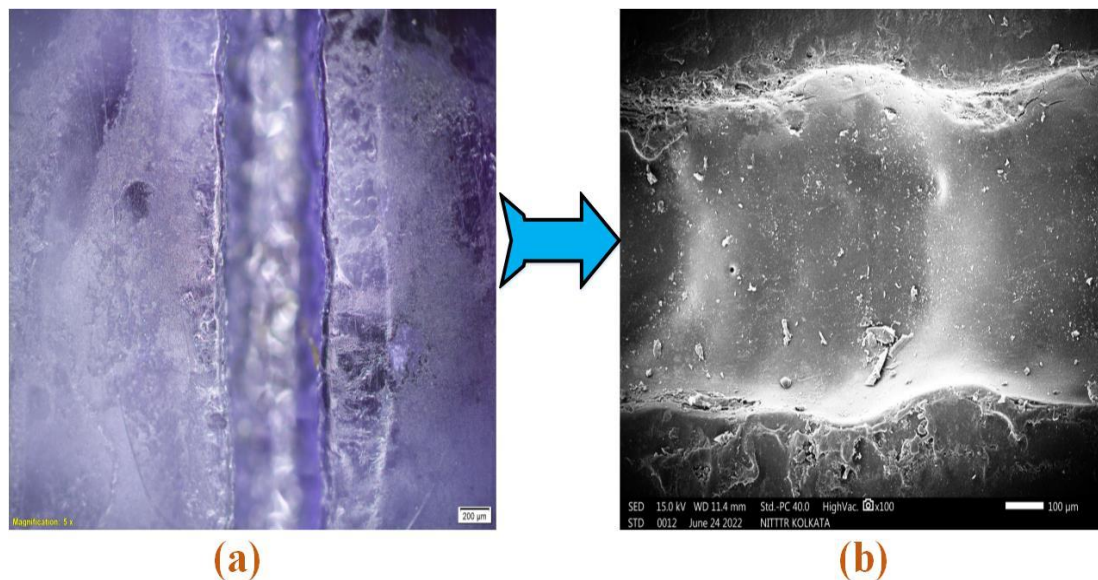


Figure 7.38 (a) Microscopic image of the micro-channel, (b) SEM micrograph

7.4.3 Outcomes

A fiber laser system is being utilized in this study. The procedure involving the micro-channels was carried out in the presence of DI water. Transparent PMMA material is used as workpiece. The absorbent material is represented by the use of black tape. During the process of machining, the primary goals that were being pursued were to maximize the depth of cut, reduce the size of the heat affected zone (HAZ), and keep the kerf breadth the same. During the course of the experimentation, the three process parameters of pulse frequency, working power, and cutting speed were all taken into

consideration. After the micro-channels had been produced, the features of those micro-channels, such as their depth of cut, kerf width, and HAZ width, were measured and analyzed. In order to formulate the mathematical connections between the various input process parameters and the various output responses, the 'Response Surface Methodology' (RSM) technique was utilized. The appropriateness of the model was evaluated using the analysis of variance method (ANOVA). The trials are planned with the help of a response surface approach technique called central composite design (CCD), which has three factors (RSM). It is possible, based on the results of the analysis of variance (ANOVA), to draw the conclusion that all of the process variables have statistically significant effects. In addition, a parametric investigation was carried out, and the researchers were able to provide a comprehensive illustration of the factors that led to the observed events. As a result of the phenomenon that was observed, one can draw the conclusion that the presence of water and a duty cycle that is closer to 100 percent in regard to pulse width plays an essential role in achieving the desired machining characteristics during laser transmission ablation in an environment that contains water. After conducting optimization, the optimal process variable settings have been obtained in order to achieve the largest depth of cut and the smallest possible kerf width while maintaining the narrowest heat impacted zone (HAZ) width. Multi-objective optimization is also performed in order to reach the ideal outcomes in depth of cut, kerf width, and HAZ width, which are, respectively, 36.3293 μm , 25.3440 μm , and 4.9816 μm . These values were determined after carrying out the previous steps of the process. The parameters that should be set for optimal performance are as follows: the pulse frequency should be set to 50.0 kHz, the operating power should be 14.34 %, and the cutting speed should be 0.20 mm/sec. It was discovered that the percentage of error that was obtained from the predicted and actual experimental results at optimal conditions was found to be quite low. This indicates that the prediction analysis of fiber laser transmission micro-channeling of thick PMMA can be considered to be of high acceptable quality.

Chapter 8

COMPARATIVE STUDY

8.1 Comparative Study of the Effect of Different Environmental Mediums on Machining Responses During Laser Transmission Micro-Channeling of Thick Transparent PMMA Material

During laser micro-channeling of transparent PMMA by a pulsed Nd: YAG laser at 1064 nm wavelength with a 100 μm beam diameter, two different environments, i.e., air and submerged underwater, are used at the same parametric condition when all the controllable process variables are kept at the same parametric settings on the same workpiece. In the same way, a fiber laser at 1064 nm wavelength with a 21 μm beam diameter in two different environments is carried out on transparent PMMA. A comparative study was conducted here to study the effect of process parameters on preselected machining responses in different media as well as in different laser generation systems. For comparative study, polynomial regression equation, percentage of contribution, multi-objective optimization, experimental data from the experimental table, and CCI & AFM analysis have been taken into account for analysis and comparison of the results to better understand the consequences of the effect and trend of parameters on responses (i.e., depth of cut, kerf width, and HAZ width).

8.2 Trend of Parametric Effects on Responses at Different Mediums in Nd:YAG and Fiber Laser System with the Help of Polynomial Regression Equation

The plots are drawn from the polynomial regression equation (Eqⁿ.6.1, Eqⁿ.6.2, Eqⁿ.6.3, Eqⁿ.7.1, Eqⁿ.7.2 and Eqⁿ.7.3). The coded data and levels are taken into account to generate the effect plot. These plots show the trend of the parametric effect on responses in air and submerged water media in different laser generation systems. The values of the plots are different because of the different laser generation systems, different beam diameters, and different parameters with different parametric settings.

(i) Trend of parametric effect at air medium in different laser systems

It is observed from Figure 8.1 that the trend of parametric effects is parallel to each other in the air medium in both laser systems. This plot shows that the trend of parametric effects is the same in both laser systems. Figure 8.1 shows that the depth of cut increases to a certain limit, then it decreases sharply. The increase in energy density and lower cutting speed causes the depth of cut to increase smoothly, but after a certain limit, the depth of cut decreases. It could be because of the effect of re-solidification of debris material in the machining zone, which could stop energy from penetrating the machining zone, or because the laser cutting interaction time is shorter, which could make the depth of cut smaller in the air medium.

From Figure 8.2, it has been seen that the parameters' effect on kerf width is parallel in both laser systems. This plot shows that the trend of parametric effects is the same in both laser systems. It is obtained from Figure 8.2 that the kerf width decreases slightly and, after a short range, it increases. This may be because of the stronger re-solidification effect, which makes the kerf width smaller, and then the kerf width gets bigger because the higher energy density in the machining area goes up.

Figure 8.3 shows the trend of the parametric effect on HAZ width in different laser systems in the air medium. It is also seen from the figure that the effects are parallel to each other in different laser systems in the air medium, which indicates that the trend is similar in both Nd: YAG and fiber laser systems. It is evident from Figure 8.3 that the HAZ width increases sharply and then decreases. It may be due to working power or lamp current being greater with higher interaction time between laser and material, causing an increment of HAZ width. With a lower interaction time between the laser and workpiece or lower power, the HAZ width may decrease.

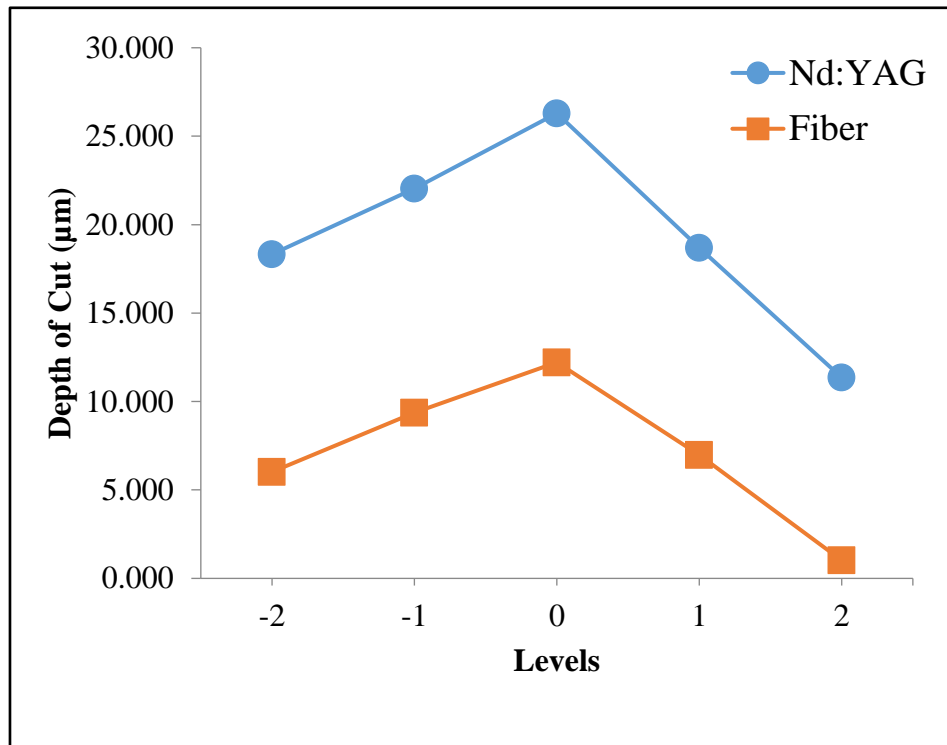


Figure 8.1 Effect of parameters on depth of cut at air medium in different laser systems

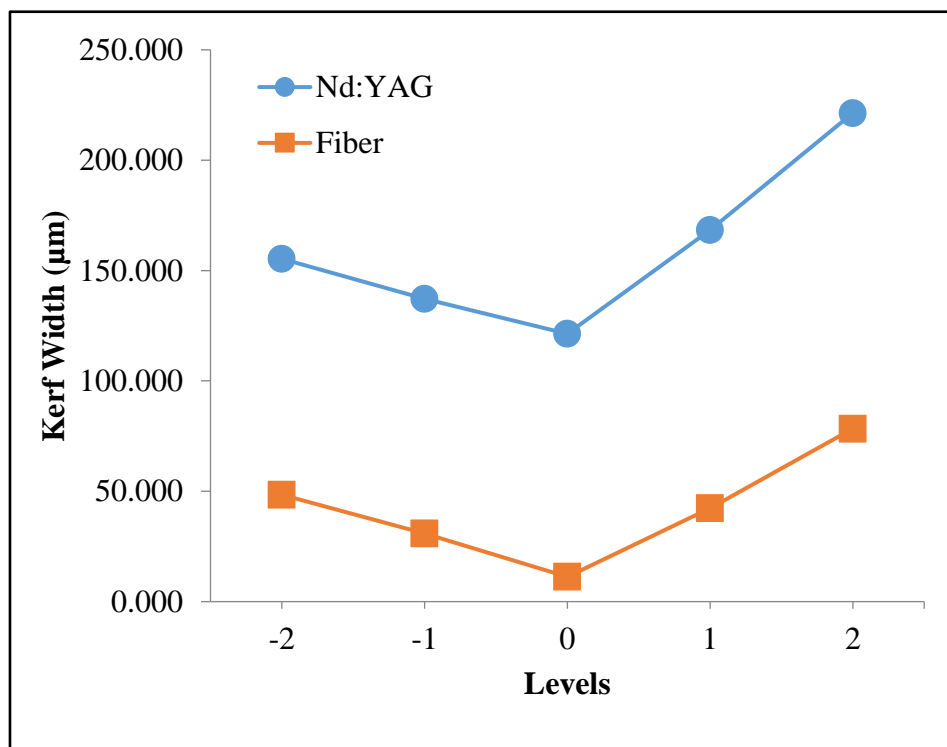


Figure 8.2 Effect of parameters on kerf width at air medium in different laser systems

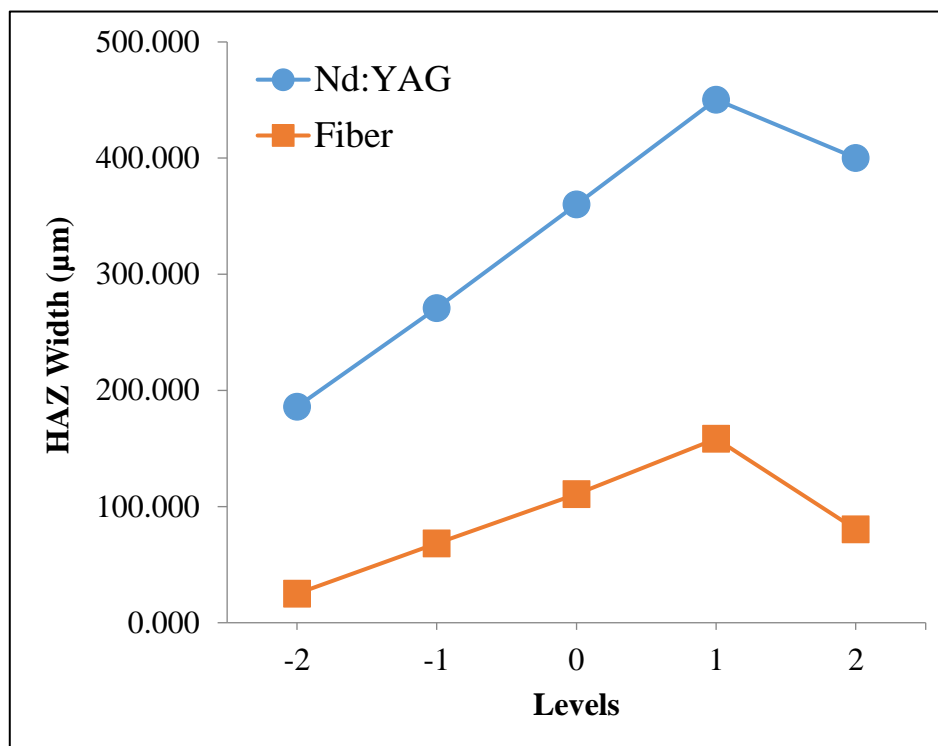


Figure 8.3 Effect of parameters on HAZ width at air medium in different laser systems

(ii) Trend of parametric effect at submerged in water medium in different laser system

Figure 8.4 shows the trend of parametric effects in the air medium using both laser systems. The trend of parametric effects is the same for both laser systems, as shown in this graph. Figure 8.4 indicates that the depth of cut increases until it reaches a limit, after which it drops quickly. The depth of cut increases steadily as energy density and cutting speed decrease, but at a certain point, the depth of cut declines. It might be due to the influence of debris material re-solidification in the machining zone, which could prevent energy from accessing the machining zone, or it could be due to the shorter laser cutting interaction time, which reduces the depth of cut in the air medium.

In both laser systems, the influence of the parameters on kerf width is parallel, as shown in Figure 8.5. The trend of parametric effects is the same in both laser systems, as shown in this graph. Figure 8.5 shows that the kerf width reduces significantly and increases after a certain range. This could be because the re-solidification effect is

stronger; resulting in a narrower kerf width, which then expands as the energy density in the machining area increases.

In the air medium, Figure 8.6 depicts the trend of the parametric effect on HAZ width in different laser systems. The effects in different laser systems in the air medium are parallel to each other in the figure, indicating that the trend is the same in both Nd:YAG and fiber laser systems. The HAZ width increases abruptly and subsequently diminishes, as shown in Figure 8.6. It may be due to the reason the working power or lamp current when combined with a longer interaction time between the laser and the material, results in a wider HAZ. The HAZ width may be reduced if the interaction time between the laser and the workpiece is reduced or if the laser power is reduced.

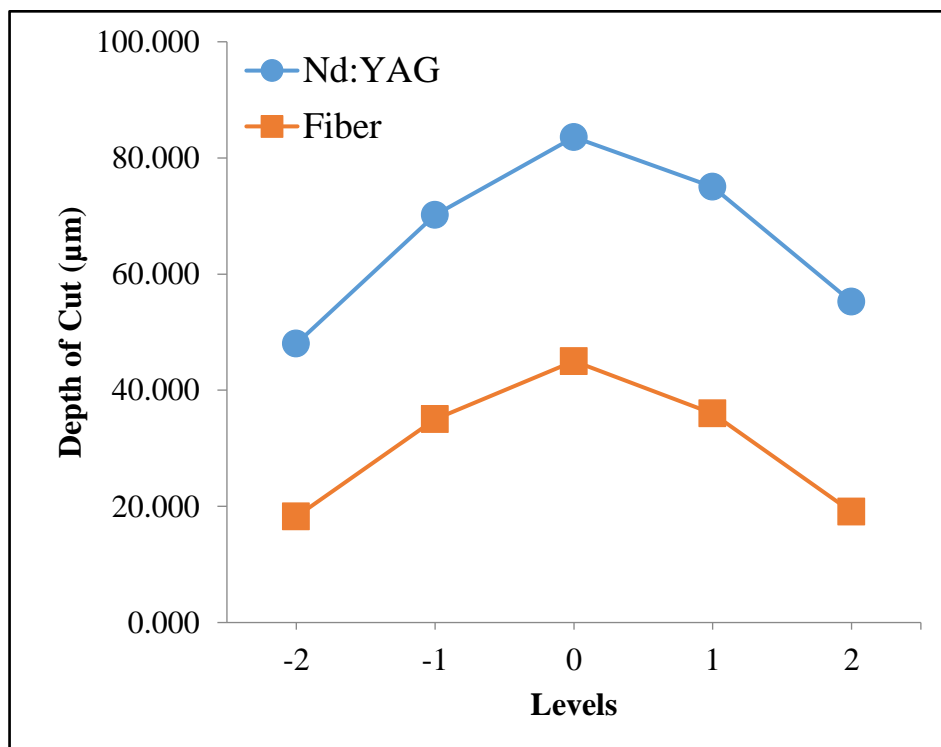


Figure 8.4 Effect of parameters on depth of cut at submerged in water medium in different laser systems

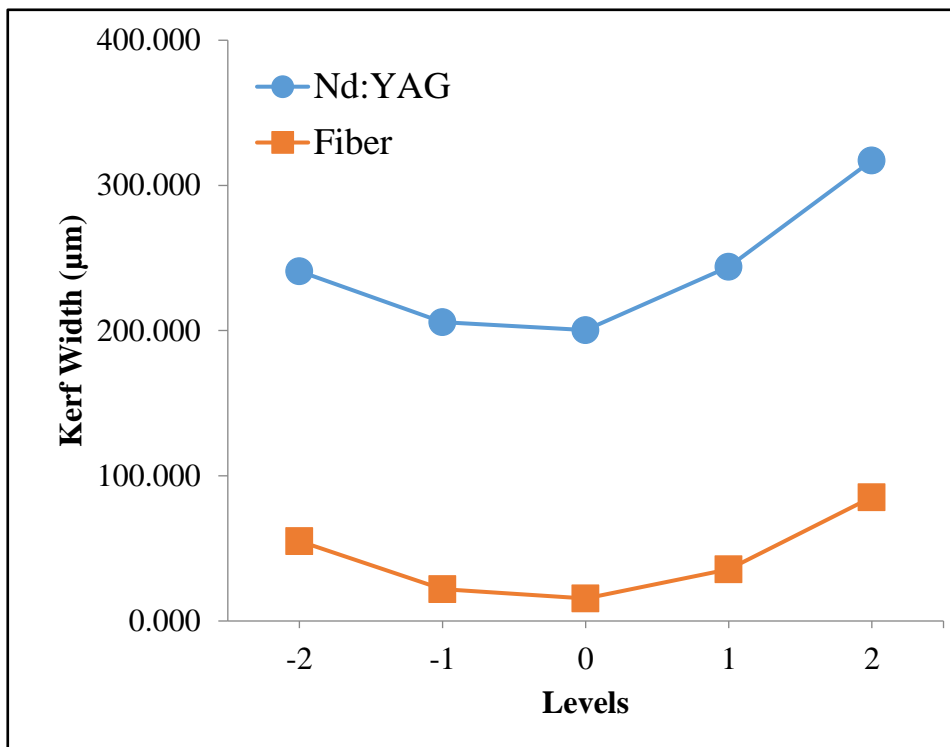


Figure 8.5 Effect of parameters on kerf width at submerged in water medium in different laser systems

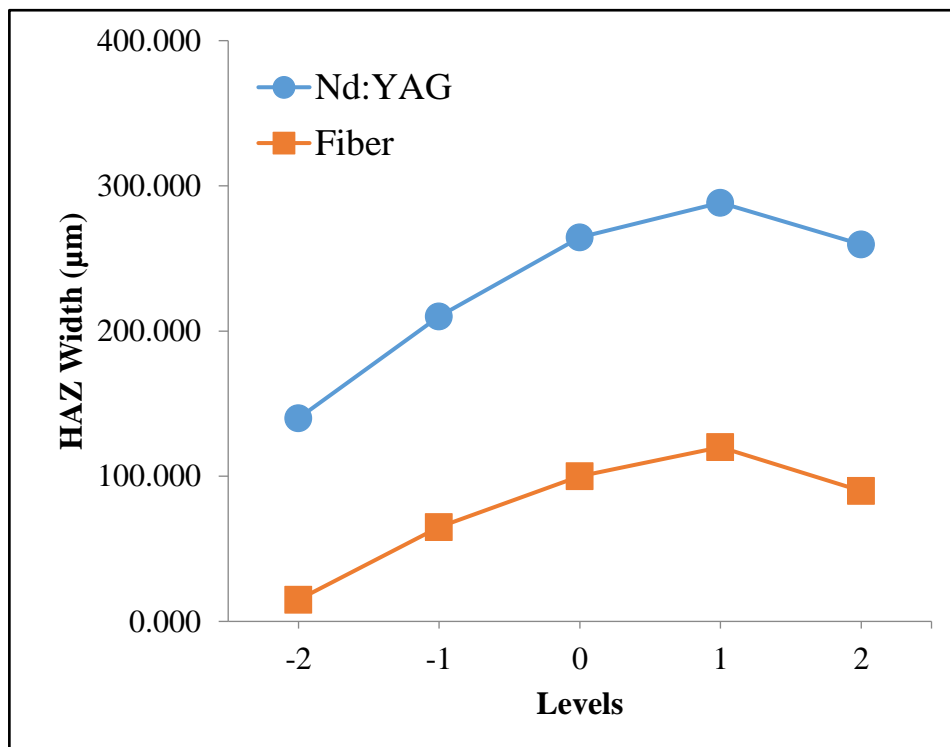


Figure 8.6 Effect of parameters on HAZ width at submerged in water medium in different laser systems

8.3 Comparative Study Based on Percentage Contribution of Parameters in Different Environmental Conditions

Micro-channel quality mainly depends on three important characteristics, i.e., depth of cut, kerf width, and HAZ width of the channel. These three major responses depend on the effective parameters of laser systems. The contribution of these effective parameters controls the micro-channel characteristics. The contributions of the parameters are calculated from the ANOVA tables (Table 6.3-6.5, 6.9-6.11, 7.3-7.5, and 7.9-7.11). In different environmental conditions, the parameters' contributions are observed.

(i) Percentage contribution of parameters in different environmental conditions in Nd:YAG laser system

Figure 8.7 shows the contribution of parameters to the depth of cut in different media. From Figure 8.7, it can be obtained that for depth of cut, the most dominating factor is pulse frequency, followed by cutting speed and lamp current in the Nd: YAG laser system at different environmental conditions (i.e., air and submerged in water). In the air medium, the contribution of pulse frequency is greater than in the submerged medium, and the contribution of lamp current and cutting speed is less in the air medium.

Figure 8.8 shows the contribution of parameters to the kerf width in different media. It has been observed from Figure 8.8, for the response i.e., kerf width, that the most dominating factor is pulse frequency followed by lamp current and cutting speed in the Nd: YAG laser system at different environmental conditions. The contribution of pulse frequency is slightly higher in the air medium than in the submerged condition, the contribution of lamp current is slightly lower in the air medium, and the contribution of cutting speed is slightly higher in the air medium than in the submerged condition in water.

Figure 8.9 shows the contribution of parameters to the HAZ width in different media. From Figure 8.9, it can be obtained that for HAZ width, the most dominating factor is lamp current, followed by cutting speed and pulse frequency in the Nd: YAG laser system at different environmental conditions (i.e., air and submerged in water). The

contribution of lamp current, pulse frequency, and cutting speed is almost the same in both dry and wet conditions.

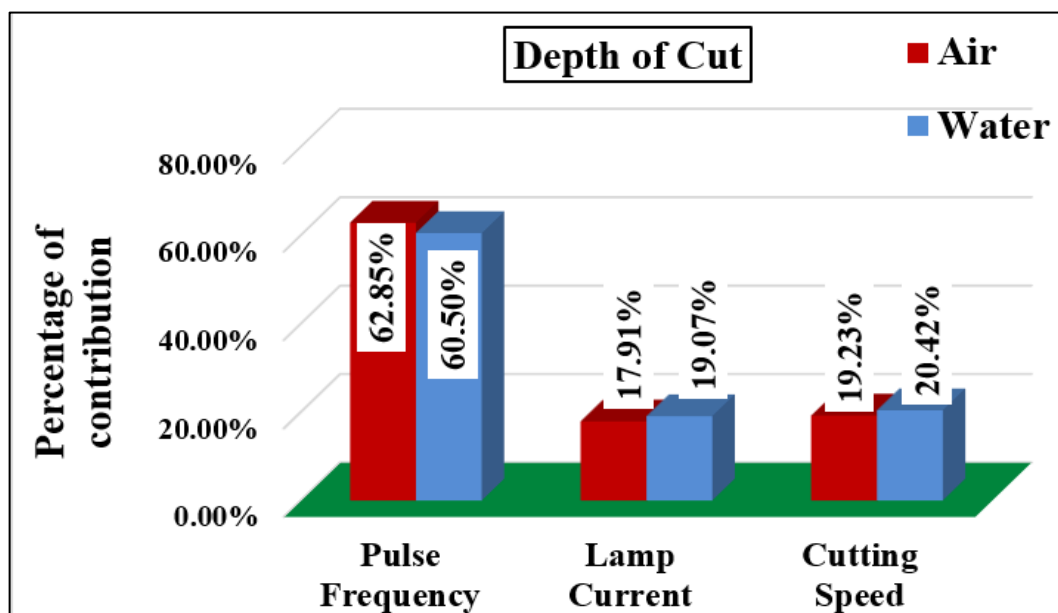


Figure 8.7 Percentage contributions of parameters on depth of cut in different mediums (i.e., Air and water)

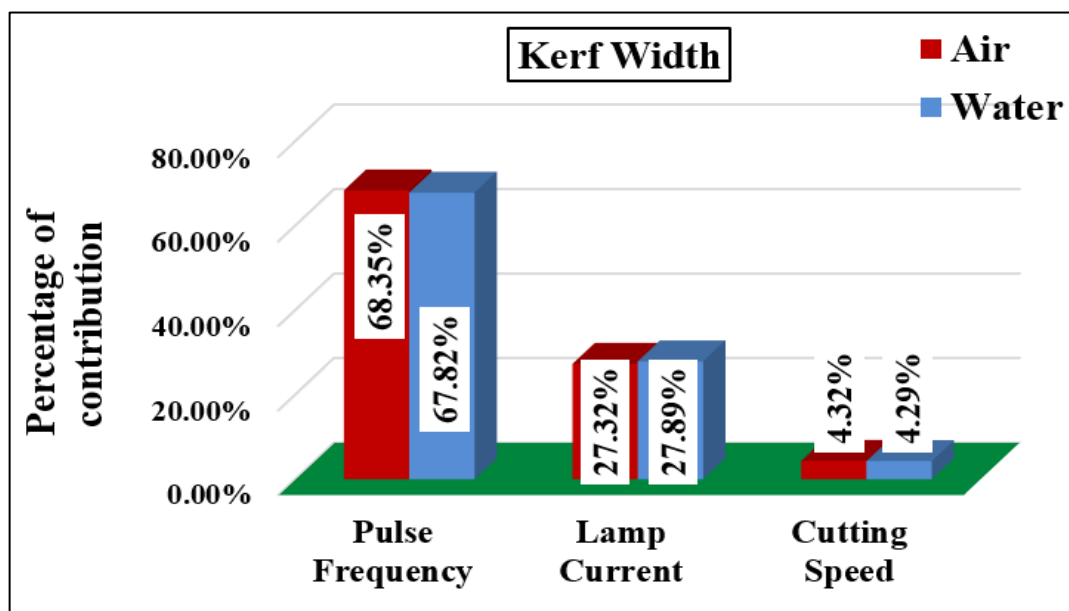


Figure 8.8 Percentage contributions of parameters on kerf width in different mediums (i.e., Air and water)

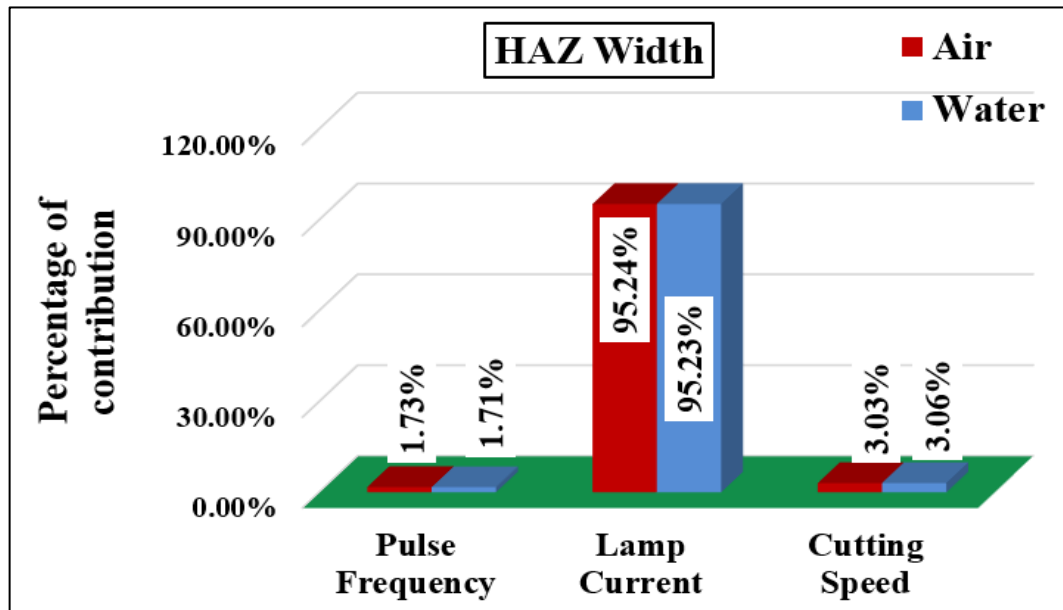


Figure 8.9 Percentage contributions of parameters on HAZ width in different mediums (i.e., Air and water)

(ii) Percentage contribution of parameters in different environmental conditions in fiber laser system

Figure 8.10 depicts the role of various criteria in determining the depth of cut in various media. Figure 8.10 shows that in the Nd: YAG laser system under various environmental conditions, pulse frequency is the most important element for depth of cut, followed by cutting speed and lamp current (i.e., air and submerged in water). The contribution of pulse frequency is greater in the air medium than in the submerged medium, whereas the contributions of lamp current and cutting speed are lower.

Figure 8.11 depicts the effect of several factors on kerf width in various media. Figure 8.11 shows that in the Nd: YAG laser system under various environmental conditions, the pulse frequency is the most dominant factor, followed by lamp current and cutting speed, for the response, i.e., kerf width. Pulse frequency contributes somewhat more in the air medium than in the submerged condition, lamp current contributes slightly less in the air medium, and cutting speed contributes slightly more in the air medium than in the submerged condition in water.

The contribution of parameters to the HAZ width in different mediums is shown in Figure 8.12. Figure 8.12 shows that lamp current is the most important element in

determining HAZ width in the Nd: YAG laser system under various environmental circumstances, followed by cutting speed and pulse frequency (i.e., air and submerged in water). In both dry and wet situations, the contributions of lamp current, pulse frequency, and cutting speed are nearly identical.

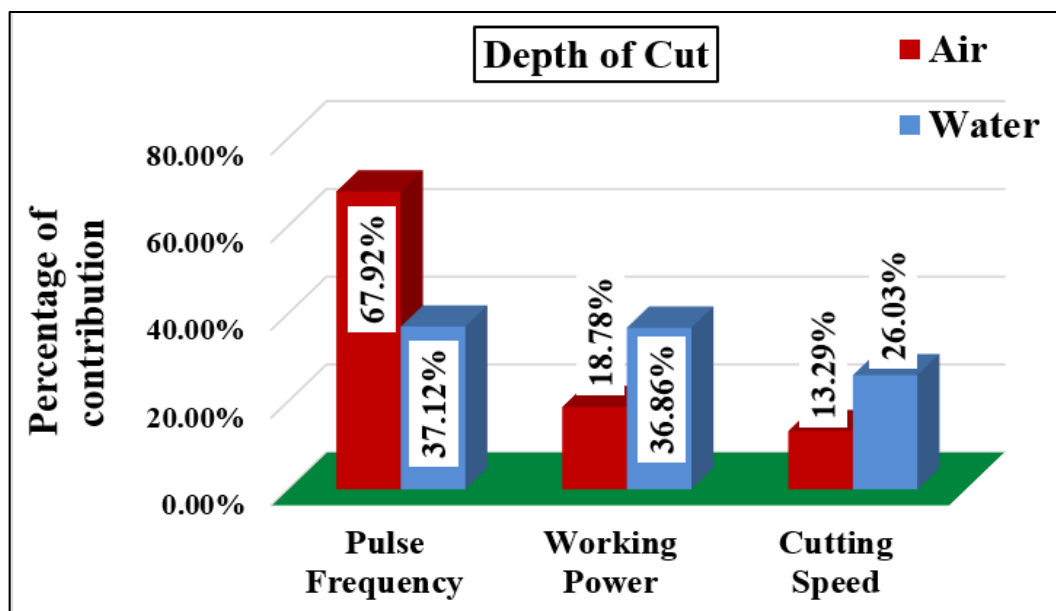


Figure 8.10 Percentage contributions of parameters on depth of cut in different mediums (i.e., Air and water)

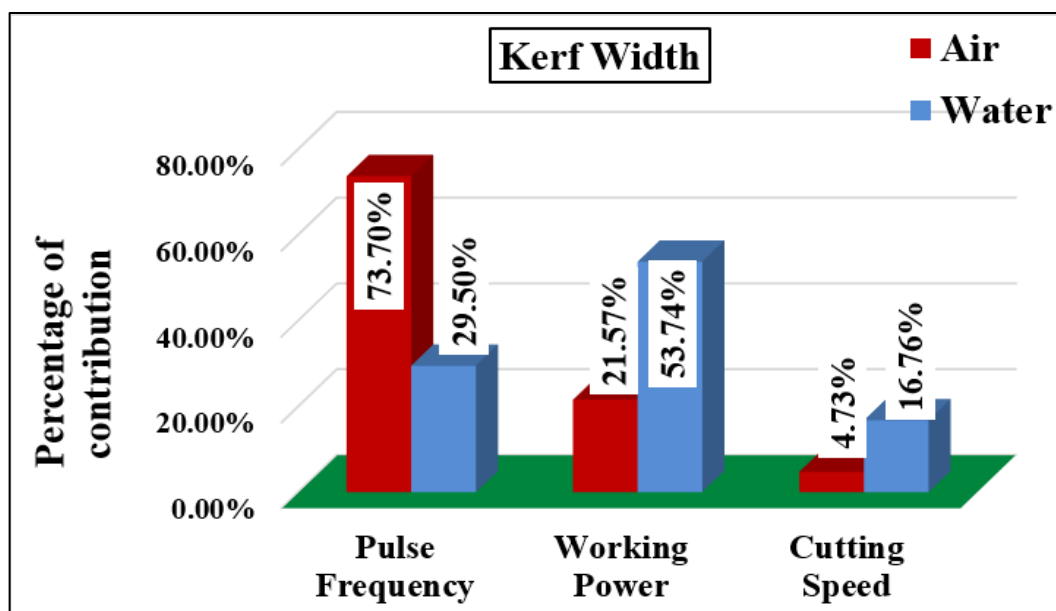


Figure 8.11 Percentage contributions of parameters on kerf width in different mediums (i.e., Air and water)

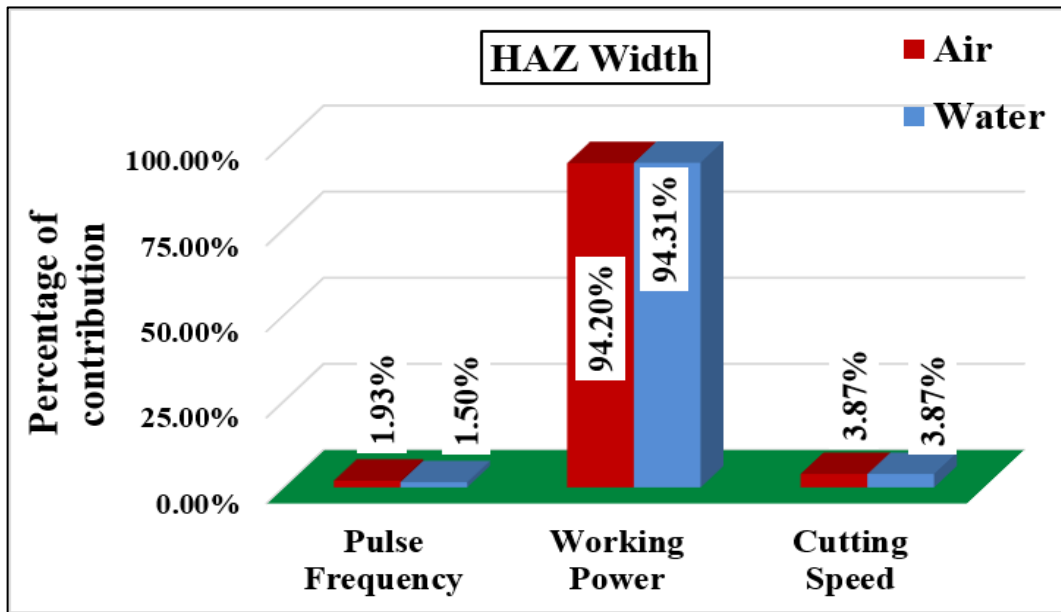


Figure 8.12 Percentage contributions of parameters on HAZ width in different mediums (i.e., Air and water)

8.4 Comparative Study Based on Multi-Objective Optimization Results in Different Environmental Conditions

Optimum results are obtained from the multi-objective optimization (Figure 6.18, 6.36, 7.18, and 7.36) at optimal parametric settings. With the help of optimal results of multi-objective optimization, the plots have been drawn between air and water medium, which can show the difference in response results in Nd: YAG and fiber lasers separately.

(i) Multi-objective optimization results in different environmental conditions in Nd:YAG laser system

Figure 8.13 shows the optimal results of air and submerged water medium in the Nd: YAG laser system. It is observed from Figure 8.13 that the result of depth of cut and kerf width is greater in the wet medium than in dry medium. Also, it can be obtained from the plot that the aspect ratio of micro-channel is better, as well as the HAZ width is lower in the water medium. So, it can be said that the characteristics of micro-channel (i.e., depth of cut, kerf width, and HAZ width) are improved in wet medium than in dry medium.

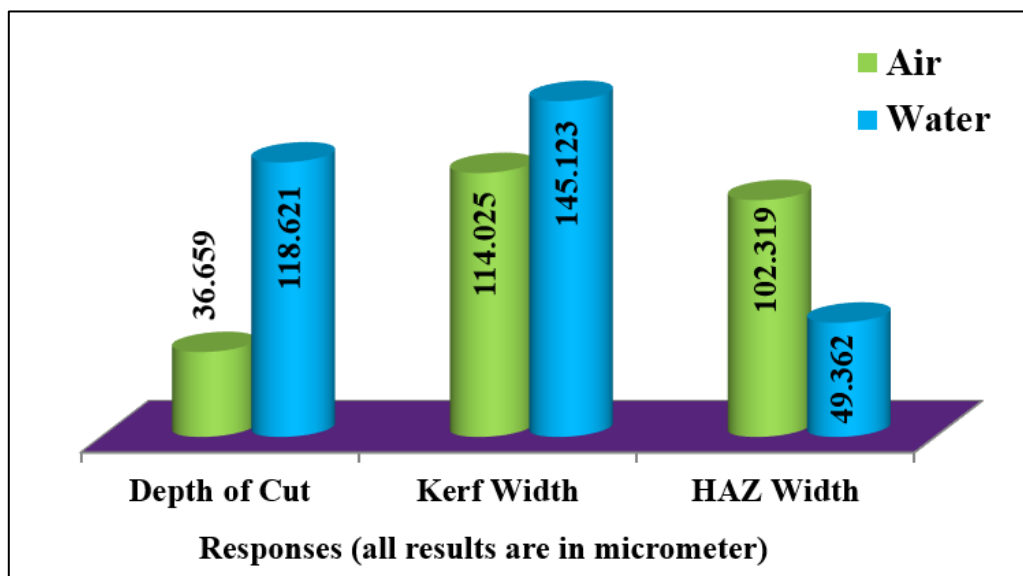


Figure 8.13 Optimal results from multi-objective optimization at different environmental conditions in Nd:YAG laser

(ii) Multi-objective optimization results in different environmental conditions in the fiber laser system

The ideal results of the air and submerged water medium in the Nd: YAG laser system is shown in Figure 8.14. Figure 8.14 shows that the result of the depth of cut and kerf width is bigger in the wet medium than in the dry medium. In addition, the plot shows that the aspect ratio of the micro-channel is better, and the HAZ width in the water medium is less. As a result, the wet medium improves the properties of micro-channel (i.e., depth of cut, kerf width, and HAZ width) over the dry medium.

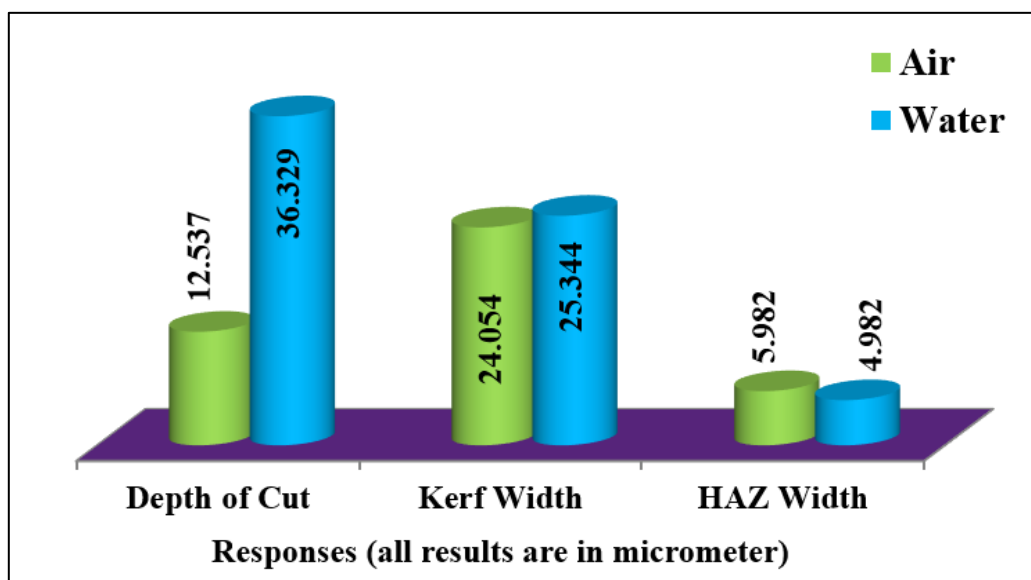


Figure 8.14 Optimal results from multi-objective optimization at different environmental conditions in Nd:YAG laser

8.5 Comparative Study Based on Average Value of Responses from Experimental Data Table

From the experimental data tables (Tables 6.2, 6.8, 7.2, and 7.8) of Nd: YAG and fiber laser systems, the average values of responses are taken into account to generate the plots. The plots are drawn for the air and water media and for both the laser systems separately.

(i) Average value of responses from experimental data table in Nd:YAG laser system at different medium

From the experimental data tables (Tables 6.2 and Table 6.8) of dry and wet medium in the Nd: YAG laser, the average responses are taken to carry out Figures 8.15, 8.16, and 8.17. It can be found from the figures that the depth of cut and kerf width is greater in the water medium than in the air. HAZ width is the minimum in the water medium. The depth of cut and kerf width is greater in the water medium, possibly as a result of bubbles bursting during machining and the adjacent zone abruptly removing material, resulting in a greater depth of cut and kerf width during underwater machining. In the air, material removal is mainly governed by the gravitational force acting on the formed molten and gaseous debris. Due to the aforesaid condition, some debris is not properly removed from the machining zone and is redistributed at the periphery of the machining area, thereby decreasing the depth of cut and kerf width. The HAZ width is less in the water medium because of the cooling effect of water. The water cuts down on the heat and stops the extra heat from spreading from the machining zone to the surface of the workpiece material.

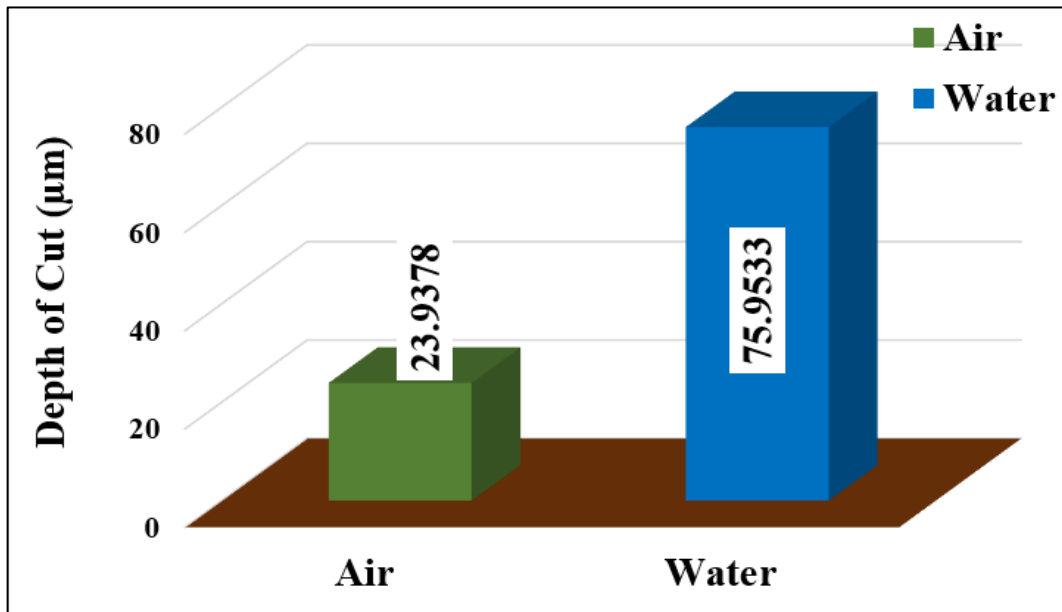


Figure 8.15 Average value of depth of cut at air & submerged in water medium for Nd:YAG laser system

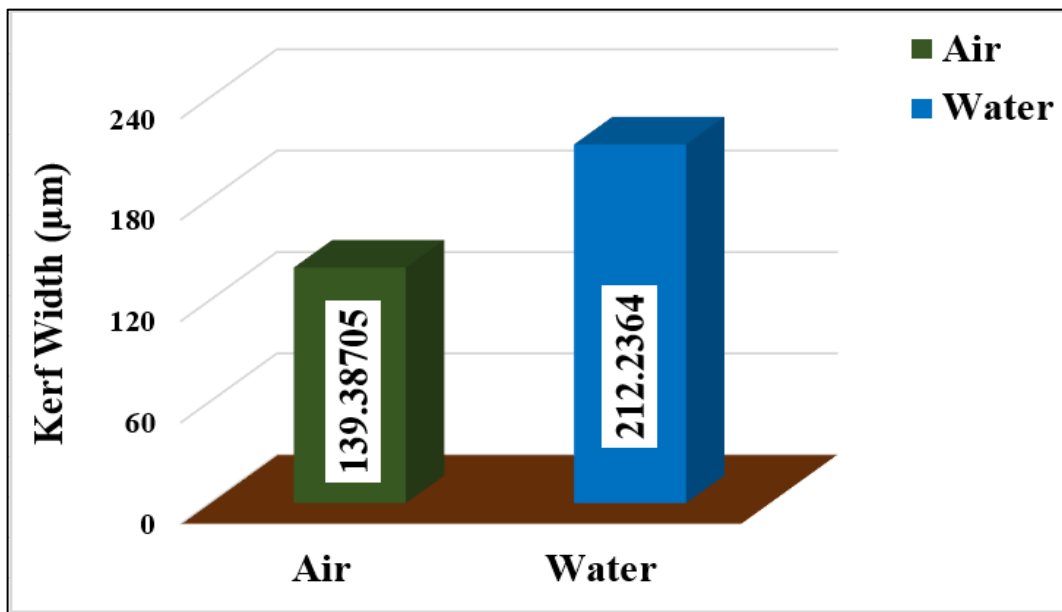


Figure 8.16 Average value of kerf width at air & submerged in water medium for Nd:YAG laser system

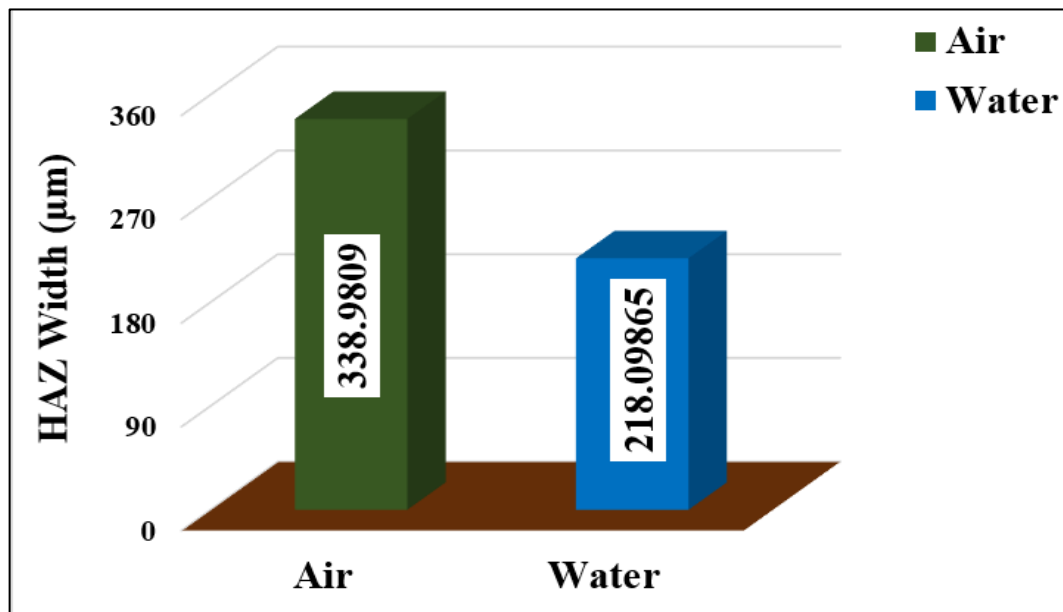


Figure 8.17 Average value of HAZ width at air & submerged in water medium for Nd:YAG laser system

(ii) Average value of responses from experimental data table in fiber laser system at different medium

The average responses are obtained from the experimental data tables (Tables 7.2 and 7.8) of dry and wet medium in the fiber laser to carry out Figures 8.18, 8.19, and 8.20. The figures show that in the water medium, the depth of cut and kerf width is greater than in the air media. HAZ width is the minimum in the water medium. During underwater machining, the depth of cut and kerf width is increased, presumably as a result of bubbles bursting during machining and the nearby zone abruptly removing material, resulting in a greater depth of cut and kerf width. The gravitational force acting on the generated molten and gaseous debris is mostly responsible for material removal in the air. As a result of the aforementioned circumstance, some debris is not effectively removed from the machining zone and is redistributed at the machining area's periphery, resulting in a reduction in depth of cut and kerf width. Because of the cooling impact of water, the HAZ width is less in the water medium. The water dissipates the heat and prevents it from spreading from the machining zone to the workpiece material's surface.

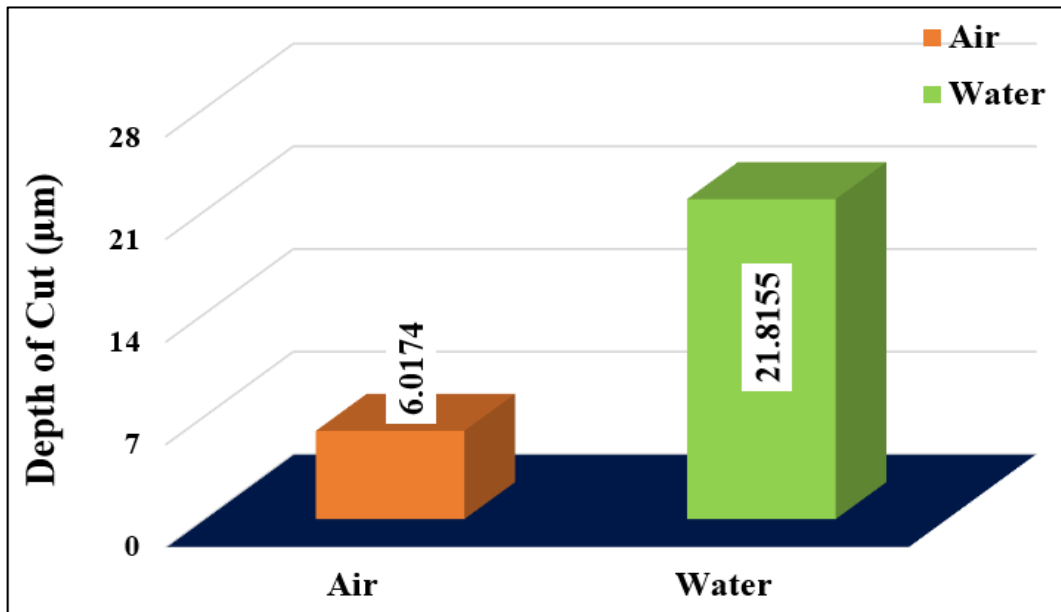


Figure 8.18 Average value of depth of cut at air & submerged in water medium for Nd:YAG laser system

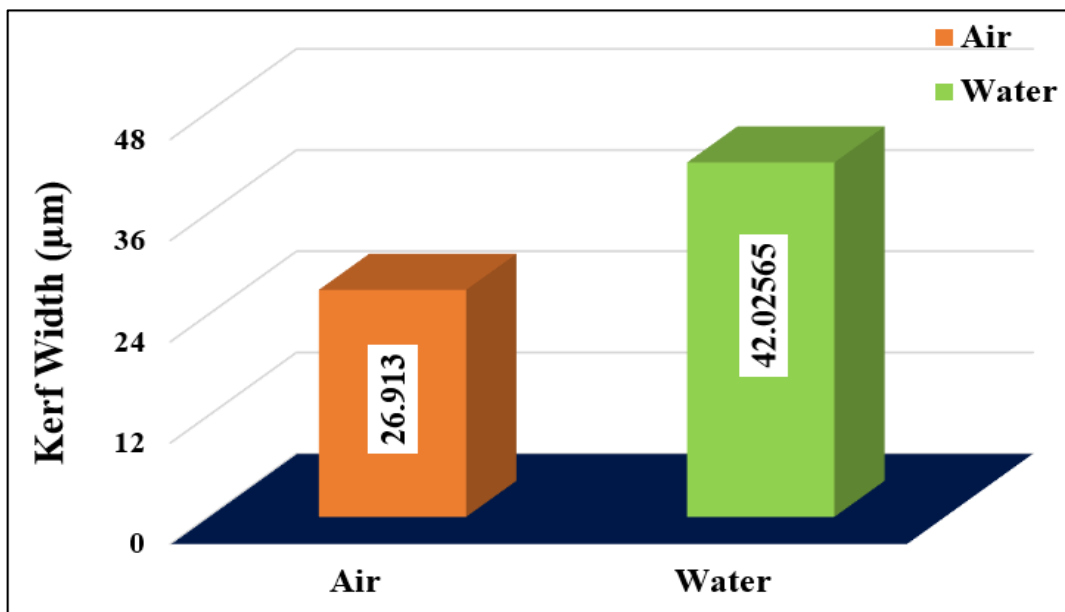


Figure 8.19 Average value of kerf width at air & submerged in water medium for Nd:YAG laser system

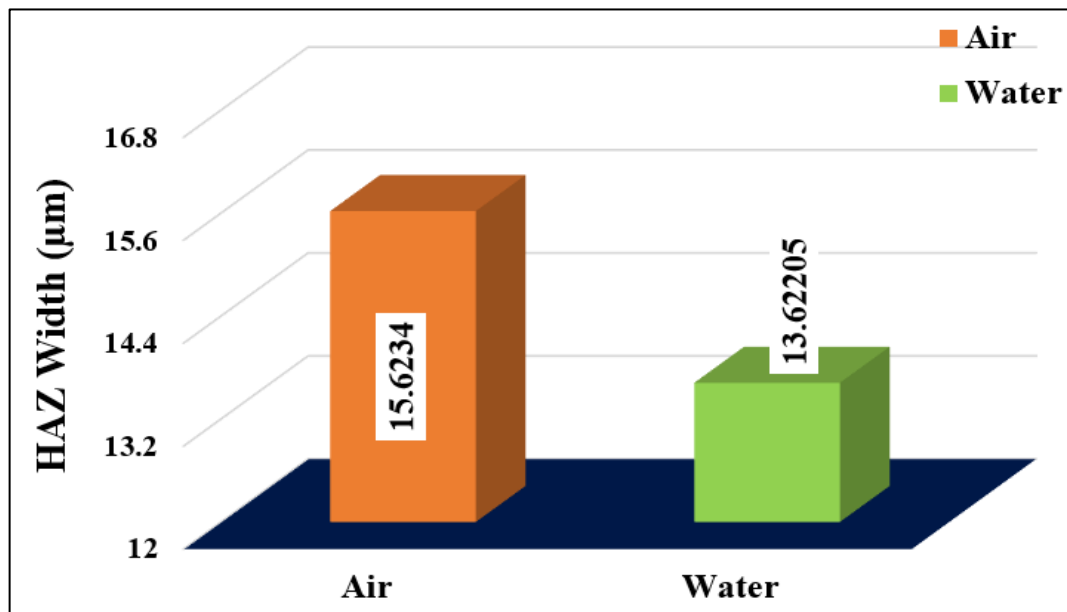


Figure 8.20 Average value of HAZ width at air & submerged in water medium for Nd:YAG laser system

8.6 Comparative study based on percentage of improvement of responses from experimental data table in different laser system

It can be found from Figure 8.21, the percentage of improvement in submerged water conditions with respect to air between the Nd: YAG and fiber laser systems. The plot depicts the percentage improvement from the experimental data table (Tables 6.2, 6.8, 7.2, and 7.8) of Nd: YAG and fiber laser in air and water environments. From Figure 8.21, it can be observed that the depth of cut and kerf width improvement percentage is greater in fiber laser and HAZ width is greater in Nd: YAG laser. The percentage of improvement is varied. It may be due to the beam diameter of both the lasers being different, as well as the parametric settings and generation of the laser system also being different, which may cause the differences.

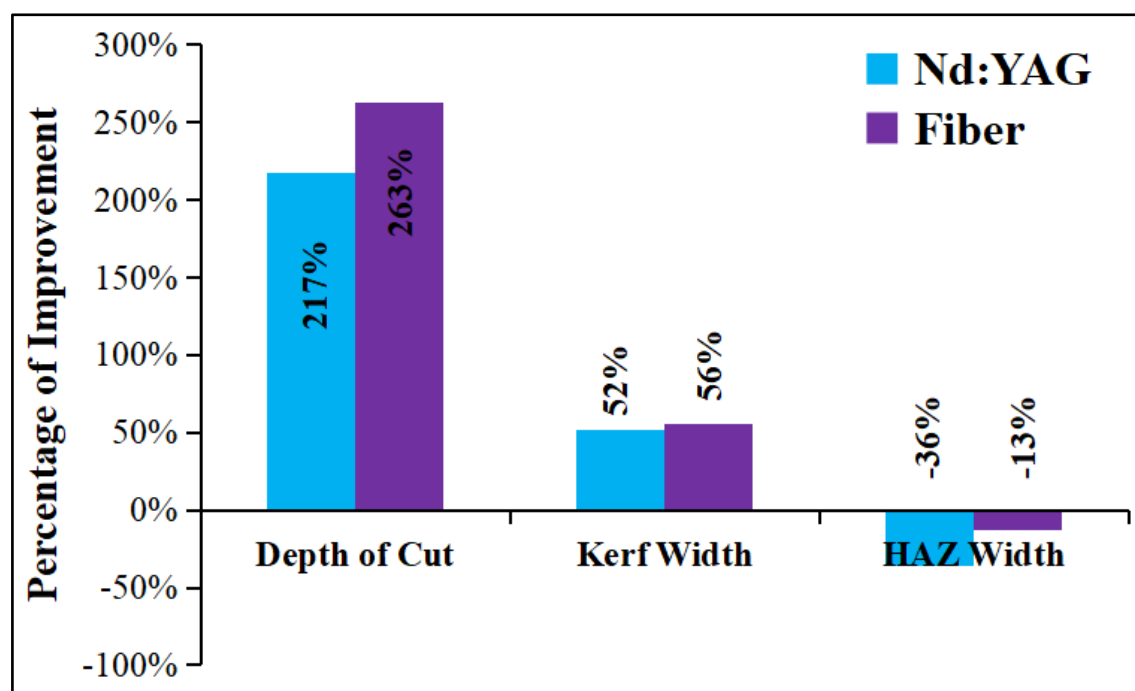


Figure 8.21 Percentage improvement of depth of cut, kerf width and HAZ width in Nd:YAG and fiber laser system

8.7 CCI And AFM Analysis of Micro-channel in Different Medium

8.7.1 Open Air

In recent years, coherence correlation interferometry (CCI) and atomic force microscopy (AFM) have been used extensively for characterization of materials on the nanometric and microscopic scale, based on their surface roughness, surface morphology, size distribution, and micropore density. The surface topography of the CCI image in 2D and 3D form of the micro-channel in air medium is shown in Figure 8.22. Figure 8.23 shows the 2D evaluation profile of the micro-channel. From Figure 8.22, it is observed that craters, peaks, hills, globules like structures are present in the micro-channel. The presence of such an irregular structure makes the channel surface uneven. This is happening due to the re-deposition and re-crystallization of molten materials in the machining zone. Figure 8.24 shows the depth profile and kerf width of the micro-channel. The maximum channel depth obtained at optimal cutting conditions is $57.239\ \mu\text{m}$, the mean depth of the channel is $35.15\ \mu\text{m}$ and the kerf width is $111.26\ \mu\text{m}$. Additionally, a 3D AFM image is captured (Figure 8.25) to measure the surface roughness value of the micro-channel. In this case, the aforementioned parameter setting (i.e. optimal cutting condition in Nd:YAG laser) provides an average surface roughness value of $1.55\ \mu\text{m}$.

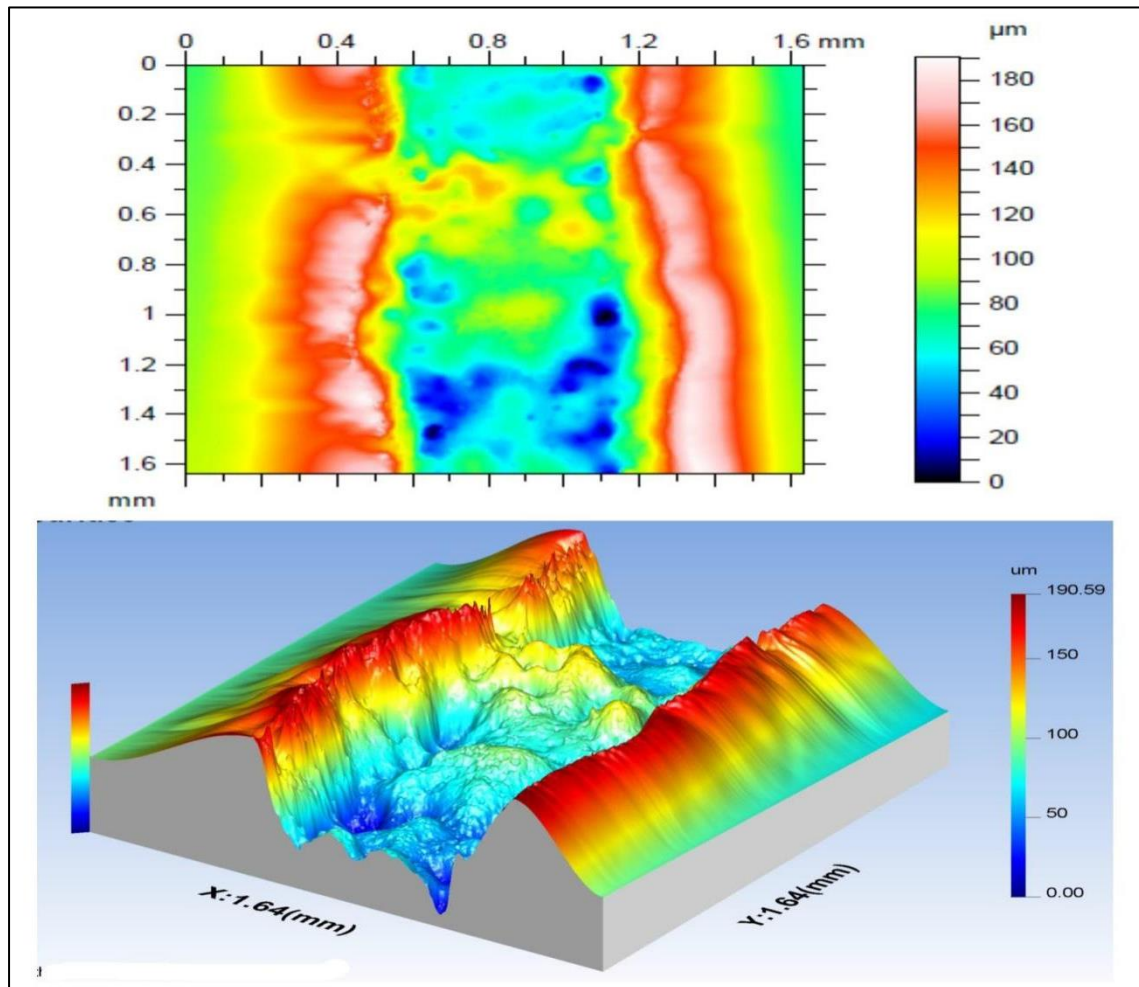


Figure 8.22 CCI image of the micro-channel (Nd:YAG laser transmission micro-machining in air medium)

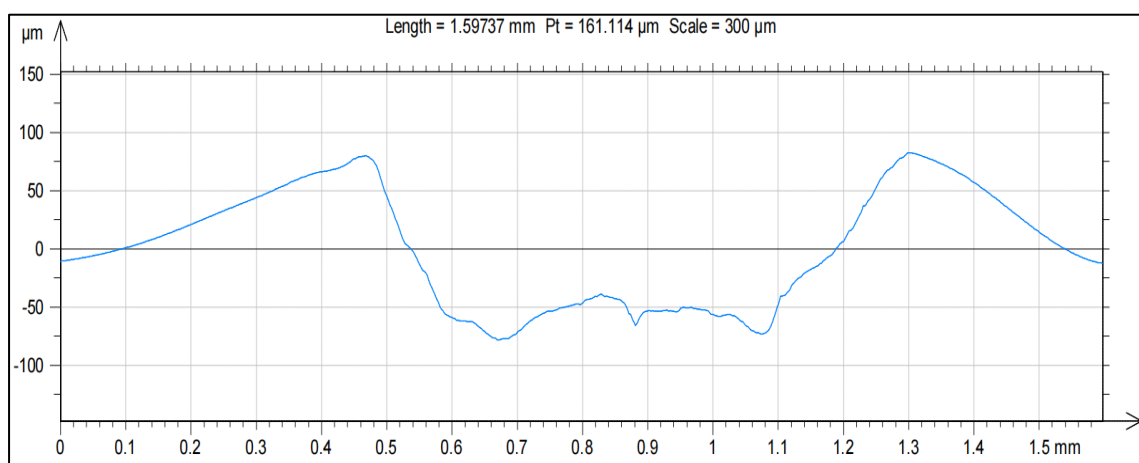


Figure 8.23 Surface roughness profile of the micro-channel (Machining in air medium)

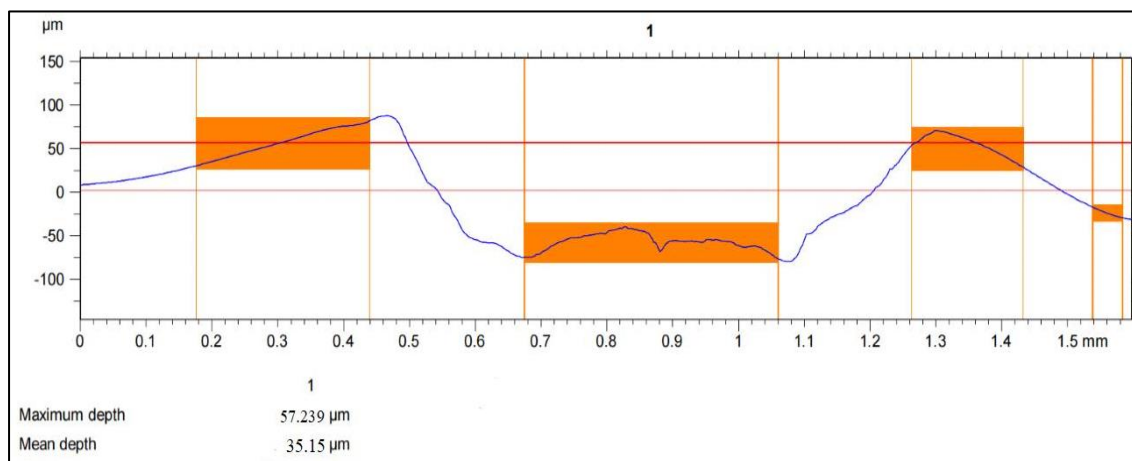


Figure 8.24 Depth profile of the micro-channel (Machining in air medium)

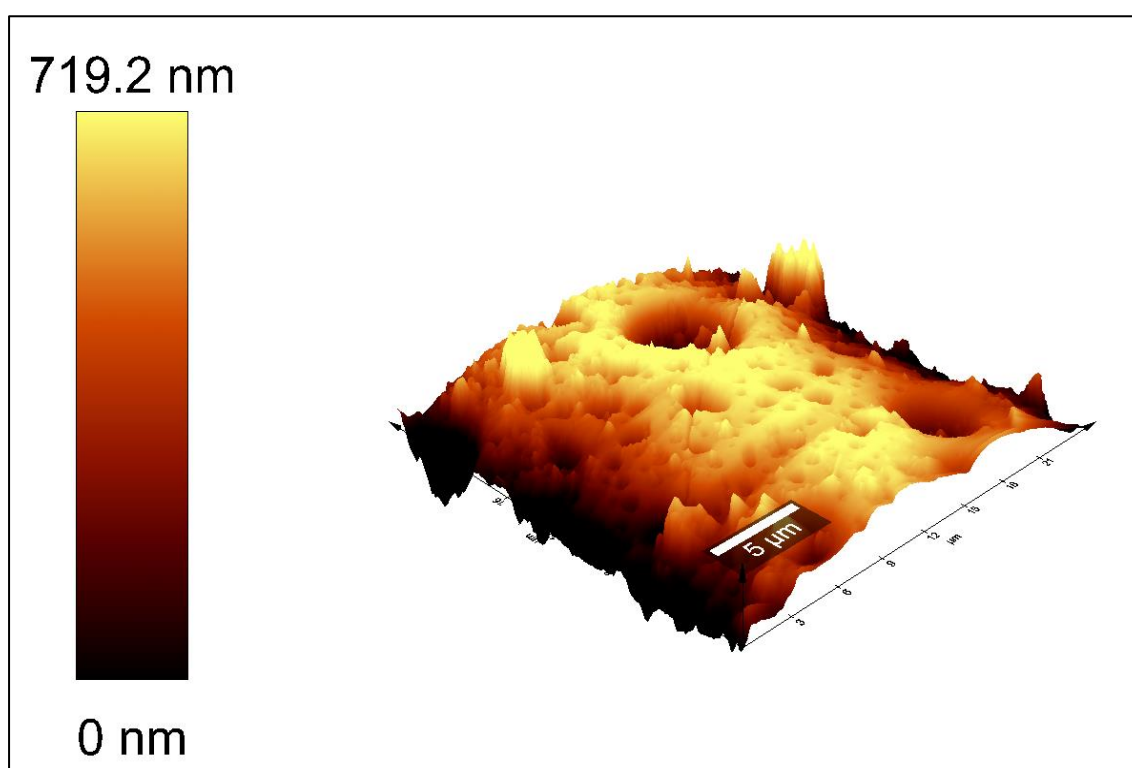


Figure 8.25 AFM image of the micro-channel (Nd:YAG laser transmission micro-machining in air medium)

8.7.2 Submerged in water

The topography and evaluation profile of the machined surface in submerged conditions is shown in Figure 8.26-8.28. Profile images (2D & 3D) are captured using a CCI microscope. It is observed that the channel surface is semi-uniform (i.e. absence of large craters, sharp peaks, and deep & narrow valleys in the machining area) whereas the depth of the profile is varied (i.e. depth decreases along the cutting direction). The maximum channel depth obtained at optimal cutting conditions is 41.256 μm , the mean depth of the channel is 34.95 μm and the kerf width is 23.04

μm . This is happening due to machining in submerged conditions (underwater) in fiber laser. In submerged conditions, water acts like a coolant and resists spattering and spreading of molten materials in the machining area. Although the majority of the molten materials are waved away, the remainder is instantly solidified and stacked onto the workpiece. In such circumstances, the surface roughness of the micro channel decreases in submerged water irrespective of open air. However, the depth profile becomes non-uniform due to the repeated melting of re-solidified materials along the feed direction. As PMMA is an advanced polymer, the melting underwater occurs slowly, but re-solidification takes place rapidly. For that reason, wide & deep crates, sharp hills, and narrow valleys are not produced in the machining zone. In addition, AFM image (shown in Figure 8.29) analysis has been carried out for in-depth understanding of the surface characteristics of machined surfaces. It is found from the AFM image that the maximum surface roughness obtained in optimal parameter settings is $0.40 \mu\text{m}$.

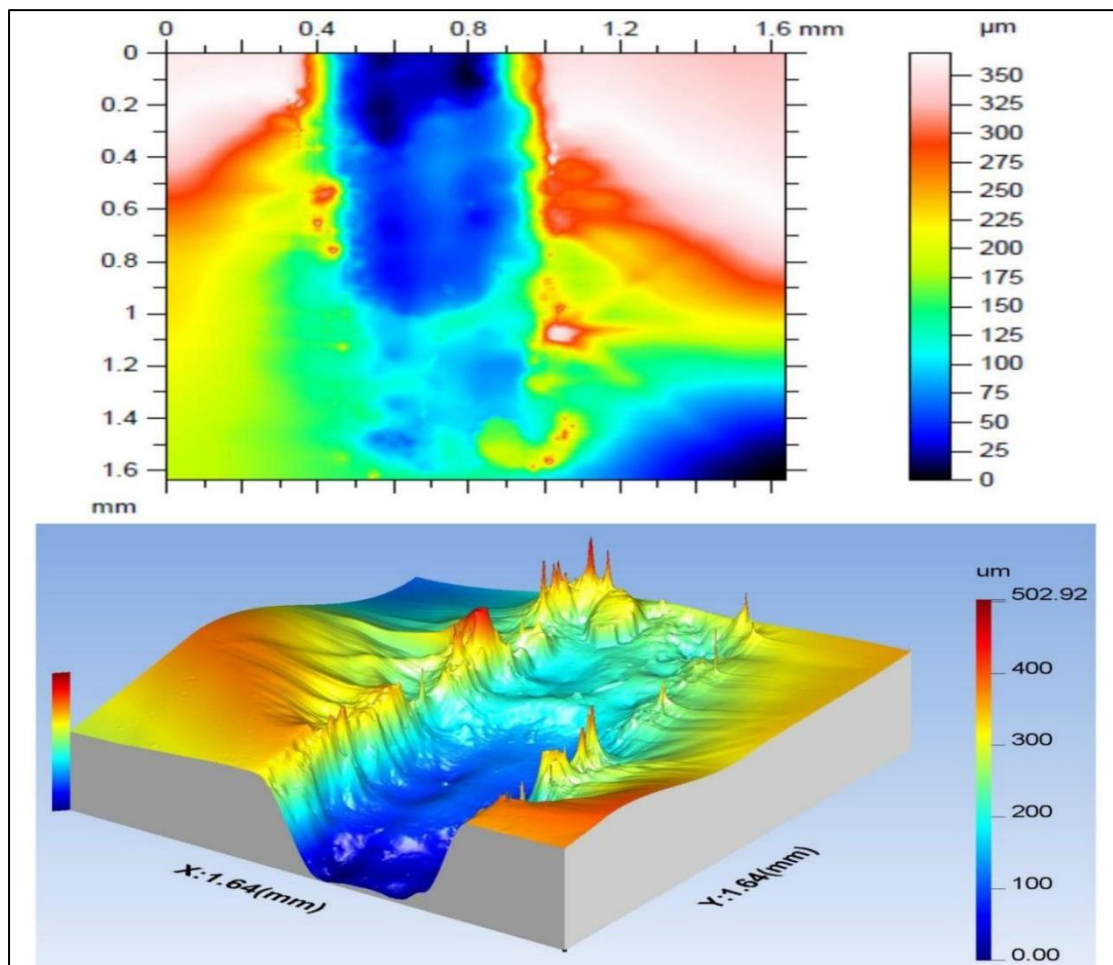


Figure 8.26 CCI image of the micro-channel (Fiber laser transmission micro-machining in underwater medium)

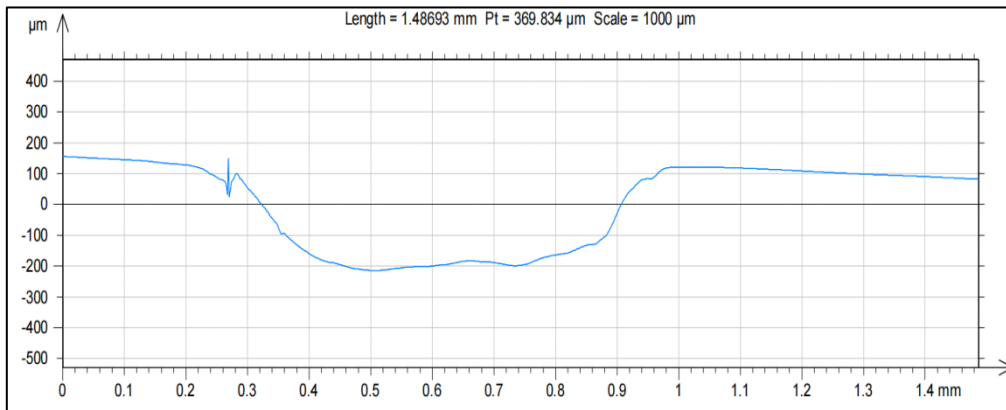


Figure 8.27 Surface profile of micro-channel (Machining in submerged medium)

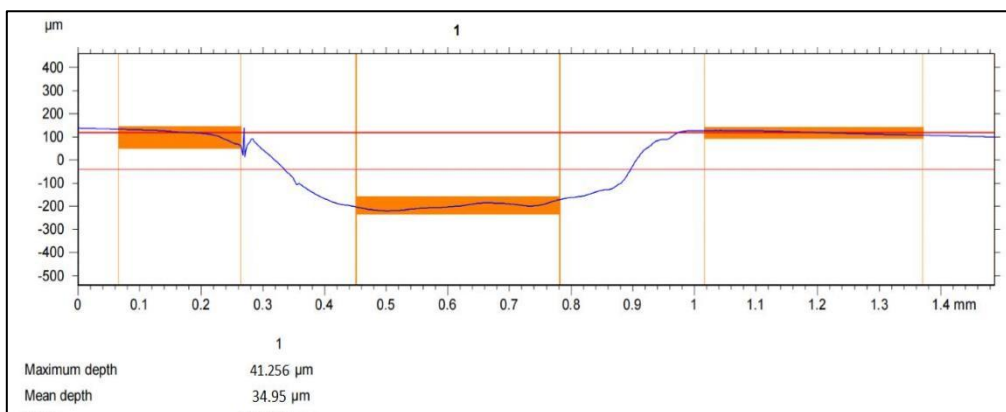


Figure 8.28 Depth profile of micro-channel (Machining in submerged medium)

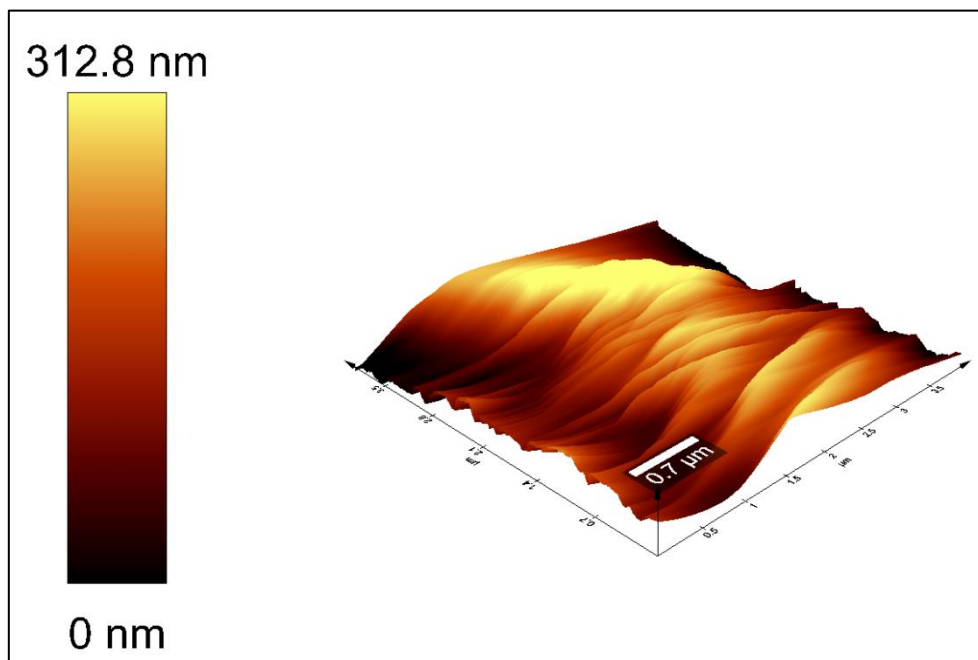


Figure 8.29 AFM image of the micro-channel (Fiber laser transmission micro-machining in underwater medium)

Chapter 9

GENERAL CONCLUSIONS AND FUTURE SCOPE OF THE WORK

9.1 General Conclusions

In the present research study, an extensive experimental investigation has been carried out on machining of thick transparent PMMA by CNC based nanosecond Pulsed Nd:YAG and fiber laser systems. Laser beam transmission machining process has been conducted on thick transparent PMMA to produce micro-channel under different assisted mediums. Qualitative and quantitative improvement of the micro channels has been explored for a better understanding of the accuracy features of the product. Additionally, mathematical modeling and optimization of the laser transmission process have been carried out to identify the process capability to its full extent. Major conclusion of the research work in line with the previously mentioned objectives is as follows:

1. Transparent PMMA (thickness = 11.324 mm) (polymethyl methacrylate) material has been selected for its wide application in research and industrial arena. As the black colour absorbs the maximum energy, a sellotape of black colour has been used as absorbent material for the present research work. With the help of X-Ray Diffraction test (XRD), the composition of the workpiece material, absorbent material i.e., black sellotape and micro-channel after machining, has been checked for confirmation of material characteristics which showed satisfactory results.
2. Different machining setups have been studied by performing pilot experiments to understand the design space to be chosen for final experimentation.
3. Laser transmission machining (material removal process) technique has been successfully carried out for micro-channeling operation on PMMA using low power laser of 50 watts and 75 watts average power.
4. It seems feasible to cut micro-channels on highly transmitted thick PMMA, with

75 watts, and 50 watts nanosecond pulsed Nd:YAG laser and fiber laser respectively in various environments. The experiments have been conducted in open atmosphere and in submerged conditions in de-ionized water by employing both Nd:YAG laser and fiber laser.

In this study, it has been observed that the change in standoff distance instead of proper focusing, hampered the micro-channel quality during laser transmission micro-channeling on highly transmitted PMMA. Standoff distance (focal distance) was kept constant and focused on the machining zone throughout the experimental procedure due to the aforementioned observations.

5. The following design specification/model has been set out for performing successful experimentation:
 - (i) Nd:YAG laser has been conducted and found suitable process parameters such as pulse frequency ranging between 25 kHz to 45 kHz, lamp current of 24 to 28 amps (9 watt to 11 watt), and cutting speed from 1.00 mm/sec to 2.00 mm/sec.
 - (ii) Trial experiments have also been conducted to carry out micro-channeling operation using fiber laser and found significant process parameters such as pulse frequency from 50 kHz to 70 kHz, working power of 13 to 17 % (6.5 watt to 8.5 watt), and cutting speed from 0.1 mm/sec to 0.6 mm/sec.
 - (iii) The effect of process parameters on machining responses has been experimentally studied using 20 sets of experiments designed on the basis of central composite design (CCD) technique of response surface methodology (RSM) approach.
 - (iv) Analysis of variance (ANOVA) analysis has been performed to check the statistical credibility of the machining variable on process outcome, i.e. depth of cut, kerf width, and HAZ width during Nd:YAG laser micro-channeling on thick PMMA.
6. The effect of different dominant process variable along with various assist mediums on machining characteristics has been discussed here intricately, two different mediums in terms of dry (with aid of open-air medium) and wet environment (submerged in de-ionized water) has been selected for performing

the micromachining operations. A rectangular shaped fixture is designed and developed with 3 mm thick transparent PMMA sheet to hold the workpiece in dry and in wet environment, de-ionized water has been used as a wet medium. Water is confined in the device in static mode and this steady state condition has been kept during each experimental run.

Following are the observations during micro-channeling operations on PMMA using Nd:YAG laser:

- (i) Due to the influence of spattering and shorter material interaction time, the kerf width of the micro-channels on PMMA tends to decrease as cutting speed is increased at various levels of laser power. For any value of laser power within the investigated range, the depth dimensions are notably low and tend to decrease at greater cutting speeds.
- (ii) The depth of cut and HAZ width of micro-channels varied significantly with pulse frequency and lamp current, while the kerf width of the micro-channels shrank significantly with decreasing lamp current and pulse frequency.
- (iii) At dry or air medium, single objective optimization results show that for obtaining maximum depth of cut 35.403 μm , a combination of pulse frequency of 30.20 kHz along with lamp current of 26.60 amps and cutting speed of 1.0 mm/sec is required. For achieving minimum kerf width (115.876 μm) along with minimum HAZ width (104.647 μm) the combination of the process parameters are pulse frequency of 39.80 kHz with lamp current of 24 amps, and cutting speed of 1.90 mm/sec; pulse frequency of 38.20 kHz with lamp current of 25.10 amps, and cutting speed of 2.0 mm/sec respectively. At wet or submerged in water medium, single objective optimization results show that for obtaining maximum depth of cut 108.469 μm , a combination of pulse frequency of 43.0 kHz along with lamp current of 26.40 amps and cutting speed of 1.0 mm/sec is required. For achieving minimum kerf width (132.561 μm) along with minimum HAZ width (55.301 μm) the combination of the process parameters are pulse frequency of 32.60 kHz with lamp current of 24 amps, and cutting speed of 2.0 mm/sec; pulse frequency of 45 kHz with lamp current of 25.80 amps, and cutting speed of 1.90 mm/sec respectively.

- (iv) Further, a multi-objective optimization at air medium is carried out to achieve the optimal results of depth of cut, kerf width, and HAZ width, which are 36.659 μm , 114.025 μm , and 102.319 μm respectively. The optimal parameter settings are pulse frequency of 32.60 kHz, lamp current of 24.42 amps and cutting speed of 1.90 mm/sec. Also, a multi-objective optimization at wet medium is also carried out to achieve the optimal results of depth of cut, kerf width, and HAZ width, which are 118.621 μm , 145.123 μm , and 49.362 μm respectively. The optimal parameter settings are pulse frequency of 25.20 kHz, lamp current of 24 amps and cutting speed of 2.0 mm/sec. The percentage of error obtained from the predicted and actual experimental results at optimal conditions is found very low at both the environmental condition, which signifies good acceptability of prediction analysis of Nd:YAG laser machining of micro-channels on PMMA.

Following are the investigations for micro-channeling operation on PMMA using fiber laser:

- (i) In-depth study of the performance characteristics of multi-diodes pumped fiber laser reveals that it is one of the most suitable machine tools to process difficult to machine materials in micro-domain. With the increment of cutting speed during different settings of laser power, the kerf width of the micro-channels on PMMA tends to reduce due to the effect of spattering and less material interaction time. The depth dimensions are significantly low and tend to decrease at higher cutting speeds for any value of laser power within the considered range.
- (ii) Depth of cut and HAZ width of the micro-channels varied with working power and pulse frequency considerably, although, the kerf width of the micro-channels reduces to a considerable extent with the decrement of working power and pulse frequency.
- (iii) At dry or air medium, single objective optimization results show that for obtaining maximum depth of cut 12.787 μm , a combination of pulse frequency of 50 kHz along with working power of 13 % (or 6.5 watt) and cutting speed of 0.6 mm/sec is required. For achieving minimum kerf width (22.705 μm) along with minimum HAZ width (5.982 μm) the combination of the process parameters are pulse frequency of 58.60 kHz with working

power of 13 %, and cutting speed of 0.59 mm/sec; pulse frequency of 70 kHz with working power of 15.128 %, and cutting speed of 0.578 mm/sec respectively. At wet or submerged water medium, single objective optimization results show that for obtaining maximum depth of cut 40.1695 μm , a combination of pulse frequency of 50 kHz along with working power of 15.98 % and cutting speed of 0.20 mm/sec is required. For achieving minimum kerf width (23.122 μm) along with minimum HAZ width (4.995 μm) the combination of the process parameters are pulse frequency of 54.02 kHz with working power of 13.43 %, and cutting speed of 0.20 mm/sec; pulse frequency of 66.011 kHz with working power of 14.253 %, and cutting speed of 0.548 mm/sec respectively.

- (iv) Multi-objective optimization at air medium is carried out to achieve the optimal results of depth of cut, kerf width, and HAZ width, which are 12.537 μm , 24.054 μm , and 5.982 μm respectively. The optimal parameter settings are pulse frequency of 51.30 kHz, working power of 13 %, and cutting speed of 0.6 mm/sec. Also a multi-objective optimization at wet medium is also carried out to achieve the optimal results of depth of cut, kerf width, and HAZ width, which are 36.329 μm , 25.344 μm , and 4.982 μm respectively. The optimal parameter settings are pulse frequency of 50.0 kHz, working power of 14.34 % (or 6.5 watt), and cutting speed of 0.20 mm/sec. The percentage of error obtained from the predicted and actual experimental results at optimal conditions is found very low at both the environmental condition, which signifies good acceptability of prediction analysis of fiber laser machining of micro-channels on PMMA.
7. It has been observed for Nd:YAG laser that the experimental results are significantly changed with the varying laser passes. It can be found that the depth of cut changes significantly with the changes of passes at a certain limit, i.e., after double pass, there are no significant changes are observed. The significant change is found at 28 amps of lamp current, pulse frequency at 35 kHz, 94% pulse width, and at 1.5mm/sec of cutting speed. It is also observed that the passes are taking a vital role in HAZ width. The most significant change is found at lamp current of 24 amps, pulse frequency at 25 kHz, 90% pulse width, and cutting speed at 2 mm/sec respectively. From the study, it is obtained that within the specific parametric range, the number of laser passes is a dominant factor

along with the other entire process variable up to a certain limit. It is also observed that an increase in number of laser pass during each experiment from two to three have a good effect on HAZ width but an adverse effect on depth of cut.

8. Comparative study in connection with different assist mediums has been successfully carried out with the following outcomes:

- (i) In the comparative study, it can be observed from the regression equation that the trends of the nature of parametric effect are almost the same in both the laser system at different environmental mediums on micro-channel characteristics (i.e., depth of cut, kerf width, and HAZ width).
- (ii) Parametric contribution from the ANOVA table shows the comparative effect on responses in different mediums.
- (iii) From multi-optimization, it is also observed that the optimal result differences in different environments.
- (iv) Average value of responses also showed the deviation of responses in different mediums.
- (v) The percentage of improvement has been calculated for Nd:YAG and fiber laser based on experimental results. It is found that the depth of cut improved 217% and 263% in Nd:YAG and fiber laser respectively. On the other hand, kerf width improved 52% and 56%, whereas HAZ width decreased with respect to air 36% and 13% in Nd:YAG and fiber laser respectively. The percentage of improvement is varied. It may be due to the beam diameter of both the lasers being different, as well as the parameter settings and generation of the laser system also being different, which may cause the differences.
- (vi) It can be concluded from the observations obtained from the CCI and AFM analysis of machined micro-channels that the underwater laser transmission micro-machining techniques employing both Nd:YAG and fiber lasers are superior w.r.t. the techniques when used in the dry medium. From the analysis, it is evident that the quality characteristics like, surface roughness, HAZ width, depth of cut, and kerf width obtained when machined in partially submerged condition are of far better quality than that of machined

micro-channel in dry medium, which illustrates the significance of underwater laser transmission micro-machining.

This research outcome provides useful information about the optimal machining of thick transparent PMMA to achieve the desired micro-machining quality in different applications like orthopedics, biomedical, DNA analysis, etc. It can be very helpful for advanced medical and research industries due to the aforesaid applications.

9.2 Future Scope of Work

During this research work some new ideas on laser beam micromachining have been grown up and based on which, the following studies can be conducted in the future.

1. To carry out laser micro-channeling process on PMMA with another assisted medium i.e., submerged in other liquid or application of other reactive or neutral gas assisted medium to understand the effect of different environments of laser micromachining operation on PMMA.
2. To carry out further study on different transparent materials for better understanding and generate technology guidance for laser processing of these kinds of engineering materials.
3. To study the effect of water flow during laser micromachining of PMMA, a new setup can be developed and a comparative study can be carried out between laser micromachining at submerged conditions in a confined state and under steady-state flow conditions.
4. To carry out further study on different absorbent materials to get better results in transmission technique.
5. The analytical study to understand the laser machining in case of transparent materials could be very good future work.

BIBLIOGRAPHY

1. Yim, Y.S., Shin, K.S., Hur, S.H., Lee, J.D., Balk, I.G., Kim, H.S., Chai, S.J., Choi, E.Y., Park, M.C., Eun, D.S. and Lee, S.B., 2003, December. 70nm NAND flash technology with 0.025/ μm /sup 2/cell size for 4Gb flash memory. In IEEE International Electron Devices Meeting 2003 (pp. 34-41). IEEE.
2. Masuzawa, T. and Tönshoff, H.K., 1997. Three-dimensional micromachining by machine tools. *CIRP Annals*, 46(2), pp. 621-628.
3. Masuzawa, T., 2000. State of The Art of Micromachining. *CIRP Annals-Manufacturing Technology*, 49(2), pp. 473-488. DOI: 10.1016/S0007-8506(07)63451-9.
4. Sen, A., Doloi, B. and Bhattacharyya, B., 2017. Fiber laser micro-machining of engineering materials. In *Non-traditional Micromachining Processes* (pp. 227-252). Springer International Publishing.
5. Dahotre, N.B. and Harimkar, S., 2008. *Laser fabrication and machining of materials*. Springer Science & Business Media.
6. Meijer, J., 2004. Laser beam machining (LBM), state of the art and new opportunities. *Journal of Materials Processing Technology*, 149(1-3), pp. 2-17.
7. Hutchinson, M.H.R., 2003. Applications of ultra-high field lasers. *Spectrochimica Acta Part B: Atomic Spectroscopy*, 58(6), pp. 1155-1161.
8. Nath, A.K., 2013. High power lasers in material processing applications: an overview of recent developments. *Laser-Assisted Fabrication of Materials*, pp. 69-111.
9. Woods, S., 2009. Understanding Materials Processing Lasers: A Comprehensive Overview Covering the Capabilities and Applicability of the Major Systems. *Laser Technik Journal*, 6(5), pp. 23-26.
10. Von, A. M., 1987. *Laser-beam Interactions with Materials, Physical Principles and Applications*, Springer-Verlag, Berlin, Heidelberg, ISBN: 0933-033X/ 2196-2812/ 978-3-642-97007-8.

11. Steen, W.M., 1991. *Laser Materials Processing*, Springer-Verlag London, ISBN: 978-1-4471-3820-4.
12. Welch, A.J. and Gardner, C., 2002. Optical and thermal response of tissue to laser radiation. *Lasers in Medicine*, pp. 27-45.
13. Duley, W.W., 1983. *Laser Processing and Analysis of Materials*. Plenum Press, New York, ISBN 978-1-4757-0195-1 82-18611/ 978-1-4757-0193-7.
14. Von Allmen, M.F. and Bertolotti, M., 1983. *Physical Processes in Laser-Materials Interactions*.
15. Perry, M.D., Pennington, D., Stuart, B.C., Tietbohl, G., Britten, J.A., Brown, C., Herman, S., Golick, B., Kartz, M., Miller, J. and Powell, H.T., 1999. Petawatt laser pulses. *Optics Letters*, 24(3), pp.160-162.
16. French, P.W., Hand, D.P., Peters, C., Shannon, G.J., Byrd, P. and Steen, W.M., 1998. Investigation of the Nd: YAG laser percussion drilling process using high speed filming. *ICALEO 98 Proc*, 85, pp. 1-10.
17. Collins, G.W., Celliers, P.M., Da Silva, L.B., Cauble, R., Gold, D.M., Foord, M.E., Holmes, N.C., Hammel, B.A., Wallace, R.J. and Ng, A., 2001. Temperature measurements of shock compressed liquid deuterium up to 230 GPa. *Physical Review Letters*, 87(16), p.165504.
18. Baeuerle, D., 2000. *Laser Processing and Chemistry* Springer Verlag. Heidelberg Berlin, 13.
19. Li, L. and Achara, C., 2004. Chemical assisted laser machining for the minimisation of recast and heat affected zone. *CIRP Annals*, 53(1), pp. 175-178.
20. Datta, M., Romankiw, L.T., Vigliotti, D.R. and Von Gutfeld, R.J., 1987. Laser etching of metals in neutral salt solutions. *Applied Physics Letters*, 51(24), pp. 2040-2042.
21. Kim, D. and Lee, H., 2001. Enhanced ablation and photoacoustic excitation in near-threshold laser ablation of liquid-coated surfaces. *Journal of Applied Physics*, 89(10), pp. 5703-5706.

22. Roy, N., Kuar, A.S. and Mitra, S., 2017. Underwater pulsed laser beam cutting with a case study. In *Microfabrication and Precision Engineering* (pp. 189-212). Woodhead Publishing.
23. Kleine, K.F., Whitney, B. and Watkins, K.G., 2002, October. Use of fiber lasers for micro cutting applications in the medical device industry. In *International Congress on Applications of Lasers & Electro-Optics* (Vol. 2002, No. 1, p. 70). Laser Institute of America.
24. Demir, A.G., Previtali, B., Colombo, D., Ge, Q., Vedani, M., Petrini, L., Wu, W. and Biffi, C.A., 2012, February. Fiber laser micromachining of magnesium alloy tubes for biocompatible and biodegradable cardiovascular stents. In *Fiber Lasers IX: Technology, Systems, and Applications* (Vol. 8237, pp. 474-482). SPIE.
25. Holmes, A.S., 2001, June. Laser fabrication and assembly processes for MEMS. In *Laser Applications in Microelectronic and Optoelectronic Manufacturing VI* (Vol. 4274, pp. 297-306). SPIE.
26. Presby, H.M., Benner, A.F. and Edwards, C.A., 1990. Laser micromachining of efficient fiber microlenses. *Applied Optics*, 29(18), pp.2692-2695.
27. Giorleo, L., Ceretti, E. and Giardini, C., 2016. Optimization of laser micromachining process for biomedical device fabrication. *The International Journal of Advanced Manufacturing Technology*, 82(5), pp. 901-907.
28. Miller, P.R., Aggarwal, R., Doraiswamy, A., Lin, Y.J., Lee, Y.S. and Narayan, R.J., 2009. Laser micromachining for biomedical applications. *JOM*, 61(9), pp. 35-40.
29. Berrie, P.G. and Birkett, F.N., 1980. The drilling and cutting of polymethyl methacrylate (Perspex) by CO₂ laser. *Optics and Lasers in Engineering*, 1(2), pp. 107-129.
30. Zhou, B., Kane, T.J., Dixon, G.J. and Byer, R.L., 1985. Efficient, frequency-stable laser-diode-pumped Nd: YAG laser. *Optics Letters*, 10(2), pp. 62-64.
31. Trotta, G., Volpe, A., Ancona, A. and Fassi, I., 2018. Flexible micro manufacturing platform for the fabrication of PMMA microfluidic devices. *Journal of Manufacturing Processes*, 35, pp. 107-117.

32. Guler, M.T., Inal, M. and Bilican, I., 2021. CO₂ laser machining for microfluidics mold fabrication from PMMA with applications on viscoelastic focusing, electrospun nanofiber production, and droplet generation. *Journal of Industrial and Engineering Chemistry*, 98, pp. 340-349.
33. McCann, R., Bagga, K., Groarke, R., Stalcup, A., Vázquez, M. and Brabazon, D., 2016. Microchannel fabrication on cyclic olefin polymer substrates via 1064 nm Nd: YAG laser ablation. *Applied Surface Science*, 387, pp. 603-608.
34. Pflöging, W., Kohler, R., Schierjott, P. and Hoffmann, W., 2009. Laser patterning and packaging of CCD-CE-Chips made of PMMA. *Sensors and Actuators B: Chemical*, 138(1), pp. 336-343.
35. Prakash, S. and Kumar, S., 2021. Determining the suitable CO₂ laser based technique for microchannel fabrication on PMMA. *Optics & Laser Technology*, 139, p.107017.
36. Zheng, C., Hu, A., Kihm, K.D., Ma, Q., Li, R., Chen, T. and Duley, W.W., 2015. Femtosecond laser fabrication of cavity microball lens (CMBL) inside a PMMA substrate for super- wide angle imaging. *Small*, 11(25), pp.3007-3016.
37. Prakash, S. and Kumar, S., 2017. Fabrication of rectangular cross-sectional microchannels on PMMA with a CO₂ laser and underwater fabricated copper mask. *Optics & Laser Technology*, 94, pp. 180-192.
38. Jiang, C.Y., Lau, W.S., Yue, T.M. and Chiang, L., 1993. On the maximum depth and profile of cut in pulsed Nd: YAG laser machining. *CIRP Annals*, 42(1), pp. 223-226.
39. Tunna, L., Kearns, A., O'Neill, W. and Sutcliffe, C.J., 2001. Micromachining of copper using Nd: YAG laser radiation at 1064, 532, and 355 nm wavelengths. *Optics & Laser Technology*, 33(3), pp. 135-143.
40. Tsai, C.H. and Chen, H.W., 2003. Laser cutting of thick ceramic substrates by controlled fracture technique. *Journal of Materials Processing Technology*, 136(1-3), pp. 166-173.
41. Kuar, A.S., Doloi, B. and Bhattacharyya, B., 2006. Modelling and analysis of pulsed Nd: YAG laser machining characteristics during micro-drilling of zirconia

- (ZrO₂). *International Journal of Machine Tools and Manufacture*, 46(12-13), pp. 1301-1310.
42. Samant, A.N. and Dahotre, N.B., 2008. Computational predictions in single-dimensional laser machining of alumina. *International Journal of Machine Tools and Manufacture*, 48(12-13), pp. 1345-1353.
 43. Biswas, R., Kuar, A.S., Sarkar, S. and Mitra, S., 2010. A parametric study of pulsed Nd: YAG laser micro-drilling of gamma-titanium aluminide. *Optics & Laser Technology*, 42(1), pp. 23-31.
 44. Kuar, A.S., Acherjee, B., Ganguly, D. and Mitra, S., 2012. Optimization of Nd: YAG laser parameters for microdrilling of alumina with multiquality characteristics via grey-Taguchi method. *Materials and Manufacturing Processes*, 27(3), pp. 329-336.
 45. Das, R.N., Egitto, F.D., Lauffer, J.M. and Markovich, V.R., 2007, May. Laser micromachining of nanocomposite-based flexible embedded capacitors. In 2007 Proceedings 57th Electronic Components and Technology Conference (pp. 435-441). IEEE.
 46. Hong, T.F., Ju, W.J., Wu, M.C., Tai, C.H., Tsai, C.H. and Fu, L.M., 2010. Rapid prototyping of PMMA microfluidic chips utilizing a CO₂ laser. *Microfluidics and Nanofluidics*, 9(6), pp. 1125-1133.
 47. Chang, T.C. and Molian, P.A., 1999. Excimer pulsed laser ablation of polymers in air and liquids for micromachining applications. *Journal of Manufacturing Systems*, 18(2), pp. 1-17.
 48. Teixidor, D., Thepsonthi, T., Ciurana, J. and Özel, T., 2012. Nanosecond pulsed laser micromachining of PMMA-based microfluidic channels. *Journal of Manufacturing Processes*, 14(4), pp. 435-442.
 49. Kallepalli, D. L. N., Desai, N. R. and Soma, V. R., 2010. Fabrication and optical characterization of microstructures in poly (methyl-methacrylate) and poly (dimethylsiloxane) using femtosecond pulses for photonic and microfluidic applications. *APPLIED OPTICS*, Optical Society of America, 49(13), pp. 2475-2489.

50. Baudach, S., Bonse, J., Krüger, J. and Kautek, W., 2000. Ultrashort pulse laser ablation of polycarbonate and polymethylmethacrylate. *Applied Surface Science*, 154, pp. 555-560.
51. Yuan, D. and Das, S., 2007. Experimental and theoretical analysis of direct-write laser micromachining of polymethyl methacrylate by CO₂ laser ablation. *Journal of Applied Physics*, 101(2), p.024901.
52. Liu, Z.Q., Feng, Y. and Yi, X.S., 2000. Coupling effects of the number of pulses, pulse repetition rate and fluence during laser PMMA ablation. *Applied Surface Science*, 165(4), pp. 303-308.
53. Marco, C. D., Suriano, R., Levi, M., Turri, S., Eaton, S., Cerullo, G. and Osellame, R., 2012. Femtosecond laser fabrication and characterization of microchannels and waveguides in methacrylate-based polymers. *Microsystem Technology*, Vol. 18, pp. 183–190, DOI: 10.1007/s00542-011-1347-2.
54. Day, D. and Gu, M., 2005, December. Microchannel fabrication in PMMA based on localized heating using high-repetition rate femtosecond pulses. In *Device and Process Technologies for Microelectronics, MEMS, and Photonics IV* (Vol. 6037, pp. 24-31). SPIE.
55. Prakash, S., Acherjee, B., Kuar, A.S. and Mitra, S., 2013. An experimental investigation on Nd: YAG laser microchanneling on polymethyl methacrylate submerged in water. *Proceedings of the Institution of Mechanical Engineers, Part B: Journal of Engineering Manufacture*, 227(4), pp. 508-519.
56. Riahi, M., 2012. Fabrication of a passive 3D mixer using CO₂ laser ablation of PMMA and PDMS moldings. *Microchemical Journal*, 100, pp. 14-20.
57. Klank, H., Kutter, J.P. and Geschke, O., 2002. CO₂-laser micromachining and back-end processing for rapid production of PMMA-based microfluidic systems. *Lab on a Chip*, 2(4), pp. 242-246.
58. Florian, C., Caballero-Lucas, F., Fernández-Pradas, J.M., Morenza, J.L. and Serra, P., 2014. Surface ablation of transparent polymers with femtosecond laser pulses. *Applied Surface Science*, 302, pp. 226-230.

59. Day, D. and Gu, M., 2005. Microchannel fabrication in PMMA based on localized heating by nanojoule high repetition rate femtosecond pulses. *Optics Express*, 13(16), pp. 5939-5946.
60. Romoli, L., Tantussi, G. and Dini, G., 2007. Layered laser vaporization of PMMA manufacturing 3D mould cavities. *CIRP Annals*, 56(1), pp. 209-212.
61. Teixidor, D., Thepsonthi, T., Ciurana, J. and Özel, T., 2012. Nanosecond pulsed laser micromachining of PMMA-based microfluidic channels. *Journal of Manufacturing Processes*, 14(4), pp. 435-442.
62. Choudhury, I.A. and Shirley, S., 2010. Laser cutting of polymeric materials: An experimental investigation. *Optics & Laser Technology*, 42(3), pp. 503-508.
63. Romoli, L., Tantussi, G. and Dini, G., 2011. Experimental approach to the laser machining of PMMA substrates for the fabrication of microfluidic devices. *Optics and Lasers in Engineering*, 49(3), pp. 419-427.
64. Bhuyan, M.K., Courvoisier, F., Lacourt, P.A., Jacquot, M., Furfaro, L., Withford, M.J. and Dudley, J.M., 2010. High aspect ratio taper-free micro-channel fabrication using femtosecond Bessel beams. *Applied Physics Letters*, American Institute of Physics, 97 (8), pp. 081102.
65. Hong, T.F., Ju, W.J., Wu, M.C., Tai, C.H., Tsai, C.H. and Fu, L.M., 2010. Rapid prototyping of PMMA microfluidic chips utilizing a CO₂ laser. *Microfluidics and Nanofluidics*, 9(6), pp. 1125-1133.
66. Wang, Z.K., Lim, M.H., Lian, D.M. and Zheng, H.Y., 2010, December. Computational profiling of laser processing glass substrate for microchannel fabrication. In *International Conference on Computational Problem-Solving* (pp. 55-58). IEEE.
67. Darvishi, S., Cubaud, T. and Longtin, J.P., 2012. Ultrafast laser machining of tapered microchannels in glass and PDMS. *Optics and Lasers in Engineering*, 50(2), pp. 210-214.
68. Huang, Y., Liu, S., Yang, W. and Yu, C., 2010. Surface roughness analysis and improvement of PMMA-based microfluidic chip chambers by CO₂ laser cutting. *Applied Surface Science*, 256(6), pp. 1675-1678.

69. Sola, D., Escartin, A., Cases, R. and Pena, J.I., 2011. Laser ablation of advanced ceramics and glass-ceramic materials: Reference position dependence. *Applied Surface Science*, 257(12), pp. 5413-5419.
70. Acherjee, B., Kuar, A.S., Mitra, S. and Misra, D., 2012. Modeling and analysis of simultaneous laser transmission welding of polycarbonates using an FEM and RSM combined approach. *Optics & Laser Technology*, 44(4), pp. 995-1006.
71. Choudhury, I.A., Chong, W.C. and Vahid, G., 2012. Hole qualities in laser trepanning of polymeric materials. *Optics and Lasers in Engineering*, 50(9), pp. 1297-1305.
72. Krüger, J., Martin, S., Mädebach, H., Urech, L., Lippert, T., Wokaun, A. and Kautek, W., 2005. Femto- and nanosecond laser treatment of doped polymethylmethacrylate. *Applied Surface Science*, 247(1-4), pp. 406-411.
73. Yalukova, O. and Sarady, I., 2006. Investigation of interaction mechanisms in laser drilling of thermoplastic and thermoset polymers using different wavelengths. *Composites Science and Technology*, 66(10), pp. 1289-1296.
74. Jiang, X., Chandrasekar, S. and Wang, C., 2015. A laser microwelding method for assembly of polymer based microfluidic devices. *Optics and Lasers in Engineering*, 66, pp. 98-104.
75. Huang, Y., Liu, S., Yang, W. and Yu, C., 2010. Surface roughness analysis and improvement of PMMA-based microfluidic chip chambers by CO₂ laser cutting. *Applied Surface Science*, 256(6), pp. 1675-1678.
76. Waddell, E.A., Locascio, L.E. and Kramer, G.W., 2002. UV laser micromachining of polymers for microfluidic applications. *JALA: Journal of the Association for Laboratory Automation*, 7(1), pp. 78-82.
77. Hong, T.F., Ju, W.J., Wu, M.C., Tai, C.H., Tsai, C.H. and Fu, L.M., 2010. Rapid prototyping of PMMA microfluidic chips utilizing a CO₂ laser. *Microfluidics and Nanofluidics*, 9(6), pp. 1125-1133.
78. Klank, H., Kutter, J.P. and Geschke, O., 2002. CO₂-laser micromachining and back-end processing for rapid production of PMMA-based microfluidic systems. *Lab on a Chip*, 2(4), pp. 242-246.

79. Yuan, D. and Das, S., 2007. Experimental and theoretical analysis of direct-write laser micromachining of polymethyl methacrylate by CO₂ laser ablation. *Journal of Applied Physics*, 101(2), p.024901.
80. Jensen, M.F., Noerholm, M., Christensen, L.H. and Geschke, O., 2003. Microstructure fabrication with a CO₂ laser system: characterization and fabrication of cavities produced by raster scanning of the laser beam. *Lab on a Chip*, 3(4), pp. 302-307.
81. Qi, H., Chen, T., Yao, L. and Zuo, T., 2009. Micromachining of microchannel on the polycarbonate substrate with CO₂ laser direct-writing ablation. *Optics and Lasers in Engineering*, 47(5), pp. 594-598.
82. Kim, C.S., Ahn, S.H. and Jang, D.Y., 2012. Developments in micro/nanoscale fabrication by focused ion beams. *Vacuum*, 86(8), pp. 1014-1035.
83. Khan Malek, C.G., 2006. Laser processing for bio-microfluidics applications (part II). *Analytical and Bioanalytical Chemistry*, 385(8), pp. 1362-1369.
84. Kruusing, A., 2004. Underwater and water-assisted laser processing: Part 2—Etching, cutting and rarely used methods. *Optics and Lasers in Engineering*, 41(2), pp. 329-352.
85. Gomez, D., Goenaga, I., Lizuain, I. and Ozaita, M., 2005. Femtosecond laser ablation for microfluidics. *Optical Engineering*, 44(5), p.051105.
86. Cheng, J.Y., Wei, C.W., Hsu, K.H. and Young, T.H., 2004. Direct-write laser micromachining and universal surface modification of PMMA for device development. *Sensors and Actuators B: Chemical*, 99(1), pp. 186-196.
87. Wu, C.Y., Shu, C.W. and Yeh, Z.C., 2006. Effects of excimer laser illumination on microdrilling into an oblique polymer surface. *Optics and Lasers in Engineering*, 44(8), pp.842-857.
88. Pan, C.T. and Hocheng, H., 1996. The anisotropic heat-affected zone in the laser grooving of fiber-reinforced composite material. *Journal of Materials Processing Technology*, 62(1-3), pp. 54-60.
89. Yilbas, B.S., 1997. Parametric study to improve laser hole drilling process. *Journal of Materials Processing Technology*, 70(1-3), pp. 264-273.

90. Yilbas, B.S., 1997. A study into CO₂ laser cutting process. *Heat and Mass Transfer*, 32(3), pp. 175-180.
91. Mathew, J., Goswami, G.L., Ramakrishnan, N. and Naik, N.K., 1999. Parametric studies on pulsed Nd: YAG laser cutting of carbon fibre reinforced plastic composites. *Journal of Materials Processing Technology*, 89, pp. 198-203.
92. Kaebernick, H., Bicleanu, D. and Brandt, M., 1999. Theoretical and experimental investigation of pulsed laser cutting. *CIRP Annals*, 48(1), pp. 163-166.
93. Low, D.K.Y., Li, L. and Corfe, A.G., 2001. Characteristics of spatter formation under the effects of different laser parameters during laser drilling. *Journal of Materials Processing Technology*, 118(1-3), pp. 179-186.
94. Most, D., Choi, J., Belenky, L.J. and Eom, C.B., 2003. Laser micromachining of SrTiO₃ single crystal. *Solid-State Electronics*, 47(12), pp. 2249-2253.
95. Booth, H.J., 2004. Recent applications of pulsed lasers in advanced materials processing. *Thin Solid Films*, 453, pp. 450-457.
96. Abedin, K.M., Coutts, D.W. and Webb, C.E., 2004. Enhanced efficiency and pulse-adjacency effects in high-repetition-rate laser machining. *Applied Physics A*, 78(5), pp. 737-740.
97. Nikumb, S., Chen, Q., Li, C., Reshef, H., Zheng, H.Y., Qiu, H. and Low, D., 2005. Precision glass machining, drilling and profile cutting by short pulse lasers. *Thin Solid Films*, 477(1-2), pp. 216-221.
98. Gillner, A., Holtkamp, J., Hartmann, C., Olowinsky, A., Gedicke, J., Klages, K., Bosse, L. and Bayer, A., 2005. Laser applications in microtechnology. *Journal of Materials Processing Technology*, 167(2-3), pp. 494-498.
99. Chen, T.C. and Darling, R.B., 2005. Parametric studies on pulsed near ultraviolet frequency tripled Nd: YAG laser micromachining of sapphire and silicon. *Journal of Materials Processing Technology*, 169(2), pp. 214-218.
100. Kuar, A.S., Paul, G. and Mitra, S., 2006. Nd: YAG laser micromachining of alumina–aluminium interpenetrating phase composite using response surface methodology. *International Journal of Machining and Machinability of Materials*, 1(4), pp. 432-444.

101. Beal, V.E., Erasenthiran, P., Hopkinson, N., Dickens, P. and Ahrens, C.H., 2006. Optimisation of processing parameters in laser fused H13/Cu materials using response surface method (RSM). *Journal of Materials Processing Technology*, 174(1-3), pp. 145-154.
102. Yung, W.K., Wu, J., Yue, T.M., Zhu, B.L. and Lee, C.P., 2007. Nd: YAG laser drilling in epoxy resin/AlN composites material. *Composites Part A: Applied Science and Manufacturing*, 38(9), pp. 2055-2064.
103. Karazi, S.M., Issa, A. and Brabazon, D., 2009. Comparison of ANN and DoE for the prediction of laser-machined micro-channel dimensions. *Optics and Lasers in Engineering*, 47(9), pp. 956-964.
104. Niino, H. and Kurosaki, R., 2011, February. Laser cutting of carbon fiber reinforced plastics (CFRP) by UV pulsed laser ablation. In *Laser Applications in Microelectronic and Optoelectronic Manufacturing (LAMOM) XVI* (Vol. 7920, pp. 240-244). SPIE.
105. Jaeschke, P., Wippo, V., Bluemel, S., Staehr, R. and Dittmar, H., 2018. Laser machining of carbon fiber-reinforced plastic composites. In *Advances in Laser Materials Processing* (pp. 121-152). Woodhead Publishing.
106. Herzog, D., Schmidt-Lehr, M., Oberlander, M., Canisius, M., Radek, M. and Emmelmann, C., 2016. Laser cutting of carbon fibre reinforced plastics of high thickness. *Materials & Design*, 92, pp. 742-749.
107. Mizunami, T. and Ehara, A., 2011. Femtosecond-pulsed laser micromachining and optical damage by an erbium-doped fiber-laser system. *Microelectronic Engineering*, 88(8), pp. 2334-2337.
108. Liu, L., Li, D.B., Tong, Y.F. and Zhu, Y.F., 2016. Fiber laser micromachining of thin NiTi tubes for shape memory vascular stents. *Applied Physics A*, 122(7), pp. 1-9.
109. Kleine, K.F. and Watkins, K.G., 2003, July. Fiber laser for micro-cutting of metals. In *Advances in Fiber Lasers* (Vol. 4974, pp. 184-192). SPIE.
110. Streifer, W., Scifres, D.R., Harnagel, G.L., Welch, D.F., Berger, J. and Sakamoto, M., 1988. Advances in diode laser pumps. *IEEE Journal of Quantum Electronics*, 24(6), pp. 883-894.

111. Ghoochani, D.E., Biglari, F.R. and Pazokian, H., 2019. Pulsed laser micro-machining of polymer for micro-channel fabrication: Theory and experiment. *Infrared Physics & Technology*, 102, p.103068.
112. Bundalo, I.L., Nielsen, K., Markos, C. and Bang, O., 2014. Bragg grating writing in PMMA microstructured polymer optical fibers in less than 7 minutes. *Optics Express*, 22(5), pp. 5270-5276.
113. Laser manual for Nd:YAG laser, Sahajanand Laser Technology, Ahemadabad, India.
114. Thyagarajan, K. and Ghatak, A.K., 1981. *Lasers: theory and applications*. Plenum Press, New York.
115. Lotsch, H.K.V., 2014. *Springer Series in Optical Sciences*, Vol.182, Springer, Atlanta. ISBN: 978-3-642-45084-6.
116. Jauregui, C., Limpert, J. and Tünnermann, A., 2013. High-power fibre lasers. *Nature photonics*, 7(11), pp. 861-867.
117. Ebewele, R.O., 2000. *Polymer Science and Technology*, ISBN: 9780429127922, DOI: 10.1201/9781420057805.
118. Low, D.K.Y., Li, L. and Byrd, P.J., 2001. The influence of temporal pulse train modulation during laser percussion drilling. *Optics and Lasers in Engineering*, 35(3), pp. 149-164.